BANDGAP ENGINEERING OF 2D SEMICONDUCTORS FOR QUANTUM AND OPTOELECTRONIC TECHNOLOGIES

by

John Pierce Fix

A thesis submitted in partial fulfillment
of the requirements for the degree

of

Doctor of Philosophy

in

Materials Science

MONTANA STATE UNIVERSITY
Bozeman, Montana

December 2025

DEDICATION

To my parents
Debra Schultz and Penn Fix

And to my sister
Louise Fix

Thank you for your support.
I could not have done this without you.

ACKNOWLEDGEMENTS

I would like to acknowledge the support of Dr. Nicholas J. Borys, the MonArk Quantum Foundry, and Idaho National Laboratory for their support throughout this work. I also want to thank my past and present colleagues in the Borys Lab Group for motivating me to leave no stone unturned throughout this process. Many of the results presented in this thesis were refined through their insightful questions and constructive critiques.

TABLE OF CONTENTS

TABLE OF CONTENTS CONTINUED

TABLE OF CONTENTS CONTINUED

TABLE OF CONTENTS CONTINUED

LIST OF TABLES

LIST OF FIGURES

Figure Page

LIST OF FIGURES CONTINUED

Figure Page

LIST OF FIGURES CONTINUED

Figure Page

LIST OF FIGURES CONTINUED

LIST OF FIGURES CONTINUED

Figure Page

LIST OF FIGURES CONTINUED

Figure Page

LIST OF FIGURES CONTINUED

LIST OF FIGURES CONTINUED

Figure Page

LIST OF FIGURES CONTINUED

LIST OF FIGURES CONTINUED

Figure Page

LIST OF FIGURES CONTINUED

Figure Page

LIST OF FIGURES CONTINUED

Figure Page

LIST OF FIGURES CONTINUED

Figure Page

LIST OF FIGURES CONTINUED

Figure Page

LIST OF FIGURES CONTINUED

LIST OF FIGURES CONTINUED

Figure Page

LIST OF FIGURES CONTINUED

Figure Page

ABSTRACT

Two-dimensional semiconductors such as transition metal dichalcogenides and thin films of gallium nitride are promising platforms for applications in quantum and optoelectronic technologies. These materials can host quantum emitters, which are key components of many quantum devices that rely on light in some form. Quantum emitters are atom-like states embedded in solid materials that emit single photons in narrow energy bands. In two-dimensional semiconductors, quantum emitters have been realized by inducing localized strain or by dilute doping, both of which create in-gap defect states and locally modulate the band gap. Understanding how these processes alter the band structure of two-dimensional semiconductors can provide insight into the formation mechanisms of quantum emitters, ultimately enabling greater control of their properties for technological applications. This dissertation presents work that (i) investigates the optical properties at the interface of a transition metal dichalcogenide lateral heterostructure that may host quantum emitters, (ii) induces quantum emitters in nanoindented transition metal dichalcogenides, and (iii) reports narrow, sub-bandgap emission from thin films of uranium-doped gallium nitride, evidencing a new set of potential actinide-based quantum emitter states. Room and low-temperature spectroscopies, sub-diffraction-limited spectroscopy, and atomic force microscopy were utilized to perform this work. To grow the novel uranium-doped gallium nitride molecular beam epitaxy was used. Together, these studies advance understanding of how strain-induced techniques, such as nanoindentation, can be used to control quantum emitter formation. Furthermore, this work introduces two novel material systems—the lateral heterostructure interface and uranium-doped gallium thin films—as new platforms to explore for new solid-state quantum emitters.

INTRODUCTION

This thesis explores three areas of research on two-dimensional (2D) semiconductors and thin films and their applications as solid-state quantum emitter (QE) sources. First, the optical properties at the interface of a lateral heterostructure are measured, as this interface may host QEs originating from quantum dot-like states. Second, QEs are induced via nanoindentation in single-layer (1L) transition metal dichalcogenides (TMDs). Third, defect-related emission is investigated in uranium (U)-doped gallium nitride (GaN). Across these three studies, the research focuses on band gap modulation through stoichiometric tuning, strain, and doping.

1.1 Transition metal dichalcogenides

TMDs are the material platform for the research presented in Chapters 3 and 4. This section discusses the formation of a direct band gap as bulk semiconducting TMDs are thinned to 1L and how this direct band gap results in strong light-matter interactions. The discussion also includes an introduction to excitons—tightly bound electron–hole pairs—and Raman scattering, which is the inelastic scattering of photons with atomic vibrations. Raman scattering is critical for determining material composition, as discussed in Chapter 3, while excitons are important for understanding QE formation in 1L-TMDs, which is discussed in Chapter 4.

TMDs are a family of materials with the chemical composition MX_2, where M represents molybdenum (Mo) or tungsten (W), and X denotes sulfur (S) or selenium (Se)[1].TMDs are layered van der Waals materials where the transition metal and chalcogen atoms coordinate through ionic-covalent interactions, in contrast to the weak van der Waals interactions between the layers. The resulting combination of weak interlayer bonding and strong intralayer bonding enables the isolation of a single atomic sheet that is three atoms thick via mechanical exfoliation or growth via chemical vapor deposition (CVD)[2]. A ball-and-stick model of a 1L-TMD is shown in Figure 1.1.

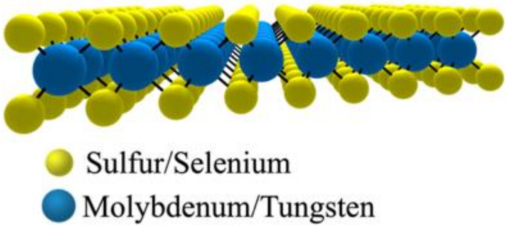

Figure 1.1 – A ball and stick model of a 1L-TMD. TMDs are materials with a composition of MX_2 where M (blue spheres) are either molybdenum or tungsten, and X (yellow spheres) is sulfur or selenium.

A schematic of the mechanical exfoliation process using scotch tape is shown in Figure 1.2. Mechanical exfoliation involves separating a bulk TMD crystal into thinner layers by overcoming the weak interlayer van der Waals interactions, producing flakes that cover a large area of the tape. The tape is then pressed onto a SiO_2/Si substrate. The 2D material adheres to the substrate, and when the tape is peeled away, the weakly bound layers of the crystals are separated, leaving thinner flakes on the substrate[3, 4].

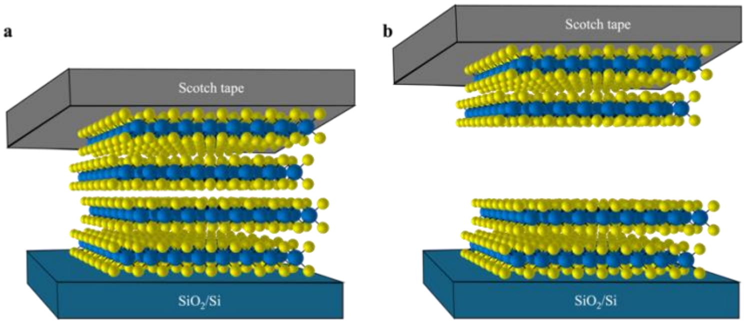

Figure 1.2 – A ball and stick model of the mechanical exfoliation of TMDs. (a) A ball and stick model of a multi-layer TMD on scotch tape being pressed onto a SiO_2/Si substrate. (b) The same ball and stick model after the tape has been peeled off the substrate, leaving a thinned-down crystal.

Images of exfoliated WSe_2 are shown in Figure 1.3. Figure 1.3a is an optical image of a bulk crystal of WSe_2, and Figure 1.3b shows a crystallite of 1L-WSe_2. The 1L-WSe_2 appears darker, and the contrast between the substrate and the material decreases compared to the bulk crystal. The variation in contrast arises from the layer-dependent absorption and reflection properties of the crystal.

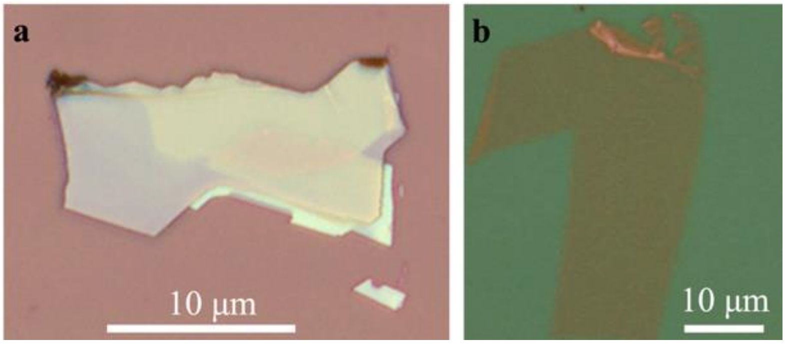

Figure 1.3 – Optical images of bulk and 1L-WSe_2 on a PMMA/SiO_2/Si substrate. (a) An optical image of a bulk WSe_2 crystal. (b) An optical image of a crystallite of 1L-WSe_2.

TMDs are of great interest for studying light-matter interactions in 2D semiconductors because the band gap transitions from indirect to direct as the number of layers decreases[2, 5-7]. As a bulk crystal, TMDs are indirect band gap semiconductors and therefore emit light inefficiently. However, as a monolayer, they become a direct band gap semiconductor. The transition occurs because of quantum confinement of the electrons in the linear combination of the out-of-plane p orbitals of the chalcogen atoms and the d orbitals of the transition metal at the center of the first Brillouin zone (Γ point). As the number of layers decreases, the valence band at the Γ point shifts to lower energy, resulting in a larger bandgap (Figure 1.4a-c). In contrast, the direct band gap at the K and K′ points remains nearly constant and becomes the lowest energy gap in the monolayer limit. Consequently, the direct band gap dominates the optical properties of 1L-TMDs (Figure

1.4c)[6]. The K′ point is not shown in Figure 1.4a-c to simplify the band diagrams. The K′ point is equal in energy to the K point but separated in momentum[5], as illustrated in Figure 1.4d.

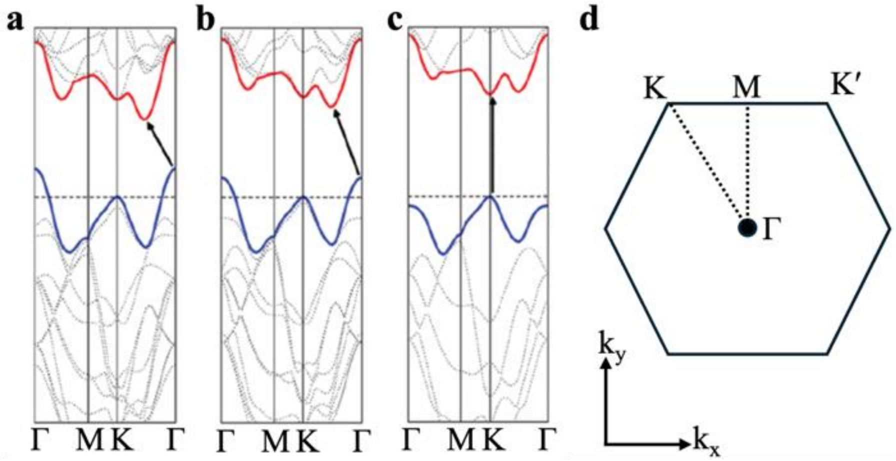

Figure 1.4 – The calculated band structures of MoS_2 crystals of different layer number. (a) Bulk MoS_2, (b) bilayer MoS_2, and (c) 1L-MoS_2. The x-axis and y-axis of (a-c) represents momentum and energy, respectively. High-symmetry points in the first Brillouin zone are marked along the x-axis. The solid black arrows indicate the lowest energy transitions between the conduction (red) and valence (blue) bands. In the bulk and bilayer MoS_2, the lowest energy transition is at the Γ point, but at the 1L limit, the lowest energy transition is at the K point. (d) A schematic of the first Brillouin zone of TMDs, with the high symmetry points labeled. The dashed lines indicate the corresponding points shown on the x-axis of (a-c). Adapted from Splendiani *et al*[6].

In the monolayer limit, TMDs exhibit strong Coulombic interactions between electrons and holes. As shown in Figure 1.5a, when an electron is excited to the conduction band by an incident photon, a positively charged hole is left in the valence band[8-11]. This hole is bound to the excited electron through Coulombic interactions (Figure 1.5b). The strength of the Coulombic interactions increases as dielectric screening is reduced in the monolayer, resulting in tightly bound electron–hole pairs known as excitons (Figure 1.5c). Excitons govern the optical properties of 1L-TMDs at the K and K′ points of the first Brillouin zone (see Figure 1.4d) and are responsible for the highly efficient light emission process known as photoluminescence (PL)[1, 2, 6].

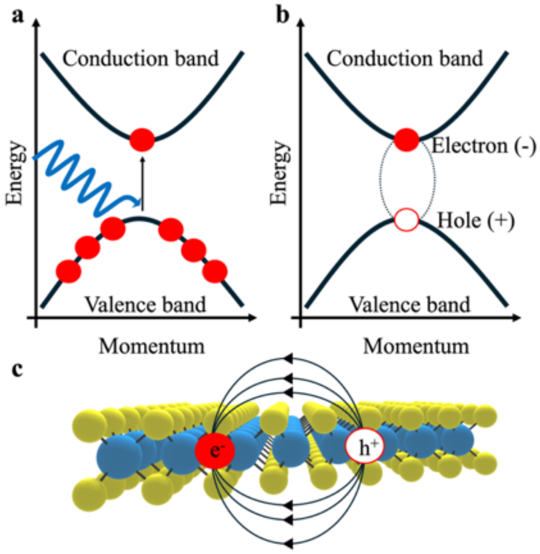

Figure 1.5 – Excitons in 1L-TMDs. (a) A two-level diagram showing a blue incident laser exciting an electron from the valence band to the lowest energy state in the conduction band. (b) The excited electron is bound to the positively charged hole, due to Coulombic interactions. (c) A schematic showing the electric field lines between the electron and hole.

A less efficient light emission process than PL is Raman scattering, which involves the inelastic scattering of photons from crystal lattice vibrations known as phonons. The dominant scattering process is Stokes scattering, which is when the incident photon is higher in energy than the scattered photon. Raman scattering is a weak process, on the order of ~10^{-8} times weaker than PL[12].

1.2 Dark and bright excitons

The experiments and research described in Chapter 4 were motivated by the overarching goal to test a mechanism for the formation of electronic states responsible for QE formation in 1L-TMDs. A critical component of this theory is the role of dark excitons in 1L W-based TMDs (W-TMDs) and whether these states are the lowest energy excited state. In this section, the concepts of dark excitons are reviewed, including how their properties depend on the chemical composition of the 1L-TMDs.

To begin this discussion, an important observation is that in W-TMDs at room temperature, the PL is bright. However, as the temperature decreases to 110 K, the PL intensity decreases. The opposite trend is observed in 1L molybdenum-based TMDs (Mo-TMDs). The temperature dependence of the PL intensity in these two material systems implies the existence of optically dark and optically bright excitons[1].

Optically dark and bright excitons are defined by the oscillator strength of the exciton. For optically bright excitons, the oscillator strength is large, and the excited electron will radiatively recombine with the hole, emitting a photon. Whether this radiative recombination occurs depends on the spin-configuration of the electron–hole pair—that is, whether the exciton forms a spin-singlet or spin-triplet state. In the spin-singlet exciton, the electron and hole spins are antiparallel, resulting in radiative recombination. In contrast, radiative recombination of the triplet exciton is spin-forbidden because an electric dipole interaction does not induce an electron spin flip[13], meaning it is a non-radiative recombination process. Figure 1.6a illustrates the triplet state, while Figure 1.6b shows the singlet state in a simple two-level system. These same concepts apply to 1L-TMDs. In the discussion of dark excitons in 1L-TMDs below, only the electron spin orientation will be referenced, rather than both the electron and hole spin orientations as shown in Figure 1.6.

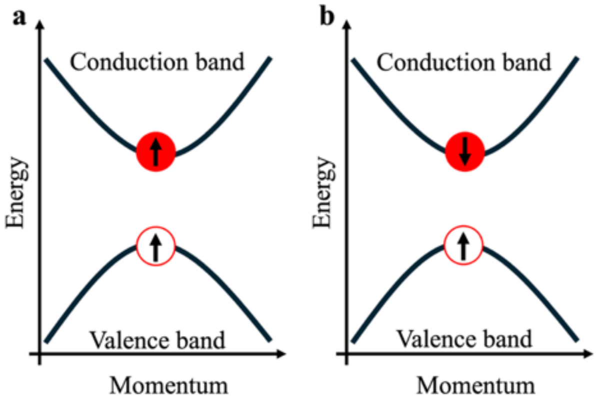

Figure 1.6 – A two-level diagram of spin-triplet and spin-singlet excitons. (a,b) The red-filled circle represents the excited electron, and the red outlined circle represents the positive hole. The black arrows represent the spin orientations of the respective particle. (a) Is a spin-triplet exciton, where the spin of the electron is parallel to the spin of the hole. (b) Represents a spin-singlet exciton where the electron spin and hole spin are antiparallel.

The existence of dark and bright exciton states in 1L W- and Mo-TMDs arises from the band structure of the conduction and valence bands at the K and K′ points—the edges of the first Brillouin zone (see Figure 1.4d). The optically bright and dark states result from the spin splitting in the conduction and valence bands, leading to spin-polarized bands. The spin-polarized bands are separated by tens of meV in the conduction band and hundreds of meV in the valence band, which is caused by spin-orbit coupling. At the K point of W-TMDs, the lower conduction band contains electrons with spin-polarization opposite to that of the upper valence band. In contrast, the electron spin-polarization of the upper conduction band matches that of the lower valence band. For the K′ point, the electron spin-polarization is opposite to that of the K point. In 1L-TMDs, optically dark excitons are the result of electron spin- and momentum-forbidden radiative relaxation processes[1, 14, 15].

In 1L W-TMDs, the electron spin-polarization of the bands causes radiative relaxation from the lower conduction band to the upper valence band to be spin-forbidden, while relaxation from the lower conduction band at the K point to the upper valence band at the K′ point is momentum-forbidden. The electron spin-polarization order of the bands in W-TMDs (Figure 1.7a) is opposite to that of Mo-TMDs[1, 14, 16] (Figure 1.7b). The spin-forbidden transitions shown in Figure 1.7a correspond to the spin-triplet excitons illustrated in Figure 1.6a. Figure 1.7a shows only the electron spin orientation, whereas Figure 1.6a depicts both the electron and hole spins.

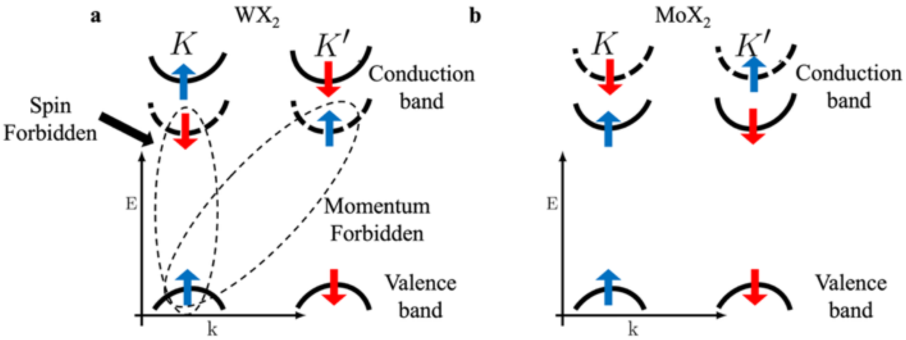

Figure 1.7 – The comparison of the lowest energy excited states in 1L W-TMDs and Mo-TMDs. (a,b) Two level diagrams of the lowest energy excited states at the K and K′ points in the first Brillouin zone. The red and blue arrows represent the electron spin orientation. (a) In W-TMDs the lowest energy excited states are optically dark excitons that are spin and momentum forbidden. (b) In contrast in Mo-TMDs the lowest energy excited states are optically bright excitons.

1.3 Transition metal dichalcogenide alloys allow for the control of the lowest energy excited state ordering

The ability to control whether the lowest-energy excited state in a 1L-TMD alloy, like molybdenum tungsten disulfide ($Mo_xW_{(1-x)}S_2$) and molybdenum tungsten diselenide ($Mo_xW_{(1-x)}Se_2$), is optically bright or dark is critical for the research discussed in Chapter 4. In this section, $Mo_xW_{(1-x)}S_2$ and $Mo_xW_{(1-x)}Se_2$ alloys are introduced to systematically modulate the band structure by controlling the transition metal composition, thereby determining whether the excited state is optically bright or optically dark.

1L-TMD alloys enable modulation of the band structure so that the lowest-energy states in the conduction band host either bright or dark excitons. Because Mo-TMDs and W-TMDs host opposite spin-polarization order in their bands, alloys of the two—such as $Mo_xW_{(1-x)}S_2$ and $Mo_xW_{(1-x)}Se_2$ —offer a unique opportunity to tune the spin-splitting by adjusting the ratio of molybdenum to tungsten. As shown theoretically in Figure 1.8, increasing the amount of Mo content in the alloy can shift the lowest-energy exciton from optically dark—as in W-TMDs—to optically bright, in Mo-TMDs[15]. Thus, 1L-TMD alloys provide an excellent platform for studying how the band structure modulation influences the formation of QEs in 1L-TMDs.

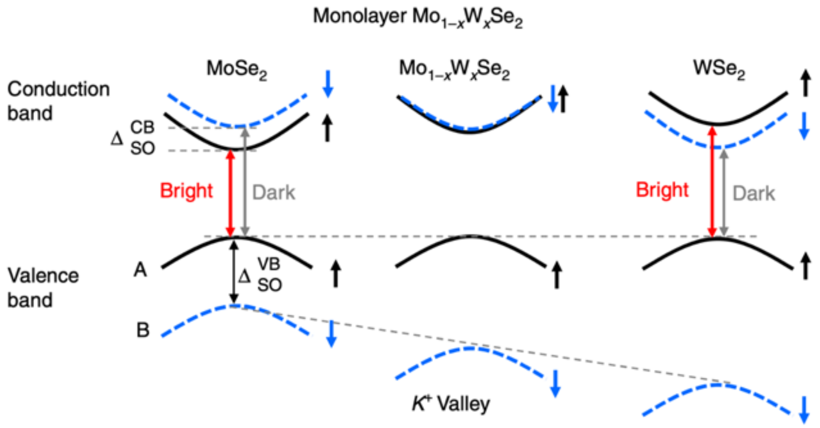

Figure 1.8 – Modulating the band structure as a function of transition metal composition in $Mo_{1-x}W_xSe_2$. The lowest energy excited state in 1L $MoSe_2$ are optically bright excitons, but in 1L WSe_2 they are optically dark. In $Mo_{1-x}W_xSe_2$ alloys, the lowest energy excited state can be switched. Adopted from Wang *et al*[15].

1.4 Quantum emitters in semiconductors

QEs are the overarching theme of this work. The discussion in this section includes an introduction to solid-state QE sources and antibunching measurements, which are used to determine whether emission lines that have a narrow bandwidth in the PL spectra are classified as

QEs. Antibunching measurements are performed on such narrowband emitters in Chapter 4 to confirm them as QEs.

QEs are light sources—analogous to atoms—that will emit exactly one photon at a time, making them desirable for quantum photonics applications. A solid-state QE source has the potential to be more easily integrated into systems for quantum computing, quantum simulation, quantum walks, and boson sampling[17]. Solid-state QE sources typically arise from defect states in a material that introduce isolated energy states within the band structure of the host material[18]. These defects can include atomic vacancies or chemical dopants. QEs exhibit distinct signatures in the PL spectra, typically at cryogenic temperatures (4 K), appearing as narrowband emission lines.

Narrowband emission lines—also called narrow emitters—are observed in the PL and can be verified as QEs through antibunching measurements, which are statistical analyses of the temporal correlation between emitted photons. Antibunching measurements are performed using a Hanbury Brown and Twiss (HBT) interferometer, which measures the second-order intensity autocorrelation function, $g^{(2)}(\tau)$. The HBT setup is relatively simple: it consists of a 50:50 beam splitter (BS) with avalanche photodiodes (APDs) positioned at both output arms. The APDs are sensitive to single photons and are connected to a time-correlated single-photon counting (TCSPC) module. The TCSPC assigns a precise time tag to each detection event, enabling time-resolved intensity correlation measurements[19-21]. A block diagram of the HBT setup is shown in Figure 1.9.

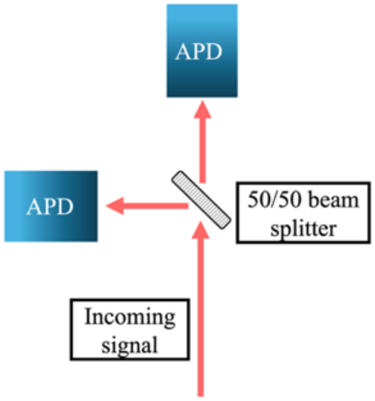

Figure 1.9 – A block diagram of a HBT Interferometer. A 50:50 beam splitter directs the incoming beam of photons into two APDs, which are equally spaced from the beam splitter.

The HBT interferometer measures the finite temporal separation of a stream of photons to determine whether the source is a QE. The second-order correlation function, shown in Equation 1.1, cross-correlates the intensities of detection events from both arms of the interferometer[19, 21].

$$g^{(2)}(\tau) = \int_{-\infty}^{\infty} I_1(t) I_2(t+\tau) d\tau \qquad \text{Eq. 1.1}$$

Here, I_1 corresponds to the intensity from one arm, and I_2 is the intensity of a detection event from the other arm at a delay time τ. For a QE, $g^{(2)}(0)$ is less than $g^{(2)}(\tau \neq 0)$, meaning that at zero-time delay, there is a dip in the correlation curve. A dip that is less than or equal to 0.5 is considered a QE[20]. This behavior is called photon antibunching[19, 21].

An antibunched emitter produces a photon stream separated by the emitter's excited-state lifetime, as in the case of emission from a single atom. In contrast, a non-antibunched (classical) emitter exhibits $g^{(2)}(0) = g^{(2)}(\tau \neq 0)$, indicating the detection event intensity is the same in the two arms of the HBT. Example $g^{(2)}(\tau)$ curves for antibunched and classical emission are shown in Figure 1.10a and 1.10b, respectively[19, 21].

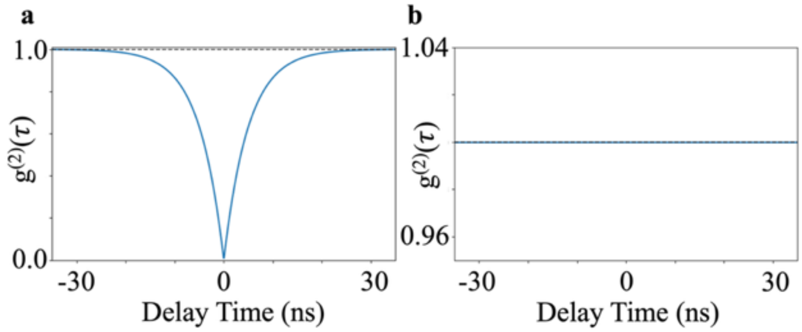

Figure 1.10 – Theoretical examples of an antibunched and a coherent emission source. (a) An antibunched curve from a single photon emitter. (b) A classical light source that shows no antibunching behavior.

1.5 Six factors that make quantum emitters high-quality and ready for applications

In this section, we will discuss six parameters that must be optimized for QEs to be utilized in applications such as quantum computing and quantum communications. To optimize these parameters, it is essential to control the source of the QEs. The level of control required for practical applications motivates the research described in Chapter 4, which investigates the formation mechanism of QEs in 1L W-TMDs. Understanding this formation mechanism enables better control and optimization of QEs for applications.

High-quality QEs are needed for applications such as quantum computing and quantum communication. In high-quality QEs, six factors are important: the ability to control the position of the emitter in the material, limited inhomogeneous broadening, short emitter lifetimes[18], high emitter brightness, and a high Debye-Waller (DW) factor, which leads to a more intense zero-phonon line[22]. The DW factor is the ratio of the integrated intensity of the zero-phonon line to the total integrated intensity of the zero-phonon line plus the phonon sidebands[23].

Photon coherence and indistinguishability are critical for applications in quantum computing and communication. To improve photon indistinguishability, it is necessary to minimize inhomogeneous broadening of the emission line, which increases certainty in the photon energy[24]. Inhomogeneous broadening arises from fluctuations in the local environment that alter the emission energy[20, 25-27]. Another factor affecting photon indistinguishability is homogeneous broadening, which is limited by the emitter's lifetime. Short emitter lifetimes are generally desired, but the short lifetime causes a proportional increase in the emission linewidth due to the energy-time uncertainty principle, expressed in Equation 1.2.

$$\Delta E \Delta t \geq \frac{\hbar}{2} \qquad \text{Eq. 1.2}$$

Here, Δt is the lifetime of the QE state and ΔE is the emission width[13], or homogenous broadening, and $\hbar$ is the reduced Planck's constant ($\hbar = 6.58\times10^{-16}$ eV). For example, if a QE has a lifetime of 1.0 ns[22], then the homogeneous broadening limit is $\Delta E \geq 0.33$ μeV.

For integration into on-chip quantum devices, the ability to control the spatial position of the QE is essential. Positional control allows for the predictable placement of emitters and the fabrication of emitter arrays[28, 29]. Emitter brightness is another critical parameter, as brighter emitters provide more photons for use in quantum operations. Brightness depends on both the extraction efficiency and the quantum efficiency of the QE source[24].

1.6 Bulk material quantum emitter sources

Discussed in this section is the rich research history of QEs from in-gap defect states in wide-band gap materials such as diamond and GaN. This section lays the foundation for motivating the research discussed in Chapter 5, which focuses on investigating the optical properties of U-doped GaN as a potential novel QE source.

Solid-state QEs have been experimentally demonstrated in several sources. The most well-known QE sources are silicon and nitrogen vacancies (NV) in diamond, commonly referred to as color centers. Defects in SiC, GaN, and GaAs quantum dots are also QEs[17]. GaN is a heavily studied wide-band gap and a direct band gap semiconductor that has been shown to host QEs that originate from quantum dot states and in-gap defect states[30-39]. GaN is an appealing source of QE because of the relatively simple growth of thin films directly onto the substrate compared to the complex methodologies of angled etching required to fabricate photonic structures composed of diamond and SiC.

Doping GaN creates in-gap states that result in PL emission from the ultraviolet (UV) to the infrared (IR)[40]. Rare-earth elements such as erbium (Er) and praseodymium (Pr) have been used to dope GaN, producing QEs associated with transitions of inner-shell 4f electrons[41, 42]. These transitions are shielded from the external environment by outer-shell electrons, resulting in sharp, spectrally stable emission[42]. The same principle applies to the actinides, which involve 5f orbitals. Uranium, for example, has been shown to exhibit emission lines in the IR[43]. The observation that rare-earth and potentially actinide dopants can produce QEs raises the intriguing possibility of using these elements as QE sources for quantum information processing or optical sensing applications.

1.7 Quantum emitters in single-layer transition metal dichalcogenides

Studying QEs in 1L-TMDs is the primary motivation for the research discussed in Chapters 3 and 4. This section focuses on the research conducted since the initial reports of QEs in 1L-WSe_2, first observed in 2015. Since the initial discovery, research has focused on 1L W-TMDs, with minimal research focused on Mo-TMDs. The existing research also indicates that QEs are induced differently in Mo-TMDs compared to W-TMDs. This section also introduces the use of an atomic force microscope (AFM) tip to create nanoindents in 1L-TMDs—a technique discussed in detail in Chapters 2 and 4.

In 2015, the first observation of spatially localized QEs was shown in 1L-WSe_2[20, 44-47]. In these groundbreaking studies, multiple low-energy emitters with narrow linewidths were observed at 4 K, distinguishing them from the typical excitonic PL in the system. The $g^{(2)}$ measurements unambiguously identified these narrow emitters as QEs. The source for the QEs was hypothesized to originate from natural defects, such as atomic vacancies, within 1L-WSe_2[45]. This hypothesis was supported by the high degree of spatial localization. Further discoveries were made about QEs in 1L-WSe_2[20, 44, 46]. Experimental evidence shows that QEs form from localized excitons in potential energy wells created by strain in 1L-WSe_2[44]. To further demonstrate that a potential well created by strain induces QEs, the 1L-WSe_2 was ripped by dragging an AFM probe along the surface[47]. The areas with narrow emitters are localized along the edges of torn material where there are regions of tensile strain.

By inducing localized tensile strain in a 1L-TMD, a potential well is created by reducing the material band gap[48]. QEs can be positioned with these wells[47, 49] because excitons experience an effect called “exciton funneling”. Exciton funneling occurs when a localized inhomogeneous strain field creates a flow of excitons toward the region of lowest energy[48, 50, 51]. Localized tensile strain can be induced by nanoindenting a sample with an AFM probe[52], forming nanobubbles in the 1L-TMD[53], or depositing a 1L-TMD on nanopillars[54]. However, a major challenge for technological adaptation is that nanopillars and nanobubbles create uncontrolled strain fields.

Nanoindentation, in contrast, allows for the control of the amount of tensile strain and the location of the strain, which makes it an appealing technique for QE formation. Figure 1.11 shows the controlled placement of the localized tensile strained regions in 1L-WS_2 using an AFM tip, achieved simply by moving the AFM tip to a specified position on the sample and setting the indentation force. The room-temperature PL integrated intensity map of 1L-WS_2 in Figure 1.11a shows 10 indents that correspond to the circles of lower intensity. The black arrow pointing right to left marks five indents of increasing strain from which a three-pixel-wide linecut is extracted. The emission energy—extracted by calculating the spectral median[55]—of the average spectra from the linecut is shown in Figure 1.11b as a function of linecut position. The emission energy shifts to lower energy at each of the five indents as the indentation force increases, and the amount of shifting increases, showing the strain tunability of the indentation method.

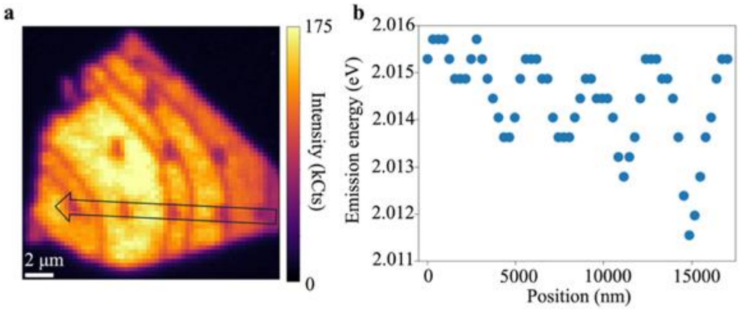

Figure 1.11 – Strain tuning using nanoindentation in 1L-WS_2. (a) An integrated RT PL intensity map of an indented 1L-WS_2, integrated over an energy range of 1.89 – 2.16 eV. The sample is indented with nine indents ranging from 34 to 84 μN of indentation force. The circular regions of low intensity correspond to the indents. The black arrow indicates a linecut extracted across the 34 – 59 μN indents, from right to left. (b) The emission energy of each of the averaged spectra from the linecut, where each spectra represents the average of three pixels.

Since 2019, when nanoindentation was first shown to induce QEs[52], numerous studies have utilized the technique on 1L-TMDs[28, 56-62]. Three of the studies focused on improving the quality of the QEs from the indents, indicated by the $g^{(2)}$ value approaching zero. The QE quality was improved by passivating broadband defect emission by electrostatically gating the WSe_2[63], creating a heterostructure with graphite and indented WSe_2[58], and through ferroelectric modulation of QEs from WS_2[64]. Nanoindentation has been used to tune exciton-plasmon coupling in WSe_2 and induce chiral QEs from WSe_2 indented on nickel phosphorus trisulfide ($NiPS_3$)[61]. QEs were electrically excited in an indented graphene/WSe_2/hBN heterostructure[62]. Researchers even used a heated AFM probe while indenting 1L-MoS_2[57]. When the heated probe punctures the 1L-TMD, it plastically deforms the 1L-TMD and displaces more polymethyl methacrylate (PMMA) with less normal force than a room-temperature probe.

The majority of the research has focused on tensile strain-induced QEs in W-TMDs, with very little research on Mo-TMDs. No evidence of tensile strain-induced QEs from 1L Mo-TMD has been reported, and only atomic vacancy-induced QEs have been observed[22]. In this study, the authors induced QEs in 1L-MoS_2 via He-ion radiation that created atomic vacancies. The proposed formation mechanism for QE formation in 1L W-TMDs that explains why tensile strain-induced QEs are not observed in Mo-TMDs is introduced in Section 1.9. This mechanism is the motivator for the research discussed in Chapter 4.

1.8 Quantum emitters from single-layer transition metal dichalcogenides offer advantages over bulk semiconductors

1L-TMDs are investigated extensively in this thesis as QE sources. In particular, Chapter 4 builds upon the last 10 years of research on QEs in 1L-TMDS. This section motivates the research into 1L-TMDs as QE sources to compete with other materials like diamond and GaN.

QEs from 1L-TMDs offer several advantages over diamond NV emission centers. The lateral and vertical positioning of QE sources through localized strain in a 1L-TMD provides greater spatial control than NV centers in diamond, which rely on the precise placement of individual atomic vacancies—a process that is effectively impossible to achieve with high accuracy. The position uncertainty of NV centers makes diamond-based systems more challenging to implement in nanophotonic circuits[22]. Additionally, the photon extraction efficiency of QEs in 1L-TMDs is higher because the emitters are confined within an atomically thin layer. In contrast, NV centers in diamond exhibit lower extraction efficiency due to the high refractive index of diamond[45].

Another appealing property of 1L-TMDs as QE sources is their ability to be stacked with other van der Waals materials to improve emitter properties. Because 1L-TMDs have weak out-of-plane chemical interactions (van der Waals forces), lattice matching is not a strict requirement when forming vertical heterostructures[65]. A recent study demonstrated that stacking graphite, another van der Waals material, on top of nanoindented 1L-WSe_2 reduced the broad defect-related emission from the indented material. This reduction increased the spectral purity of the QEs by isolating the emitters more effectively. Higher purity corresponds to a lower $g^{(2)}$ value, where the measured antibunching curve (described in Section 1.4) approaches zero[58]. Lateral heterostructures, therefore, offer an additional means to tune and optimize the QE properties of 1L-TMDs for device applications.

To fully realize the advantages of QEs from 1L-TMDs, it is essential to understand the underlying formation mechanism for QEs. A proposed mechanism for QE formation in 1L-TMDs is discussed in the next section.

1.9 Proposed formation mechanism for quantum emitters in tungsten-based transition metal dichalcogenides

The theoretical formation mechanism for QEs in W-TMDs, which involves the hybridization of dark excitons and point defect states, is discussed in this section. Also discussed is how using 1L-TMD alloys provides a unique opportunity to test the role of dark excitons, which serves as the motivation for the work conducted in Chapter 4.

In 2019, Linhart *et al.* proposed a theoretical mechanism for QE formation in 1L W-TMD semiconductors[66]. The authors suggested that when localized tensile strain is applied, it induces the hybridization of the lowest energy excited state in the conduction band—corresponding to optically dark excitons—with in-gap defect states. This hybridized state is a spin-singlet state as discussed in Section 1.2, which enables radiative recombination in a transition that would otherwise be spin-forbidden. A schematic of this process is shown in Figure 1.12.

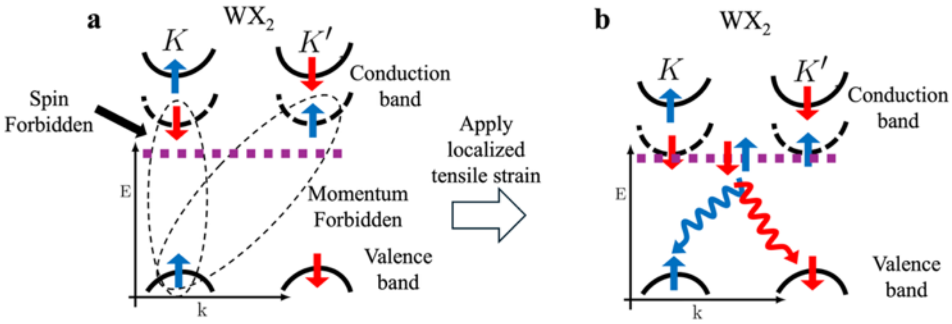

Figure 1.12 – The theoretical mechanism for SPE formation in 1L W-TMDs. The band structure in momentum space of WX$_2$, where X = S or Se. (a) The highest valence band and lowest conduction band states at the K and K′ points. Red and blue arrows indicate electron spin orientations. The black dashed circles mark the optically dark excitons. The purple dashed line denotes an in-gap defect state. (b) Under localized tensile strain, the conduction band states hybridize with the defect state, enabling radiative recombination and single-photon emission. Adapted from Linhart *et al*[66].

To test this proposed mechanism, we used 1L-$Mo_xW_{(1-x)}S_2$ and $Mo_xW_{(1-x)}Se_2$ alloys, as changing the molybdenum to tungsten ratio allows modulation of the band gap to be more W-like or Mo-like[15]. As discussed in Section 1.3, increasing the Mo concentration shifts the lowest-energy exciton from being optically dark in W-TMDs to optically bright in Mo-TMDs. Localized tensile strain was applied via nanoindentation using identical indentation forces for each alloy composition. Our original hypothesis was that at a specific molybdenum to tungsten concentration, QEs will no longer be observed because the lowest energy excited state is no longer optically dark. Details of this study are discussed in Chapter 4.

1.10 Conclusions

This section summarizes Chapters 2-6 of this thesis, highlighting the main messages and how they relate to the main focus of investigating solid-state QE sources.

Chapter 2 describes the key techniques and instrumentation used in Chapters 3, 4, and 5. For example, the room-temperature PL and Raman microscopy were critical for many of the experiments presented in those chapters. A particularly important technique discussed is the nanoindentation process, introduced in Section 1.7, along with the optimizations that enabled the results in Chapter 4.

In Chapter 3, the initial goal was to investigate QEs at the interface of a 1L-MoS_2/WS_2 lateral heterostructure. However, PL measurements of possible QEs were impossible due to the quenching effects from the gold substrate on which the heterostructures were transferred. As a result, the focus shifted to understanding the interface's chemical composition and spatial extent using room-temperature tip-enhanced Raman scattering (TERS). The TERS measurements revealed that the interface ranged from 50–600 nm in width and consisted of a non-uniform $Mo_xW_{(1-x)}S_2$ alloy.

Chapter 4 explores the role of dark excitons in the QE formation mechanism described in Section 1.9 by applying localized strain via nanoindentation to various $Mo_xW_{(1-x)}Se_2$ and $Mo_xW_{(1-x)}S_2$ alloys. The goal was to identify an alloy composition at which QEs ceased forming, indicating a transition where the lowest energy excited state became optically bright. The main challenge in this study was producing consistent and reliable tensile strain. Nanoindentation often caused tearing of the monolayer, preventing reproducible strain formation across alloy compositions. Consequently, a secondary goal was established—to understand and optimize the indentation process itself. This goal was achieved: when the AFM tip was intentionally dulled, the material tore, but when the tip remained sharp, the material stayed intact and strained. Although the primary goal was not achieved, an essential capability—inducing repeatable localized strain—was established, laying the groundwork for future investigations discussed in Section 6.2.1.

Chapter 5 describes collaborative work with Idaho National Laboratory (INL) aimed at growing U-doped GaN thin films to investigate potential QEs from uranium dopants. The two main challenges were the thin-film growth process and performing single-dopant PL measurements at 4 K. Three samples were grown via molecular beam epitaxy (MBE), and two were confirmed to be U-doped GaN. Narrow emission lines around 1.30 eV were observed from the two U-doped samples, suggesting potential QEs originating from the uranium dopants. However, these emission lines have not yet been confirmed as QEs due to the high concentrations of uranium atoms and the inability to isolate a single dopant state. Thus, while the initial goal was only partially achieved, the successful growth of U-doped GaN and the preliminary observation of narrow emission lines represent a promising step forward.

Finally, Chapter 6 concludes the thesis by summarizing the results from Chapters 3, 4, and 5 and proposing future experiments based on these findings. Particularly exciting is the prospect of applying the optimized nanoindentation technique developed in Chapter 4 to induce strain in 1L-TMD alloys, enabling a more direct investigation of the dark exciton's role in QE formation.

References

(1) Zhang, X. X.; You, Y.; Zhao, S. Y.; Heinz, T. F. Experimental Evidence for Dark Excitons in Monolayer WSe_2. *Phys Rev Lett* **2015**, *115* (25), 257403. DOI: 10.1103/PhysRevLett.115.257403.

(2) Mak, K. F.; Lee, C.; Hone, J.; Shan, J.; Heinz, T. F. Atomically thin MoS_2: a new direct-gap semiconductor. *Phys Rev Lett* **2010**, *105* (13), 136805. DOI: 10.1103/PhysRevLett.105.136805.

(3) Huang, Y.; Sutter, E.; Shi, N. N.; Zheng, J.; Yang, T.; Englund, D.; Gao, H. J.; Sutter, P. Reliable Exfoliation of Large-Area High-Quality Flakes of Graphene and Other Two-Dimensional Materials. *ACS Nano* **2015**, *9* (11), 10612-10620. DOI: 10.1021/acsnano.5b04258.

(4) Novoselov, K. S.; Geim, A. K.; Morozov, S. V.; Jiang, D.; Zhang, Y.; Dubonos, S. V.; Grigorieva, I. V.; Firsov, A. A. Electric field effect in atomically thin carbon films. *Science* **2004**, *306* (5696), 666-669. DOI: 10.1126/science.1102896.

(5) Butler, S. Z.; Hollen, S. M.; Cao, L.; Cui, Y.; Gupta, J. A.; Gutierrez, H. R.; Heinz, T. F.; Hong, S. S.; Huang, J.; Ismach, A. F.; et al. Progress, challenges, and opportunities in two-dimensional materials beyond graphene. *ACS Nano* **2013**, *7* (4), 2898-2926. DOI: 10.1021/nn400280c.

(6) Splendiani, A.; Sun, L.; Zhang, Y.; Li, T.; Kim, J.; Chim, C. Y.; Galli, G.; Wang, F. Emerging photoluminescence in monolayer MoS_2. *Nano Lett* **2010**, *10* (4), 1271-1275. DOI: 10.1021/nl903868w.

(7) Wang, Q. H.; Kalantar-Zadeh, K.; Kis, A.; Coleman, J. N.; Strano, M. S. Electronics and optoelectronics of two-dimensional transition metal dichalcogenides. *Nat Nanotechnol* **2012**, *7* (11), 699-712. DOI: 10.1038/nnano.2012.193.

(8) Echeverry, J. P.; Urbaszek, B.; Amand, T.; Marie, X.; Gerber, I. C. Splitting between bright and dark excitons in transition metal dichalcogenide monolayers. *Physical Review B* **2016**, *93* (12). DOI: 10.1103/PhysRevB.93.121107.

(9) Klingshirn, C. F. *Semiconductor Optics*; Springer, 2012.

(10) Mueller, T.; Malic, E. Exciton physics and device application of two-dimensional transition metal dichalcogenide semiconductors. *npj 2D Materials and Applications* **2018**, *2* (1). DOI: 10.1038/s41699-018-0074-2.

(11) Schneider, C.; Glazov, M. M.; Korn, T.; Hofling, S.; Urbaszek, B. Two-dimensional semiconductors in the regime of strong light-matter coupling. *Nat Commun* **2018**, *9* (1), 2695. DOI: 10.1038/s41467-018-04866-6.

(12) Gardiner, D. J. Introduction to Raman Scattering. Springer Berlin Heidelberg, 1989; pp 1-12, DOI: 10.1007/978-3-642-74040-4_1.

(13) Kalt, H.; Klingshirn, C.; Kalt, H. *Linear optical properties of semiconductors*; Springer, 2019.

(14) Kośmider, K.; González, J. W.; Fernández-Rossier, J. Large spin splitting in the conduction band of transition metal dichalcogenide monolayers. *Physical Review B* **2013**, *88* (24). DOI: 10.1103/PhysRevB.88.245436.

(15) Wang, G.; Robert, C.; Suslu, A.; Chen, B.; Yang, S.; Alamdari, S.; Gerber, I. C.; Amand, T.; Marie, X.; Tongay, S.; et al. Spin-orbit engineering in transition metal dichalcogenide alloy monolayers. *Nat Commun* **2015**, *6*, 10110. DOI: 10.1038/ncomms10110.

(16) Wang, G.; Robert, C.; Glazov, M. M.; Cadiz, F.; Courtade, E.; Amand, T.; Lagarde, D.; Taniguchi, T.; Watanabe, K.; Urbaszek, B.; et al. In-Plane Propagation of Light in Transition Metal Dichalcogenide Monolayers: Optical Selection Rules. *Phys Rev Lett* **2017**, *119* (4), 047401. DOI: 10.1103/PhysRevLett.119.047401.

(17) Aharonovich, I.; Englund, D.; Toth, M. Solid-state single-photon emitters. *Nature Photonics* **2016**, *10* (10), 631-641. DOI: 10.1038/nphoton.2016.186.

(18) Gupta, S.; Yang, J. H.; Yakobson, B. I. Two-Level Quantum Systems in Two-Dimensional Materials for Single Photon Emission. *Nano Lett* **2019**, *19* (1), 408-414. DOI: 10.1021/acs.nanolett.8b04159.

(19) Grußmayer, K. S.; Herten, D.-P. Photon Antibunching in Single Molecule Fluorescence Spectroscopy. Springer International Publishing, 2014; pp 159-190, DOI: 10.1007/4243_2014_71.

(20) Srivastava, A.; Sidler, M.; Allain, A. V.; Lembke, D. S.; Kis, A.; Imamoglu, A. Optically active quantum dots in monolayer WSe_2. *Nat Nanotechnol* **2015**, *10* (6), 491-496. DOI: 10.1038/nnano.2015.60.

(21) Walls, D. F. M., G,J. *Quantum Optics*, Second ed.; Springer Berlin Heidelberg, 2008. DOI: 10.1007/978-3-540-28574-8.

(22) Klein, J.; Sigl, L.; Gyger, S.; Barthelmi, K.; Florian, M.; Rey, S.; Taniguchi, T.; Watanabe, K.; Jahnke, F.; Kastl, C.; et al. Engineering the Luminescence and Generation of Individual Defect Emitters in Atomically Thin MoS_2. *ACS Photonics* **2021**, *8* (2), 669-677. DOI: 10.1021/acsphotonics.0c01907.

(23) Chen, Y.-C.; Lin, S.-C.; Chou, J.-P.; Tsai, Y.-C.; Huang, C.-T.; Lee, C.-J.; Chang, W.-H. Stable Single Photon Emitters with Large Debye–Waller Factor in Silica. *ACS Photonics* **2025**, *12* (3), 1461-1469. DOI: 10.1021/acsphotonics.4c02001.

(24) Moody, G.; Sorger, V. J.; Blumenthal, D. J.; Juodawlkis, P. W.; Loh, W.; Sorace-Agaskar, C.; Jones, A. E.; Balram, K. C.; Matthews, J. C. F.; Laing, A.; et al. 2022 Roadmap on integrated quantum photonics. *Journal of Physics: Photonics* **2022**, *4* (1). DOI: 10.1088/2515-7647/ac1ef4.

(25) Hong, M.; Miller, A.; León-Montiel, R. d. J.; You, C.; Magaña-Loaiza, O. S. Engineering Super-Poissonian Photon Statistics of Spatial Light Modes. *Laser & Photonics Reviews* **2023**, *17* (10). DOI: 10.1002/lpor.202300117.

(26) Paralikis, A.; Piccinini, C.; Madigawa, A. A.; Metuh, P.; Vannucci, L.; Gregersen, N.; Munkhbat, B. Tailoring polarization in WSe_2 quantum emitters through deterministic strain engineering. *NPJ 2D Mater Appl* **2024**, *8* (1), 59. DOI: 10.1038/s41699-024-00497-2.

(27) Ramezani, F.; Strasbourg, M.; Parvez, S.; Saxena, R.; Jariwala, D.; Borys, N. J.; Whitaker, B. M. Predicting quantum emitter fluctuations with time-series forecasting models. *Sci Rep* **2024**, *14* (1), 6920. DOI: 10.1038/s41598-024-56517-0.

(28) Lai, Y.-Y.; Chen, P.-H.; Chen, C.-A.; Lee, Y.-H.; Deng, H. Single-Photon Emission from Rewritable Nanoimprinted Localized Emitter Arrays in Atomically Thin Crystals. *ACS Photonics* **2022**, *9* (3), 752-757. DOI: 10.1021/acsphotonics.1c01543.

(29) Strasbourg, M. C.; Yanev, E. S.; Darlington, T. P.; Faagau, K.; Holtzman, L. N.; Barmak, K.; Hone, J. C.; Schuck, P. J.; Borys, N. J. Characterization of quantum dot-like emitters in programmable arrays of nanowrinkles of 1L-WSe$_2$. *Journal of Applied Physics* **2024**, *136* (4). DOI: 10.1063/5.0214410.

(30) Berhane, A. M.; Jeong, K.-Y.; Bradac, C.; Walsh, M.; Englund, D.; Toth, M.; Aharonovich, I. Photophysics of GaN single-photon emitters in the visible spectral range. *Physical Review B* **2018**, *97* (16). DOI: 10.1103/PhysRevB.97.165202.

(31) Berhane, A. M.; Jeong, K. Y.; Bodrog, Z.; Fiedler, S.; Schroder, T.; Trivino, N. V.; Palacios, T.; Gali, A.; Toth, M.; Englund, D.; et al. Bright Room-Temperature Single-Photon Emission from Defects in Gallium Nitride. *Adv Mater* **2017**, *29* (12). DOI: 10.1002/adma.201605092.

(32) Dalla, N.; Kulboka, P.; Kobecki, M.; Misiak, J.; Prystawko, P.; Turski, H.; Kossacki, P.; Jakubczyk, T. Off-resonant photoluminescence spectroscopy of high-optical quality single photon emitters in GaN. *Solid State Communications* **2025**, *397*. DOI: 10.1016/j.ssc.2025.115845.

(33) Geng, Y.; Jena, D.; Fuchs, G. D.; Zipfel, W. R.; Rana, F. Optical Dipole Structure and Orientation of GaN Defect Single-Photon Emitters. *ACS Photonics* **2023**, *10* (10), 3723-3729. DOI: 10.1021/acsphotonics.3c00917.

(34) Geng, Y.; Nomoto, K. Ultrafast spectral diffusion of GaN defect single photon emitters. *Applied Physics Letters* **2023**, *123* (17). DOI: 10.1063/5.0171855.

(35) Holmes, M. J.; Kako, S.; Choi, K.; Arita, M.; Arakawa, Y. Single Photons from a Hot Solid-State Emitter at 350 K. *ACS Photonics* **2016**, *3* (4), 543-546. DOI: 10.1021/acsphotonics.6b00112.

(36) Hong, K. S.; Lim, H. J.; Ko, Y. H.; Kim, K. J.; Lee, J.; Song, J. H.; Kim, S. H.; Choi, J.; Lee, S. G.; Lee, W. J. Boosting Single-Photon Extraction Efficiency in GaN Through Radiative Mode Conversion. *Laser & Photonics Reviews* **2025**, *19* (10). DOI: 10.1002/lpor.202401966.

(37) Jun, S.; Choi, M.; Kim, B.; Morassi, M.; Tchernycheva, M.; Song, H. G.; Yeo, H. S.; Gogneau, N.; Cho, Y. H. Enhancement of Single-Photon Purity and Coherence of III-Nitride Quantum Dot with Polarization-Controlled Quasi-Resonant Excitation. *Small* **2023**, *19* (5), e2205229. DOI: 10.1002/smll.202205229.

(38) Kim, H.; Song, Y. H.; Ko, Y. H.; Cho, Y. H. Spatial Distribution Control of Room-Temperature Single Photon Emitters in the Telecom Range from GaN Thin Films Grown on Patterned Sapphire Substrates. *Advanced Quantum Technologies* **2024**, *8* (2). DOI: 10.1002/qute.202400177.

(39) Nguyen, M.; Zhu, T.; Kianinia, M.; Massabuau, F.; Aharonovich, I.; Toth, M.; Oliver, R.; Bradac, C. Effects of microstructure and growth conditions on quantum emitters in gallium nitride. *APL Materials* **2019**, *7* (8). DOI: 10.1063/1.5098794.

(40) Reshchikov, M. A.; Morkoç, H. Luminescence properties of defects in GaN. *Journal of Applied Physics* **2005**, *97* (6). DOI: 10.1063/1.1868059.

(41) Sato, S.-i.; Deki, M.; Nakamura, T.; Nishimura, T.; Stavrevski, D.; Greentree, A. D.; Gibson, B. C.; Ohshima, T. Photoluminescence properties of praseodymium ions implanted into submicron regions in gallium nitride. *Japanese Journal of Applied Physics* **2019**, *58* (5). DOI: 10.7567/1347-4065/ab142b.

(42) Zavada, J. M. Revisiting Impurity Doping of III-Nitride Materials for Photonic Device Applications. *ECS Transactions* **2013**, *50* (6), 253-259. DOI: 10.1149/05006.0253ecst.

(43) Wittke, J. P.; Kiss, Z. J.; Duncan, R. C.; McCormick, J. J. Uranium-doped calcium fluoride as a laser material. *Proceedings of the IEEE* **1963**, *51* (1), 56-62. DOI: 10.1109/proc.1963.1659.

(44) Chakraborty, C.; Kinnischtzke, L.; Goodfellow, K. M.; Beams, R.; Vamivakas, A. N. Voltage-controlled quantum light from an atomically thin semiconductor. *Nat Nanotechnol* **2015**, *10* (6), 507-511. DOI: 10.1038/nnano.2015.79.

(45) He, Y. M.; Clark, G.; Schaibley, J. R.; He, Y.; Chen, M. C.; Wei, Y. J.; Ding, X.; Zhang, Q.; Yao, W.; Xu, X.; et al. Single quantum emitters in monolayer semiconductors. *Nat Nanotechnol* **2015**, *10* (6), 497-502. DOI: 10.1038/nnano.2015.75.

(46) Koperski, M.; Nogajewski, K.; Arora, A.; Cherkez, V.; Mallet, P.; Veuillen, J. Y.; Marcus, J.; Kossacki, P.; Potemski, M. Single photon emitters in exfoliated WSe_2 structures. *Nat Nanotechnol* **2015**, *10* (6), 503-506. DOI: 10.1038/nnano.2015.67.

(47) Tonndorf, P.; Schmidt, R.; Schneider, R.; Kern, J.; Buscema, M.; Steele, G. A.; Castellanos-Gomez, A.; van der Zant, H. S. J.; Michaelis de Vasconcellos, S.; Bratschitsch, R. Single-

photon emission from localized excitons in an atomically thin semiconductor. *Optica* **2015**, *2* (4). DOI: 10.1364/optica.2.000347.

(48) Castellanos-Gomez, A.; Roldan, R.; Cappelluti, E.; Buscema, M.; Guinea, F.; van der Zant, H. S.; Steele, G. A. Local strain engineering in atomically thin MoS_2. *Nano Lett* **2013**, *13* (11), 5361-5366. DOI: 10.1021/nl402875m.

(49) Kern, J.; Niehues, I.; Tonndorf, P.; Schmidt, R.; Wigger, D.; Schneider, R.; Stiehm, T.; Michaelis de Vasconcellos, S.; Reiter, D. E.; Kuhn, T.; et al. Nanoscale Positioning of Single-Photon Emitters in Atomically Thin WSe_2. *Adv Mater* **2016**, *28* (33), 7101-7105. DOI: 10.1002/adma.201600560.

(50) Moon, H.; Grosso, G.; Chakraborty, C.; Peng, C.; Taniguchi, T.; Watanabe, K.; Englund, D. Dynamic Exciton Funneling by Local Strain Control in a Monolayer Semiconductor. *Nano Lett* **2020**, *20* (9), 6791-6797. DOI: 10.1021/acs.nanolett.0c02757.

(51) Tyurnina, A. V.; Bandurin, D. A.; Khestanova, E.; Kravets, V. G.; Koperski, M.; Guinea, F.; Grigorenko, A. N.; Geim, A. K.; Grigorieva, I. V. Strained Bubbles in van der Waals Heterostructures as Local Emitters of Photoluminescence with Adjustable Wavelength. *ACS Photonics* **2019**, *6* (2), 516-524. DOI: 10.1021/acsphotonics.8b01497.

(52) Rosenberger, M. R.; Dass, C. K.; Chuang, H. J.; Sivaram, S. V.; McCreary, K. M.; Hendrickson, J. R.; Jonker, B. T. Quantum Calligraphy: Writing Single-Photon Emitters in a Two-Dimensional Materials Platform. *ACS Nano* **2019**, *13* (1), 904-912. DOI: 10.1021/acsnano.8b08730.

(53) Shepard, G. D.; Ajayi, O. A.; Li, X.; Zhu, X. Y.; Hone, J.; Strauf, S. Nanobubble induced formation of quantum emitters in monolayer semiconductors. *2D Materials* **2017**, *4* (2). DOI: 10.1088/2053-1583/aa629d.

(54) Branny, A.; Kumar, S.; Proux, R.; Gerardot, B. D. Deterministic strain-induced arrays of quantum emitters in a two-dimensional semiconductor. *Nat Commun* **2017**, *8*, 15053. DOI: 10.1038/ncomms15053.

(55) Bao, W.; Borys, N. J.; Ko, C.; Suh, J.; Fan, W.; Thron, A.; Zhang, Y.; Buyanin, A.; Zhang, J.; Cabrini, S.; et al. Visualizing nanoscale excitonic relaxation properties of disordered edges and grain boundaries in monolayer molybdenum disulfide. *Nat Commun* **2015**, *6*, 7993. DOI: 10.1038/ncomms8993.

(56) Abramov, A. N.; Chestnov, I. Y.; Alimova, E. S.; Ivanova, T.; Mukhin, I. S.; Krizhanovskii, D. N.; Shelykh, I. A.; Iorsh, I. V.; Kravtsov, V. Photoluminescence imaging of single photon emitters within nanoscale strain profiles in monolayer WSe_2. *Nat Commun* **2023**, *14* (1), 5737. DOI: 10.1038/s41467-023-41292-9.

(57) Chang, S.; Yan, Y.; Geng, Y. Local Nanostrain Engineering of Monolayer MoS_2 Using Atomic Force Microscopy-Based Thermomechanical Nanoindentation. *Nano Lett* **2023**, *23* (20), 9219-9226. DOI: 10.1021/acs.nanolett.3c01809.

(58) Chuang, H. J.; Stevens, C. E.; Rosenberger, M. R.; Lee, S. J.; McCreary, K. M.; Hendrickson, J. R.; Jonker, B. T. Enhancing Single Photon Emission Purity via Design of van der Waals Heterostructures. *Nano Lett* **2024**, *24* (18), 5529-5535. DOI: 10.1021/acs.nanolett.4c00683.

(59) Cunningham, P. D.; Proscia, N. V.; LaGasse, S. W.; O'Hara, D. J.; McCreary, K. M.; Chuang, H.-J.; Povolotskyi, M.; Vurgaftman, I.; Jonker, B. T.; Simpkins, B. S. Site-Specific Exciton–Plasmon Coupling in Nanoindented WSe_2. *ACS Photonics* **2024**, *11* (8), 3250-3258. DOI: 10.1021/acsphotonics.4c00644.

(60) Lee, S.-J.; Chuang, H.-J.; Yeats, A. L.; McCreary, K. M.; O'Hara, D. J.; Jonker, B. T. Ferroelectric Modulation of Quantum Emitters in Monolayer WS_2. *ACS Nano* **2024**, *18* (36), 25349-25358. DOI: 10.1021/acsnano.4c10528.

(61) Li, X.; Jones, A. C.; Choi, J.; Zhao, H.; Chandrasekaran, V.; Pettes, M. T.; Piryatinski, A.; Tschudin, M. A.; Reiser, P.; Broadway, D. A.; et al. Proximity-induced chiral quantum light generation in strain-engineered $WSe_2/NiPS_3$ heterostructures. *Nat Mater* **2023**, *22* (11), 1311-1316. DOI: 10.1038/s41563-023-01645-7.

(62) So, J. P.; Kim, H. R.; Baek, H.; Jeong, K. Y.; Lee, H. C.; Huh, W.; Kim, Y. S.; Watanabe, K.; Taniguchi, T.; Kim, J.; et al. Electrically driven strain-induced deterministic single-photon emitters in a van der Waals heterostructure. *Sci Adv* **2021**, *7* (43), eabj3176. DOI: 10.1126/sciadv.abj3176.

(63) Stevens, C. E.; Chuang, H. J.; Rosenberger, M. R.; McCreary, K. M.; Dass, C. K.; Jonker, B. T.; Hendrickson, J. R. Enhancing the Purity of Deterministically Placed Quantum Emitters in Monolayer WSe_2. *ACS Nano* **2022**, *16* (12), 20956-20963. DOI: 10.1021/acsnano.2c08553.

(64) Lee, S. J.; Chuang, H. J.; Yeats, A. L.; McCreary, K. M.; O'Hara, D. J.; Jonker, B. T. Ferroelectric Modulation of Quantum Emitters in Monolayer WS_2. *ACS Nano* **2024**, *18* (36), 25349-25358. DOI: 10.1021/acsnano.4c10528.

(65) Liu, Y.; Weiss, N. O.; Duan, X.; Cheng, H.-C.; Huang, Y.; Duan, X. Van der Waals heterostructures and devices. *Nature Reviews Materials* **2016**, *1* (9). DOI: 10.1038/natrevmats.2016.42.

(66) Linhart, L.; Paur, M.; Smejkal, V.; Burgdorfer, J.; Mueller, T.; Libisch, F. Localized Intervalley Defect Excitons as Single-Photon Emitters in WSe_2. *Phys Rev Lett* **2019**, *123* (14), 146401. DOI: 10.1103/PhysRevLett.123.146401.

CHAPTER 2

METHODS

The body of work presented in this thesis focuses on experimental research involving 2D TMDs and GaN thin films. Throughout this research, various experimental techniques were employed to characterize, manipulate, and grow these materials. This chapter discusses the installation and commissioning of a combined optical and atomic force microscope (AFM) system, which was used extensively for the experimental characterization of the materials. The optimization of the nanoindentation technique is also described, which is the method used to induce strain in 1L-TMDs. To close this chapter, the two growth techniques of chemical vapor transport (CVT) and molecular beam epitaxy (MBE) are introduced. These two growth techniques were used to grow bulk crystals of TMD alloys and GaN thin films, respectively.

2.1 TRIOS system: coupling an atomic force microscope and optical microscope

Room-temperature steady-state Raman and PL spectroscopy, as well as room-temperature AFM, were utilized for most of the experiments described in this thesis. As part of this thesis, the optical path for an instrument that integrates an atomic force microscope (AFM) with an optical microscope—the HORIBA Scientific TRIOS Versatile AFM Optical Coupling system—was constructed and installed. The TRIOS is a fully functional AFM and optical microscope platform capable of performing room-temperature confocal and tip-enhanced Raman and PL spectroscopies.

Figure 2.1 presents a block diagram of the optical path coupling light into the commercially built TRIOS system, which is labeled and outlined by a black dashed line. An image of the TRIOS vertical frame corresponding to Figure 2.1 is shown in Figure 2.2.

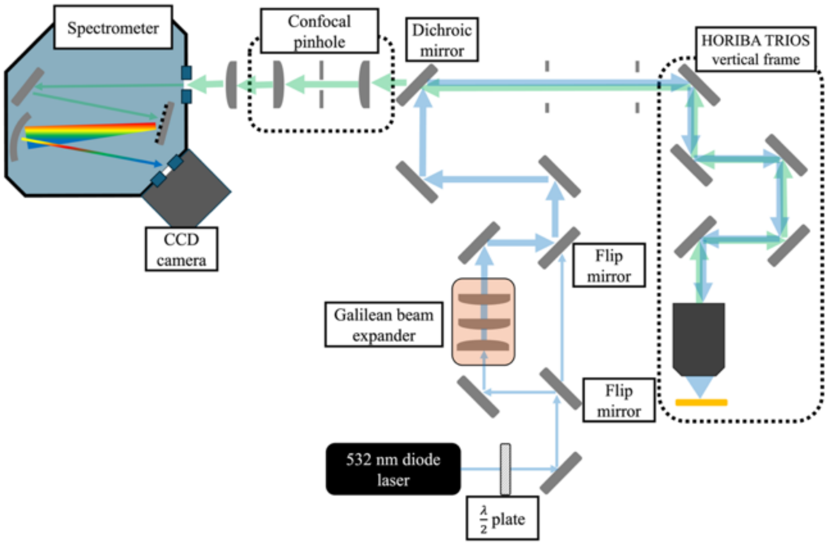

Figure 2.1– A block diagram of the confocal and nano-optical microscope. The HORIBA TRIOS vertical frame is a commercial system composed of an AFM coupled to an optical microscope. The laser paths denoted in the diagram are custom-built for the vertical frame. The two flip mirrors are used to differentiate between the optical paths for nano-optical measurements and conventional confocal microscopy.

The TRIOS vertical frame serves as the core of the microscope system. The optical paths that couple light into the vertical frame are illustrated in the block diagram in Figure 2.1. A 633 nm HeNe laser or a 532 nm continuous-wave (CW) diode laser is used as the excitation source for most of the measurements presented in this thesis. The polarization of the laser is adjusted by a λ/2 plate, which rotates the plane of linearly polarized light to the desired orientation. For tip-enhanced measurements, the polarization of the incident laser is particularly critical.

During confocal measurements, the two flip mirrors are raised, directing the light into a Galilean beam expander with a fixed expansion of 2.5×. In contrast, for tip-enhanced measurements, the flip mirrors are lowered, allowing the light to bypass the beam expander. The differences between these optical paths are discussed later in this chapter.

The laser is reflected by a long-pass dichroic mirror designed to reflect the excitation wavelength while transmitting the collected signal. The reflected beam is coupled into the HORIBA vertical frame, where it is focused onto either the sample surface or the apex of a gold-coated AFM tip. The emitted signal follows the same optical path in reverse: it passes through the vertical frame, is transmitted by the dichroic mirror, and is focused onto a 200 μm diameter confocal pinhole aligned with the optical axis of the spectrometer. The light transmitted through the pinhole is then collimated and focused onto the entrance slit of the spectrometer. Inside the spectrometer, the signal is dispersed by a reflective grating and detected by a CCD camera.

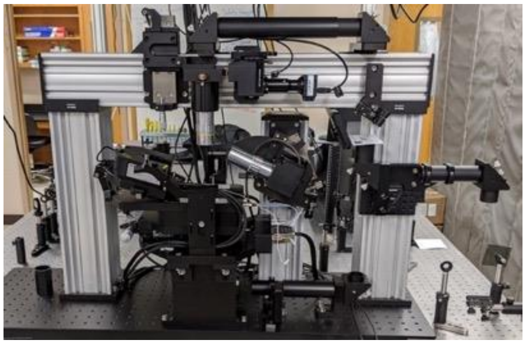

Figure 2.2 – An image of the TRIOS vertical frame.

A block diagram of the TRIOS vertical frame is shown in Figure 2.3. Three objectives are available on the TRIOS system and are mounted on the optical rails, as illustrated in Figure 2.3. The top objective, labeled 1, is used for AFM measurements and can be modified to perform confocal Raman and PL spectroscopy. The side objective, labeled 2, is used for tip-enhanced measurements such as tip-enhanced Raman spectroscopy (TERS) and tip-enhanced photoluminescence (TEPL). The bottom objective, labeled 3, is used for confocal Raman and PL measurements.

The top objective was utilized in all three research studies presented in this thesis (Chapters 3–5). The bottom objective was used in Chapters 4 and 5, and the side objective was used exclusively in Chapter 3. To couple light into the side or bottom objectives, two mirrors—one oriented upward and the other downward—can be mounted in the position marked "interchangeable mirrors."

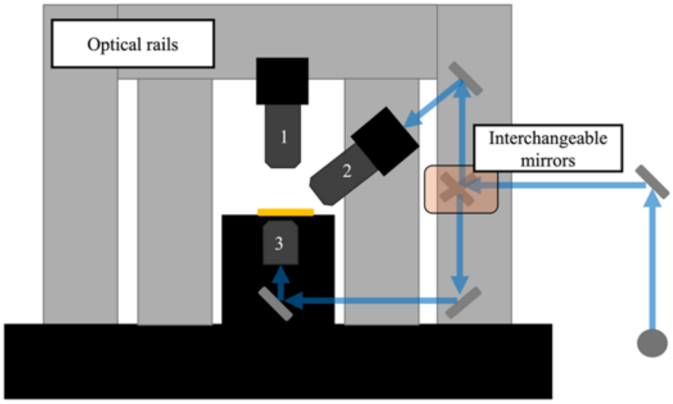

Figure 2.3 – A schematic of the vertical frame for TRIOS optical microscope. The system includes three objectives: the top objective serves as an observation microscope during AFM measurements, while the bottom and side objectives are used for confocal and tip-enhanced microscopy, respectively. Switching between the bottom and side objectives is facilitated by magnetically attached interchangeable mirrors.

To conduct TERS and TEPL measurements, the incident laser is coupled into the side objective of the TRIOS system. To direct light to the side objective (Mitutoyo M Plan Apo 100× / 0.70 NA), a mirror is placed in the "interchangeable mirror" mount to direct light upward. The orientation of the mirrors on the TRIOS vertical board system is shown in Figure 2.4. The long working distance of 6.0 mm for this objective is critical, as it ensures that when the laser spot is focused on the AFM tip, the objective does not interfere with the sample stage during scanning.

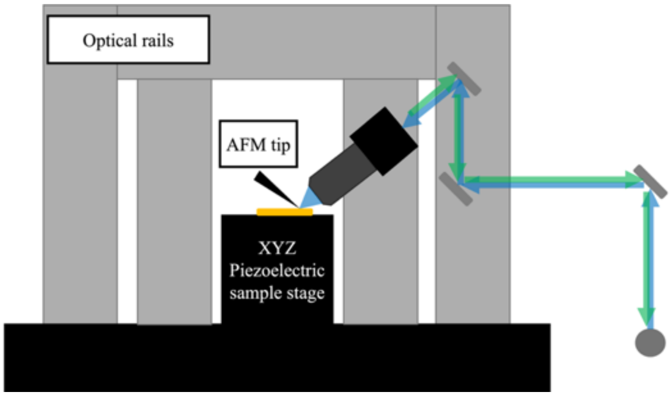

Figure 2.4 – A schematic of the tip-enhanced microscopy optical path for the TRIOS vertical board.

For room-temperature confocal PL and Raman measurements, the incident laser is coupled into the bottom objective. To couple the laser into the bottom objective, the interchangeable mirror is replaced with a downward-oriented mirror. The laser is coupled into the objective as shown in Figure 2.5. This objective is a Nikon LU Plan Fluor 100×/0.90 NA objective. The large numerical aperture (NA) of 0.90 allows for high-resolution imaging during confocal measurements.

2.1.1 TRIOS system: tip-enhanced measurements

This section focuses on the side objective and how the tip-enhanced measurements were performed. To optically measure the nanoscale interfaces of 2D material lateral heterostructures, as discussed in Chapter 3, sub-diffraction-limited resolution is required. To achieve such high resolution in Chapter 3, we used TERS. TERS is a technique that combines AFM and a conventional confocal laser system.

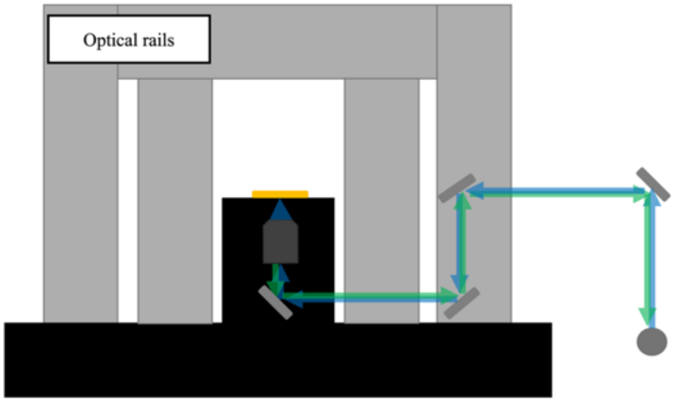

Figure 2.5 – A schematic of the confocal microscopy optical path for the TRIOS vertical board.

Confocal Raman and PL spectroscopies collect signals in the far field. When the detected signal originates from a region less than one wavelength away from the sample surface, it is considered a near-field signal. Any signal originating from farther away is classified as far-field. In a confocal microscope, the far-field, propagating wave will reach the image plane, resulting in diffraction-limited images, while the near-field signal will not reach the image plane[1].

The near-field component is an evanescent wave that remains significant up to approximately 10 nm from the surface. Measuring this near-field signal enables sub-diffraction-limit imaging. To obtain such images, the near-field signal must be effectively scattered into the far field, and both the signal and the scattering process must be enhanced. These effects are induced by the metallic AFM probe used in TERS[1-3].

Scattering of the near-field signal into the far field can, in principle, be achieved by any nanoscale object. Because the apex of an AFM probe has dimensions on the order of tens of nanometers, it efficiently scatters the near-field signal into the far field due to its proximity to the source. Enhancement of the near-field signal, however, requires a metallic AFM probe with a resonant optical response to the incident laser, which generates a spatially confined electromagnetic field at the probe apex. This confined field enables sub-diffraction-limit resolution imaging and facilitates the isolation of the near-field signal from the far-field background[1, 3].

The metal used as the coating on the AFM probe determines the choice of incident laser. Typically, the probe is coated with either gold or silver. Gold is preferred because it provides substantial signal enhancement at longer wavelengths in the red spectral range and is stable under ambient conditions. Silver, on the other hand, enables signal enhancement with incident light in the blue-green spectral region. However, silver-coated AFM probes are prone to oxidation and degrade under ambient conditions[3].

The formation of the enhanced nano-light source arises from the oscillation of free electrons in the metallic coating of the AFM probe by the electric field of the laser. These oscillating free electrons are known as plasmons[1, 3, 4]. The plasmons generate an oscillating electromagnetic field confined to the surface of the metallic film, referred to as surface plasmon polaritons (SPPs)[1, 3, 4]. When resonantly excited, the SPPs produce a strong evanescent electromagnetic field near the metallic surface. This evanescent field is a non-propagating wave, confined to tens of nanometers from the surface. The spatial confinement of the evanescent field at the apex of the metallic AFM probe constitutes the nano-light source[3].

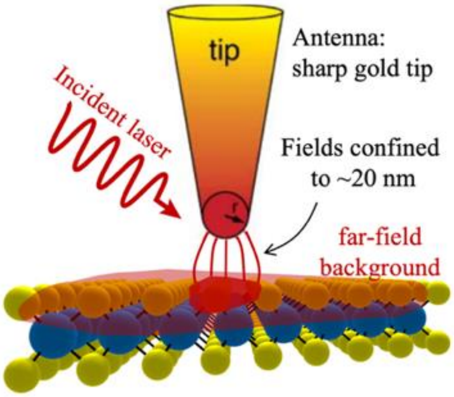

Figure 2.6 – A schematic of a laser-illuminated gold AFM probe. The incident laser illuminates the apex of the probe and the sample surface. Electromagnetic fields are confined only at the apex of the probe. Adapted from Atkin *et al*[2].

When the metallic AFM probe comes into contact with a material, the nano-light source enhances the Raman signal intensity by a factor of 10^3–10^5 [1, 3]. Because a diffraction-limited spot illuminates both the tip and the sample to generate the nano-light source, Raman scattering occurs in both the near-field and the far-field. The corresponding signals are collected from a total area of approximately 1.0 × 1.0 μm^2, while only a small region on the order of 20 × 20 nm^2 is exposed to the enhanced fields of the probe. The schematic in Figure 2.6 illustrates the collection areas of the far-field and near-field signals. The near-field and far-field contributions are convolved, and the near-field signal can be isolated by treating the far-field signal as a background.

To deconvolve the far-field background from the near-field signal, the Horiba software collects both the far-field signal and the convolved near and far-field signals at the same measurement point. This collection technique is possible because, in the Horiba system, the AFM probe operates in alternating tapping mode. At each scan point, the probe first oscillates in tapping mode and then makes direct contact with the sample when the system switches to contact mode. In tapping mode, the AFM tip oscillates up and down at a resonant frequency determined by the cantilever stiffness. In contact mode, the probe is not oscillating, and the tip remains in contact with the sample. When the AFM tip is oscillating, it is in close proximity to the surface only for very short instances of time, and the signal that is collected is dominated by the far-field response. When the probe switches to contact mode, the near-field-dominant signal is collected[4]. By acquiring the far-field signal before collecting the near-field-dominant signal, the two contributions can be deconvolved by subtracting the far-field signal from the near-field-dominant signal.

Near-field signal enhancement also depends on the polarization of the incident laser. When the light is vertically polarized, the electric field is aligned with the long axis of the probe, creating the strongest dipole. A 5× increase in intensity for vertically polarized light compared to horizontally polarized light is shown in Figure 2.7.

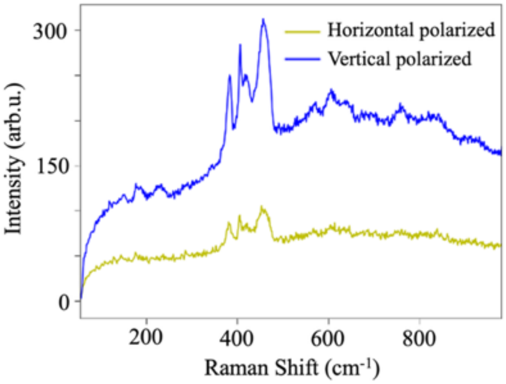

Figure 2.7 – TERS signal enhancement dependence on the incident laser polarization. The blue spectra represent the incident laser vertically polarized, and the yellow spectra represents when the incident laser is horizontally polarized.

To further enhance the Raman signal, gap-mode TERS can be employed, which involves creating a metallic nanogap between the apex of the gold AFM probe and a gold substrate. A nano-light source is already established at the apex of the gold AFM probe. When the AFM probe approaches within 5 nm or less of the gold substrate, a nanoscale plasmonic cavity enhances the local electric field, as shown in Figure 2.8.

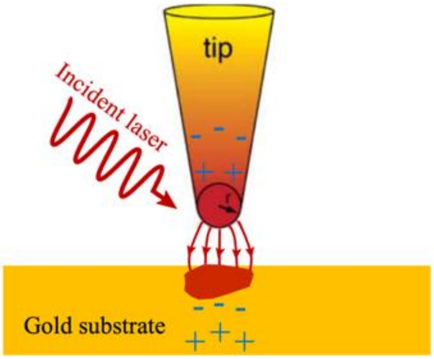

Figure 2.8 – A schematic of a gold AFM probe over a gold substrate creating a plasmonic nanocavity. The confined electric field at the probe apex induces a plasmonic nanocavity between the gold tip and substrate. The blue plus and minus signs indicate the oscillating charges creating the enhanced field. Adapted from Atkin *et al*[2].

2.1.2 Electromagnetic field polarization in gap-mode TERS

The electric field in gap-mode TERS is predominantly polarized in the Z-direction (along the axis of the probe), directly below the AFM tip. However, as described in this section, at positions still within the hot spot but away from the axis of the probe, there are polarization components that are parallel to the plane of the sample. These polarization states can couple to in-plane Raman modes and be substantially enhanced when an incident laser resonant with the sample's optically active electronic transition is used. This selectivity is demonstrated in Chapter 3.

Gap-mode TERS is an effective method for enhancing the Raman signal, and by exploiting the resonance Raman scattering phenomenon, selective enhancement of in-plane Raman modes can be achieved. Resonance Raman scattering occurs when the incident laser energy is close to or matches the electronic band gap of the material, increasing the Raman signal[1, 5]. In resonant gap-mode TERS, Jaculbia *et al.*[5] showed that in-plane Raman modes can be selectively enhanced over out-of-plane modes. In their study, the authors measured gap-mode TERS on isolated copper naphthalocyanine (CuNc) using a resonant laser. The incident laser was resonant with the in-plane optically allowed transition between the highest occupied molecular orbital (HOMO) and the lowest unoccupied molecular orbital (LUMO). The out-of-plane electronic transition between the HOMO and LUMO is optically forbidden, meaning that the in-plane Raman modes are enhanced by resonant Raman scattering, whereas the out-of-plane modes are not.[5]

A similar selectivity is observed in Chapter 3, where the in-plane Raman mode $E'(\Gamma)$ of 1L-MoS_2 experiences resonance gap-mode TERS enhancement. The resonance enhancement in 1L-MoS_2 arises because the optically active electronic transition is in-plane, while the out-of-plane transition is optically dark[6]. The electric field of the plasmonic nanocavity couples to the in-plane transition, producing resonant enhancement of in-plane Raman modes such as $, E'(\Gamma)$.

2.1.3 TRIOS system proof of concept: measuring TERS of tellurium nanowires

As a proof of concept demonstrating the capabilities of our TRIOS system, TERS measurements were performed on tellurium (Te) nanowires provided by Dr. Hugh Churchill's group at the University of Arkansas. Previous work using confocal (far-field) Raman spectroscopy has shown that bent nanowires exhibit strain, evidenced by shifts to lower or higher wavenumbers compared to straight nanowires[4]. To investigate the bent nanowires at the nanoscale, a TERS integrated intensity map of a Te nanowire, integrated from 105–135 cm^{-1}, is shown in Figure 2.9. The map reveals a nanowire width of approximately 100 nm. Comparison of four average spectra—two collected from the inside of the curve and two from the outside—shows that the inside spectra are shifted to higher wavenumbers, while the outside spectra are shifted to lower wavenumbers. The Raman mode shift to lower wavenumbers indicates tensile strain on the outer edge of the nanowire compared to the inside edge[7].

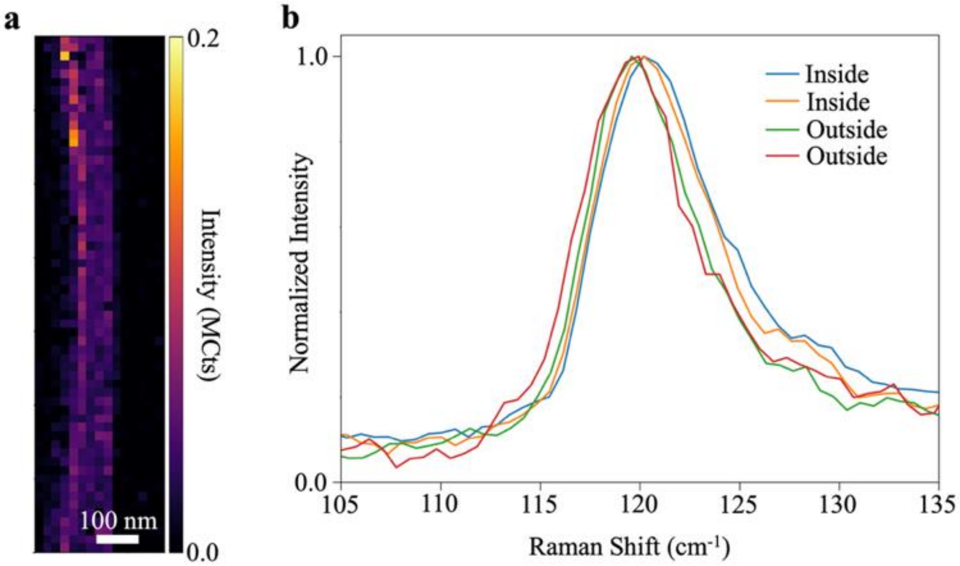

Figure 2.9 – A TERS intensity map of a Te nanowire and average spectra. (a) A TERS integrated intensity map, integrated from 105 to 135 cm^{-1}. (b) Comparison of average TERS spectra, calculated over 2×29 $pixels^2$. Spectra were collected from two locations on the inside and two on the outside of the curve, corresponding to the left and right sides of the intensity map in (a).

TERS measurements were repeated on a different nanowire. The integrated intensity map (Figure 2.10a) was taken at the apex of the curved wire, where maximum strain is expected. The three average spectra in Figure 2.10b show that the spectra from the inside of the curve are shifted to lower wavenumbers, while the spectra from the outside of the curve are shifted to higher wavenumbers, compared to the spectra collected from the middle of the nanowire. The ability to resolve these spectral differences across a ~100 nm length scale is not achievable using a conventional confocal microscope.

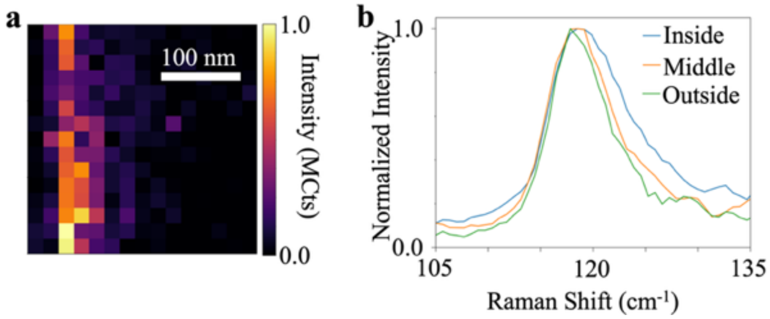

Figure 2.10 – A TERS intensity map of a Te nanowire and average spectra comparison. (a) An integrated intensity map, integrated from 105 to 135 cm^{-1}. (b) A comparison of average spectra, calculated over 1×4 pixels^2. The spectra were collected from three locations: inside, middle, and outside of the curve. These locations correspond to the left side, middle and right side of (a).

2.1.4 TRIOS system: confocal spectroscopy

Room-temperature confocal Raman and PL spectroscopy were critical characterization tools throughout the work presented in this thesis. Achieving a diffraction-limited laser spot was essential for Chapter 4 to resolve features on the 300–1000 nm length scale in Raman and PL intensity maps. One component of this setup, shown in Figure 2.1, is the Galilean beam expander, which increases the beam size by 2.5×, from approximately 4 mm to 10 mm, to achieve a diffraction-limited spot. To minimize the laser spot size, the excitation laser must overfill the back aperture of the objective[8], as schematically illustrated in Figure 2.11.

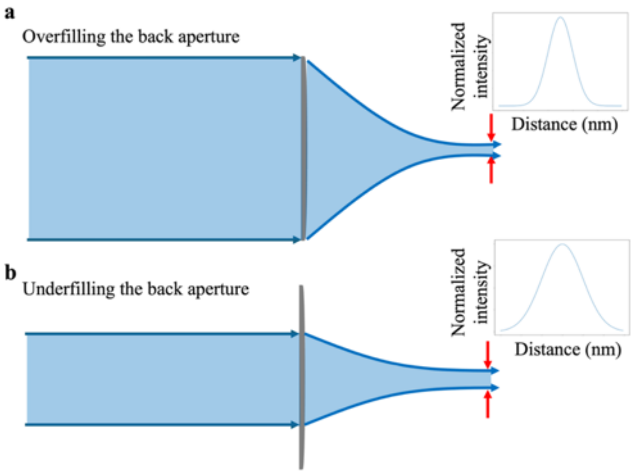

Figure 2.11 – Overfilled aperture and underfilled aperture. (a) The case where the incident laser light overfills the aperture, resulting in the smallest Gaussian full width at half maximum (FWHM) at the positions indicated by the red arrows. (b) When the aperture is underfilled, the focused laser spot exhibits a larger FWHM.

Figure 2.11a illustrates the laser light overfilling the back aperture of an objective. In this case, the incident laser, which has a Gaussian profile, is bent at the sharpest angle, minimizing the Gaussian FWHM and producing the smallest possible laser spot. In contrast, Figure 2.11b shows the incident laser underfilling the aperture. The laser is bent at a smaller angle, resulting in a larger FWHM and, consequently, a larger focused spot. The beam expander not only enlarges the beam but also ensures that the light is collimated, meaning all rays propagate in the same direction.

Another key factor in achieving the smallest laser spot is ensuring that the objective viewing camera and the objective itself are in the same focal plane. When the sample is in focus on the viewing camera, the laser spot generated by focusing a well-collimated beam is also in focus. To align the focal planes, the distance between the tube lens and the CCD in the viewing camera is adjusted. This is done by moving the lens until a distant light source—in our case, a flashlight approximately 100 feet away—is brought into focus. To verify that the laser spot approaches the diffraction limit, a 594 nm CW diode laser was used to measure the reflectance of a bulk piece of WSe_2. Using Equation 2.1 and the parameters of the objective and incident laser, the theoretical diffraction limit (d) of the system is 330 nm.

$$d = \frac{\lambda}{2 \cdot \mathrm{NA}} \qquad \text{Eq.2.1}$$

In Equation 2.1, λ is the incident laser wavelength (594 nm), and NA is the numerical aperture of the objective (0.90). The actual laser spot size was 650 nm, which, considering optical imperfections such as dust on the mirrors, is sufficient for the measurements presented in this work. The laser spot size was determined, as shown in Figure 2.12, by extracting the maximum intensity of the reflected laser light along a line cut from the substrate onto a bulk TMD flake. The distance between the 88% and 12% maximum intensity points was calculated and taken as the laser spot size. These 88% and 12% intensity levels were chosen because the laser spot has a Gaussian profile, and the FWHM corresponds to 12% and 88% of the integrated intensity.

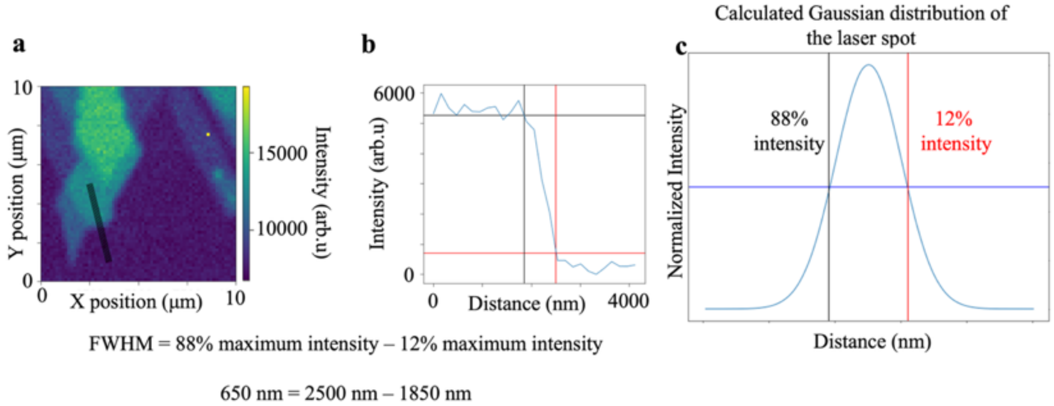

Figure 2.12 – Determination of the laser spot size from an intensity map. (a) Reflected laser intensity map of bulk MoS_2, with a three-pixel-wide linecut taken from the substrate onto the MoS_2. (b) The maximum intensity along the linecut from (a). The intersections of the red and black lines mark the 88% and 12% intensity levels, corresponding to the FWHM positions of the Gaussian profile. (c) A calculated Gaussian distribution to represent the laser spot, where the FWHM defines the size of the focused laser spot.

2.1.5 TRIOS system: nanoindentation

The nanoindentation technique, introduced in this section, was used to create localized tensile strain for QEs in 1L-TMD alloys and W-TMDs. This technique was critical for the research presented in Chapter 4. The TRIOS system is equipped with a fully functional AIST-NT SmartSPM HE002 AFM head, capable of contact, tapping, non-contact, phase imaging, lateral force, conductive, magnetic force, Kelvin probe, electric force, and lithography measurement modes, including nanoindentation.

The substrate for indented samples consists of a Si/SiO_2 wafer spin-coated with a deformable layer such as PMMA, which is subsequently hard-baked. Crystallites of 1L-TMDs are then transferred or mechanically exfoliated onto the top of the PMMA film. The area to be indented is selected and scanned by XYZ piezo motors, whose high precision is critical for the nanoindentation process. Once the desired scan area is imaged, the scan is loaded into a software module called Curves_map, which allows the user to specify the locations of indents and the extent to which the Z piezo motor will move the sample stage toward the AFM probe.

When the scan is loaded into Curves_map, the AFM tip and sample are held at a constant position by the electronic feedback loop. In the software, the Z-movement (or Z-displacement) can be set to -2000 nm, indicating that the sample stage will move 2000 nm toward the AFM probe. Figure 2.13 shows the SiO_2/Si substrate and illustrates how the sample stage moves in the -Z direction as a function of the defined Z-displacement.

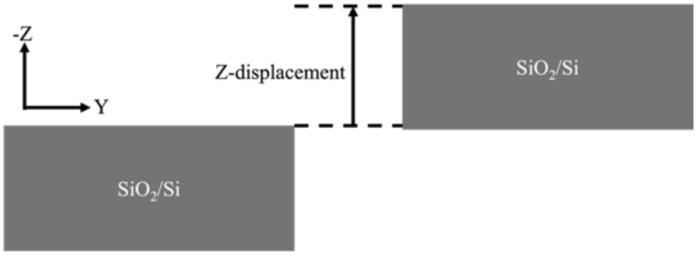

Figure 2.13 – A schematic illustrating the z-displacement of the AFM sample stage.

The AFM probe plastically deforms the PMMA as the tip pushes the 1L-TMD downward. The PMMA acts as a mold, holding the 1L-TMD in place. Once the indentation is complete, the probe retracts, leaving a tip-shaped indent. The indentation force is calculated by calibrating the Horiba software. A schematic of this indentation process is shown in Figure 2.14.

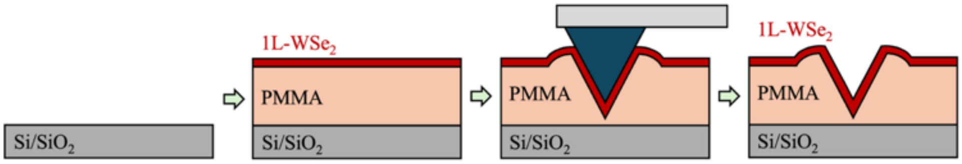

Figure 2.14 – The nanoindentation process. A single layer of WSe_2 is exfoliated onto a deformable substrate (PMMA) spin-coated onto Si/SiO_2. The AFM probe is brought into contact with the probe, pressing the probe into the surface until the WSe_2 and PMMA deform. After retraction, a tip-shaped indent remains.

The notion that the AFM tip produces a perfectly tip-shaped indent represents the ideal scenario. In practice, imperfections arise in the indents for several reasons, including—but not limited to—lateral slippage of the tip, mechanical fracture of the tip, and anisotropic accumulation of material on one side of the tip relative to the other. The topography map shown in Figure 2.15 provides a more accurate representation.

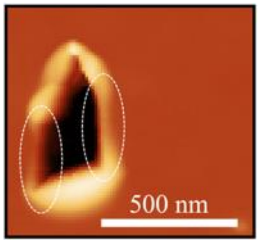

Figure 2.15 – A height map of an indent made with z = 2000 nm (indentation force = 53 μN) in PMMA. The white dashed circles indicate regions where the material was stretched.

Outlined with white dashed lines are areas where the indent appears to have been stretched. This stretching results from the tip sliding during the indentation process, causing the indent to elongate and not accurately reflect the tip shape. Tip sliding occurs because the cantilever bends at large Z-displacements. Figure 2.16 shows that, as the AFM cantilever bends at the hinge point, the AFM tip follows an arching path that tilts it forward, away from its initial position. The lateral slipping of the tip during bending is responsible for the elongation of the indents.

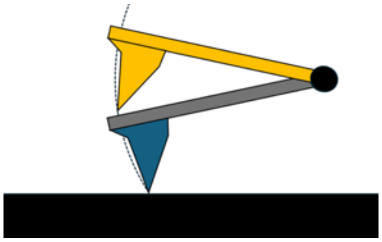

Figure 2.16 – A schematic of how the AFM cantilever bends at a single pivot point. The black circle marks the pivot where the cantilever is attached to the Si wafer. The gray and blue cantilever and tip sit at a 12° angle in the TRIOS system. The yellow cantilever shows its behavior when bent to an extreme. The dashed black arch marks the path of the AFM tip as the cantilever pivots.

2.1.6 TRIOS system: nanoindentation angle setting

To create consistent and reproducible indents, it was necessary to optimize the indentation technique, which required understanding the behavior of the AFM tip during the process. The optimization described in this section provided important insights into the indentation process, as demonstrated in Chapter 4. The following section discusses strategies to limit AFM tip slipping when it is pressed more deeply into the sample. As the sample stage moves toward the AFM tip, the cantilever bends, causing the tip to tilt away from its original contact point, as shown in Figure 2.16. As this angle increases, the probe slides. The sliding process is illustrated schematically in panels a and b of Figure 2.17. In Figure 2.17b, the indent does not match the geometry of the AFM tip.

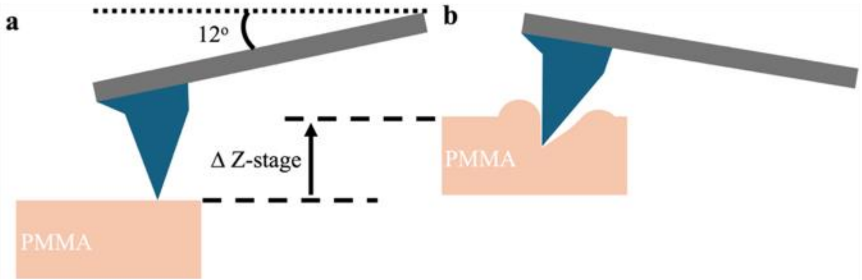

Figure 2.17 – A schematic of the AFM tip dynamics during indentation. (a) The AFM probe sits at 12° in the AFM tip holder, in contact with the sample. (b) The indent is stretched as the probe slides forward while the cantilever bends.

To minimize indent elongation, the software includes a setting to introduce lateral displacement in the Y-direction as the indentation progresses to large Z-displacement values (corresponding to higher indentation forces). This lateral movement keeps the apex of the tip at the same point on the sample throughout the indentation process. Maintaining the probe in the same position on the sample ensures that the buildup of PMMA at the edges of the indent is symmetric, as shown in Figures 2.18a and 2.18b. The symmetric buildup around the indent indicates that minimal tip slipping occurred during the indentation. The lateral displacement is controlled by Equation 2.2.

$$Y = Z \cdot \tan(\theta) \qquad \text{Eq. 2.2}$$

Where Z is the distance the sample stage moves into the AFM probe, and θ is the input angle into the software. The Z-displacement is controlled by Equation 2.3.

$$Z = To \cdot \cos(\theta) \qquad \text{Eq. 2.3}$$

"To" is the target Z-displacement, in nm, in the software. If θ is not calibrated properly, the Y-displacement can introduce indent elongation as shown in Figure 2.18c and d. An asymmetric PMMA buildup occurs on the right side of the tip, as demonstrated in Figure 2.18d.

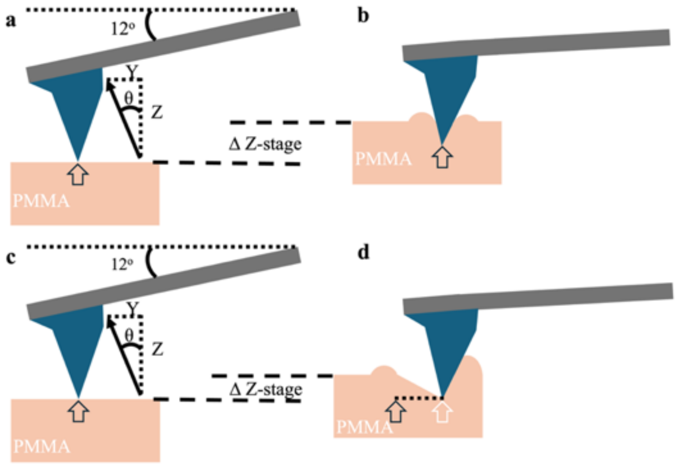

Figure 2.18– Schematics demonstrating lateral displacement during indentation. (a, b) The probe angle introduces lateral stage movement in the y direction as the stage moves upward in Z, keeping the probe in the same position on the sample. (c, d) If the angle is not adjusted correctly, the stage moves too far in y, causing the indent to elongate.

To calibrate the Y-displacement, an array of indents was made in 1L-WSe_2, with the desired Z-displacement set to 2000 nm (indentation force = 53 µN) and the input angle (θ) varied from 0°

to 60° in steps of 2°. The results are shown in the AFM height map in Figure 2.19a. For each of the 30 indents, the Z and Y-displacements were measured and plotted in Figures 2.19b and 2.19c, respectively. As the input angle increased, the Z-displacement decreased while the Y-displacement increased.

When θ ranged from 0° to 10°, the Y-displacement was too small, allowing the tip to slip and causing asymmetric buildup. Between 12° and 20°, the indents exhibited symmetric buildup, indicating that the Y-displacement maintained the tip at the same position on the sample during indentation. From 22° to 30°, the Y-displacement began to produce asymmetric PMMA buildup. Beyond 30°, the Y-displacement exceeded 1000 nm, which can lead to unpredictable PMMA buildup.

From the results shown in Figure 2.19, the ideal input angle was determined to be between 12° and 20°. For the work in Chapter 4, an input angle of 12° was used based on these measurements and vendor recommendations. However, for future experiments, angles of 18° or 20° may be preferred, as these indents appear most symmetric, contrary to the vendor's instructions.

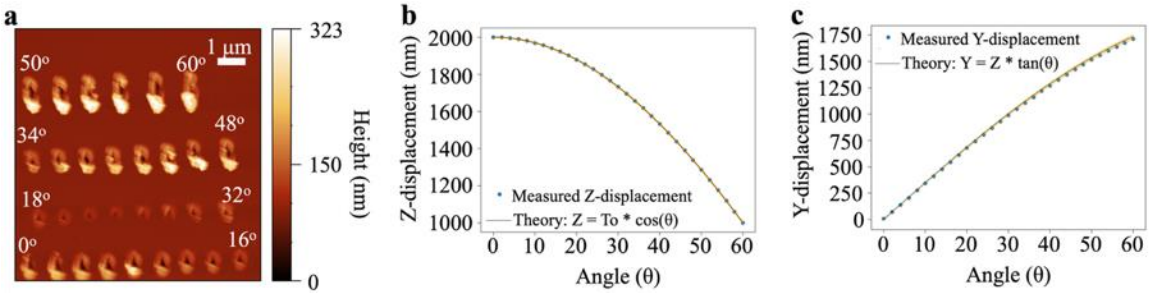

Figure 2.19 – Z and Y-displacement as a function of input angle for a set Z-displacement of 2000 nm. (a) Topography map of 30 indents with increasing input angles: first row 0–16°, second row 18–32°, third row 34–48°, and fourth row 50–60°. (b, c) Measured z and y displacements (blue circles) compared to the model predictions (black line), with the orange shaded region showing the absolute error. Z-displacement decreases and Y-displacement increases as the input angle increases.

2.1.7 TRIOS system: nanoindentation AFM tip dulling

A critical step in the nanoindentation technique was dulling the AFM probe before indentation to avoid tearing the material. As discussed in Chapter 4, using dulled probes is essential for reproducible strain; otherwise, tearing can occur. The steps taken to dull fresh AFM probes are described below.

In the initial nanoindentation work[9], the authors emphasized the need to dull the AFM probe before using it to indent 1L-TMDs. To dull the probes, a fresh probe was scanned in contact mode. The large normal force during scanning breaks the tip, effectively dulling it.

To measure the tip radius, an object such as a quantum dot or nanobead is imaged with the AFM, and the tip radius is deconvolved from the measured topography[10]. Both the AFM tip and the measured object are approximated as circles. The apex of AFM tips is described by the tip radius, making the circular approximation reasonable[11]. The point at which the circles first make contact is the tangent point, as illustrated in Figure 2.20.

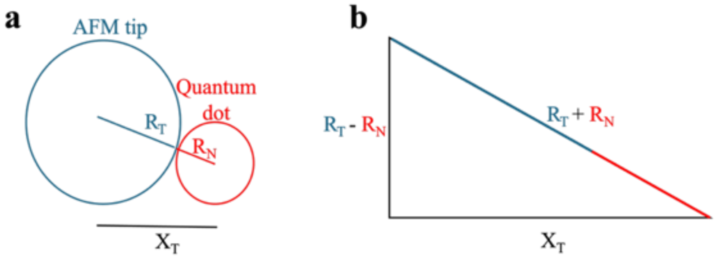

Figure 2.20 – Geometric method to calculate the AFM tip radius. (a) The AFM tip (blue) and quantum dot (red) are treated as perfect circles with radii R_T and R_N, respectively. X_T is the total lateral distance between the tip and the quantum dot. (b) Right triangle used to calculate the tip radius (R_T).

In Figure 2.20a, R_T and R_N represent the AFM tip radius and nanoparticle radius, respectively, and X_T is the total horizontal distance between the tip and the particle at the point of first contact. From the tangent point, a right triangle can be constructed, as shown in Figure 2.20b, allowing derivation of an equation to calculate the effective radius of curvature of the AFM tip. From Figure 2.20b, solving for X_T yields Equation 2.4.

$$X_T = \sqrt{(R_T + R_N)^2 - (R_T - R_N)^2} \qquad \text{Eq. 2.4}$$

Simplify Equation 2.4 by expanding the parentheses in the square root to get Equation 2.5.

$$X_T = \sqrt{4R_N R_T} \qquad \text{Eq. 2.5}$$

Finally, solve for R_T to get Equation 2.6.

$$R_T = \frac{(X_T)^2}{4R_N} \qquad \text{Eq. 2.6}$$

In Equation 2.6, the quantum dot radius (R_N) is known and can be measured from an AFM topography map of the quantum dots. The total lateral distance (X_T) between the tip and the quantum dot is also measured from AFM. The AFM tip radius (R_T) can then be calculated using Equation 2.6.

The quantum dots used were cadmium selenide (CdSe) with a radius of 4 nm. A single quantum dot was measured with a fresh AFM probe, after which the AFM was switched to contact mode. In contact mode, two to three 1×1 μm^2 scan areas were imaged. The normal force of the probe during contact mode ranged from 400 to 800 nN, depending on how much the probe needed to be dulled. As expected, a higher normal force produced a duller probe. The system was then switched back to tapping mode, and the same quantum dot was measured again to calculate the tip radius before and after indentation. An example of extracting R_N and X_T from AFM linecuts of a CdSe quantum dot is shown in Figure 2.21.

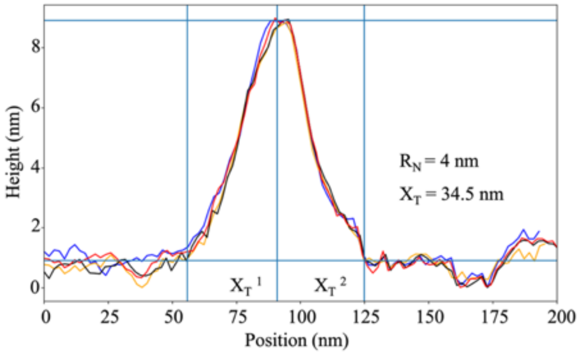

Figure 2.21 – AFM height linecuts of a CdSe quantum dot before tip dulling. The quantum dot radius (R_N) is approximately 4 nm. X_T is measured as the average distance from where the AFM tip first contacts the quantum dot to the peak height (middle blue vertical line) and to the final contact point, labeled X_{T^1} and X_{T^2}.

The tip radius determined using the process shown in Figure 2.21 is 74.35 nm. Further confirmation of tip dulling after this process is provided in Figure 2.22, which compares SEM images of a fresh AFM probe (Figure 2.22a) and the same probe after dulling (Figure 2.22b). The SEM images demonstrate that the dulling process effectively blunts the tip. However, as discussed in Chapter 4, the non-uniform surface can still cause material tearing.

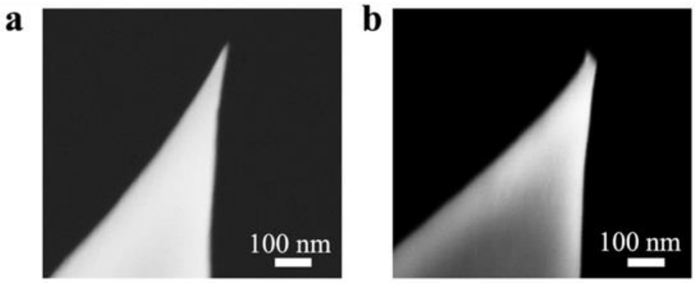

Figure 2.22 – SEM of a fresh AFM tip (a) and the same tip after dulling (b).

2.2 Material growth

2.2.1 Chemical vapor transport growth

Chemical vapor transport (CVT) is a bulk crystal growth technique that was used to grow 16 $Mo_xW_{(1-x)}S_2$ and $Mo_xW_{(1-x)}Se_2$, which were important for the research in Chapter 4 and are featured in the future research directions discussed in Section 6.2.1. These alloys were grown to study the role of dark excitons in the formation of strain-induced QEs. Bulk crystals of TMD alloys were grown via CVT at Penn State University in collaboration with the 2D Crystal Consortium – Materials Innovation Platform (2DCC-MIP). Dr. Sen Huat Lee provided guidance through the CVT growth process, and Dr. Suguru Yoshida oversaw X-ray diffraction (XRD) and energy dispersive X-ray (EDX) measurements to confirm the crystal structure and material composition of the crystals.

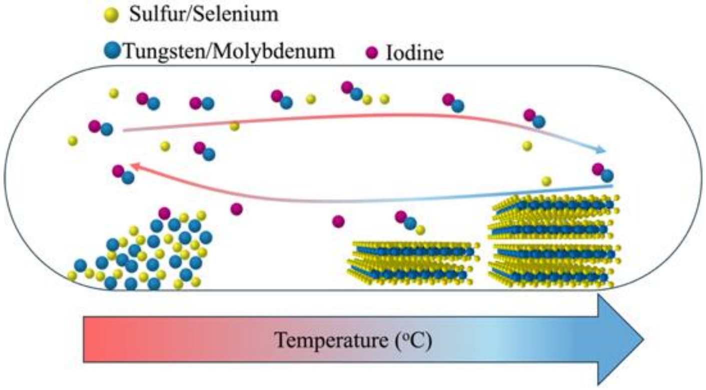

Figure 2.23 – Chemical vapor transport schematic. (a) Cartoon of the CVT process showing a vacuum-sealed quartz ampoule containing a mixed powder of transition metals (W/Mo) and chalcogens (S/Se), along with a carrier agent (iodine). The ampoule is placed in a tube furnace with a temperature gradient. On the hot side the chalcogen atoms move into the gas phase, and the carrier agent forms a volatile compound with the transition metal. These species migrate toward the colder end, where the chalcogen binds to the metal and crystallizes, forming bulk crystals.

CVT is a growth process in which the elemental powders composing the desired bulk crystal are mixed together and sealed in a quartz ampule with a carrier agent, such as iodine, under vacuum. The sealed ampule is then placed in a tube furnace, and a temperature gradient is applied. The side of the ampule containing the starting material is heated to a higher temperature than the crystallization side, which initially contains no material. The elements in the elemental powder move into the gas phase and, driven by the temperature gradient, migrate from the hot side to the cold side, where crystal growth occurs. For elements such as tungsten and molybdenum, which do not easily enter the gas phase, a carrier agent like iodine binds to the transition metal, stabilizing it in the gas phase[12-14]. A schematic of the CVT growth process is shown in Figure 2.23.

The TMD alloys grown at the 2DCC included $Mo_xW_{(1-x)}S_2$, $Mo_xW_{(1-x)}Se_2$, and $W(Se_{1-x}S_x)_2$. For the $Mo_xW_{(1-x)}S_2$, $Mo_xW_{(1-x)}Se_2$ alloys, a full range of molybdenum to tungsten concentrations was targeted, from W-rich to 50:50 to Mo-rich. Images of some of the bulk crystals grown are shown in Figure 2.24.

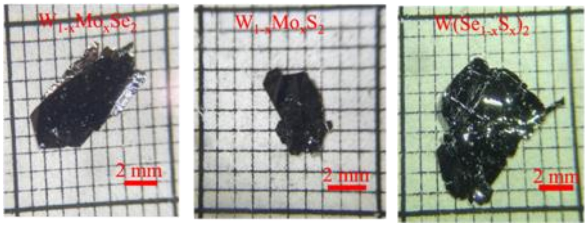

Figure 2.24 – Optical images of crystals grown at the 2DCC.

2.2.2 Molecular beam epitaxy growth of gallium nitride thin films

Molecular beam epitaxy (MBE) is a thin-film growth technique that was used to grow the thin films employed in the research described in Chapter 5. This work was conducted in collaboration with Dr. Brelon May at the Idaho National Laboratory in Idaho Falls, ID. Training was received on the MBE growth system, and hexagonal GaN thin films doped with actinide elements, such as uranium, were grown using their chamber. Their MBE system is the first to have U installed in a material cell. Optical images of the three ~1.0 × 1.0 cm^2 U-doped GaN samples are shown in Figure 2.25. Optical measurements were performed on these samples to investigate novel QEs for qubit applications.

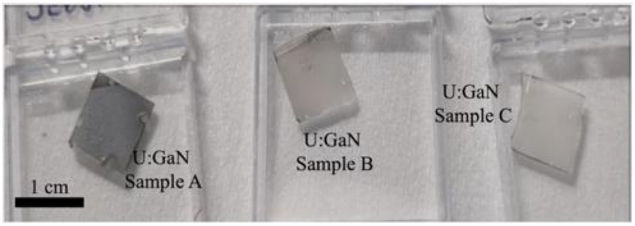

Figure 2.25 – Optical images of the first U-doped GaN samples grown at INL. The highest concentration to lowest concentration of uranium in samples A through C, respectively.

References

(1) Dhara, S.; Jariwala, D.; Das, S. *Nanoscopy and Nanospectroscopy*; 2023. DOI: 10.1201/9781003248323.

(2) Atkin, J. M.; Berweger, S.; Jones, A. C.; Raschke, M. B. Nano-Optical Imaging and Spectroscopy of Order, Phases, and Domains in Complex Solids. *Advances in Physics* **2012**, *61* (6), 745-842. DOI: 10.1080/00018732.2012.737982.

(3) Verma, P. Tip-Enhanced Raman Spectroscopy: Technique and Recent Advances. *Chem Rev* **2017**, *117* (9), 6447-6466. DOI: 10.1021/acs.chemrev.6b00821.

(4) Novotny, L.; Hecht, B. *Principles of Nano-Optics*; 2012. DOI: 10.1017/cbo9780511794193.

(5) Jaculbia, R. B.; Imada, H.; Miwa, K.; Iwasa, T.; Takenaka, M.; Yang, B.; Kazuma, E.; Hayazawa, N.; Taketsugu, T.; Kim, Y. Single-molecule resonance Raman effect in a plasmonic nanocavity. *Nat Nanotechnol* **2020**, *15* (2), 105-110. DOI: 10.1038/s41565-019-0614-8.

(6) Wang, G.; Robert, C.; Glazov, M. M.; Cadiz, F.; Courtade, E.; Amand, T.; Lagarde, D.; Taniguchi, T.; Watanabe, K.; Urbaszek, B.; et al. In-Plane Propagation of Light in Transition Metal Dichalcogenide Monolayers: Optical Selection Rules. *Phys Rev Lett* **2017**, *119* (4), 047401. DOI: 10.1103/PhysRevLett.119.047401.

(7) Basnet, R.; Doha, M.; Hironaka, T.; Pandey, K.; Davari, S.; Welch, K.; Churchill, H.; Hu, J. Growth and Strain Engineering of Trigonal Te for Topological Quantum Phases in Non-Symmorphic Chiral Crystals. *Crystals* **2019**, *9* (10). DOI: 10.3390/cryst9100486.

(8) Yu, C. H.; Yu, Y.; Adsit, L. M.; Chang, J. T.; Barchini, J.; Moberly, A. H.; Benisty, H.; Kim, J.; Young, B. K.; Heng, K.; et al. The Cousa objective: a long-working distance air objective for multiphoton imaging in vivo. *Nat Methods* **2024**, *21* (1), 132-141. DOI: 10.1038/s41592-023-02098-1.

(9) Rosenberger, M. R.; Dass, C. K.; Chuang, H. J.; Sivaram, S. V.; McCreary, K. M.; Hendrickson, J. R.; Jonker, B. T. Quantum Calligraphy: Writing Single-Photon Emitters in a Two-Dimensional Materials Platform. *ACS Nano* **2019**, *13* (1), 904-912. DOI: 10.1021/acsnano.8b08730.

(10)Eaton, P.; West, P. *Atomic Force Microscopy*; 2010. DOI: 10.1093/acprof:oso/9780199570454.001.0001.

(11) Ramirez-Aguilar, K. A.; Rowlen, K. L. Tip Characterization from AFM Images of Nanometric Spherical Particles. *Langmuir* **1998**, *14* (9), 2562-2566. DOI: 10.1021/la971277o.

(12) Binnewies, M.; Glaum, R.; Schmidt, M.; Schmidt, P. Chemical Vapor Transport Reactions – A Historical Review. *Zeitschrift für anorganische und allgemeine Chemie* **2013**, *639* (2), 219-229. DOI: 10.1002/zaac.201300048.

(13) Binnewies, M.; Schmidt, M.; Schmidt, P. Chemical Vapor Transport Reactions – Arguments for Choosing a Suitable Transport Agent. *Zeitschrift für anorganische und allgemeine Chemie* **2017**, *643* (21), 1295-1311. DOI: 10.1002/zaac.201700055.

(14) Schmidt, P.; Binnewies, M.; Glaum, R.; Schmidt, M. Chemical Vapor Transport Reactions– Methods, Materials, Modeling. In *Advanced Topics on Crystal Growth*, 2013; DOI: 10.5772/55547.

CHAPTER 3

NANOSCALE RAMAN CHARTERIZATION OF A 2D SEMICONDUCTOR LATERIAL HETEROSTRUCTURE INTERFACE

Contribution of authors and co-authors

Manuscript in Chapter 3

Author: Sourav Garg

Contributions: conceived this work, material growth, sample fabrication, and wrote the manuscript.

Author: J. Pierce Fix

Contributions: conceived this work, conducted TERS measurements, data analysis, figure formatting, and wrote the manuscript.

Co-Author: Andrey V. Krayev

Contributions: conceived this work, conducted TERS measurements, data analysis, and wrote the manuscript.

Co-Author: Connor Flanery

Contributions: sample fabrication and writing the manuscript.

Co-Author: Michael Colgrove

Contributions: sample fabrication and writing the manuscript.

Co-Author: Audrey R. Sulkanen

Contributions: gold transfer of CVD-grown materials and writing the manuscript.

Co-Author: Minyuan Wang

Contributions: gold transfer of CVD-grown materials and writing the manuscript.

Co-Author: Gan-Yu Liu

Contributions: gold transfer of CVD-grown materials and writing the manuscript.

Co-Author: Ncholas J. Borys

Contributions: conceived this work, wrote the manuscript.

Co-Author: Patrick Kung

Contributions: conceived this work, wrote the manuscript.

Summary of major contributions made to this work

The initial interest in investigating the interface of a lateral heterostructure of 1L-TMDs was to look for QEs from quantum dot-like states in the interface[1]. One of the first PL measurements at 4K I performed in Dr. Borys's lab was of the sample in this investigation. Because the sample was on a gold substrate, the PL was quenched. Our efforts then turned specifically to tip-enhanced Raman scattering (TERS) measurements.

In this work, Dr. Andrey Krayev and I shared responsibility for the TERS measurements. Dr. Krayev performed TERS measurements on the heterostructure used in this work, while I conducted TERS measurements on the six samples in Figure S3.5. The six samples included 1L-WS_2, MoS_2, and four commercially grown $Mo_xW_{1-x}S_2$ alloys. Figure S3.5 shows that under resonant conditions, the 140-240 cm^{-1} Raman modes in the alloys have the highest intensity. We also showed in Figure S3.5 that by changing the molybdenum to tungsten ratio in the $Mo_xW_{1-x}S_2$ alloys, we can tune the resonance conditions, which results in a change in the intensity of the 140-240 cm^{-1} Raman modes.

I also led the analysis of all the experimental data and the preparation of Figures 3.1-3.7 in the manuscript. We were able to gain insight into the nature of the interface of the lateral heterostructure because of the analysis in Figures 3.4-3.7. The nonuniform interface width was made clear by Figures 3.4 and 3.6, while the changing molybdenum to tungsten concentrations across the interface were demonstrated in Figures 3.5 and 3.7 due to the systematic shifting of the Raman modes between ~430-450 cm^{-1}. In Figure 3.5, we also observed a change in intensity of the 140-240 cm^{-1} Raman modes, while in Figure 3.7, we did not see the 140-240 cm^{-1} Raman modes at all. This observation led to the conclusion that the 140-240 cm^{-1} Raman modes are resonantly active, which is a key finding of this work.

Manuscript information

Sourav Garg[†] , J. Pierce Fix[†] , Andrey V. Krayev, Connor Flanery, Michael Colgrove, Audrey R. Sulkanen, Minyuan Wang, Gang-Yu Liu, Nicholas J. Borys , and Patrick Kung

Published in ACS Nano

Status of Manuscript:

☐Prepared for submission to a peer-reviewed journal

☐Officially submitted to a peer-reviewed journal

☐Accepted by a peer-reviewed journal

☒ Published in a peer-reviewed journal

Abstract

The nature of the interface in lateral heterostructures of 2D monolayer semiconductors including its composition, size, and heterogeneity critically impacts the functionalities it engenders on the 2D system for next-generation optoelectronics. Here, we use tip-enhanced Raman scattering (TERS) to characterize the interface in a single-layer MoS_2/WS_2 lateral heterostructure with a spatial resolution of 50 nm. Resonant and non-resonant TERS spectroscopies reveal that the interface is alloyed with a size that varies over an order of magnitude—from 50-600 nm—within a single crystallite. Nanoscale imaging of the continuous interfacial evolution of the resonant and non-resonant Raman spectra enables the deconvolution of defect-activation, resonant enhancement, and material composition for several vibrational modes in single-layer MoS_2, $Mo_xW_{1-x}S_2$, and WS_2. The results demonstrate the capabilities of nanoscale TERS spectroscopy to elucidate macroscopic structure-property relationships in 2D materials and to characterize lateral interfaces of 2D systems on length scales that are imperative for devices.

Introduction

Two-dimensional (2D) transition metal dichalcogenide (TMD) semiconductors provide a rich platform for the study of low-dimensional many-body phenomena[2] and for the development of next-generation optoelectronic and photonic technologies that exploit strong light-matter interactions in the atomically-thin limit.[3-5] Lateral 2D heterostructures[6-9] extend these capabilities with nanoscale interfaces between 2D materials with different stoichiometries, band structures, strain, and/or carrier densities. 2D heterostructures with *p-n* junction characteristics,[10] precisely engineered band alignment,[11] interfacial electroluminescence,[12] and efficient thermal transport[13] have been experimentally realized. The resulting interfaces provide an additional nanoscale knob for tailored exciton dissociation,[14] interfacial exciton formation,[1] carrier transport,[15, 16] photocurrent generation,[17, 18] polariton lenses,[19] and 1D charge-density waves.[19] With precision growth techniques, superstructures comprised of multiple transitions and interfaces can be embedded into a single 2D crystalline system, giving rise to even richer hierarchical heterostructures.[20, 21]

In order to fully harness the technological potential of 2D lateral heterostructures, it is crucial to understand the nanoscale structure and heterogeneity of the interface. High-resolution scanning transmission electron microscopy (STEM) measurements have revealed that the atomic structures of the interface range from atomically sharp[7] to more gradual alloyed[6] transitions. However, such atomically-resolved characterization has not elucidated how the interface changes on length scales larger than 10 nm and with different orientations, both of which are critical for understanding devices based on 2D lateral heterostructures. Scanning probe microscopy (SPM) techniques can bridge the atomically insightful length scales of STEM to the larger length scales that are needed for understanding device performance. Kelvin probe force microscopy (KPFM)[11, 22-24] has been used to map the built-in fields in *p-n* junctions and differences in work functions in lateral 2D heterostructures. Near-field scanning microwave microscopy (SMM)[25, 26] has been used to image local photoconductivity. While these techniques are powerful characterization approaches, they lack unambiguous stoichiometric sensitivity and probe a response that convolves the structure of the interface with non-local electrostatic properties. Nano-optical tip-enhanced photoluminescence (nano-PL) is sensitive to material composition and has been used to characterize nanoscale charge transfer processes[27] and the stoichiometry of larger junction regions.[28, 29] However, nano-PL techniques are limited to samples that exhibit strong PL emission, and the large linewidths of PL spectra limit their sensitivity to composition. Raman spectroscopy is capable of overcoming these two limitations, providing a characterization approach that is highly versatile and highly sensitive. Yet, to date, nanoscale Raman imaging and spectroscopy have not been used to probe the interfaces in 2D lateral heterostructures.

Here, we show that tip-enhanced Raman scattering (TERS) imaging and spectroscopy is a powerful and complementary characterization technique for heterostructure interfaces in 2D TMD semiconductors. Spatial resolutions of at least 50 nm are achieved, and we show that both resonant and non-resonant TERS measurements are sensitive to the local stoichiometry of the heterojunction. The TERS measurements are complemented with KPFM imaging of the heterostructure and are shown to work on a system where photoluminescence (PL) is strongly quenched by an underlying gold substrate. From the TERS characterization, we find that the transition region of the heterostructure drastically varies in spatial extent with sizes ranging from ~600 nm to less than 50 nm within the same crystallite. Using the nanoscale vibrational fingerprinting, we assess the local alloying of the heterostructure and map the evolution of the Raman spectrum across the heterostructure interface. Insight on the origins and nature of multiple Raman modes is gained by mapping their nanoscale transformation across the interface. Overall, TERS is demonstrated as an effective way to study the nanoscale properties of heterostructure interfaces that complements other imaging techniques, laying a foundation for deeper multimodal studies that connect the interfacial structure and composition to macroscopic device performance.

Results and Discussion

Characterization of the as-grown lateral heterostructure

Single-layer (1L) lateral 2D heterostructures consisting of a 1L-MoS_2 core surrounded by a 1L-WS_2 shell were grown on polished sapphire wafers using low-pressure chemical vapor deposition (CVD; see Methods). As-grown crystals were first characterized using several SPM techniques that were cross-correlated with confocal PL imaging and spectroscopy. As discussed in detail in the Methods section, the TERS, SPM, and confocal characterization were performed with a commercial combined AFM and optical microscopy system (Xplora-Nano AFM-Raman, Horiba Scientific). SPM characterization of a representative lateral heterostructure crystal is summarized in Figure 3.1. Figure 3.1a shows a schematic of the lateral heterostructure which consists of a 1L-MoS_2 triangular core that is surrounded by a 1L-WS_2 shell. The optical image of the sample (Figure 3.1b) reveals that the typical shape of the 1L-MoS_2/1L-WS_2 lateral heterostructure crystallites is triangular with jagged edges, which are thought to arise due to growth conditions such as the chalcogen saturation and gas flow rate.[30] Additional optical imaging of the heterostructure crystallites are provided in the SI that demonstrate the jagged peripheral edges also form in the 1L-WS_2 shell (Figure S3.1 in the SI). The AFM topography of the lateral heterostructure (Figure

3.1c) shows that the transition between the 1L-MoS_2 and the 1L-WS_2 is flat, which confirms the predominantly lateral nature of the heterojunction. A small increase in the topography of the heterostructure of ~0.5 nm is observed around the periphery of the 1L-MoS_2 core. This topographic feature, which is smaller than the thickness of 1L-MoS_2 and 1L-WS_2, is attributed to a change in the interaction between the AFM probe and the 2D material as the composition changes (rather than as a sign of overlapping materials). As can be seen from both the topography and the contact potential difference (CPD; Figure 3.1d) maps, the interface between the 1L-MoS_2 core and the surrounding 1L-WS_2 is not a straight crystalline edge. Instead, the boundary of the 1L-MoS_2 core consists of small, predominantly triangular protrusions. A capacitance map of the same area is shown in Figure 3.1e, which further confirms the contrast between the two materials of the single-layer heterostructure.

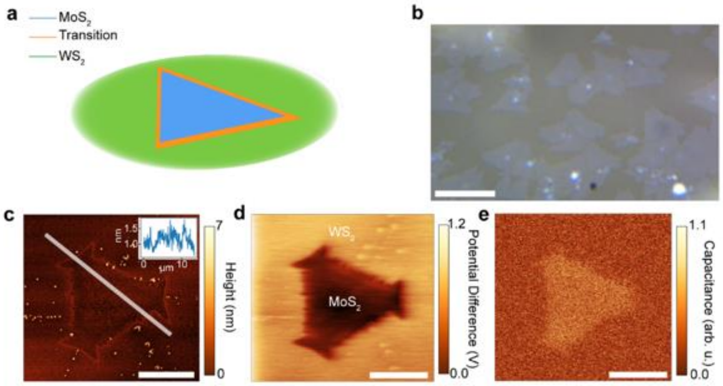

Figure 3.1 – Scanning-probe characterization of the as-grown 2D lateral heterostructure of 1L-MoS_2 and 1L-WS_2. (a) Schematic of the 2D lateral heterostructure which is composed of a core of 1L-MoS_2 that is separated from a shell of 1L-WS_2 by a transition region composed of a 1L-$Mo_xW_{1-x}S_2$ alloy of varying width. (b) Optical image of the as-grown lateral heterostructures. Scale bar: 50 µm. (c) AFM topography, (d) CPD, and (e) capacitance images of the single lateral heterostructure crystallite. Inset in (c): topographic profile of the lateral heterostructure along the path denoted by the white line in (c). Scale bars in (c), (d), and (e): 5 µm.

Figure 3.2 presents confocal μPL imaging and spectroscopy of the same 2D lateral heterostructure crystallite that is shown in Figure 3.1. Spatially-resolved PL emission was recorded over the wavelength range of 550 nm to 750 nm under CW laser excitation (532 nm, 300 μW, 25 ms/pixel integration). Figures 2a-2d map out the integrated intensity of the PL spectrum for the entire emission band (Figure 3,2a), a high-energy band for the 1L-WS_2 (Figure 3.2b), an intermediate band between those of the two pure materials (Figure 3.2c), and a low-energy band for the 1L-MoS_2 (Figure 3.2d). Bright PL emission from all regions of the 2D lateral heterostructure confirms the monolayer nature of the 1L-MoS_2 core and surrounding 1L-WS_2 as shown in the full spectra in Figure 3.2e. In the 1L-MoS_2 core, the PL is centered at ~670 nm (1.85 eV), which is expected for the emission of 1L-MoS_2. In the surrounding 1L-WS_2, the PL is ~6× brighter than the 1L-MoS_2 core and is centered at ~628 nm (1.97 eV), as expected for 1L-WS_2. In the interfacial region between the 1L-MoS_2 and 1L-WS_2, the PL intensity increases compared to the 1L-MoS_2 core and its spectrum is positioned at an intermediate wavelength of 638 nm (1.94 eV). As a result, a peripheral ring of bright emission in the intermediate band is formed at the heterostructure interface (Figure 3.2c).

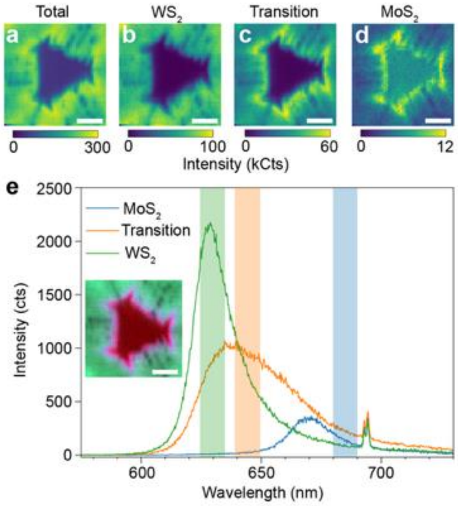

Figure 3.2 – Confocal μPL imaging and spectroscopy of the as-grown 2D lateral heterostructure of 1L-MoS_2 and 1L-WS_2. Spatial maps of (a) the total emission intensity, (b) a 10 nm emission band for 1L-WS_2, (c) a 10 nm intermediate band for the transition region, and (d) a 10 nm emission band for 1L-MoS_2. (e) Example spectra for the 1L-MoS_2 core, 1L-WS_2 shell, and the transition region. The shaded regions indicate the bands used to generate the images in (b)-(d). The narrow emission lines between 690-770 nm are ruby emission from the sapphire substrate. Inset: combined images of the 1L-MoS_2, 1L-WS_2, and the transition regions rendered in the red, green, and blue channels, respectively. All scale bars: 4 μm.

The spectrum of the intermediate PL in the heterojunction region indicates that the interface is comprised of a ternary alloy of 1L-$Mo_xW_{1-x}S_2$.[31-33] The average relative Mo and W content in this alloy region can be estimated from the spectral position using Vegard's Law, Equation 3.1, that describes the change in the PL energy with alloy stoichiometry:

$$E_{Mo_xW_{1-x}}(x) = (x)E_{MoS_2} + (1-x)E_{WS_2} - b(1-x)x. \tag{Eq.3.1}$$

Here, the b is the bowing factor, which has been reported as 0.25 eV[31] for TMD alloys. Using this relationship and the emission energies here, the composition would be coarsely estimated to be 1L-$Mo_{0.09}W_{0.91}S_2$ in the interfacial region (*i.e.*, $x \approx 0.09$). However, the linewidth of the PL spectrum in the interfacial region (~130 meV, FWHM) is substantially larger than those of the 1L-MoS_2 (~50 meV, FWHM) and the 1L-WS_2 (~65 meV), suggesting the presence of disorder. As shown below, the interfacial disorder is dominated by a continuous range of alloy compositions and transition widths. The heterostructure is a more complex optoelectronic system than an atomically sharp interface or just a simple uniform alloy composition, necessitating characterization with higher spatial resolutions.

Disentangling nanoscale phenomena at the heterostructure interface necessitates a different approach than conventional SPM and confocal optical techniques. The diffraction-limited resolution of the μPL (and μRaman) characterization limits the ability to directly probe structure-property relationships of the 2D lateral heterostructure interface at length scales smaller than a few hundred nanometers. For SPM techniques that have a higher spatial resolution, unambiguous signatures of material alloying and interfacial disorder are not available. Bridging this divide, nano-optical characterization such as nano-PL,[28, 29, 34-39] nano-absorption,[40] and TERS (*i.e.*, nano-Raman)[36, 41, 42] enables materials characterization with nanoscale spatial resolutions, especially for 2D material systems. Nano-optical techniques utilize a nanoscale plasmonic antenna to nano-focus optical fields to sub-wavelength volumes which can then be used to study highly localized light-matter interactions.[43] In particular, TERS enables vibrational fingerprinting of materials at the nanoscale. Sub-nanometer spatial resolutions have been achieved in ultrahigh vacuum (UHV) with STM modalities.[44-47] Under ambient conditions, AFM-based TERS can routinely achieve resolutions of 10-20 nm,[36, 48] offering a 50× improvement over μRaman. Moreover, 2D materials are particularly amenable to gap-mode TERS techniques (Figure 3.3a) that enhance the signal-to-noise ratio by positioning the nano-optical antenna in close proximity to a smooth metal film (<5 nm) to create a nanoscale plasmonic cavity that enhances the local electric field even further. With the ability to provide high signal-to-noise nanoscale vibrational fingerprinting, gap-mode TERS is a compelling technique to probe the nanoscale properties of interfaces in lateral 2D heterostructures in a manner that synergizes the strengths of inelastic optical spectroscopy (*e.g.*, Figure 3.2) with the spatial resolution of SPM techniques (*e.g.*, Figure 3.1).

Semi-resonant TERS imaging and spectroscopy

Gap-mode TERS characterization requires the 2D system to be supported by a smooth metallic substrate. To implement the gap-mode TERS characterization here, the 2D crystals were transferred to a gold film using a previously established procedure[49] (see Methods). A thin gold film (~70 nm) was deposited onto the surface of the as-grown 2D crystallites on the sapphire growth substrate under high vacuum. Then, a Si wafer was attached to the outer gold surface using an epoxy resin. Once the epoxy cured, the gold-sapphire interface was separated by peeling. The 2D lateral heterostructures are more strongly bound to the Au film and are thus separated from the sapphire substrate. The process results in the transfer of the 2D lateral heterostructures from the sapphire surface to being inlaid in the gold film,[49, 50] exposing the pristine surfaces of the 2D lateral heterostructures that were previously in contact with the sapphire substrate.

An optical image of the 2D lateral heterostructure that was characterized in Figures 1 and 2 after the gold-assisted transfer process is shown in Figure 3.3b. Using optical contrast microscopy, the same single-layer crystallites were easily identified before and after the gold-assisted transfer process (see Figure S3.2 in the SI). As can be seen by the AFM characterization in Figures 3.3c and 3.3d, the transfer process preserves the smooth topography of the 2D lateral heterostructure. The variation in the topography in Figure 3.3c is less than 0.5 nm indicating that tearing or fracturing did not occur during the transfer process. Further KPFM characterization of the 2D lateral heterostructure partially embedded in the gold shows clear contrast in the CPD between the 1L-MoS_2 core and the surrounding 1L-WS_2 shell (Figures 3.3e and 3.3f), which reflects the differences in work functions between the two materials. The difference in the CPD between the 1L-MoS_2 and 1L-WS_2 is ~150 mV, consistent with earlier reports.[23, 24] The CPD imaging on the Au surface (Figure 3.3e) more clearly reveals that the apparent boundary between the 1L-WS_2 and 1L-MoS_2 is intricately profiled, exhibiting sharp saw-tooth-like protrusions of 1L-MoS_2 into the surrounding 1L-WS_2. The extent of the transition between the 1L-MoS_2 and 1L-WS_2 in terms of the CPD is 500-1000 nm, which, as shown below, is significantly larger than what is measured using TERS. The likely origin of this difference is the sensitivity of CPD measurements to the work function of the material, which depends on both the stoichiometry and the depletion region of the heterostructure. As a result, CPD measurements will report a transition width that is larger than the size of the material interface as determined by just stoichiometry (see Table S1 for a summary of prior CPD measurements of 2D heterostructure which all report similar size scales)[51-53].

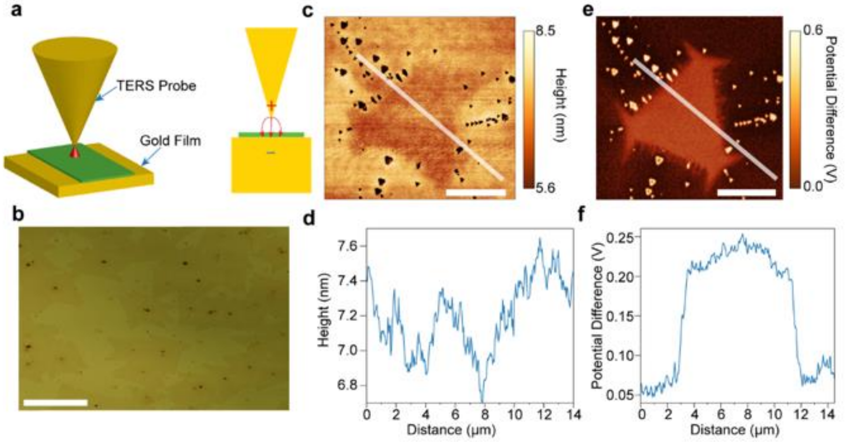

Figure 3.3 – Hybrid Au-2D lateral heterostructure system for gap-mode TERS characterization. (a) Schematic of gap-mode TERS where the 2D material is stripped from its growth substrate using an Au-assisted stripping technique. As a result of the template stripping process, the lateral heterostructure is embedded in the Au. (b) Optical image of a stripped 2D 1L-MoS_2/1L-WS_2 lateral heterostructure. Scale bar: 50 μm. (c) AFM image of the lateral heterostructure embedded in the Au. Scale bar: 5 μm. (d) Topographic profile of the 2D heterostructure along the white line in (c). (e) CPD image of the lateral heterostructure embedded in Au. Scale bar: 5 μm. (f) CPD profile along the white line in (e), which corresponds to the topographic profile in (c) and (d).

Gap-mode TERS characterization of the 2D lateral heterostructure provides deeper insight into the nature of the interface. The TERS imaging and spectral analysis using laser excitation at 638 nm are presented in Figure 3.4. To facilitate direct comparison, Figure 3.4a replicates the region of the CPD imaging in Figure 3.3e for the region that was characterized with gap-mode TERS. We note that this region does not have any characteristics in the SPM imaging that distinguish it from the other transition regions in the crystallite. The laser excitation at 638 nm is weakly resonant with both the long-wavelength tail of absorption for the 1S exciton state in 1L-WS_2 and the short-wavelength tail of the absorption of the 1S exciton state of the 1L-MoS_2. Under these semi-resonant conditions, the TERS spectra (cf. Figure 3.4b) from the 1L-MoS_2 core and the 1L-WS_2 shell (*i.e.*, away from the heterojunction interface) exhibit many features that are similar to resonant μRaman spectroscopy[54, 55] but have notable differences that highlight the potential for gap-mode TERS to augment insight gained from far-field μRaman measurements. For the 1L-WS$_2$ shell, the prominent mode at 417 cm^{-1} corresponds to the $A'(\Gamma)$ mode, whereas the cluster of modes from 296 cm^{-1} to 355 cm^{-1} reflects the resonant nature of the laser excitation.[55] Complementing these prominent modes, four low-energy vibrational modes are identified at 148, 176, 200, and 215 cm^{-1}. Previous studies have reported three of these four modes (146.5, 176, and 214 cm^{-1}) and have assigned them to the $\mathrm{ZA}(M)$, $\mathrm{E}'(M)^{\mathrm{TO2}} - \mathrm{LA}(M)$ or $\mathrm{LA}(M)$, and $\mathrm{E}''(M)^{\mathrm{TO1}} - \mathrm{TA}(M)$ modes, respectively[56-58]. However, the relative intensities of these peaks relative to, for instance, the $A'(\Gamma)$ mode are larger in gap-mode TERS (compared to those observed in μRaman on a dielectric interface).[55-58] In addition, the gap-mode TERS spectrum of the 1L-WS$_2$ also exhibits a mode at 433 cm^{-1}, which to our knowledge has not been observed in far-field μRaman measurements. Prior combined scanning tunneling microscopy (STM) and TERS measurements of 1L-WS$_2$ have correlated this mode to S vacancies,[59] which as discussed below, agrees with our observations here.

The gap-mode TERS spectrum of the 1L-MoS$_2$ (Figure 3.4b, blue) also reflects the semi-resonant nature of the laser excitation at 638 nm. The most prominent feature is the vibrational mode observed at 455 cm^{-1}. While this mode is known to emerge under resonant conditions, its assignment has not been unambiguously established. It could arise from the combination of $2\mathrm{LA}(M)$ and the normally IR active $A_2''/A_{2u}(\Gamma)$ modes or from the higher energy component $\mathrm{E}''(M)^{\mathrm{TO1}} + \mathrm{ZA}(M)$ mode.[54, 57] As will be discussed below, the TERS imaging here also directly links this mode to the 433 cm^{-1} mode in the 1L-WS$_2$, suggesting that its origin is also related to S vacancies. At the lower energies, multiple modes are observed between 320 cm^{-1} to 440 cm^{-1}. For non-resonant Raman scattering, two modes are anticipated in this spectral region. The first mode corresponds to $E'(\Gamma)$ at 386 cm^{-1} and $A'(\Gamma)$ at 405 cm^{-1}. Prior reports[54, 57, 60] of resonant Raman scattering spectra of 1L-MoS$_2$ on dielectric substrates do not observe modes between 386 cm^{-1} and 405 cm^{-1}. On gold, it has been shown[61] that charge transfer splits the $A'(\Gamma)$ mode, producing a second mode at 400 cm^{-1} which was also accompanied by a ~7 cm^{-1} shift of the $E'(\Gamma)$ mode to lower wavenumbers. Here, we observe the intermediate mode at 400 cm^{-1} but do not observe the shift of the $E'(\Gamma)$ mode. These differences that are observed in the resonant Raman spectra of 1L-WS$_2$ and 1L-MoS$_2$ between conventional μRaman and gap-mode TERS could be due to a number of potential factors such as less strain in our system, a stronger out-of-plane polarization in gap-mode TERS as well as subtle interactions with the tip (*i.e.*, induced strain[38] or charge transfer[62]). Identifying the underlying mechanisms is outside the scope of the current work and will be the subject of future investigations that will focus on a careful comparison of polarization-resolved μRaman to gap-mode TERS.

Figures 3.4c and 3.4d report the integrated peak intensity for the most prominent modes that are exclusive to 1L-MoS$_2$ and 1L-WS$_2$, respectively. To improve the contrast, these images report the peak intensity which is calculated by integrating the intensity of the spectrum in a specific band after subtraction of a linear background. The peak-filtering analysis provides an alternative for extracting peak intensities to multi-peak fitting routines, which necessitate relatively high signal to noise ratios, especially when dealing with overlapping peaks (see Section 4 in the SI for details). A transition region between the 1L-MoS$_2$ core and the 1L-WS$_2$ shell is identified and its width dramatically varies between a pixel-limited size to a few hundred nanometers at the tips of the triangular protrusions of 1L-MoS$_2$. The gap-mode TERS spectrum acquired from this transition region (Figure 3.4b, orange) is most similar to that of the 1L-WS$_2$ shell in terms of the spectral positions and relative intensities of the major peaks but has substantial distinguishing features. The first obvious difference is that a pronounced mode at 444 cm^{-1} is observed and lies between the positions of the 455 cm^{-1} mode of the 1L-MoS$_2$ and the 433 cm^{-1} S-vacancy defect mode of the 1L-WS$_2$. Second, the intensities of the 200 cm^{-1} and 215 cm^{-1} modes are substantially higher for the transition region as compared to that of 1L-WS$_2$. The increase in the intensity of these modes suggests that they can be used to image the transition region directly with a large amount of contrast. Figure 3.4e shows the integrated peak intensity of these modes over the lateral 2D heterostructures and demonstrates that these modes are the strongest in the transition region where the prominent modes for 1L-MoS$_2$ and 1L-WS$_2$ are the weakest. It also confirms the size variations of the transition region separating the core and shell of the lateral 2D heterostructure. By using independent color channels to render the intensities for the 1L-MoS$_2$ (red), 1L-WS$_2$ (green), and transition region (blue), a full-color image can be generated that shows how these different regions align with one another, depicting the nanoscale structural configuration of the transition region (Figure 3.4f).

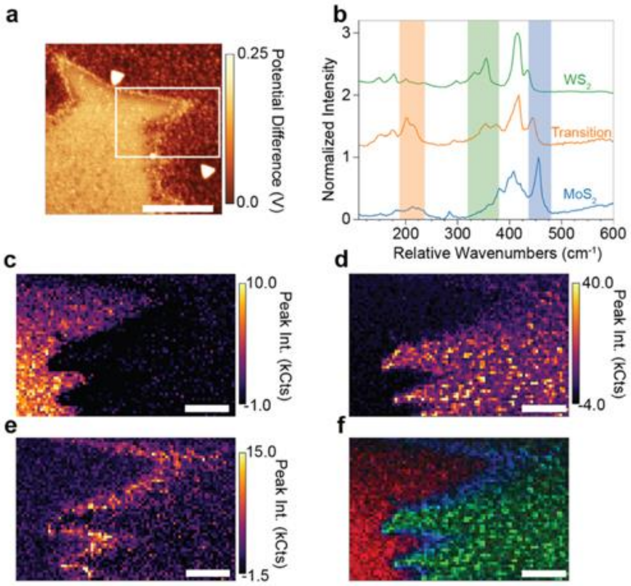

Figure 3.4 – semi-resonant TERS imaging and spectroscopy of the heterostructure interface. (a) CPD image of the region characterized with TERS. Scale bar: 2 µm. (b) Representative semi-resonant TERS spectra of the 1L-MoS$_2$ core, 1L-WS$_2$ shell, and transition regions of the lateral heterostructure. The spectra are averages over the following areas: 350 pixels from a 370×840 nm^2 area for MoS$_2$, 42 pixels from a 222×168 nm^2 for transition, and 400 pixels from a 740×270 nm^2 for WS$_2$. A constant background corresponding to the dark counts of the detectors was removed from each spectrum. (c) Spatial map of the peak intensity in the 440-480 cm^{-1} band of 1L-MoS$_2$. (d) Spatial map of the peak intensity in the 320-380 cm^{-1} band of the 1L-WS$_2$ shell. (e) Spatial map of the peak intensity in the 180-220 cm^{-1} resonant band associated with the alloyed transition region. (f) Combined image of the TERS bands with the 1L-MoS$_2$ band in the red channel, the alloyed transition band in the blue channel, and the 1L-WS$_2$ band in the green channel. Scale bars for (c)-(f) are 400 nm. The peak intensity maps enhance the contrast of the different regions by integrating the intensity of any peaks in the corresponding bands that remain after removing a linear background (see SI for details). The pixel-size in the TERS imaging is 25×25 nm^2 and signals were acquired with 250 ms/pixel integration times.

Considering the µPL characterization (*i.e.*, Figure 3.2), the distinct Raman bands in the transition region are potential nanoscale reporters of alloy formation between the 1L-MoS$_2$ and 1L-WS$_2$ regions. To test this hypothesis, we conducted two control measurements on known alloyed samples (see Sections 5 and 6 in the SI for details). In the first control, we carried out TERS characterization of CVD-grown 1L-Mo$_x$W$_{1-x}$S$_2$ crystallites where the growth produces a spatial gradient of composition. In the second, we performed gap-mode TERS spectroscopy of a series of known 1L-$Mo_xW_{1-x}S_2$ alloys that were mechanically exfoliated from commercially available bulk crystals. These measurements confirmed that the appearance and intensification of the modes between 140 cm^{-1} and 220 cm^{-1} under resonant excitation at 632.8 nm are associated with the alloying in $Mo_xW_{1-x}S_2$ compounds. These modes are practically absent in pure 1L-MoS_2 and 1L-WS_2 and reach maximum intensity in the alloyed compounds tested when the tungsten to molybdenum ratio is 2.32. Because these modes are observed throughout the 1L-WS_2 region of the 2D lateral heterostructure, these controls indicate that there is a persistent alloying in the shell region away from the junction, which is further supported by the TERS imaging of the transition region reported below (see also Figure S3.7 in the SI). In terms of the mode in the transition region at 444 cm^{-1}, no such mode was observed in the control measurements on single layers exfoliated from bulk crystals. Additionally, in the pure 1L-WS_2 that was mechanically exfoliated, the 433 cm^{-1} mode is not observed, which is consistent with the expectation that the bulk crystals have fewer chalcogen vacancies than the CVD-grown crystallites. Finally, the linewidths of the PL spectra of the control alloys are smaller than that of the transition region, again indicating the presence of interfacial disorder as previously discussed.

From the TERS imaging presented in Figure 3.4, the width of the alloyed transition between the 1L-WS_2 shell and 1L-MoS_2 core varies dramatically, ranging from the resolution limit of the measurement (*i.e.*, <50 nm) to ~600 nm. Figure 3.5 reports the progression of the TERS spectra across a representative transition region that is broad (~600 nm in length; Figure 3.5a) and one that is sharp (<50 nm in length; Figure 3.5b). Over the broad transition region, the TERS spectrum continuously transforms from that of 1L-MoS_2 to alloyed 1L-$Mo_xW_{1-x}S_2$ to 1L-WS_2. This evolution provides insight into the relationships of the modes across the different materials.

The 455 cm^{-1} mode of the 1L-MoS$_2$ continuously shifts to lower wavenumbers in the alloyed region and ultimately converges to the 433 cm^{-1} mode in the 1L-WS$_2$, which directly connects these respective modes in 1L-MoS$_2$ and 1L-Mo$_x$W$_{1-x}$S$_2$ to the mode in 1L-WS$_2$ that is activated by S vacancies. Similarly, the cluster of modes between 400-420 cm^{-1} in the 1L-MoS$_2$ evolves into the 417 cm^{-1} mode in the 1L-WS$_2$. In contrast to a continuous shift, the 1L-MoS$_2$ modes in the range of 380-400 cm^{-1} gradually weaken over the transition region, whereas the 1L-WS$_2$ mode at ~360 cm^{-1} intensifies over the transition region nearer to the 1L-WS$_2$ shell as the composition becomes W-rich. The low-energy modes (140–220 cm^{-1}) become brightest halfway across the transition region. Because these modes are resonantly enhanced, this onset marks the alloy composition at which the A exciton state is maximally resonant with the excitation laser, providing direct evidence that the heterostructure interface is composed of the full range of alloy compositions.

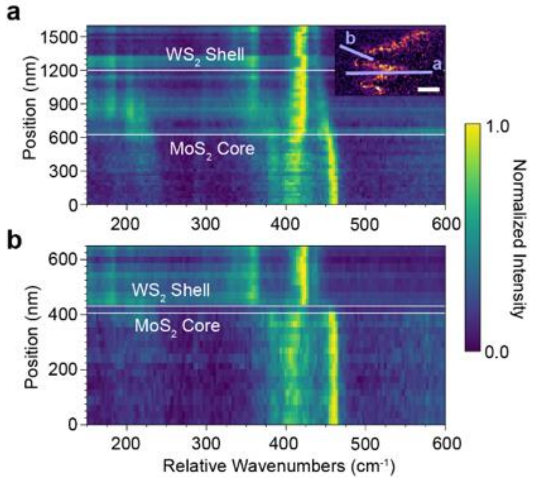

Figure 3.5 – characterization of the evolution of the semi-resonant TERS spectra across the broad and sharp transition regions in a 2D lateral heterostructure. (a) The evolution of the semi-resonant TERS spectrum across the broad transition region (path ‘a’ in the inset). Inset: spatial map of the TERS peak intensity in the spectral region of 180-220 cm^{-1} (duplicated from Figure 3.4d). Scale bar: 400 nm. The light-blue lines mark the path from which the spectra are interpolated. (b) The evolution of the semi-resonant TERS spectrum across the sharp transition region (path ‘b’ in the inset). For both (a) and (b), the TERS spectra are interpolated from a 50×25 nm^2 region at each position along the respective paths. The beginning and end of the transition regions are estimated as the points where the Raman spectra, specifically the mode at ~450 cm^{-1} in the MoS_2 and ~410 cm^{-1} in the WS_2, ceases to systematically change with position along the paths. A constant background corresponding to the dark counts of the detectors is removed from each spectrum.

The two representative transition regions shown in Figure 3.5 confirm that the size of the heterostructure interface can vary by at least an order of magnitude on the same 2D heterostructure crystal. Due to the resolution-limited size of the sharp transition region (Figure 3.5b), the transition from the 1L-MoS_2 to the 1L-WS_2 is discrete and does not exhibit further changes beyond the interface of the two materials. Given prior high-resolution TEM characterization and the alloyed nature of the broad transition, the sharp transition is likely similarly alloyed at length scales below our current resolution. Strikingly, the heterogeneity in the size of these transition regions occurs on microscopic length scales within the same 2D crystallite. The distance between these two regions is ~400 nm, essentially eliminating the possibility that the different concentrations of reactants during growth as the origin of the heterogeneity. Rather, we hypothesize that the origin of the heterogeneity may lie in the different reactivities of edges with different orientations.

Non-resonant TERS imaging and spectroscopy

To further probe the transition region and the nature of the Raman modes observed under semi-resonant excitation, we performed TERS characterization with non-resonant laser excitation at 785 nm (Figure 3.6), which is lower in energy than the optical bandgaps of both 1L-WS_2 and 1L-MoS_2. Under these conditions, the TERS spectra of the 1L-WS_2, 1L-MoS_2, and transition regions are substantially different than their counterparts under semi-resonant excitation (cf. Figures 3.6a, 3.6b, and 3.4b). The resonant and non-resonant TERS measurements were conducted on the same region of the sample to facilitate direct comparison. The topography of this region is reported in the SI (see Figure S3.6) and does not exhibit any topographic features that correspond to the transition. With the non-resonant excitation, the lower-energy Raman modes in the 140-220 cm^{-1} range are no longer observed anywhere in the 2D heterostructure. Further, the intensity of the $E'(\Gamma)$ peak at ~353 cm^{-1} is greatly reduced in the 1L-WS_2 shell and the transition region. Instead, the non-resonant Raman spectrum is dominated by the lower-energy compositional-dependent $A'(\Gamma)$ mode which evolves from 405 cm^{-1} in the 1L-MoS_2 core to 420 cm^{-1} in the 1L-WS_2 shell. Comparable behavior for this mode has been observed in μRaman spectroscopy of 1L-$Mo_xW_{1-x}S_2$ alloys, spanning a similar range of energies.[57, 63] At higher energies (450-460 cm^{-1}), the presumed defect mode remains active under non-resonant laser excitation and evolves in the opposite direction as the $A'(\Gamma)$ mode. It decreases in energy from 455 cm^{-1} in the 1L-MoS_2 core to 435 cm^{-1} in the 1L-WS_2 shell. In the transition region, this mode bridges the two energies and appears at 442 cm^{-1}, and as shown in the SI (see Figure S3.4) and below, depends on the particular alloy composition. By mapping the peak intensity of this mode in high-energy (436-456 cm^{-1}), intermediate-energy (430-450 cm^{-1}), and low-energy (420-440 cm^{-1}) bands around this mode, the 1L-WS_2 shell, transition, and 1L-MoS_2 core regions can be clearly discerned (Figures 3.6c-3.6f) and agree with the same type of imaging under resonant excitation (Figure 3.4).

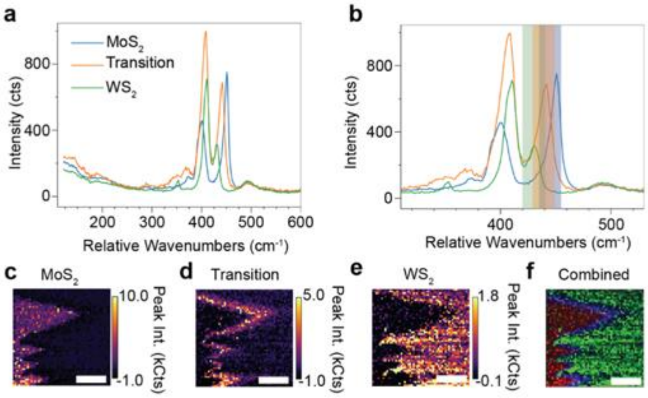

Figure 3.6 – non-resonant TERS imaging and spectroscopy of the heterostructure interface. TERS spectrum acquired under non-resonant excitation over (a) 120-600 cm^{-1} and (b) zoomed into the range of 310-530 cm^{-1}. The spectra are averages over the following areas: 400 pixels from a 240×960 nm^2 area for MoS_2, 110 pixels from a 240×264 nm^2 for transition, and 400 pixels from a 480×480 nm^2 for WS_2. A constant background corresponding to the dark counts of the detectors is removed from each spectrum. Peak intensity maps of the (c) high-energy (436-456 cm^{-1}; blue band in panel b), (d) intermediate-energy (430-450 cm^{-1}; orange band in panel b), and (e) low-energy (420-440 cm^{-1}; green band in panel b) bands for the 1L-MoS_2 core, alloyed transition region, and 1L-WS_2 shell, respectively. (c) Combined intensity map of the images in (b) with the 1L-MoS_2 band in the red channel, alloy band in the blue channel, and 1L-WS_2 band in the red channel. Scale bars for (c)-(f): 400 nm. The peak intensity maps enhance the contrast of the different regions by integrating the intensity of any peaks in the corresponding bands that remain after removing a linear background (see SI for details). The pixel size of the TERS imaging is 24×24 nm^2 and the signals were acquired with 100 ms/pixel integration times.

The differences in the Raman spectra between resonant and non-resonant laser excitation provide insight into the nature of the observed modes. When the laser excitation energy corresponds to an electronic transition in the material, resonant enhancement of weak/forbidden Raman modes can occur.[64] Furthermore, in gap-mode TERS, the polarization of the electric field is predominantly normal to the surface (*i.e.*, out-of-plane). In such a configuration, it was recently shown on small molecular systems that non-resonant excitation preferentially enhances out-plane modes, whereas the resonant excitation can dramatically and preferentially enhance in-plane modes.[45] The suppressed intensity of the $\mathrm{E}'(\Gamma)$ mode (at ~386 cm^{-1} in the 1L-MoS_2) under non-resonant conditions suggests that similar selectivity in enhancement occurs in 2D TMDs as the in-plane mode is substantially brighter under resonant excitation. Likewise, the practical absence of the rarely reported peaks within the 140-220 cm^{-1} range demonstrates that they are forbidden (*i.e.*, very weak) modes under non-resonant conditions. Further, the resonant enhancement of these modes explains their observed dependence on alloy concentration as discussed above. The resonance energy of the 1S transition of the A exciton evolves from 1.85 eV in pure 1L-MoS_2 to 2.0 eV in pure 1L-WS_2 following Vegard's law (cf. discussion above) and is maximally resonant with the 633 nm excitation at an alloy concentration of 1L-$Mo_{0.23}W_{0.77}S_2$. This optimal composition agrees well with the TERS spectra reported in the SI (See Figure S3.5) for different alloy compositions, where the maximum intensity of these modes is determined to occur at an alloy composition between 1L-$Mo_{0.15}W_{0.85}S_2$ and 1L-$Mo_{0.30}W_{0.70}S_2$.

Finally, in Figure 3.7, the evolution of the non-resonant TERS spectra from the 1L-MoS_2 core to the 1L-WS_2 is analyzed. As under the resonant excitation conditions, transition regions that are pixel-limited in size are identified alongside those that are over 500 nm in size, confirming the heterogeneity of the 2D lateral heterostructure interface. Figures 3.7a and 3.7b trace the evolution of the TERS spectra across representative broad (~500 nm) and sharp (~100 nm) transition regions, respectively. As under resonant excitation conditions, the modes under non-resonant excitation continuously evolve from the 1L-MoS_2 to the 1L-WS_2 across the broad region (a line in Figure 3.7a inset). Both of the 405 cm^{-1} and the 455 cm^{-1} modes in the 1L-MoS_2 shift into the 420 cm^{-1}

and 435 cm^{-1} modes in the 1L-WS$_2$, respectively. In the transition region, each of these modes appears at intermediate energies between the respective extremes. As the energies of these modes depend on the alloy composition, this observation confirms the alloyed nature of the transition region. Beyond the transition region in the MoS$_2$ core and the WS$_2$ shell, the energies of these modes do not evolve further (see Figure S3.7 in the SI). Future multimodal measurements that correlate these TERS signatures with, for example, nano-Auger imaging[34] could further confirm these observations and provide additional clarity into the origin of the many modes observed in the TERS spectrum as well as the heterogeneous nature of the transition region at length scales below 50 nm.

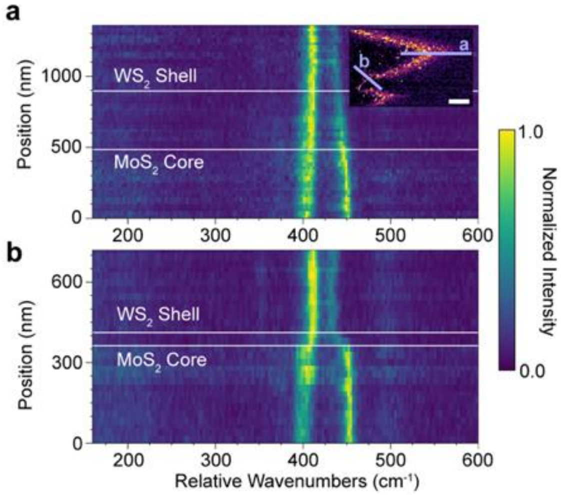

Figure 3.7 – characterization of the broad and sharp transition regions of the interface in a 2D lateral heterostructure using non-resonant TERS. (a) The evolution of the non-resonant TERS spectrum across the broad transition region (path ‘a’ in the inset). Inset: spatial map of the TERS peak intensity in the spectral region of 430-450 cm^{-1} (duplicated from Figure 6d). Scale bar: 400 nm. The light-blue lines mark the path from which the spectra are interpolated. (b) The evolution of the non-resonant TERS spectrum across the sharp transition region (path ‘b’ in the inset). For both (a) and (b), the TERS spectra are interpolated from a 48×24 nm^2 region at each position along the respective paths. The beginning and end of the transition regions are estimated as the points where the Raman spectra, specifically the mode at ~450 cm^{-1} in the MoS$_2$ and ~410 cm^{-1} in the WS$_2$, ceases to systematically change with position along the paths. A constant background corresponding to the dark counts of the detectors is removed from each spectrum.

Conclusions

In conclusion, TERS is a facile and informative characterization technique for heterostructure interfaces in lateral heterostructures between 2D materials. Here, the interface between a lateral heterostructure of 1L-MoS_2 and 1L-WS_2 has been characterized with a synergistic combination of resonant TERS, non-resonant TERS, confocal μPL, AFM, and KPFM imaging techniques. In particular, the TERS and other scanning probe techniques provide critical nanoscale information that bridges the gap between atomically-resolved STEM studies and diffraction-limited μPL/μRaman studies. On these intermediate length scales at which TERS is ideally suited to probe, we find that the transition region can be highly heterogeneous in size, ranging from widths of <50 nm to 600 nm in a single crystallite. We hypothesize that the different sizes of the transition region result from different reactivities of the edges that form during the growth process. Future studies that use scanning tunneling microscopy and/or nano-second harmonic generation imaging to probe the chemical nature of the edges could test this hypothesis by providing more insight into the structure and reactivity of the edges on the nanoscale. Further, for the TERS characterization, the contributions of resonant excitation and alloy composition have been deconvolved for low-energy vibrational modes in the range of 140-240 cm^{-1}. By mapping the continuous nanoscale evolution of the transition region from 1L-MoS_2, to 1L-$Mo_xW_{1-x}S_2$, to 1L-WS_2, we unambiguously link the 455 cm^{-1} mode in 1L-MoS_2 to the 433 cm^{-1} defect-activated mode in 1L-WS_2 and reveal how the mode changes with alloy composition. This mode serves as an excellent nanoscale reporter of the composition of the transition region and is used to characterize the heterogeneity in the size of the interface in the 2D heterostructure. These studies provide important insight into the nanoscale properties of the heterostructure interfaces in 2D materials and set the stage for combining TERS characterization with other microscopy modalities and prototype optoelectronic devices to quantitatively understand the role of the heterostructure interface in device performance.

Methods

Heterostructure growth

The single-layer MoS_2/WS_2 lateral heterostructures were grown by low-pressure chemical vapor deposition in a multizone quartz tube. High purity MoS_2 and WS_2 precursor powders (both 99.9%, Alfa Aesar) were finely mixed and placed in a quartz boat at the center of the tube while the epi-ready sapphire substrates were placed downstream at a lower temperature. No prior substrate surface treatment or preparation was used beyond solvent cleaning. The growth was performed at a pressure of 10 mbar under 20 sccm argon flow, with the temperature of the precursors ramped to 970 °C, for a duration of 20 min. The tube temperature for the substrate region was ramped from 790 to 810 °C during the growth. Subsequently, the temperature was allowed to cool down naturally.

Optical, scanning probe, and TERS characterization

The AFM and TERS characterization presented in the main manuscript were conducted on an XploRA-Nano AFM-Raman system (HORIBA Scientific) using Access-SNC-Au TERS probes (Applied Nanostructures). TERS maps were collected using patented SpecTop^{TM} mode, where, in every pixel of the map, the tip is placed in direct contact with the sample and the Raman data are collected. Then, to move to the next pixel, the system is rapidly placed into semicontact (tapping) mode to minimize the ware of both the tip and the sample. Measurements of the TERS response of the gold-transferred exfoliated $Mo_xW_{(1-x)}S_2$ crystals presented in the SI were performed on a TRIOS AFM-Raman platform (HORIBA Scientific) coupled to an imaging spectrograph (Andor) and an electron multiplying charged coupled device (EM-CCD). There TERS measurements of the exfoliated samples were performed using 632.8 nm continuous wave excitation and incident laser intensity of 50 μW. For all TERS spectra, a constant background is subtracted to account for the dark counts of the detectors and any broad emission. The dark counts are estimated from a constant baseline intensity at low wavenumber spanning from 100-400 cm^{-1}. This background is relatively constant over the course of the TERS measurements and did not exhibit strong pixel-to-pixel or row-to-row variations.

Transfer of 2D crystallites onto gold thin films

To perform gap mode TERS measurements, the crystals needed to be on a gold substrate. A thin gold film (~70 nm) was deposited onto the sample under high vacuum (1.0×10^{-7} Torr) using a thermo evaporator (model DV502-A, Denton Vacuum Inc., Moorestown, NJ). Then, a Si wafer was attached to the outer gold surface using an epoxy resin. Once the epoxy cured, the gold film and sapphire substrate were separated by peeling, transferring the 2D lateral heterostructures to the gold surface. Figure S3.2 in the SI provides evidence of the transfer of the 2D crystallites from sapphire to the gold surface upon peeling.

Associated content

Supporting information available

Additional data and discussions that describe the results of the gold transfer process, the peak filtering analysis, the control spectroscopy measurements, a comparison of prior characterization results, and the experimental techniques are presented in the Supporting Information, which is available online.

Relevant financial interest

HORIBA Scientific is the manufacturer of AFM and Raman equipment used in this study. Collaborative research with industry and academia is a part of the job responsibilities of A. K.

Pre-print version

A preprint of this work is available: Garg, S.; Fix, J. P.; Krayev, A. V.; Flanery, C.; Colgrove, M.; Sulkanen, A. R.; Wang, M.; Liu, G.; Borys, N. J.; Kung, P.; Nanoscale Raman Characterization of a 2D Semiconductor Lateral Heterostructure Interface. 2021, arXiv:2111.00135. arXiv. https://arxiv.org/abs/2111.00135 (accessed December 9, 2021).

Acknowledgments

N.J.B. acknowledges support from the Murdock Charitable Trust through award SR-201811596 and the NSF Q-AMASE-i program (Award# 1906383). This work was performed in part at the Montana Nanotechnology Facility, a member of the National Nanotechnology Coordinated Infrastructure (NNCI), which is supported by the National Science Foundation (Grant# ECCS-2025391). Support from the University of Alabama ORED SGP is also acknowledged.

Supporting information: Nanoscale Raman characterization of a 2D semiconductor lateral heterostructure interface

Optical images of jagged exterior edges of the WS_2 shell of the heterostructure crystallites on gold

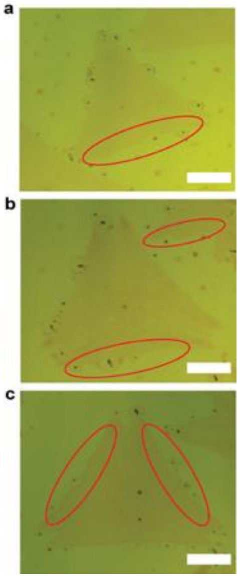

Figure S3.1 – (a,b,c) Optical images of heterostructure crystallites on a gold film with jagged exterior edges in the 1L-WS_2 shell. Scale bars in (a), (b) and (c): 10 µm. Red ovals highlight jagged regions.

Transfer of 2D nanostructures onto Au thin films

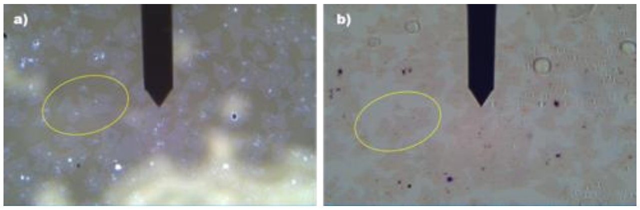

Figure S3.2 - (a) Optical microscopy image of the MoS_2/WS_2 crystals on sapphire surface. The top feature in (a) and (b) is a AFM prob. (b) The same area after peeling indicate the location where the 2D nanocrystals were peeled off from the sapphire surface. (a) and (b) have the same scale bar. Scale bar in (a): 100 μm.

The sample before and after peeling were imaged using optical microscopy, as shown in Figure S3.2a and Figure S3.2b respectively. A cluster of 2D heterostructures shown in Figure S3.2a (yellow enclosure) appear as bright contrast in optical microscope. The same area was imaged again after peeling. The location where the old cluster region appears darker indicating the successful transfer from the sapphire surface onto the Au thin film.

Transition widths from prior CPD imaging results

Table S3.1– Summary of transition widths reported in prior CPD imaging measurements.

Reference in the main text	**Figure in reference**	**Heterostructure**	**Width (nm)**
10	4d	$WS_2/WS_{1.44}Se_{0.56}$	1400
	4g	$WS_2/WS_{1.04}Se_{0.96}$	780
	4i	WS_2/WSe_2	3160
22	4e	WSe_2/MoS_2 (dark)	550
	4e	WSe_2/MoS_2 (illuminated)	660
23	3e	WS_2/MoS_2	1700
24	4b	WS_2/MoS_2	2760

Table S3.1 summarizes the measured widths of transition regions in 2D lateral heterostructures using CPD imaging that have been reported in the prior studies cited in the main text. The widths were extracted by digitizing the published CPD line traces.

Peak filtering analysis

To make the TERS intensity maps in Figures 3.4 and 3.6 in the main manuscript, a peak filtering analysis was used to isolate peaks within the spectral window from background tails from other neighboring peaks. The function fits a linear line to four points that include the two data points with the highest and lowest wavenumbers on the high and low-energy sides of the selected spectral range, respectively (see green line in Figure S3.3d, e). The four data points are defined by the spectral range analyzed, and the same data points are consistently used to analyze the TERS spectrum and calculate the peak intensity of each pixel. They are not adjusted on a per-pixel basis. The linear fit is then subtracted from the raw data leaving an isolated peak when a peak is clearly in the band. In Figure S3.3a we have shown the wavenumber range used to map the transition area. The intensity map shown in Figure S3.3b demonstrates an integrated intensity map over the defined wavenumber range in Figure S3.3a but without the peak filtering. The transition area in Figure S3.3b is difficult to see due to interference from overlapping modes in the MoS_2 and WS_2 in this range. In contrast, Figure S3c shows the intensity map after the peak filtering. In Figures S3.3c, the intensity from the transition region is isolated with minimal interference from the MoS_2 and WS_2. In Figures S3.3d and S3.3e, we plot the raw averaged spectra in the defined wavenumber range from the transition and WS_2 areas respectively before and after the peak filter was applied. These spectra show that we can effectively isolate the ~440 cm^{-1} peak in the transition area so interference from overlapping peaks, like the ~433 cm^{-1} peak in Figure S3.3e, is minimized.

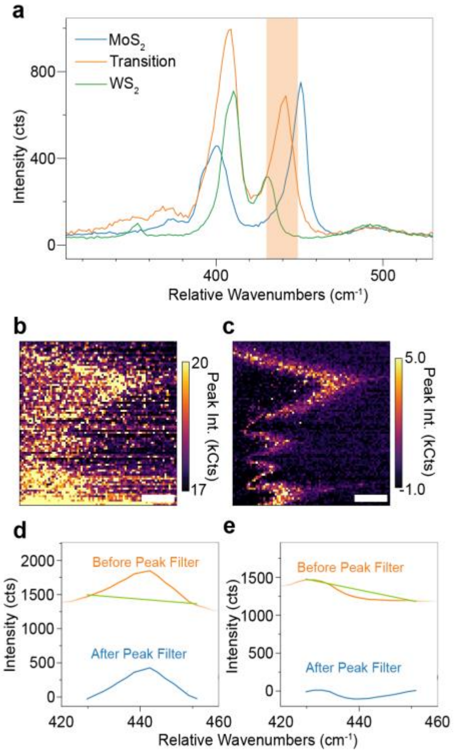

Figure S3.3 – Explanation of the peak filtering analysis. (a) TERS spectra acquired under non-resonant excitation with the orange band marking the wavenumber range of interest (430-450 cm^{-1}). (b) Integrated intensity map of the wavenumber range defined in panel (a) without the peak filtering analysis. (c) Peak intensity map of the wavenumber range defined in panel (a). Scale bars in (b) and (c): 400 nm. (d) The average TERS spectrum of the transition region before (orange) and after (blue) the peak filtering analysis over the wavenumber range 430-450 cm^{-1}. The curves are offset for clarity. (e) The average spectrum for the 1L-WS$_2$ shell before (orange) and after (blue) the peak filtering analysis over the wavenumber range 430-450 cm^{-1}. The curves are offset vertically for clarity. In panels (d) and (e), the green lines indicate the linear fits that was were subtracted in the peak filtering analysis.

Alloy composition gradient analysis

To prove that the spectral position of the 442 cm^{-1} peaks in the TERS spectra does depend on the alloying ratio in the $Mo_xW_{1-x}S_2$ compound, we performed a systematic study on the correlation between the position of this peak in TERS spectra of gold-transferred crystals with the position of the PL peak in the same crystals on the growth sapphire substrate. The correlation results were obtained on a gradient composition sample where the PL peak position in $Mo_xW_{1-x}S_2$

crystals varied from 635.5 nm to 658 nm depending on the location of the crystal on the substrate. The spectral position of the composition-sensitive peak in TERS spectra of the same crystals after the gold-assisted transfer consistently changes from 437 cm^{-1} to 444 cm^{-1} (see Figure S3.4 and Table S3.1).

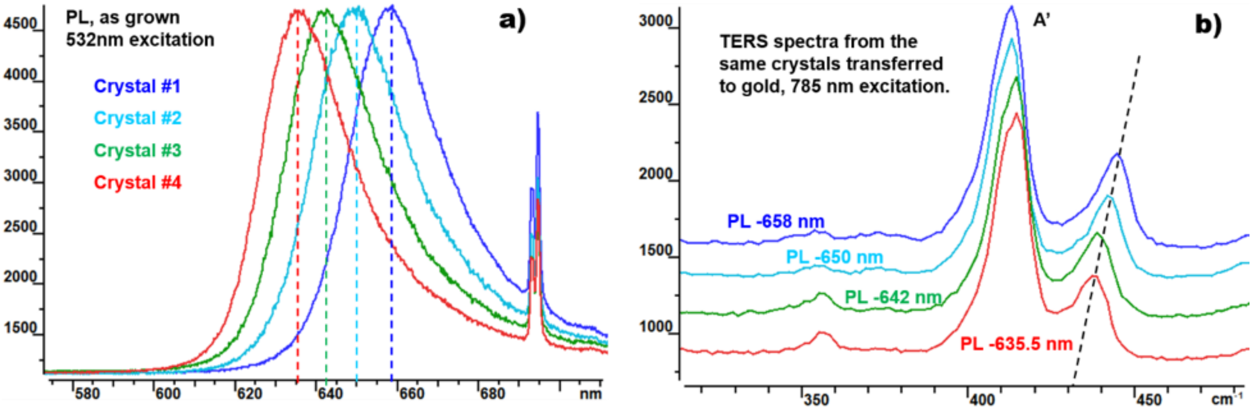

Figure S3.4 – (a) Confocal PL spectra from four different $Mo_xW_{(1-x)}S_2$ crystals with varying compositions. The PL spectra that were acquired with 532 nm laser excitation are normalized to the same intensity. (b) Corresponding TERS spectra from the same crystals after the gold-assisted transfer. Spectra are normalized by the intensity of the A' peak and offset vertically for clarity.

Thus, we can claim with certainty that the position of the TERS peak in the 430-450 cm^{-1} range depends on the alloying ratio in $Mo_xW_{1-x}S_2$ compounds, though the exact correspondence between the PL peak maximum and the TERS peak position may be different for different samples. For example, varying concentrations of sulfur deficiencies, doping, and/or contributions of charged exciton emissions in different samples may cause such a discrepancy, including inducing changes in the position of the combined PL peak. The composition of each flake (Table S3.1) is estimated from the PL spectrum using Vegard's Law as discussed in the manuscript.

Table S3.2 – Summary of the relation between the position of the PL peak in the as-grown crystals with the position of the composition-sensitive TERS peak after the gold-assisted transfer.

	Crystal #1	**Crystal #2**	**Crystal #3**	**Crystal #4**
PL	658 nm	650 nm	642 nm	635.5 nm
TERS	443.9 cm^{-1}	441.6 cm^{-1}	438 cm^{-1}	437 cm^{-1}
Composition	$Mo_{0.29}W_{0.71}S_2$	$Mo_{0.19}W_{0.81}S_2$	$Mo_{0.11}W_{0.89}S_2$	$Mo_{0.05}W_{0.95}S_2$

Resonant TERS of single-layer alloys exfoliated from bulk crystals

To find the alloy composition in 1L-$Mo_xW_{1-x}S_2$ at which the 140-240 cm^{-1} Raman modes have the highest intensity we performed resonant TERS measurements of four alloy compositions of 1L-$Mo_xW_{1-x}S_2$, 1L-MoS_2, and 1L-WS_2 that were mechanically exfoliated from bulk crystals, which ideally have lower amounts of defects. Figure S3.5 shows the progression of the TERS spectra of these samples from pure WS_2 to pure MoS_2. The spectra in Figure S3.5 are averages from a scan area of ~500×500 nm^2. A broad PL background was removed from each spectrum using a polynomial fit. We observe the highest intensity in the 140-240 cm^{-1} modes in the $Mo_{0.15}W_{0.85}S_2$ and $Mo_{0.30}W_{0.70}S_2$ alloys. As the tungsten concentration decreases in the alloys, the 140-240 cm^{-1} modes decrease in intensity until we reach pure MoS_2 where the modes are weak indicating a possible alloying effect in the material. We note that the high energy mode associated with S vacancies as discussed in the manuscript for 1L-WS_2 are not present in the TERS spectra of the exfoliated 1L-WS_2 measured here.

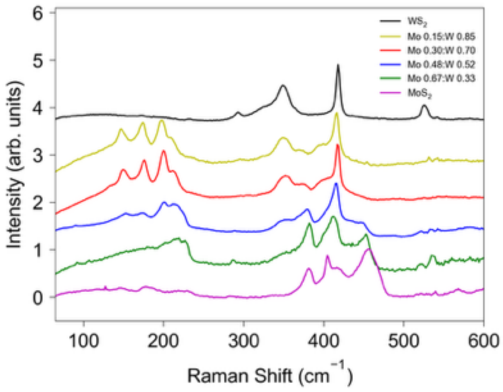

Figure S3.5 – Evolution of the TERS spectra of exfoliated and gold-transferred monolayers of different composition. Appearance of characteristic Raman peaks within 140-240 cm^{-1} range material composition evolves from pure WS$_2$ to alloyed Mo$_x$W$_{(1-x)}$S$_2$ compound is clearly seen. The intensity of these Raman bands is maximized at the W/Mo ratio of about 2.32 and then decreases coming to practically zero in pure MoS$_2$.

Topography of region studied by TERS

Figure S3.6 below presents the detailed characterization of the topography and CPD of the region analyzed in the TERS imaging presented in Figures 3.4 and 3.5 in the main manuscript.

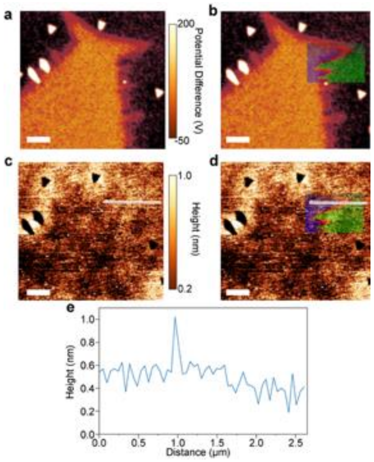

Figure S3.6 – (a) CPD image of the region characterized with TERS. (b) CPD image with TERS image superimposed. (c) AFM image of the region characterized with TERS. (d)AFM image with TERS image superimposed. (e) Topographic profile of the 2D heterostructure along the white line in (c and d). Scale bar: 1 µm. Superimposed TERS map is of the region measured for Figures 3.4 and 3.6.

Extended line traces beyond the interfacial region for the resonant and non-resonant TERS measurements

To demonstrate that the TERS spectrum does not evolve beyond the transition region, we have extended the line traces over the largest extent of the data from Figures 3.5 and 3.7. The extended line traces are shown below in Figure S3.7.

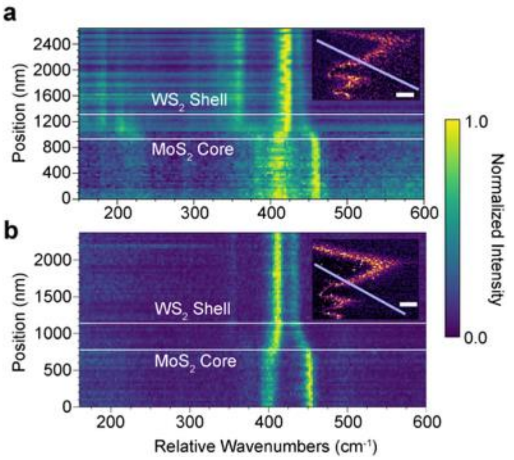

Figure S3.7 – characterization of the transition regions of the interface in a 2D lateral heterostructure using resonant and non-resonant TERS. (a) The evolution of the resonant TERS spectrum across the extent of the data (path shown in the inset). Inset: spatial map of the TERS peak intensity in the spectral region of 430-450 cm^{-1} (duplicated from Figure 3.6d). Scale bar: 400 nm. The light-blue lines mark the path from which the spectra are interpolated. (b) The evolution of the non-resonant TERS spectrum across the extent of the data (path shown in the inset). For both (a) and (b), the TERS spectra are interpolated from a 48×24 nm^2 region at each position along the respective paths. The beginning and end of the transition regions are estimated as the points where the Raman spectra, specifically the mode at ~450 cm^{-1} in the MoS$_2$ and ~410 cm^{-1} in the WS$_2$, ceases to systematically change with position along the paths. A constant background corresponding to the dark counts of the detectors was removed from each spectrum.

References

(1) Lau, K. W.; Calvin; Gong, Z. R.; Yu, H. Y.; Yao, W. Interface Excitons at Lateral Heterojunctions in Monolayer Semiconductors. *Physical Review B* **2018**, *98* (11), 115427. DOI: 10.1103/PhysRevB.98.115427.

(2) Mueller, T.; Malic, E. Exciton physics and device application of two-dimensional transition metal dichalcogenide semiconductors. *npj 2D Materials and Applications* **2018**, *2* (1). DOI: 10.1038/s41699-018-0074-2.

(3) Mak, K. F.; Shan, J. Photonics and Optoelectronics of 2D Semiconductor Transition Metal Dichalcogenides. *Nature Photonics* **2016**, *10* (4), 216-226. DOI: 10.1038/nphoton.2015.282.

(4) Schneider, C.; Glazov, M. M.; Korn, T.; Hofling, S.; Urbaszek, B. Two-dimensional semiconductors in the regime of strong light-matter coupling. *Nat Commun* **2018**, *9* (1), 2695. DOI: 10.1038/s41467-018-04866-6.

(5) Cheng, J.; Wang, C.; Zou, X.; Liao, L. Recent Advances in Optoelectronic Devices Based on 2D Materials and Their Heterostructures. *Advanced Optical Materials* **2019**, *7* (1). DOI: 10.1002/adom.201800441.

(6) Huang, C.; Wu, S.; Sanchez, A. M.; Peters, J. J.; Beanland, R.; Ross, J. S.; Rivera, P.; Yao, W.; Cobden, D. H.; Xu, X. Lateral Heterojunctions within Monolayer $MoSe_2$-WSe_2 Semiconductors. *Nat Mater* **2014**, *13* (12), 1096-1101. DOI: 10.1038/nmat4064.

(7) Zhang, X. Q.; Lin, C. H.; Tseng, Y. W.; Huang, K. H.; Lee, Y. H. Synthesis of Lateral Heterostructures of Semiconducting Atomic Layers. *Nano Lett* **2015**, *15* (1), 410-415. DOI: 10.1021/nl503744f.

(8) Pant, A.; Mutlu, Z.; Wickramaratne, D.; Cai, H.; Lake, R. K.; Ozkan, C.; Tongay, S. Fundamentals of Lateral and Vertical Heterojunctions of Atomically Thin Materials. *Nanoscale* **2016**, *8* (7), 3870-3887. DOI: 10.1039/c5nr08982d.

(9) Meng, L.; Zhang, Y.; Hu, S.; Wang, X.; Liu, C.; Guo, Y.; Wang, X.; Yan, X. Two Dimensional WS_2 Lateral Heterojunctions by Strain Modulation. *Applied Physics Letters* **2016**, *108* (26). DOI: 10.1063/1.4954991.

(10) Li, M. Y.; Shi, Y.; Cheng, C. C.; Lu, L. S.; Lin, Y. C.; Tang, H. L.; Tsai, M. L.; Chu, C. W.; Wei, K. H.; He, J. H.; et al. Epitaxial Growth of a Monolayer WSe_2-MoS_2 Lateral *P-N* Junction with an Atomically Sharp Interface. *Science* **2015**, *349* (6247), 524-528. DOI: 10.1126/science.aab4097.

(11) Zheng, B.; Ma, C.; Li, D.; Lan, J.; Zhang, Z.; Sun, X.; Zheng, W.; Yang, T.; Zhu, C.; Ouyang, G.; et al. Band Alignment Engineering in Two-Dimensional Lateral Heterostructures. *J Am Chem Soc* **2018**, *140* (36), 11193-11197. DOI: 10.1021/jacs.8b07401.

(12) Li, M. Y.; Pu, J.; Huang, J. K.; Miyauchi, Y.; Matsuda, K.; Takenobu, T.; Li, L. J. Self-Aligned and Scalable Growth of Monolayer WSe_2-MoS_2 Lateral Heterojunctions. *Adv Funct Mater* **2018**, *28* (17), 1706860. DOI: 10.1002/adfm.201706860.

(13) Yasaei, P.; Murthy, A. A.; Xu, Y.; Dos Reis, R.; Shekhawat, G. S.; Dravid, V. P. Spatial Mapping of Hot-Spots at Lateral Heterogeneities in Monolayer Transition Metal Dichalcogenides. *Adv Mater* **2019**, *31* (24), e1808244. DOI: 10.1002/adma.201808244.

(14) Wu, W.; Zhang, Q.; Zhou, X.; Li, L.; Su, J.; Wang, F.; Zhai, T. Self-Powered Photovoltaic Photodetector Established on Lateral Monolayer MoS_2-WS_2 Heterostructures. *Nano Energy* **2018**, *51*, 45-53. DOI: 10.1016/j.nanoen.2018.06.049.

(15) Zhang, J.; Xie, W.; Zhao, J.; Zhang, S. Band Alignment of Two-Dimensional Lateral Heterostructures. *2D Materials* **2016**, *4* (1). DOI: 10.1088/2053-1583/aa50cc.

(16) Ang, Y. S.; Yang, H. Y.; Ang, L. K. Universal Scaling Laws in Schottky Heterostructures Based on Two-Dimensional Materials. *Phys Rev Lett* **2018**, *121* (5), 056802. DOI: 10.1103/PhysRevLett.121.056802.

(17) Chen, D. R.; Hofmann, M.; Yao, H. M.; Chiu, S. K.; Chen, S. H.; Luo, Y. R.; Hsu, C. C.; Hsieh, Y. P. Lateral Two-Dimensional Material Heterojunction Photodetectors with Ultrahigh Speed and Detectivity. *ACS Appl Mater Interfaces* **2019**, *11* (6), 6384-6388. DOI: 10.1021/acsami.8b19093.

(18) Tang, C. W.; He, Z.; Chen, W. B.; Jia, S.; Lou, J.; Voronine, D. V. Quantum Plasmonic Hot-Electron Injection in Lateral WSe_2/$MoSe_2$ Heterostructures. *Physical Review B* **2018**, *98* (4), 041402. DOI: 10.1103/PhysRevB.98.041402.

(19) Zhang, Q.; Zhen, Z.; Yang, Y.; Gan, G.; Jariwala, D.; Cui, X. Negative Refraction Inspired Polariton Lens in Van Der Waals Lateral Heterojunctions. *Applied Physics Letters* **2019**, *114* (22). DOI: 10.1063/1.5098346.

(20) Han, Y.; Li, M. Y.; Jung, G. S.; Marsalis, M. A.; Qin, Z.; Buehler, M. J.; Li, L. J.; Muller, D. A. Sub-Nanometre Channels Embedded in Two-Dimensional Materials. *Nat Mater* **2018**, *17* (2), 129-133. DOI: 10.1038/nmat5038.

(21) Zhang, Z.; Chen, P.; Duan, X.; Zang, K.; Luo, J.; Duan, X. Robust Epitaxial Growth of Two-Dimensional Heterostructures, Multiheterostructures, and Superlattices. *Science* **2017**, *357* (6353), 788-792. DOI: 10.1126/science.aan6814.

(22) Shearer, M. J.; Li, M.-Y.; Li, L.-J.; Jin, S.; Hamers, R. J. Nanoscale Surface Photovoltage Mapping of 2D Materials and Heterostructures by Illuminated Kelvin Probe Force Microscopy. *The Journal of Physical Chemistry C* **2018**, *122* (25), 13564-13571. DOI: 10.1021/acs.jpcc.7b12579.

(23) Chen, K.; Wan, X.; Xie, W.; Wen, J.; Kang, Z.; Zeng, X.; Chen, H.; Xu, J. Lateral Built-In Potential of Monolayer MoS_2-WS_2 In-Plane Heterostructures by a Shortcut Growth Strategy. *Adv Mater* **2015**, *27* (41), 6431-6437. DOI: 10.1002/adma.201502375.

(24) Chen, K.; Wan, X.; Wen, J. X.; Xie, W. G.; Kang, Z. W.; Zeng, X. L.; Chen, H. J.; Xu, J. B. Electronic Properties of MoS_2-WS_2 Heterostructures Synthesized with Two-Step Lateral Epitaxial Strategy. *Acs Nano* **2015**, *9* (10), 9868-9876. DOI: 10.1021/acsnano.5b03188.

(25) Chu, Z.; Han, A.; Lei, C.; Lopatin, S.; Li, P.; Wannlund, D.; Wu, D.; Herrera, K.; Zhang, X.; MacDonald, A. H.; et al. Energy-Resolved Photoconductivity Mapping in a Monolayer-Bilayer WSe_2 Lateral Heterostructure. *Nano Lett* **2018**, *18* (11), 7200-7206. DOI: 10.1021/acs.nanolett.8b03318.

(26) Berweger, S.; Zhang, H.; Sahoo, P. K.; Kupp, B. M.; Blackburn, J. L.; Miller, E. M.; Wallis, T. M.; Voronine, D. V.; Kabos, P.; Nanayakkara, S. U. Spatially Resolved Persistent Photoconductivity in MoS_2-WS_2 Lateral Heterostructures. *ACS Nano* **2020**, *14* (10), 14080-14090. DOI: 10.1021/acsnano.0c06745.

(27) Kim, Y.; Yun, S. J.; Lee, E.; Kim, J. Near-Field Visualization of Charge Transfer at $MoSe_2$/WSe_2 Lateral Heterojunction. *Optical Materials Express* **2019**, *9* (4). DOI: 10.1364/ome.9.001864.

(28) Sahoo, P. K.; Zong, H.; Liu, J.; Xue, W.; Lai, X.; Gutiérrez, H. R.; Voronine, D. V. Probing Nano-Heterogeneity and Aging Effects in Lateral 2D Heterostructures using Tip-Enhanced Photoluminescence. *Optical Materials Express* **2019**, *9* (4). DOI: 10.1364/ome.9.001620.

(29) Xue, W.; Sahoo, P. K.; Liu, J.; Zong, H.; Lai, X.; Ambardar, S.; Voronine, D. V. Nano-Optical Imaging of Monolayer $MoSe_2$-WSe_2 Lateral Heterostructure with Subwavelength Domains. *Journal of Vacuum Science & Technology A* **2018**, *36* (5). DOI: 10.1116/1.5035437.

(30) Cao, Y.; Luo, X.; Han, S.; Yuan, C.; Yang, Y.; Li, Q.; Yu, T.; Ye, S. Influences of Carrier Gas Flow Rate on the Morphologies of MoS_2 Flakes. *Chemical Physics Letters* **2015**, *631-632*, 30-33. DOI: 10.1016/j.cplett.2015.05.001.

(31) Chen, Y.; Xi, J.; Dumcenco, D. O.; Liu, Z.; Suenaga, K.; Wang, D.; Shuai, Z.; Huang, Y. S.; Xie, L. Tunable Band Gap Photoluminescence from Atomically Thin Transition-Metal Dichalcogenide Alloys. *ACS Nano* **2013**, *7* (5), 4610-4616. DOI: 10.1021/nn401420h.

(32) Wang, Z.; Liu, P.; Ito, Y.; Ning, S.; Tan, Y.; Fujita, T.; Hirata, A.; Chen, M. Chemical Vapor Deposition of Monolayer $Mo_{(1-x)}W_{(x)}S_2$ Crystals with Tunable Band Gaps. *Sci Rep* **2016**, *6*, 21536. DOI: 10.1038/srep21536.

(33) Park, J.; Kim, M. S.; Park, B.; Oh, S. H.; Roy, S.; Kim, J.; Choi, W. Composition-Tunable Synthesis of Large-Scale $Mo_{1-x}W_xS_2$ Alloys with Enhanced Photoluminescence. *ACS Nano* **2018**, *12* (6), 6301-6309. DOI: 10.1021/acsnano.8b03408.

(34) Bao, W.; Borys, N. J.; Ko, C.; Suh, J.; Fan, W.; Thron, A.; Zhang, Y.; Buyanin, A.; Zhang, J.; Cabrini, S.; et al. Visualizing nanoscale excitonic relaxation properties of disordered edges and grain boundaries in monolayer molybdenum disulfide. *Nat Commun* **2015**, *6*, 7993. DOI: 10.1038/ncomms8993.

(35) Darlington, T. P.; Carmesin, C.; Florian, M.; Yanev, E.; Ajayi, O.; Ardelean, J.; Rhodes, D. A.; Ghiotto, A.; Krayev, A.; Watanabe, K.; et al. Imaging Strain-Localized Excitons in Nanoscale Bubbles of Monolayer WSe_2 at Room Temperature. *Nat Nanotechnol* **2020**, *15* (10), 854-860. DOI: 10.1038/s41565-020-0730-5.

(36) Kastl, C.; Chen, C. T.; Kuykendall, T.; Shevitski, B.; Darlington, T. P.; Borys, N. J.; Krayev, A.; Schuck, P. J.; Aloni, S.; Schwartzberg, A. M. The Important Role of Water in Growth of Monolayer Transition Metal Dichalcogenides. *2D Materials* **2017**, *4* (2), 021024. DOI: 10.1088/2053-1583/aa5f4d.

(37) Park, K.-d.; Jiang, T.; Clark, G.; Xu, X.; Raschke, M. B. Radiative Control of Dark Excitons at Room Temperature by Nano-Optical Antenna-Tip Purcell Effect. *Nature Nanotechnology* **2018**, *13* (1), 59-64. DOI: 10.1038/s41565-017-0003-0.

(38) Park, K. D.; Khatib, O.; Kravtsov, V.; Clark, G.; Xu, X.; Raschke, M. B. Hybrid Tip-Enhanced Nanospectroscopy and Nanoimaging of Monolayer WSe_2 with Local Strain Control. *Nano Lett* **2016**, *16* (4), 2621-2627. DOI: 10.1021/acs.nanolett.6b00238.

(39) Cui, Q.; Ceballos, F.; Kumar, N.; Zhao, H. Transient Absorption Microscopy of Monolayer and Bulk WSe_2. *ACS Nano* **2014**, *8* (3), 2970-2976. DOI: 10.1021/nn500277y.

(40) Umakoshi, T.; Tanaka, M.; Saito, Y.; Verma, P. White Nanolight Source for Optical Nanoimaging. *Sci Adv* **2020**, *6* (23), eaba4179. DOI: 10.1126/sciadv.aba4179.

(41) Gadelha, A. C.; Ohlberg, D. A. A.; Rabelo, C.; Neto, E. G. S.; Vasconcelos, T. L.; Campos, J. L.; Lemos, J. S.; Ornelas, V.; Miranda, D.; Nadas, R.; et al. Localization of Lattice Dynamics in Low-Angle Twisted Bilayer Graphene. *Nature* **2021**, *590* (7846), 405-409. DOI: 10.1038/s41586-021-03252-5.

(42) Huang, T.-X.; Cong, X.; Wu, S.-S.; Lin, K.-Q.; Yao, X.; He, Y.-H.; Wu, J.-B.; Bao, Y.-F.; Huang, S.-C.; Wang, X.; et al. Probing the Edge-Related Properties of Atomically Thin MoS_2 at Nanoscale. *Nature Communications* **2019**, *10* (1). DOI: 10.1038/s41467-019-13486-7.

(43) Atkin, J. M.; Berweger, S.; Jones, A. C.; Raschke, M. B. Nano-Optical Imaging and Spectroscopy of Order, Phases, and Domains in Complex Solids. *Advances in Physics* **2012**, *61* (6), 745-842. DOI: 10.1080/00018732.2012.737982.

(44) Crampton, K. T.; Lee, J.; Apkarian, V. A. Ion-Selective, Atom-Resolved Imaging of a 2D Cu_2N Insulator: Field and Current Driven Tip-Enhanced Raman Spectromicroscopy Using a Molecule-Terminated Tip. *Acs Nano* **2019**, *13* (6), 6363-6371. DOI: 10.1021/acsnano.9b02744.

(45) Jaculbia, R. B.; Imada, H.; Miwa, K.; Iwasa, T.; Takenaka, M.; Yang, B.; Kazuma, E.; Hayazawa, N.; Taketsugu, T.; Kim, Y. Single-molecule resonance Raman effect in a plasmonic nanocavity. *Nat Nanotechnol* **2020**, *15* (2), 105-110. DOI: 10.1038/s41565-019-0614-8.

(46) Jiang, S.; Zhang, Y.; Zhang, R.; Hu, C. R.; Liao, M. H.; Luo, Y.; Yang, J. L.; Dong, Z. C.; Hou, J. G. Distinguishing Adjacent Molecules on a Surface using Plasmon-Enhanced Raman Scattering. *Nature Nanotechnology* **2015**, *10* (10), 865-869. DOI: 10.1038/nnano.2015.170.

(47) Zhang, R.; Zhang, Y.; Dong, Z. C.; Jiang, S.; Zhang, C.; Chen, L. G.; Zhang, L.; Liao, Y.; Aizpurua, J.; Luo, Y.; et al. Chemical Mapping of a Single Molecule by Plasmon-Enhanced Raman Scattering. *Nature* **2013**, *498* (7452), 82-86. DOI: 10.1038/nature12151.

(48) Su, W.; Kumar, N.; Krayev, A.; Chaigneau, M. *In Situ* Topographical Chemical and Electrical Imaging of Carboxyl Graphene Oxide at the Nanoscale. *Nat Commun* **2018**, *9* (1), 2891. DOI: 10.1038/s41467-018-05307-0.

(49) Krayev, A.; Bailey, C. S.; Jo, K.; Wang, S.; Singh, A.; Darlington, T.; Liu, G. Y.; Gradecak, S.; Schuck, P. J.; Pop, E.; et al. Dry Transfer of Van Der Waals Crystals to Noble Metal Surfaces To Enable Characterization of Buried Interfaces. *Acs Applied Materials & Interfaces* **2019**, *11* (41), 38218-38225. DOI: 10.1021/acsami.9b09798.

(50) Jo, K.; Kumar, P.; Orr, J.; Anantharaman, S. B.; Miao, J.; Motala, M. J.; Bandyopadhyay, A.; Kisslinger, K.; Muratore, C.; Shenoy, V. B.; et al. Direct Optoelectronic Imaging of 2D Semiconductor-3D Metal Buried Interfaces. *ACS Nano* **2021**, *15* (3), 5618-5630. DOI: 10.1021/acsnano.1c00708.

(51) Reuter, D.; Werner, C.; Wieck, A. D.; Petrosyan, S. Depletion Characteristics of Two-Dimensional Lateral *P-N*-Junctions. *Applied Physics Letters* **2005**, *86* (16). DOI: 10.1063/1.1897829.

(52) Ilatikhameneh, H.; Ameen, T.; Chen, F.; Sahasrabudhe, H.; Klimeck, G.; Rahman, R. Dramatic Impact of Dimensionality on the Electrostatics of *P-N* Junctions and Its Sensing and Switching Applications. *IEEE Transactions on Nanotechnology* **2018**, *17* (2), 293-298. DOI: 10.1109/tnano.2018.2799960.

(53) Gurugubelli, V. K.; Karmalkar, S. Analytical Theory of the Space-Charge Region of Lateral *p-n* Junctions in Nanofilms. *Journal of Applied Physics* **2015**, *118* (3). DOI: 10.1063/1.4926478.

(54) Gołasa, K.; Grzeszczyk, M.; Bożek, R.; Leszczyński, P.; Wysmołek, A.; Potemski, M.; Babiński, A. Resonant Raman Scattering in MoS_2—From Bulk to Monolayer. *Solid State Communications* **2014**, *197*, 53-56. DOI: 10.1016/j.ssc.2014.08.009.

(55) Berkdemir, A.; Gutierrez, H. R.; Botello-Mendez, A. R.; Perea-Lopez, N.; Elias, A. L.; Chia, C. I.; Wang, B.; Crespi, V. H.; Lopez-Urias, F.; Charlier, J. C.; et al. Identification of Individual and Few Layers of WS_2 Using Raman Spectroscopy. *Scientific Reports* **2013**, *3*, 1755. DOI: 10.1038/srep01755.

(56) Molina-Sanchez, A.; Wirtz, L. Phonons in Single-Layer and Few-Layer MoS_2 and WS_2. *Physical Review B* **2011**, *84* (15), 155413. DOI: 10.1103/PhysRevB.84.155413.

(57) Zhang, X.; Qiao, X. F.; Shi, W.; Wu, J. B.; Jiang, D. S.; Tan, P. H. Phonon and Raman Scattering of Two-Dimensional Transition Metal Dichalcogenides from Monolayer, Multilayer to Bulk Material. *Chemical Society Reviews* **2015**, *44* (9), 2757-2785. DOI: 10.1039/c4cs00282b.

(58) Molas, M. R.; Nogajewski, K.; Potemski, M.; Babinski, A. Raman Scattering Excitation Spectroscopy of Monolayer WS_2. *Sci Rep* **2017**, *7* (1), 5036. DOI: 10.1038/s41598-017-05367-0.

(59) Lee, C.; Jeong, B. G.; Yun, S. J.; Lee, Y. H.; Lee, S. M.; Jeong, M. S. Unveiling Defect-Related Raman Mode of Monolayer WS_2 *Via* Tip-Enhanced Resonance Raman Scattering. *ACS Nano* **2018**, *12* (10), 9982-9990. DOI: 10.1021/acsnano.8b04265.

(60) Pimenta, M. A.; Del Corro, E.; Carvalho, B. R.; Fantini, C.; Malard, L. M. Comparative Study of Raman Spectroscopy in Graphene and MoS_2-Type Transition Metal Dichalcogenides. *Acc Chem Res* **2015**, *48* (1), 41-47. DOI: 10.1021/ar500280m.

(61) Velicky, M.; Rodriguez, A.; Bousa, M.; Krayev, A. V.; Vondracek, M.; Honolka, J.; Ahmadi, M.; Donnelly, G. E.; Huang, F.; Abruna, H. D.; et al. Strain and Charge Doping Fingerprints of the Strong Interaction between Monolayer MoS_2 and Gold. *J Phys Chem Lett* **2020**, *11* (15), 6112-6118. DOI: 10.1021/acs.jpclett.0c01287.

(62) Su, W.; Kumar, N.; Mignuzzi, S.; Crain, J.; Roy, D. Nanoscale Mapping of Excitonic Processes in Single-Layer MoS_2 Using Tip-Enhanced Photoluminescence Microscopy. *Nanoscale* **2016**, *8* (20), 10564-10569. DOI: 10.1039/c5nr07378b.

(63) Chen, Y.; Dumcenco, D. O.; Zhu, Y.; Zhang, X.; Mao, N.; Feng, Q.; Zhang, M.; Zhang, J.; Tan, P. H.; Huang, Y. S.; et al. Composition-Dependent Raman Modes of $Mo_{(1-x)}W_{(x)}S_2$ Monolayer Alloys. *Nanoscale* **2014**, *6* (5), 2833-2839. DOI: 10.1039/c3nr05630a.

(64) Jorio, A.; Saito, R.; Dresselhaus, G.; Dresselhaus, M. S. Quantum Description of Raman Scattering. In *Raman Spectroscopy in Graphene Related Systems*, 2011; pp 103-119, DOI: 10.1002/9783527632695.ch5.

CHAPTER 4

DETERMINATION OF THE ROLES OF STRAIN AND TEARING IN SINGLE PHOTON EMISSION FROM NANOINDENTED WSe_2

Contribution of authors and co-authors

Joseph Stage*,J. Pierce Fix*, Matthew Strasbourg, Amir Darabi, Torrey McLoughlin, Sheikh Parvez, Elijah Stuvland, Andrew Lingley, and Nicholas J. Borys

Manuscript in Chapter 4

Author: Joseph Stage

Contributions: conceived this work, conducted 4 K photoluminescence measurements, fabricated samples, developed the inversion process, and wrote the manuscript.

Author: J. Pierce Fix

Contributions: conceived this work, conducted the room-temperature photoluminescence and AFM mapping, optimized the nanoindentation technique, and wrote the manuscript.

Co-Author: Matthew Strasbourg

Contributions: built the optical microscope the 4 K photoluminescence measurements were taken on.

Co-Author: Amir Darabi

Contributions: optimizing the nanoindentation technique.

Co-Author: Torrey McLoughlin

Contributions: conducted nano-Auger spectroscopy measurements on the inverted indents.

Co-Author: Sheikh Parvez

Contributions: fabrication of samples.

Co-Author: Elijah Stuvland

Contributions: helped with the inversion process.

Co-Author: Andrew Lingley

Contributions: provided guidance on optimizing the inversion process.

Co-Author: Nicholas J. Borys

Contributions: conceived this work, wrote the manuscript.

Summary of major contributions made to this work

The overarching goal of the research presented in this chapter was to understand the role of the dark exciton in the theoretical formation mechanism of QEs in W-TMDs, introduced in Section 1.9. The proposed mechanism suggests that, in 1L W-TMDs, under localized tensile strain and in the presence of point defects, hybridization occurs between the lowest-energy excited state (dark excitons) and the defect state. The resulting hybridized state enables radiative recombination of the excited state, leading to the formation of a QE[1]. As discussed in Section 1.7, previous research has primarily focused on the effects of tensile strain and point defects. The role of dark excitons in this mechanism has been largely overlooked.

To address this gap, we aimed to elucidate the role of the dark exciton by controllably inducing tensile strain in 1L-$Mo_xW_{(1-x)}S_2$ and $Mo_xW_{(1-x)}Se_2$ alloys. These 1L-TMD alloys enable tuning of the lowest-energy excited state from dark excitons in W-rich alloys to bright excitons in Mo-rich alloys[2]. We hypothesize that beyond a certain molybdenum to tungsten ratio, QEs will no longer form, corresponding to the point where the dark exciton is no longer the lowest-energy excited state. To test this hypothesis, we required a series of TMD alloys spanning compositions from W-rich to Mo-rich, as well as a reliable method to control the amount of localized tensile strain induced in each alloy.

A series of $Mo_xW_{(1-x)}S_2$ is commercially available, and four compositions were purchased with x = 0.15, 0.30, 0.48, and 0.67. To induce localized tensile strain, nanoindentation using an AFM tip was selected, as it allows strain fields to be confined precisely to the chosen indentation sites[3]. Other methods, such as using nanocones[4], often produce nanoscale wrinkles that result in uncontrolled and irreproducible strain environments.

The initial experiments focused on nanoindenting the most W-rich alloy, $Mo_{0.15}W_{0.85}S_2$, under the assumption that at 85% W content, the dark exciton would remain the lowest-energy excited state. Initial attempts to induce QEs in this alloy produced weak, localized emission, as shown in Figure 4.1. Although the emission was faint, it indicated that nanoindentation was inducing narrow emission. However, brighter and more distinct emitters were needed to confirm the narrow emission as QEs.

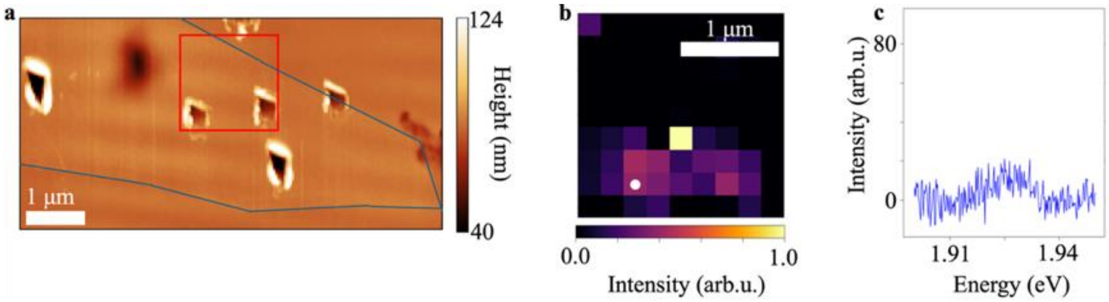

Figure 4.1 – The first indents in 1L- $Mo_{0.15}W_{0.85}S_2$. **(a)** Topography map showing the indents made in the 1L-$Mo_{0.15}W_{0.85}S_2$, outlined by blue lines. The red square indicates the area from which the integrated intensity map in (b) was take from. **(b)** A 4 K PL integrated intensity map, integrated over the energy range 1.91 – 1.94 eV. The white dot marks the location the of the point spectra in (c). **(c)** A point spectra of the emission localized at the nanoindents.

After many additional indents, brighter emitters were eventually observed, as shown in Figure 4.2. However, it remained difficult to clearly associate these emitters with the indentation sites, partly due to strong background emission from defects. Similar to the initial results, the emission was not sufficiently convincing to confirm the formation of QEs. These observations raised two key questions: (i) Was an alloy with a higher tungsten concentration needed? and (ii) Is the nanoindentation process effectively inducing tensile strain in the 1L-$Mo_{0.15}W_{0.85}S_2$?

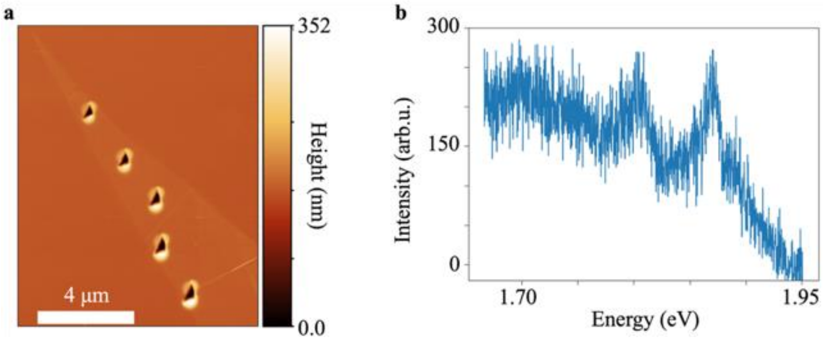

Figure 4.2 – Additional indents made in 1L-$Mo_{0.15}W_{0.85}S_2$ showing little evidence of localized emission. (a) Topography map of the indents in 1L-$Mo_{0.15}W_{0.85}S_2$. (b) A 4 K PL point spectra from the indented 1L-$Mo_{0.15}W_{0.85}S_2$.

To address the second question—whether the indentation process effectively induces strain—we turned to previous literature, which reports that, when comparing room temperature PL spectra collected on and away from indented regions, a redshift of approximately 10 meV is observed[5]. This shift to lower energy is evidence of tensile strain. However, after indenting the 1L-$Mo_{0.15}W_{0.85}S_2$ alloy and calculating the emission energy using the spectral median, no systematic redshift was observed around the indentation sites, as shown in Figure 4.3. The absence of localized tensile strain in the RT PL data suggests that our indentation process did not produce strain in the same manner as previously reported.

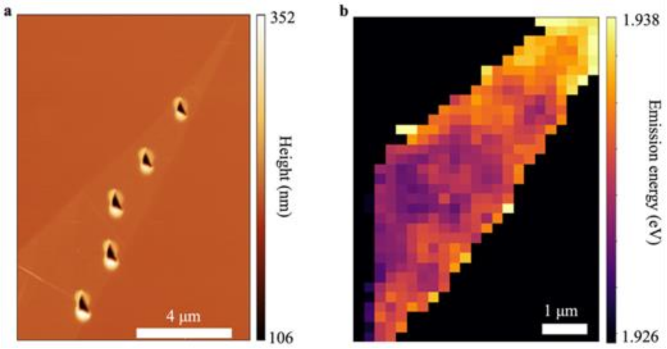

Figure 4.3 – No room temperature evidence of localized tensile strain in indented 1L-$Mo_{0.15}W_{0.85}S_2$. (a) Topography map of the indents made in the 1L- $Mo_{0.15}W_{0.85}S_2$. (b) Emission energy map of the room temperature PL from the indented 1L-$Mo_{0.15}W_{0.85}S_2$.

Because commercially available alloys did not cover the full composition range needed for this study, additional $Mo_xW_{(1-x)}S_2$ and $Mo_xW_{(1-x)}Se_2$ alloys were synthesized. This opportunity arose through collaboration with the 2D Crystal Consortium (2DCC) at The Pennsylvania State University, where we learned to grow bulk alloy crystals. Details of this work are provided in Section 2.2.1. At the 2DCC, eight bulk crystals of each alloy type—$Mo_xW_{(1-x)}S_2$ and $Mo_xW_{(1-x)}Se_2$—were successfully grown. Expanding our study to include the selenide alloys was especially valuable, as much of the research on QEs has focused on WSe_2. The most W-rich $Mo_xW_{(1-x)}S_2$ alloy we obtained was $Mo_{0.02}W_{0.98}S_2$.

To test whether QE states could be observed in 1L-$Mo_{0.02}W_{0.98}S_2$, we turned to a less controlled but effective method of inducing localized tensile strain—nanobubbles. Nanobubbles naturally form in 1L-TMDs during sample fabrication due to environmental contaminants such as polymer residues. With the assistance of my colleague Sheikh Parvez, a heterostructure consisting of 1L-$Mo_{0.02}W_{0.98}S_2$ on hexagonal boron nitride (hBN) was fabricated, supported by a SiO_2/Si substrate. The hBN layer provided an atomically flat surface, ensuring that any induced strain originated primarily from the nanobubbles.

Evidence of localized, narrow emission from the nanobubbles is presented in Section 6.2.1. Also shown in Section 6.2.1 is a redshift in the room temperature PL from regions containing nanobubbles compared to areas away from them, indicating that the nanobubble regions are under tensile strain. The observation of strain-induced redshifts in the room temperature PL data refocused our attention on understanding why nanoindentation failed to induce similar localized tensile strain.

We hypothesized that the AFM tip was tearing the monolayer material during the indentation process. To test this hypothesis, we required at least two samples: one showing no evidence of strain in the room temperature PL data, and another exhibiting a measurable PL redshift indicative of tensile strain. With these samples, we could directly examine the indented regions to determine whether the material had been physically damaged. In close collaboration with my colleague Joe Stage, we initiated experiments to test this hypothesis.

In this work, Joe Stage and I contributed equally. Due to the limited availability of alloy material, we transitioned to WSe_2, a well-studied system known to host QEs, as discussed in Section 1.7. Joe was responsible for sample fabrication, including the dry-transfer and material inversion processes, as well as the cryogenic (4 K) PL measurements. I performed the room temperature characterization, which included AFM topography mapping, room temperature PL measurements, and AFM-based nanoindentation of the 1L-WSe_2 samples with an AFM tip. From this study, we developed a characterization method to determine whether indented material has been torn using room temperature PL. Additionally, we were the first group to report the inversion of nanoindents in 1L-WSe_2.

Manuscript information

Joseph Stage[*],J. Pierce Fix[*], Matthew Strasbourg, Amir Darabi, Torrey McLoughlin, Sheikh Parvez, Elijah Stuvland, Andrew Lingley, and Nicholas J. Borys

Status of Manuscript:

☒Prepared for submission to a peer-reviewed journal

☐Officially submitted to a peer-reviewed journal

☐Accepted by a peer-reviewed journal

☐ Published in a peer-reviewed journal

Abstract

Single photon emission in two-dimensional single-layer WSe_2 is an attractive solid-state phenomenon for the on-demand generation of quantum states of light. The electronic states that are responsible for single photon generation preferentially form in regions of localized tensile strain, making them uniquely able to be deterministically positioned and strain-engineered. Nanoindentation of the single-layer WSe_2 and other 2D semiconductors on a pliable substrate is a promising approach to take advantage of these opportunities. However, it is hindered by key questions on the structural integrity of the indented 2D material, the resulting strain generated, and the location of the emitters. In this work, we report a detailed study of the structure of indented 1L-WSe_2 that is enabled by a new fabrication process that inverts the indents into protruding pillars that can be probed using electron microscopy. We explicitly identify strain relaxation of the indented 1L-WSe_2 due to tearing in a subset of indents and confirm that the formation of single photon emitting states still occurs in these systems, likely at the extremities of the tear. For indents that are confirmed to be intact (i.e., not torn), we assess the ability to strain engineer the single photon emitters. While strain does not strongly affect the emission energy or the brightness, we find that increased strain in the indent reduces the spatial density of emitter states. This trend indicates that an optimal amount of strain is needed for emitter formation and/or the emitters preferentially form on the periphery of the indent. Our investigation provides critical insight into the most relevant structure-property relationships for using nanoindentation to reliably and systematically engineer quantum light sources in single-layer WSe_2 and other 2D semiconductors.

Introduction

From new developments to improvements in performance, many aspects of quantum technologies stand to benefit from a system that produces tailorable quantum states of light on demand. Solid-state single photon emitters (SPEs) based on strongly localized electronic states in semiconducting and insulating materials may be able to fulfill this need, having physical properties that yield many potential technological advantages and opportunities[6-10]. One of the most appealing opportunities is their ultimate integration into an electrically triggerable device with a micron or sub-micron footprint that is suitable for photonic integrated circuits. In addition to emitting single photons with sufficiently high purity and indistinguishability, solid-state SPE systems that are ideal for such device integration also need to be amenable to advanced manufacturing and nanofabrication, including having the versatility to be deterministically positioned and heterogeneously integrated with photonic and nanophotonic systems such as waveguides and cavities.

Several aspects of the localized states responsible for single photon emission in single-layer WSe_2 (1L-WSe_2)—a prototypical 2D semiconductor—make them appealing solid-state SPEs. Since the initial reports of SPEs in 1L-WSe_2[11-18], prototype electrically triggerable devices have been demonstrated[5, 18-21], strain-engineering has been explored[4, 15, 22-24], and non-classical emission has been reported at temperatures up to 160 K[25, 26]. Additionally, it is well established that the SPE-active state preferentially forms in regions of localized tensile strain[9, 15, 22, 27, 28], a property that can be leveraged to achieve deterministic placement of the SPE state on a submicron level[3, 5, 29-36]. Nanoindentation, where a nanoscale atomic force microscopy (AFM) probe is used to plastically indent 1L-WSe_2 on top of a deformable polymer, is an elegant method to deterministically position regions of localized tensile strain as well as deliberately tailor the amount of strain with the indentation force. Since the first report of utilizing nanoindentation to generate SPE states[3], it has been leveraged to demonstrate how graphite can improve photon purity[31], as well as deterministically place an SPE state in an electrically triggered device[5] and near a plasmonic structure[37]. Despite these initial successes, several questions about the nanoindentation procedure and the extent to which SPEs can be strain-engineered with the technique persist. The roles, whether deleterious or advantageous, of micro- and nanoscale tearing are unknown. The properties of the SPEs appear to be only weakly dependent on the amount of strain in the indent and it remains unclear where within the indented structure the SPE states exist[29]. These unresolved issues are critical impediments to truly achieving reproducible production of SPE states in 2D semiconductors using nanoindentation.

Here, we report a detailed study of the structure of the indented 1L-WSe_2 that resolves the presence of tearing. Using photoluminescence spectroscopy and imaging, we confirm that the tearing results in a significant amount of strain relaxation across the entire indent structure. Remarkably, despite the strain relaxation, we confirm that SPEs form in the indents where tearing occurs, which strongly suggests that in these cases, the SPE states are localized to the tear. Further, we leverage our ability to discern tearing to assess the ability to strain-engineer the SPE states in indents that remain intact and where the strain is preserved. By explicitly eliminating the instances where tearing occurs, we find that increasing the amount of strain in the indent by increasing the indentation force does not significantly alter the physical properties of the generated SPE states. However, we do find that as the indentation force increases, the spatial density of the SPE states decreases, which suggests that either an optimal range of tensile strain exists for the formation of

SPE states or that the SPE states preferentially localize to the periphery of the indent, as was concluded from super-resolution imaging measurements[29]. Our results substantially improve the understanding of the SPE formation process in indented 1L-WSe_2 and, as a result, the ability to leverage nanoindentation as a highly controllable process to position and strain-engineer SPEs in all 2D semiconductor systems.

Results

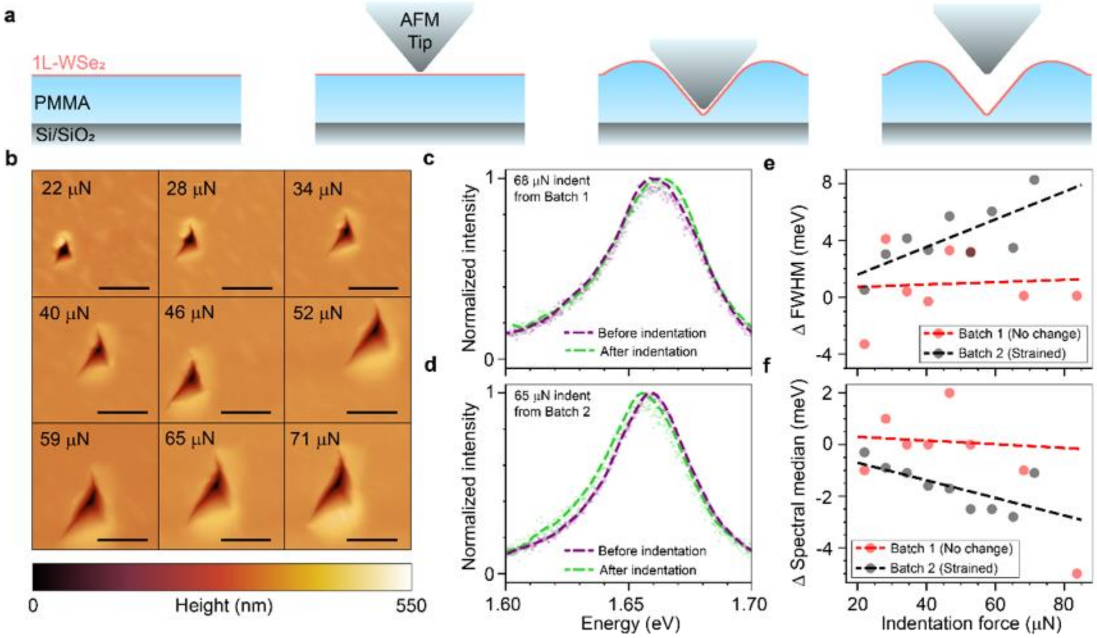

Figure 4.4 – The nanoindentation process and room temperature PL characterization. **(a)** A schematic of the indentation process. An AFM tip is positioned over a 1L-WSe_2 flake on a PMMA/SiO_2 substrate. The substrate is moved into the tip, where the WSe_2 and PMMA are deformed into the shape of the tip. When the substrate is retracted, an indent in the shape of the tip is left. AFM scale bars are 400 nm. **(b)** High-resolution AFM scans of nine indents made with indentation forces ranging from 22 – 71 µN. **(c, d)** The average PL spectra of before and after indenting from Batch 1 and Batch 2, respectively. **(e)** The difference in the full-width half maximum (FWHM) of the PL spectra between after and before indentation. A positive difference corresponds to an increase in FWHM after indentation. **(f)** The difference in PL emission energy, calculated by taking the difference between before and after indenting. Negative values correspond to a redshift or decrease in emission energy after indenting.

Figure 4.4a illustrates the process of generating the localized strain in the 1L-WSe_2 using nanoindentation[3, 5, 29-36, 38]. The samples are comprised of 1L-WSe_2 that was directly exfoliated onto a PMMA film that is ~350 nm thick. To indent the 1L-WSe_2, an atomic force microscope (AFM) probe is brought into initial contact at a fixed location on the 1L-WSe_2/PMMA layer. The contact force can then be increased by further raising the sample into the AFM probe, where at sufficiently large forces, the PMMA is plastically deformed into an indent. Because of strong adhesion, the 1L-WSe_2 is suspected to be conformally stretched along the profile of the indent, resulting in a region of localized strain where the amount of strain is dependent upon the size (e.g. depth) of the indent. The geometry/structure of the indent, and thus the generated strain, depends on the nano- and microscale structure of the AFM probe combined with the displacement of the PMMA resulting in a peripheral build-up region around the indent. Further, the depth, width, and size of the build-up region for a given indent depends on the force constant of the AFM probe cantilever used during indentation and the additional z-displacement of the sample beyond the initial contact point.

Prior studies of localized strain in 2D semiconductors generated by nanoindentation used blunted probes and z-displacements ranging from 200-2000 nm[3]. Using the cantilever force constant, the applied forces in these studies spanned 1-80 μN. In comparison, we use as-supplied commercial Tap300Al-G probes (Supplementary Figure 4.1) and z-displacements of 1000-3000 nm corresponding to forces from 22-84 μN (see methods and Supplementary Figure 4.2). Figure 4.4b shows the topography of a representative set of indents from our process, demonstrating how the structure of the buildup regions as well as the size and depths of the indents depend on the indentation force. To probe the strain generated, the average PL spectrum from a 900×900 nm^2

region at each indentation site was recorded both before and after indentation. The before-and-after comparison of the PL spectra reveals two distinct behaviors. In the first case (Figure 4.4c), the PL of the indented region is unaffected by the indentation process: both the peak energy and spectral width of the PL are the same before and after the indentation process. The lack of observable change in the PL indicates that the nanoindentation process did not impart a significant amount of strain to the region. In the second case (Figure 4.4d), the indentation process shifts the PL spectrum to lower energies and increases the spectral linewidth. Such lower energy and broader PL are expected from a region with localized, inhomogeneous tensile strain[13, 22, 25, 39-42], indicating that the indentation process generated a measurable amount of strain.

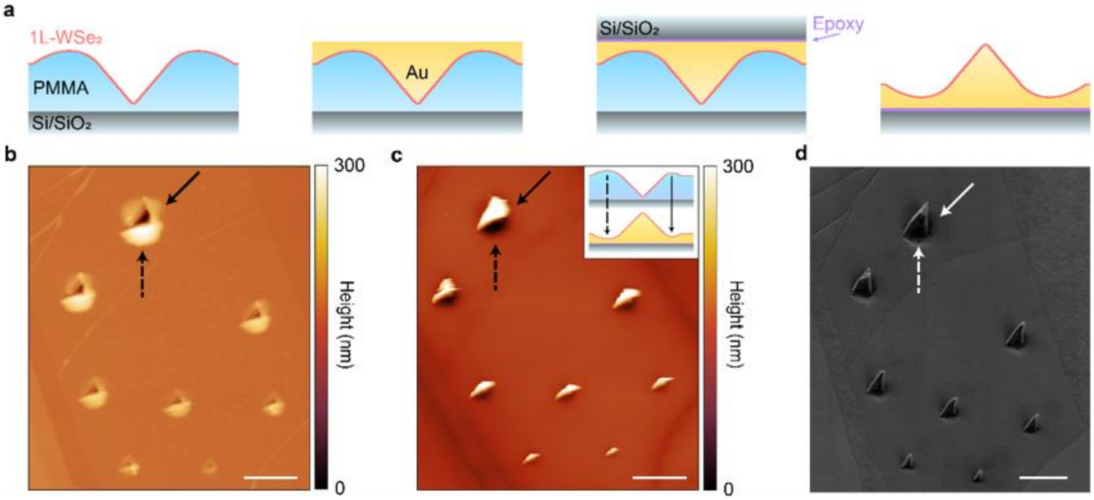

Figure 4.5 – Inverting the nanoindents. **(a)** A schematic demonstrating the inversion process. Starting with an indented 1L-WSe_2/ PMMA/SiO_2/Si sample, a ~550 nm thick layer of gold is deposited on the sample, filling the indent with gold, and leaving a gold surface on which a second SiO_2/Si substrate is epoxyed. The PMMA holding the initial SiO_2/Si substrate is dissolved leaving an inverted indent **(b, c)** AFM topography maps of Batch 1 indents and the corresponding inverted structure, respectively. The inset in (c) is a schematic demonstrating that the asymmetric PMMA buildup in the indents becomes valleys when inverted. The black (white) dashed and solid lines mark how the larger and smaller buildup regions around the indent correspond to the larger and smaller valleys when inverted. **(d)** SEM of the inverted indents in panel c. The scale bars are 1 µm.

For a given "batch" of indents (i.e., a set of nanoindents created with the same AFM probe and identical tip-sample-cantilever geometry), the before-and-after behavior is uniform up to a critical indentation force: either all indents exhibit signatures of localized strain or not. Figures 1e and 1f report how the nanoindentation-induced changes in the energy and width of the PL of 1L-WSe_2 depend on the indentation force for both types of batches. Neither the energy nor the linewidth of the PL substantially changes for the set of indents labeled "Batch 1". For this batch, signatures of strain are only observed at the highest indentation force of 84 μN (z-displacement of 3000 nm), resulting in an abrupt redshift of ~5 meV. We suspect that this shift at the greatest force is due to a significant structural perturbation beyond indentation and has been observed in prior studies of indents with lateral dimensions on the length scale of 4 μm[30]. In contrast, for the indents of Batch 2, greater indentation forces generate both larger redshifts and increases in linewidth, indicating force-induced increases of strain and structural inhomogeneity. In particular, the shifts in emission energy are consistent with observations made for similar strain profiles of prior studies[5]. These approximately linear relationships indicate that with the right processing conditions (e.g., AFM probe and tip-sample-cantilever geometry), the indentation force provides a degree of tunability of the localized strain. Comparing the different behaviors between the two batches of indents, we hypothesize that the indentation-induced strain in the indents of Batch 1 has relaxed, likely due to the tearing of the 1L-WSe_2[43], whereas in Batch 2, the 1L-WSe_2 remains intact, preserving the indentation-induced strain.

To more directly probe the presence of tearing within the indented material, we developed a process to invert the indents into protruding pillars so that the structure of the 1L-WSe_2 within the indent can be assessed using scanning electron microscopy (SEM). For inversion, we follow a template stripping process that is summarized in Figure 4.5a. In short, a 550 nm-thick gold film is deposited on top of the indented 1L-WSe_2/PMMA stack. Care is taken to ensure the evaporated gold is incident parallel to the normal surface to minimize any shadow masking effects and ensure the indents are uniformly filled (see methods and Supplementary Figure 4.3) After deposition, a second Si/SiO_2 substrate is epoxied to the exposed surface of the gold film. Once cured, the Si/SiO_2/epoxy/Au/1L-WSe_2/PMMA is stripped from the original substrate, and the residual PMMA is removed with a solvent wash. This inversion process has a high success rate of ~90%, which we suspect is aided by chalcogen vacancies in the TMDs binding with the gold layer[44-47]. With that said, the inversion process also works for other 2D materials (WS_2, h-BN) and filling layers (PDMS, SiO_2, Ti).

The inverted structure is a coarse replication of the AFM probe that was used for the indentation (see Supplementary Figure 4.4). However, the radius of curvature of the apex of the inverted structure is ~2-5× larger than that of the indenting AFM probe. This enlargement is likely caused by the slipping of the AFM probe during indentation (see Supplementary Figure 4.5). Like prior nanoindentation studies[3, 5, 29-36], a bulge is present around the periphery of the indent/inversion (black (white) solid and dashed arrows in Figure 4.5b-d). This bulge arises from the buildup of PMMA as it is pushed away from the indented region but is not uniformly distributed around the indent. We suspect that the tilt of the indenting AFM probe concentrates PMMA on one side of the indent (Supplementary Figure 4.6). The high resolution AFM micrographs of the indents and inversions confirm the asymmetric bulge (key features of the inverted structure in relation to the original indent inset in Figure 4.5c). The bulge in the indentation appears as a depression in the inverted structures, demonstrating how the inversion process preserves the structure of the original indents. Figure 4.5d shows a SEM micrograph of the inverted structures (at a 45° tilt). Within these images, the structure of the 1L-WSe$_2$ is resolvable, confirming that the 1L-WSe$_2$ is preserved during the inversion process.

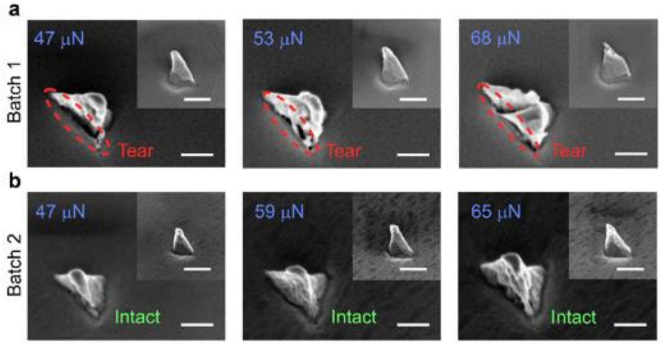

Figure 4.6 – SEM of Batch 1 and 2 inverted indents. **(a)** SEM images of inverted indents from Batch 1. The red dash ovals mark tears in the 1L-WSe$_2$. This tearing is in sharp contrast to Batch 2 where no tearing is observed in **(b)**. The insets are of the same inverted indents but rotated 180° to show the other side. The blue values in each panel are the indentation forces used to make the indent. Main figure scale bars are 200 nm (insets are 400 nm).

Assessment of tearing of the 1L-WSe$_2$ is accomplished with more detailed SEM imaging at a 45° tilt angle. Figure 4.6 shows higher-resolution imaging of individual indentations from Batch 1 (Figures 4.6a) and Batch 2 (Figures 4.6b) from both sides of the indent. The indents from Batch 1, where the room-temperature spectroscopy indicated the occurrence of strain relaxation, have dark voids that are spanned by filaments of 1L-WSe$_2$ at the depressions that occur at the base of the inverted indents, signifying tearing of the 1L-WSe$_2$. These depressions in the inverted structures correspond to the bulges of the original indents. Generally, the signatures of tearing are only observed on one side of the inverted structure, and they occur on the same side for a given batch of indents. Additional examples of torn inversions and how they depend on z-displacement, contact angle, and tip condition, can be found in the Supplementary Figure 4.7. In contrast, the indents from Batch 2 where the room-temperature spectroscopy showed indentation-force dependent strain are devoid of analogous signatures of tearing. We note that the indents of Batch 1 and Batch 2 were made using nearly the same process. The only variations were the specific AFM probe used and the specific geometry of how it was mounted in the AFM. We suspect three potential origins of the tears. First, and most importantly, is the use of a dulled AFM probe during indentation, creating a larger and less uniform contact surface. Second is a misalignment in the contact angle used, causing the tip to slide on the WSe_2 surface from an insufficient/excessive in-plane motion of the stage. Lastly is the yaw tilt of the probe within the AFM tip mount, causing spatially inhomogeneous strain generation during the indent.

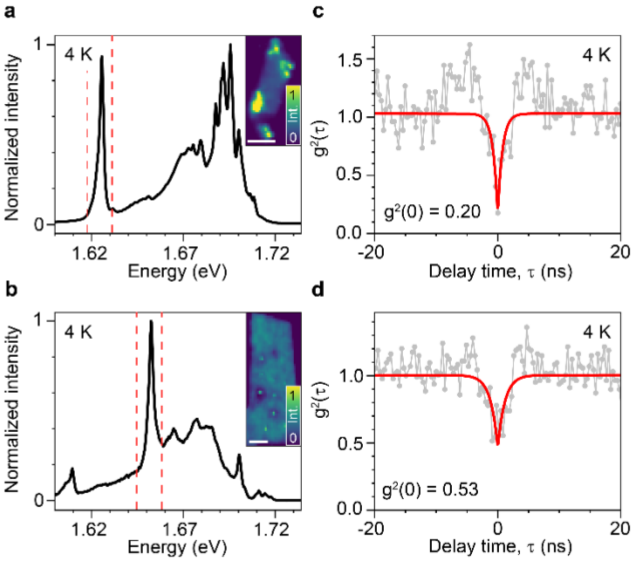

Figure 4.7 – Confirmation of single-photon emitters in Batch 1 and 2. **(a, b)** Average PL spectra at 4 K of an indent from Batch 1 and Batch 2, respectively. The inset in (a) is the integrated intensity map of Batch 1 integrated over the range 1.52 – 1.84 eV. The inset in (b) is the integrated intensity map of Batch 2 integrated over the range 1.51 – 1.83 eV. The scale bars of the insets are 5 µm. **(c, d)** Second order correlation function ($g^{(2)}(\tau)$) of the emitters marked by red dashed lines in (a) and (b), respectively. Both emitters measured show antibunching behavior with $g^{(2)}(0)$ below or near 0.5.

The nanoindentation procedure semi-deterministically positions quantum emitters in 1L-WSe_2[3, 5, 29-36]. However, the role of the observed tearing effect in both the formation and strain-engineering of the quantum emitters has not been established. Figure 4.7 shows that quantum light sources emerge in both batches of indents. Localized emission in narrow wavelength bands is observed at the indentation sites for the torn indents of Batch 1 (Figure 4.7a and inset). However, as contrasted in Figure 4.7b, the PL of the intact indents is much more uniformly localized to the indentation sites. Detailed imaging of the indents over different emission bands is provided in Supplementary Figures 4.8-4.9. The spectra of the localized PL at cryogenic temperatures from a representative torn indent in Batch 1 (where the strain has relaxed) and an intact indent in Batch 2 (where the strain is preserved), are shown in the main panels of Figures 4a and 4b, respectively. Despite the disparity in strain relaxation, narrowband emission from localized states is observed from both types of indentation sites. The quantum nature of the emission from both indentation sites is confirmed with antibunching measurements presented in Figures 4c and 4d. For the torn indentation (Figure 4.7c), a high single photon purity of 80% is observed whereas the brightest emitters from the intact indent (Figure 4.7d) overlaps with a broadband background, reducing the single photon purity to 47%. It is well known that localized tensile strain is a critical precursor to the formation of quantum light sources in 1L-WSe_2[1, 9, 11, 48], so the emergence of these states in the torn, strain-relaxed indents is not immediately anticipated. Although the strain is relaxed, we suspect that localized strain exists in the immediate vicinity of the tear, providing a secondary route for the formation of the quantum emitters[11]. For such torn indents, the emitter properties at an indentation site (i.e., number of emitters, emitter energy, brightness, etc.) are not expected to depend on the indentation force (beyond achieving mechanical failure) since the strain beyond the tear is relaxed. Several prior studies have reported such a weak or nonexistent dependence of emitter properties on indentation force[3, 36], indicating that tear-induced formation of quantum emitters could be prevalent and cannot be excluded based on the observation of emitter states.

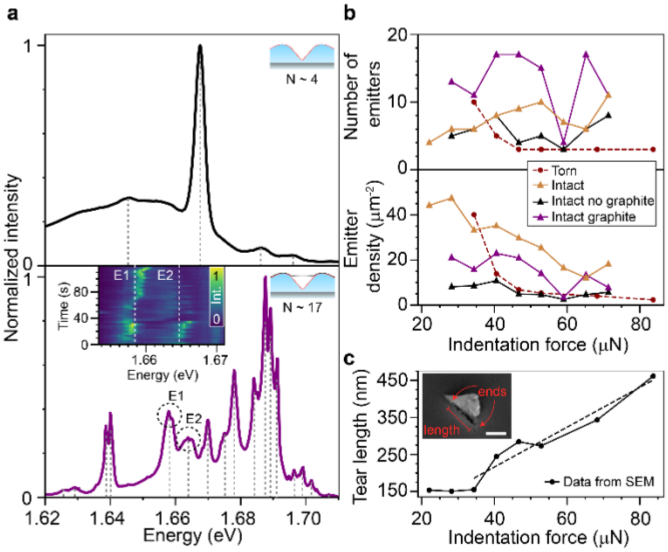

Figure 4.8 – Emitter density and emitter count dependence on indentation force: (a) Average 4 K PL spectra from an intact indent without graphite (top) and an intact indent with graphite (bottom). N is the number of emitters counted from the average spectra. The schematics in (a) represent the indents with or without graphite. The inset in (a, bottom) is the time series of the emitters circled in black and marked E1 and E2. The corresponding emitters in the time series are marked with white dashed lines. (b) Emitter number and emitter density with respect to indent area as a function of indentation force. In (b), the red circles correspond to Batch 1 (torn), and the yellow triangles correspond to Batch 2 (intact). The Batch 3 indents without graphite are marked by the black triangles, and the indents with graphite are represented by the purple triangles. (c) The tear length of each indent in Batch 1 as a function of indentation force. The tear lengths were measured from SEM images. The dashed black line is a guide to the eye. An example of how the tear was measured is shown in the SEM inset. SEM image scale bar is 200 nm.

Finally, for both the intact and torn indents, we measured the strain-tunability of the emitter populations and their properties for indentation forces ranging from 22-71 μN (1000-2600 nm z-displacement). As shown in the Supplementary Figure 4.10, even after verifying the presence of strain in the indents (c.f. Figure 4.4), clear relationships between the indentation force, emitter energies, and brightnesses were not observed, indicating that the ability to use the indentation force alone to imbue emitters with specific characteristics is limited. However, as shown in Figure 4.8, the indentation force affects the number and spatial densities of emitters that form at an indent, shedding new light on the formation mechanism and locations of the emitters. To measure the emitter populations meaningfully, however, two major challenges exist for obtaining accurate counts. First, a broadband background emission obscures weaker narrowband emitters (Figure 4.8a). So, first, we counted emitters in the presence of this pronounced background. Then, to suppress this background, we overlaid a batch of intact indents in 1L-WSe_2 with a thin layer of graphite (8 nm) that was previously shown to quench the background and improve the spectral isolation of the localized emitter states[31]. The enhanced PL emission of the localized states over the background is shown in the lower panel of Figure 4.8a. In addition to a strong suppression of the background, the addition of the graphite activated a larger number of additional emitters that were not resolvable in the original indent. The second challenge to address is the temporal fluctuations of the emitter states as exemplified in the temporal evolution of the PL spectrum of a single indentation site. To reduce the effects of these fluctuations, we identified emissive states in the time-averaged spectra shown in Figures 5a, and then confirmed that each line displayed independent fluctuations (i.e., spectral diffusion/wandering) using PL time series such as the inset in Figure 4.8a[49]. For instance, the emission peaks encircled in the black-dashed line in Figure 4,8a are examples of single states that are fluctuating. Such cases were treated as a single localized emitting state. Individual PL spectra used for emitter counting can be found in Supplementary Figures 4.11-4.13.

Following the above counting protocol, Figure 4.8b shows how the number of emitters depends on the indentation force for torn indents, intact indents, and intact indents overlaid with graphene. The probed indentation forces range from 22-84 µN (1000-3000 nm z-displacement). For Batches 1 (torn) and 3 (intact no graphite and intact graphite), the smallest forces used did not generate localized emitters, and we excluded those points from the plot. For all cases where the indents are intact, the absolute number of emitters weakly depends on the indentation force for smallest forces, which is most evident in the intact indents of Batch 2 (intact). Beyond 41 µN (~1600 nm z-displacement), the number of emitters appears to be independent of the indentation force. This general behavior was observed in two independent batches of indents. We note the indent made with 59 µN (2200 nm z-displacement) in Batch 3 is a significant outlier. The overall PL intensity at this site was also vastly reduced, indicating that an issue likely occurred during the indentation process for this site. The trend for the torn indents is dramatically different: as the indentation force increases, the number of emitters *decreases* with a rate that drastically slows beyond ~50 µN

While the number of emitters reveals a clear discrepancy between intact and torn indents, a strong dependence on the force is not observed for the intact indents. In contrast, Figure 4.8b also shows that the *areal density* of the localized emitters shows a stronger dependence on the indentation force. The surface area, which includes the indented and build-up regions, is determined with high resolution AFM imaging. For intact indents, the emitter density decreases linearly with increasing force, indicating that either quantum emitter formation favors a specific range of tensile strains and/or the emitters are localized to a specific feature of the indent such as its apex or surround build-up region. For instance, recent studies have shown the importance of nanoscale wrinkles in the formation of quantum emitter states in 1L-WSe_2[4, 50, 51]. A potential hypothesis is that such wrinkles are suppressed within the indent and confined to the surrounding buildup regions. Such localization to the build-up region agrees with prior super resolution measurements[29]. Empirically (see Supplementary Figure 4.14), the area of the buildup regions increases linearly with indentation force (as opposed to quadratically for the surface area of the indent itself), which, if the emitters are localized to that region, would lead to the observed decrease in emitter density.

The more dramatic decrease in both the absolute number of emitters as well as the emitter density for the torn indents corroborates our hypothesis that the emitters are localized to the tear. As shown in Figure 4.8c, the length of the tear is constant up to 34 μN and then increases linearly with indentation force (see Supplementary Figure 4.15 for SEM images). At 34 μN, an abrupt increase in the number of emitters occurs, which then rapidly decreases with greater forces until a constant number of three emitters. We believe that this behavior indicates that the emitters are localized to specific regions of the tear. If this is not the case and the emitters are uniformly distributed along the length of the tear, we would expect a linearly decreasing trend as seen in the intact indents. We suspect that the 34 μN threshold marks a critical threshold for strain relaxation in the 1L-WSe_2. Along these lines, we interpret the rapid decrease of the number of emitters between 34-48 μN to increasing relaxation of the strain by the tear until maximum relaxation beyond 48 μN. At the point of maximum relaxation, we only observe three emitters per site, regardless of the force used.

Discussion

For the intact indents, whether the localized emitters are predominantly in the indent itself or in the peripheral build-up region around the indent remains unresolved. While, as noted above, the decrease in the emitter density could be explained by localization to the build-up region, we note that the strong suppression of the number of emitters in the torn indents along with the observation that the tearing is isolated to a single side of the indent indicate that the emitters are predominantly located within the indent itself for the intact indents. Our rationale is that it is unlikely that the tearing on a single side would substantially relax the strain in the buildup region on the other sides. Our hypothesis is further supported by the fact that the overlaying the indents with graphite enhances the formation of the SPE states. Any emitters in the build-up region should be preferentially quenched due to their close proximity to the graphite. Further exploration of this issue motivates future studies that, for instance, leverage a dielectric material for the inversion process so that emitters are not quenched and can be localized using nano-optical or super resolution microscopy techniques[4, 28, 51-54]. More quantitative structural models of the strain in both the torn and intact indents would shed additional light on this open question.

In conclusion, our study provides a detailed characterization of the structure of indented 1L-WSe_2 for the purpose of deterministically creating SPE states. Using a inversion process, we are able to assess the physical structure of the indented 1L-WSe_2 and differentiate between indents where the 2D semiconductor is torn from those where it remains intact. For the intact indents, clear signatures of strain are identified in room-temperature PL characterization: the indentation process results in a localized red-shift and broadening of the PL. The magnitude of the red-shift and broadening increase with increasing indentation force, indicating that larger indentation forces generate greater amounts of localized strain. In contrast, in the idents where the 2D semiconductor is torn, the tear sufficiently relaxes the localized strain such that neither a shift nor broadening of the PL spectrum can be resolved. Remarkably, when focusing on the intact indents, the indentation force does not systematically alter the emitter energies nor the emitter intensities. However, we find that the larger localized strains from the greater indentation forces reduce the density of the localized emitters within an indent, providing strong evidence that the resulting emitters are either localized to a limited region within the indent, possibly because they only form over a limited range of tensile strain. For the indents where tearing occurs, the dependence of the number of emitters on the indentation force is dramatically different, indicating that the localized emitters states are isolated to specific regions of the indent. These measurements provide critical insight for using nanoindentations processes to create quantum light sources in 2D semiconductors as well as for the ability to strain-engineer the states.

Methods

Sample fabrication

Exfoliating WSe_2 onto PMMA: Polymethyl methacrylate (PMMA) layers on Si/SiO_2 were made by spinning 950K A4 PMMA at 1500 rpm followed by an 80°C bake for 45 mins. WSe_2 flakes were then exfoliated onto PMMA using an adapted Scotch tape method[55]. First, WSe_2 was exfoliated onto X4 polydimethylsiloxane (PDMS) that was treated in a light UV ozone for 2 mins and then the WSe_2/PDMS was used to exfoliate onto PMMA that was treated in the same UV ozone. Here, PDMS was used to exfoliate onto PMMA rather than typical tapes due to the reduced residue we observed.

Generation of nanoindents: To generate the nanoindents in the 2D material, we followed the initial protocol set by Rosenburger *et al*[3] and we used an AIST-NT SmartSPM HE002 AFM from HORIBA Scientific. In the AFM software, we used the nanoindentation application in the software in "Zsweep" mode, which allows for control of the Z-axis piezo motor of the AFM sample stage. When the location of an indent was defined, the desired indentation force was set by inputting the z-displacement, which is the distance the AFM stage moved into the AFM tip. The z-displacement ranged from 1000 – 3000 nm or 22-84 μN in indentation force. At these indentation forces, the AFM tip slips, meaning the tip does not stay in the defined location throughout the indentation process. To minimize the slipping, we introduced a lateral movement of the sample stage along the y-axis to keep the tip in the same initial position during the indentation process.

Inversion of nanoindents: To invert a batch of nanoindented 2D materials on PMMA, samples are placed in an electrom-beam evaporator directly above the crucible to ensure normal incidence during evaporation. For Au inversion, a layer of Au 150 – 200 nm thicker than the deepest indent depth of a given batch was deposited at 2 Å/s (550 nm in total). Due to the PMMA surface, certain compact evaporators may have issues of polymerized PMMA or substantial flim stress caused by excessive electron and charged ion irradiation that can be solved with added magnets and shields[56]. After evaporation, a thin layer of epoxy is spun onto the exposed Au surface at 6000 rpm and a second Si/SiO2 substrate is attached. Once curred, a razor blade stuck into the corners of the sample stack should separate the two substrates and the 2D material/Au/epoxy/SiO2/Si can be quickly (soaking may degrade epoxy layer) rinsed in Acetone to remove residual PMMA residue.

Wet transfer of thin Graphite: To transfer graphite layers onto WSe_2 indents graphite was first exfoliated onto an Si/SiO_2 substrate using the Scoth tape method[55]. Afterwards flakes with thicknesses ranging from 6-10 nm were identified using AFM and a thin layer of 10:1 Sylgard 184 PDMS was spun on at 4000 rpm. After curing in a 100°C oven for ~60 mins the chip is submerged in a 1M solution of NaOH in DIW heated to 90°C to lightly etch the SiO_2 surface and encourage liftoff of the graphite/PDMS stamp[57, 58]. Once bubbles have begun to form on the perimeter of the chip (~15 mins) the film may separate from the Si/SiO_2 or may require gentle assistance from a pair of tweezers. To remove excess NaOH residue, the film is left in a DIW bath for ~12 hours. Lastly, the film can be retrieved from the DIW, dried with Nitrogen, and transferred over the WSe_2 indents using the viscoelastic stamping method[59, 60].

Optical measurements

Room-temperature photoluminescence: The room-temperature PL measurements were conducted in ambient atmosphere using a commercially built microscope (HORIBA Scientific TRIOS system). We coupled a 532 nm CW diode laser in the microscope and focused the laser onto the sample using a Nikon LU Plan Fluor 100X (0.9 NA) objective. The sample is scanned using a XY piezo moter, and this scanning confocal microscope has a spatial resolution of ~630 nm. The room-temperature PL spectra were recorded using a grating spectrometer (Andor Kymera) and CCD camera (Andor iXon Ultra 888 EMCCD).

Cryogenic PL: Cryogenic PL measurements were taken inside of a liquid helium cooled Montana Instruments s50 Cryostation (4 K) equipped with optical access. 532 nm CW laser light was focused on the sample with a Nikon infinity corrected S Plan Fluor 40X (0.6 NA) objective equipped with a correction collar to compensate for a thin glass window above the sample. This home-built scanning confocal microscope has a spatial resolution of ~1 µm. PL spectra were then recorded using a grating spectrometer (Horiba iHR320) and CCD camera (Andor idus 416). Single-photon antibunching measurements were conducted by isolating a narrow band of quantum emission using the exit slit of our grating spectrometer as a monochromator and guiding this light into a Hanbury-Brown and Twiss (HBT) interferometer. The single-photon avalanche photodiodes that make up the arms of the HBT were connected to a PicoQuant HydraHarp 400 that acted as our time tagging module.

Supplementary information: determination of the roles of strain and tearing in single photon emission from nanoindented WSe_2

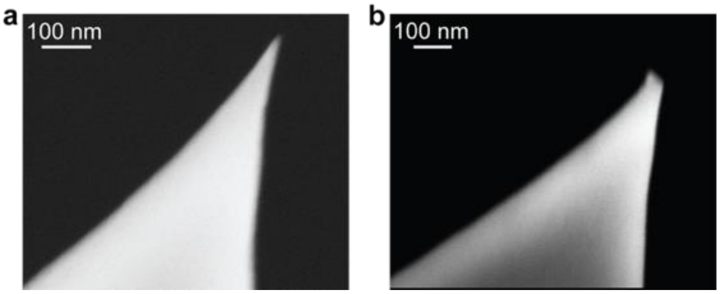

Supplementary Figure 4.1 – Comparing new and dulled AFM tips via SEM. **(a)** SEM images of a new Tap300Al-G AFM, k= 40 N/m probe before dulling. **(b)** SEM of the same AFM probe after dulling.

Supplementary note 1: Details indentation and indentation force calculation

To indent the 1L-WSe_2, we used Tap300Al-G AFM probes with a spring constant (k) of 40 N/m and a tip radius of 10 nm. During the nanoindentation process, the location of each indent and the movement of the sample stage into the probe (z-displacement) were set. This allows for control of the location and indentation force of each indent. At z-displacements over 1000 nm, a lateral displacement in the y-direction is introduced to keep the AFM tip in the same initial location throughout the indentation process. In the software, the y-displacement is set by inputting an angle. We can convert the z-displacement to indentation force by creating a calibration equation based on the indentation force (μN) that the software calculates as a function of z-displacement (see Supplementary Figure 4.2). After 3050 nm of z-displacement, the reflected laser from the cantilever reaches the edge of the photodiode, and the indentation force calculation provided by the software becomes inaccurate. Motivating the need for a calibration equation to calculate indentation force from the z-displacement. Note that the software reports the z-displacement as negative values. The resulting equation from the linear fit is shown below.

$$\text{Indentation force } (\mu\text{N}) = -0.031\ (\frac{\mu\text{N}}{\text{nm}}) * z + (-8.8\ \mu\text{N})$$

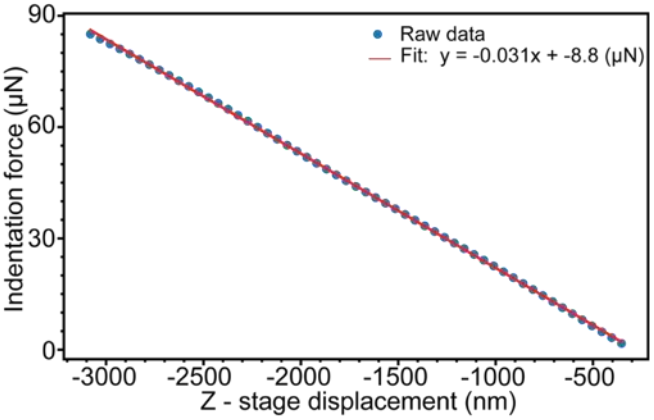

Supplementary Figure 4.2 – Indentation force calibration. Calculating an equation to convert z-displacement into indentation force in µN. The y-axis is the raw signal of the indentation force.

Supplementary note 2: Development of inversions with <u>non-normal incidence Au evaporation</u>

During the inversion process, having the evaporated Au incident normal to the substrate ensures uniform filling of the indent as shown in Supplementary Figure 4.3a. On the other hand, Supplementary Figure 4.3b shows how a non-normal evaporation can lead to shadow masking near the apex. SEM imaging of an inversion made with non-normal incidence evaporation can be seen in Supplementary Figure 4.3c where the apex is nominally void.

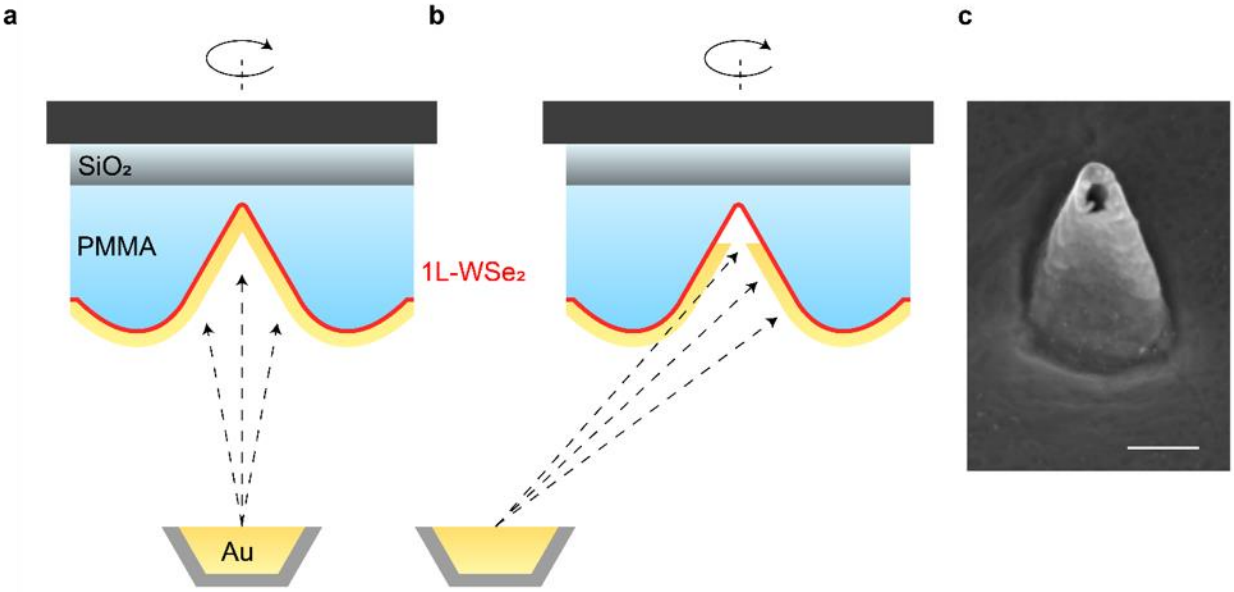

Supplementary Figure 4.3 – Effect of non-normal incidence during inversion (a) Schematic showing perfect filling of am indent when normal incidence is used **(b)** Schematic of non-normal incidence evaporation leading to shadow masking at the apex of the indent / inversion **(c)** SEM image of an inversion generated with non-normal incidence evaporation (scale bar = 200 nm).

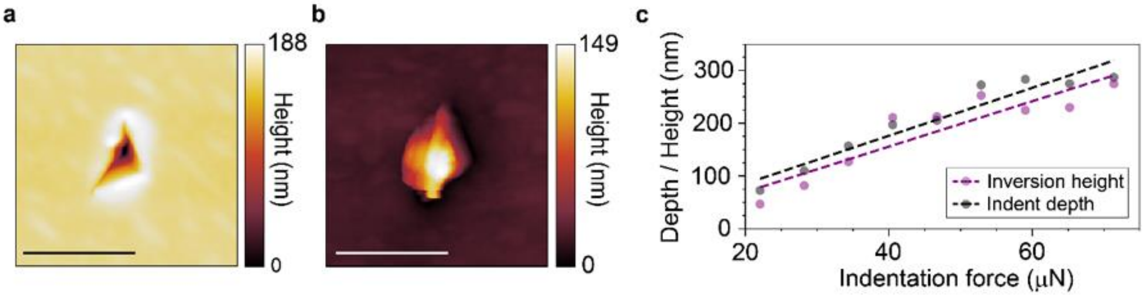

Supplementary Figure 4.4 – Inversions are near replications of nanoindents **(a, b)** High resolution AFM images of an 34 μN indent and inversion respectively **(c)** Depth of indents made using indentation forces ranging from 22 – 71 μN and heights of the corresponding inversions

Supplementary note 3: Sliding of the AFM tip from a misaligned contact angle

Due to the declination angle of the AFM cantilever with respect to the PMMA surface, a y-translation of the AFM stage is incorporated during indentation to maintain the position of the tip apex. The amount of y-translation required to maintain the tip position is prescribed in the

Horiba AIST software through the "contact angle" and the optimal value is a function of cantilever stiffness, declination angle, and substrate elastic modulus. Supplementary Figure 4.5a schematically shows an example indentation with a contact angle of 0° (no y-translation of the AFM stage). As the AFM stage is brought up into the tip, sliding occurs from the cantilever deflection leading to an enlarged side and increased indent radius of curvature. In comparison, Supplementary Figure 4.5b represents an indent made with a perfectly aligned contact angle. Here, the stage moves into the tip the same distance that the apex would be translated from the cantilever deflection. The indent generated is then a more accurate replication of the AFM tip geometry.

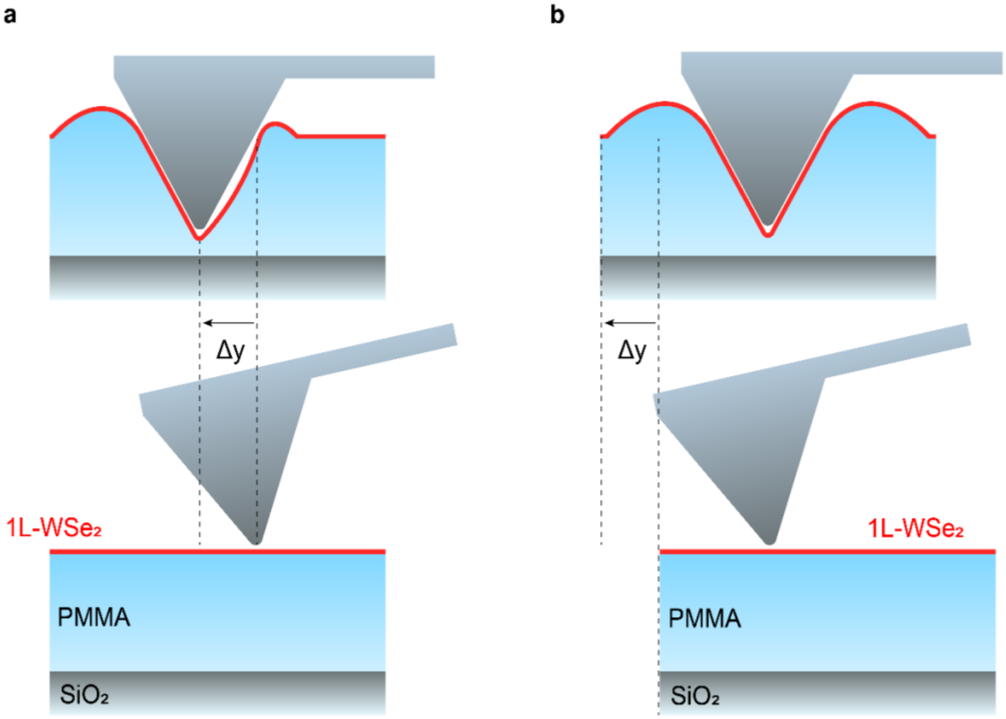

Supplementary Figure 4.5 – Sliding of AFM tip from misaligned contact angle. **(a)** Schematic representing an indent made with a contact angle of 0° (no y-translation of the AFM stage) **(b)** Schematic representing an indent made with a perfectly aligned contact angle.

Supplementary note 4: Yaw tilt of the AFM cantilever generating an asymmetric buildup region

Yaw tilt is described as a rotation of the cantilever with respect to the PMMA surface when looking at the cantilever head on. This can occur from small misalignments in the mounting of the AFM tip (dust under the Si, AFM tip fabrication issues) or from the substrate surface being tilted. During indentation, yaw tilt leads to an asymmetry in the build region. The side that the tip is rotated into will generate a larger build up region since PMMA is pushed towards that direction (seen in Supplementary Figure 4.6).

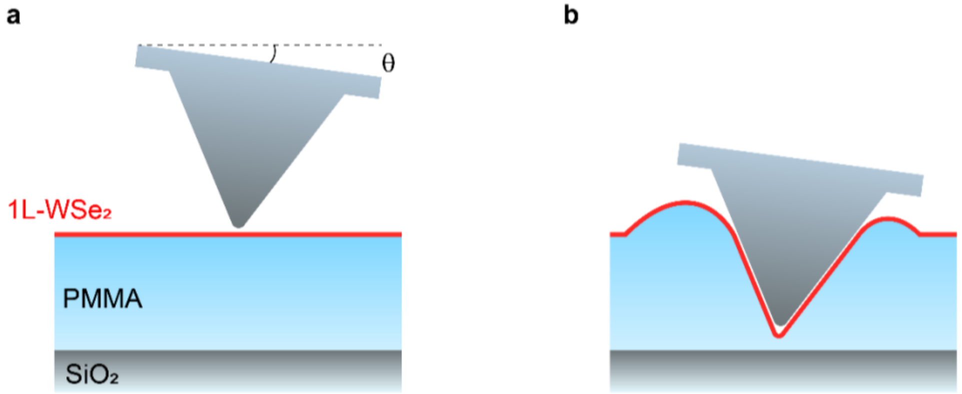

Supplementary Figure 4.6 – Yaw tilt generating an asymmetric buildup region **(a)** Schematic of an AFM tip with yaw tilt (θ) positioned above the PMMA surface prior to indentation **(b)** Schematic of indentation where the AFM cantilever has yaw tilt leading to an asymmetric build up region.

Supplementary note 5: Tearing in indented materials from dulled AFM tips with different y-displacements (angles)

To see the effect of the y-displacement, defined by the angle setting in the AFM software, on the indents, we made two inverted indent arrays with a constant indentation force of 53 μN, shown in Supplementary Figure 4.7. The array shown in Supplementary Figure 4.7a was made with a dulled Tap300Al-G AFM, k = 40 N/m probe. As the y-displacement is increased and limits the effect of the AFM tip slipping forward during the indentation process, the base of the inverted indent gets smaller, which means the AFM tip stays in the initial location of the tip (see Supplementary Figure 4.7a). This is the behavior seen from 0° to 24°. In contrast, from 26° to 60° the y-displacement causes the natural tip slipping to increase, resulting in the inverted indent base to elongate and appear stretched. Smaller SEM images are taking of the inverted indents and two examples are shown in shown in Supplementary Figure 4.7b and c. In Supplementary Figures 4.7b and c tears are observed in the 1L-WSe$_2$. Tears like the ones seen in Supplementary Figure 4.7b and c are observed in all the other inverted indents in Supplementary Figure 4.7a. In contrast, the inverted indents in Supplementary Figure 4.7d and e are made with the same probe before dulling, but they do not show tearing.

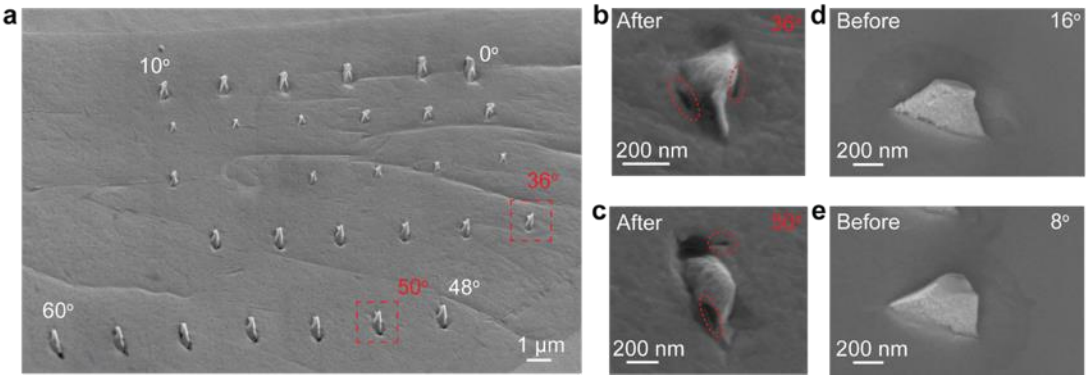

Supplementary Figure 4.7 – Two inverted 1L-WSe$_2$ indent arrays made with the same AFM probe before and after dulling. The same indentation force was used, and the angle was changed from 0 to 60° in steps of 2° for both arrays of indents. **(a)** SEM of an array of inverted indents made with a dulled Tap300Al-G, k = 40 N/m AFM probe. The angles set the y-displacement of the sample stage. The Indentation force for all the indents in panels **(a – e)** was 53 µN. **(b,c)** SEM of two indents outlined by red squares in (a) made with angles of 36° and 50° respectively. The red ovals mark tears in the 1L-WSe$_2$. **(d, e)** SEM of inverted indents made with the fresh AFM probe, meaning the probe was not dulled. The indents were made with 16° (d) and 8° (e) and do not show signs of tearing as seen in (b) and (c).

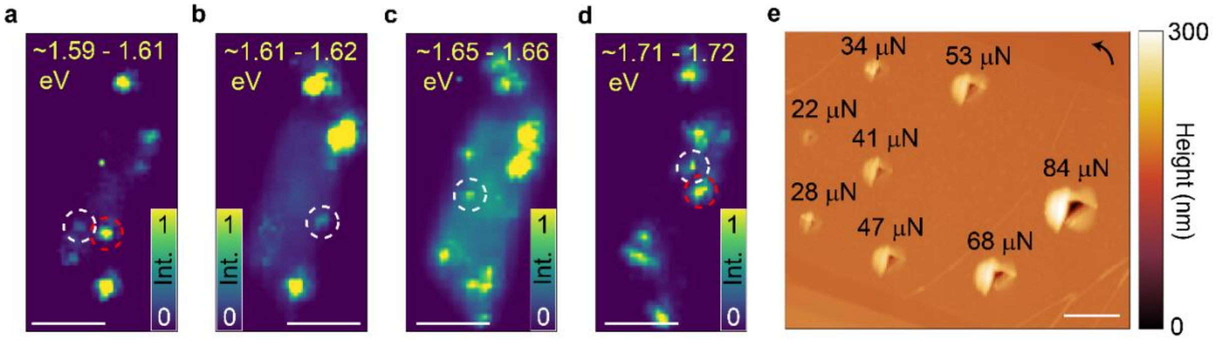

Supplementary Figure 4.8 – Locating indentation sites in Batch 1 **(a)** Hyperspectral image integrated from ~1.59 – 1.61 eV used to identify the 34 & 41 μN indents in white & red respectively **(b)** Hyperspectral image integrated from ~1.61 – 1.62 eV used to identify the 47 μN indent **(c)** Hyperspectral image integrated from ~1.65 – 1.66 eV used to identify the 53 μN indent **(d)** Hyperspectral image integrated from ~1.71 – 1.72 eV used to identify the 68 & 84 μN indents in red & white respectively (scale bars = 5 μm) **(e)** AFM image of the indents in Batch 1 ranging in indentation force from 22 – 84 μN (scale bar = 1 μm). Black arrow indicates a 90° rotation to match the hyperspectral images.

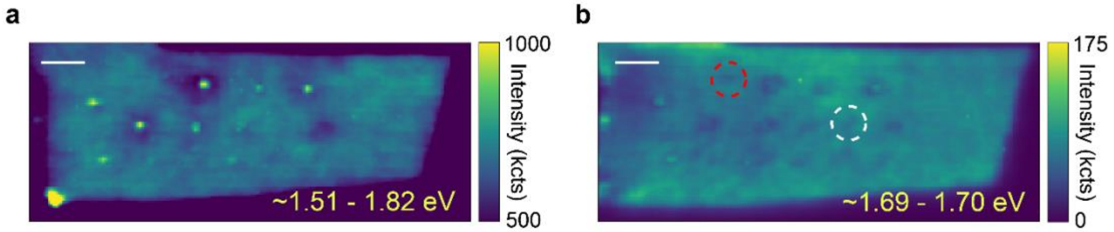

Supplementary Figure 4.9 – Locating indentation sites in Batch 2 **(a)** Hyperspectral image integrated from 1.51 – 1.82 eV **(b)** Hyperspectral image integrated from 1.69 – 1.70 eV used to identify the 28 & 65 μN indents in white & red respectively (scale bar = 10 μm).

Supplementary note 6: Properties of the emitter ensemble at each site in Batch 3

4 K PL taken at each indentation site of Batch 3 was used to investigate if properties of the emitter ensemble had dependence on indentation force. Similar to previous reports, in Supplementary Figure 4.10a-d we note no trend of integrated PL intensity, average emitter energy, highest emitter energy, or lowest emitter energy to indentation force (strain)[3, 36]. These metrics were extracted using average PL spectra from a 120 s PL time series both before and after graphite

was added to quench excessive background emission[61]. Determination of average, highest, and lowest emitter energy was done using the emitters identified from the emitter counting protocol.

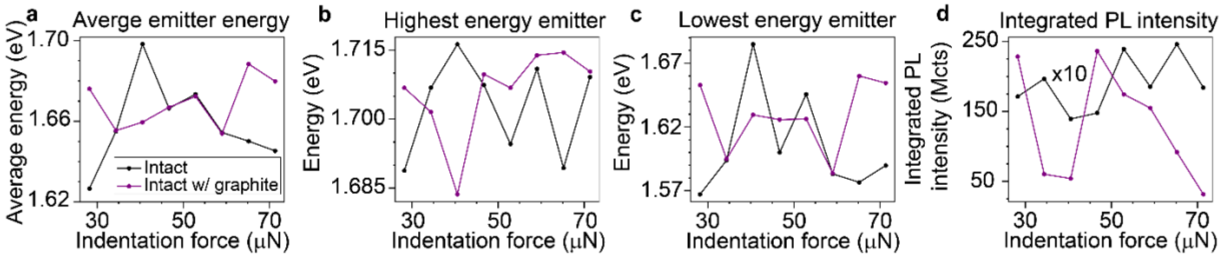

Supplementary Figure 4.10 – Emitter ensemble properties of each site in Batch 3. **(a)** Average energy of the emitter ensemble at each indentation site **(b, c)** Lowest and highest energy emitter of the ensemble at each site respectively **(d)** Integrated PL intensity of all emission (1.575 – 1.725 eV) at each indentation site.

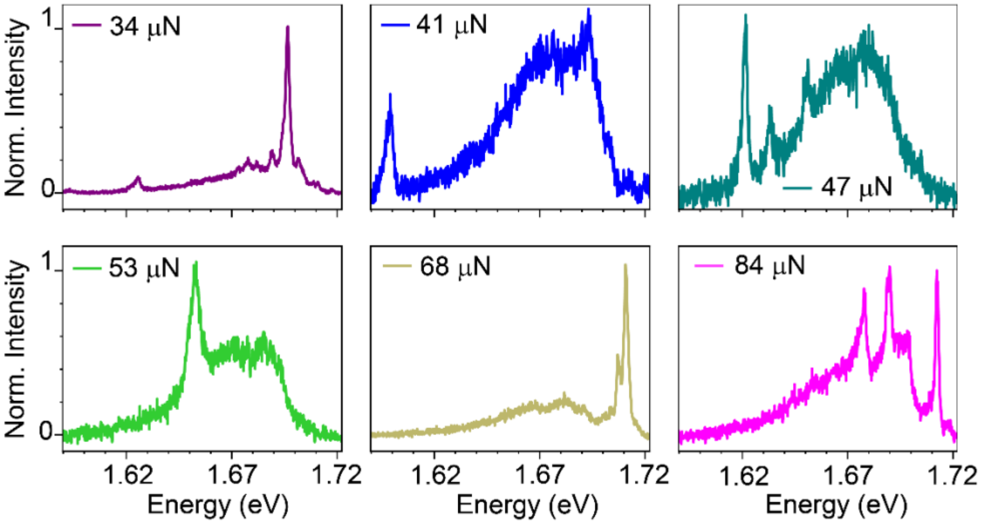

Supplementary Figure 4.11 – PL spectra of each site in Batch 1. PL spectra of indentation sites made with indentation forces ranging from 34 – 84 μN

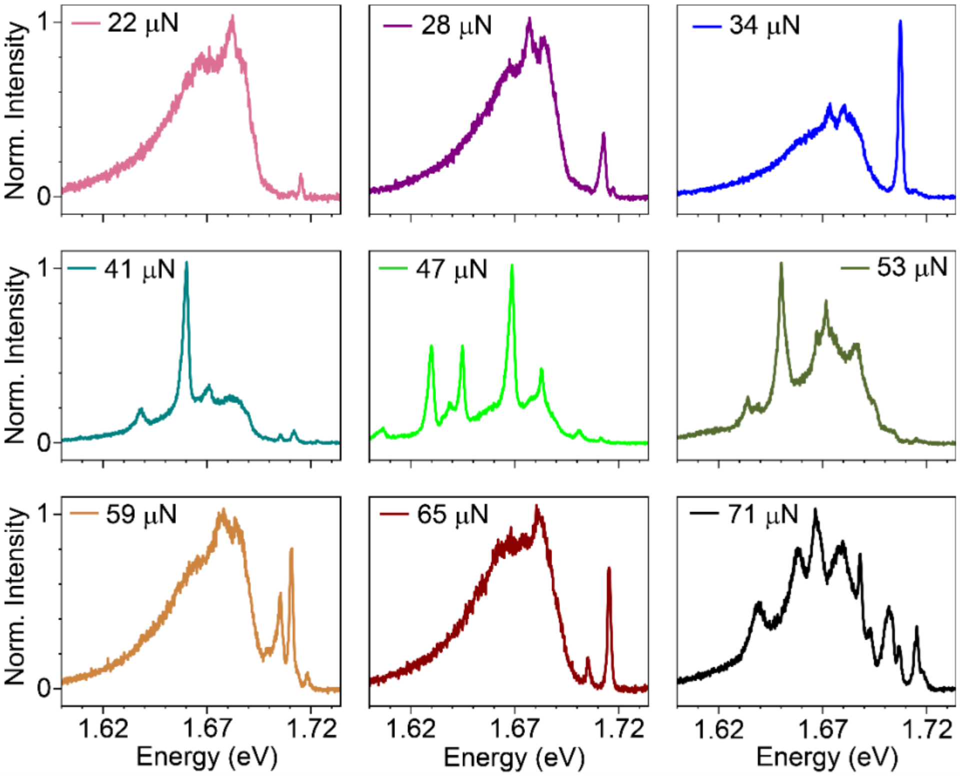

Supplementary Figure 4.12 – PL spectra of each site in Batch 2. PL spectra of indentation sites made with indentation forces ranging from 22 – 71 μN

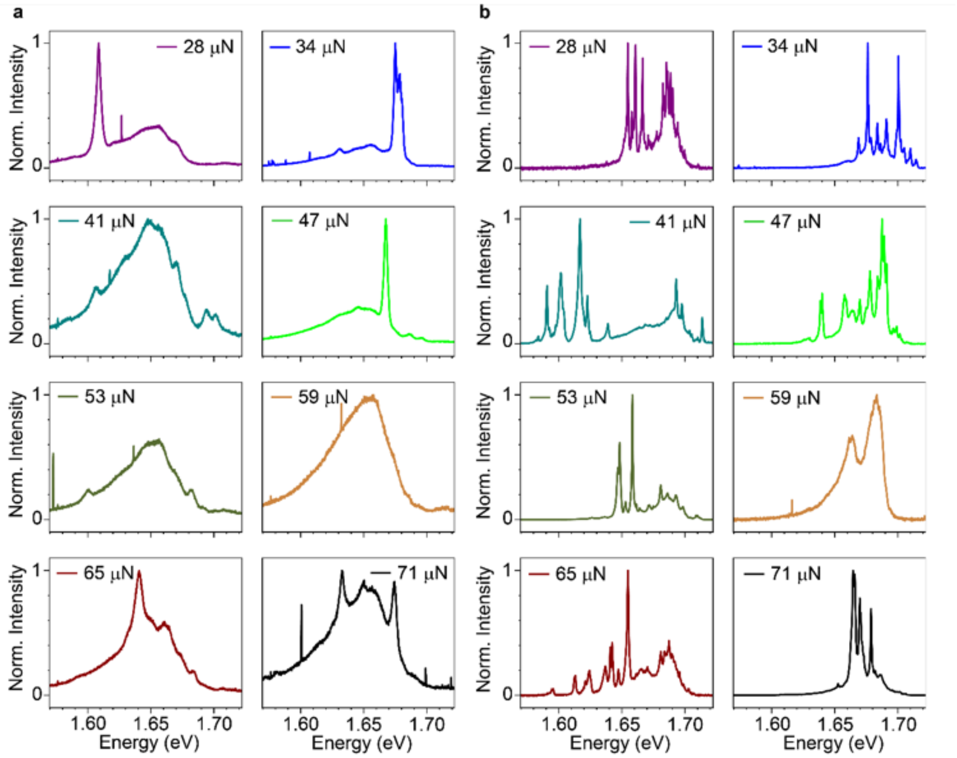

Supplementary Figure 4.13 – Average PL spectra of each site in Batch 3. Average PL spectra of indentation sites made with indentation forces ranging from 28 – 71 μN **(a)** Average PL spectra from a 120 s PL time-series without graphite **(b)** Average PL spectra from a 120 s PL time-series with graphite

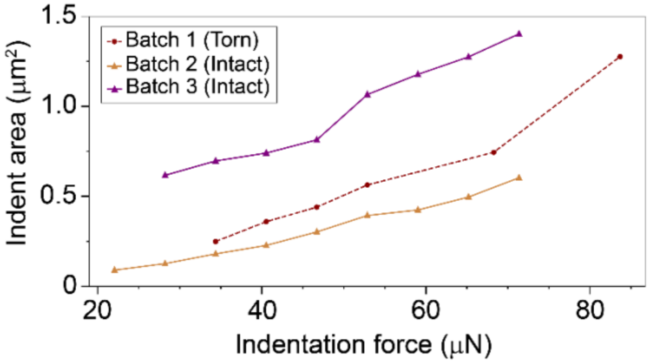

Supplementary Figure 4.14 – Total indent area of each site. Areas including the indent and buildup region of each site acquired from high resolution AFM imaging.

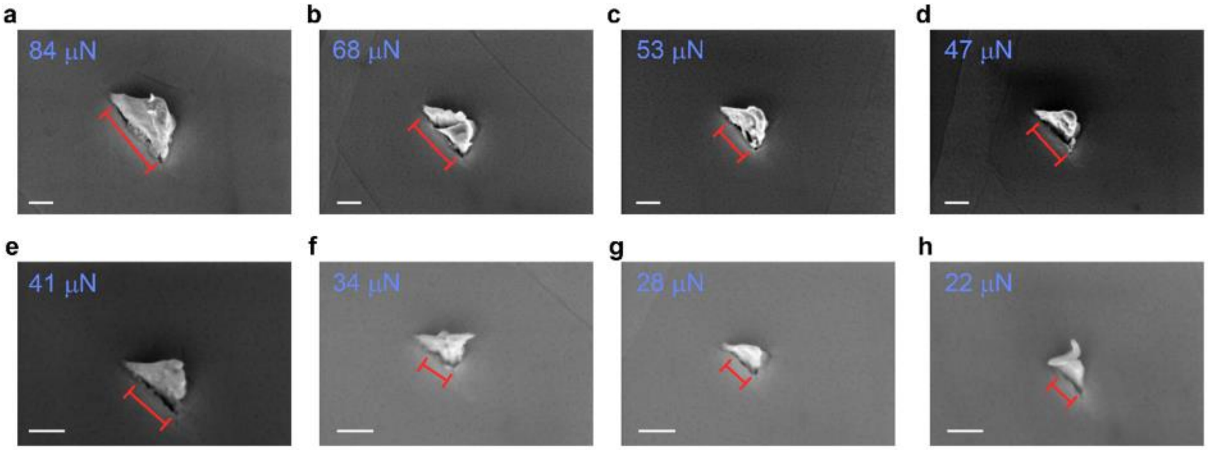

Supplementary Figure 4.15 – Tear length of Batch 1 indents using SEM imaging. **(a-h)** SEM images of Batch 1 inversions. Torn regions are highlighted using a red line and the indentation force used to generate each indent is also listed (scale bars = 200 nm).

References

(1) Linhart, L.; Paur, M.; Smejkal, V.; Burgdorfer, J.; Mueller, T.; Libisch, F. Localized Intervalley Defect Excitons as Single-Photon Emitters in WSe_2. *Phys Rev Lett* **2019**, *123* (14), 146401. DOI: 10.1103/PhysRevLett.123.146401.

(2) Wang, G.; Robert, C.; Suslu, A.; Chen, B.; Yang, S.; Alamdari, S.; Gerber, I. C.; Amand, T.; Marie, X.; Tongay, S.; et al. Spin-orbit engineering in transition metal dichalcogenide alloy monolayers. *Nat Commun* **2015**, *6*, 10110. DOI: 10.1038/ncomms10110.

(3) Rosenberger, M. R.; Dass, C. K.; Chuang, H. J.; Sivaram, S. V.; McCreary, K. M.; Hendrickson, J. R.; Jonker, B. T. Quantum Calligraphy: Writing Single-Photon Emitters in a Two-Dimensional Materials Platform. *ACS Nano* **2019**, *13* (1), 904-912. DOI: 10.1021/acsnano.8b08730.

(4) Yanev, E. S.; Darlington, T. P.; Ladyzhets, S. A.; Strasbourg, M. C.; Trovatello, C.; Liu, S.; Rhodes, D. A.; Hall, K.; Sinha, A.; Borys, N. J.; et al. Programmable nanowrinkle-induced room-temperature exciton localization in monolayer WSe_2. *Nat Commun* **2024**, *15* (1), 1543. DOI: 10.1038/s41467-024-45936-2.

(5) So, J. P.; Kim, H. R.; Baek, H.; Jeong, K. Y.; Lee, H. C.; Huh, W.; Kim, Y. S.; Watanabe, K.; Taniguchi, T.; Kim, J.; et al. Electrically driven strain-induced deterministic single-photon emitters in a van der Waals heterostructure. *Sci Adv* **2021**, *7* (43), eabj3176. DOI: 10.1126/sciadv.abj3176.

(6) Montblanch, A. R.; Barbone, M.; Aharonovich, I.; Atature, M.; Ferrari, A. C. Layered materials as a platform for quantum technologies. *Nat Nanotechnol* **2023**, *18* (6), 555-571. DOI: 10.1038/s41565-023-01354-x.

(7) Yu, Y.; Seo, I. C.; Luo, M.; Lu, K.; Son, B.; Tan, J. K.; Nam, D. Tunable single-photon emitters in 2D materials. *Nanophotonics* **2024**, *13* (19), 3615-3629. DOI: 10.1515/nanoph-2024-0050.

(8) Sortino, L.; Zotev, P. G.; Phillips, C. L.; Brash, A. J.; Cambiasso, J.; Marensi, E.; Fox, A. M.; Maier, S. A.; Sapienza, R.; Tartakovskii, A. I. Bright single photon emitters with enhanced quantum efficiency in a two-dimensional semiconductor coupled with dielectric nano-antennas. *Nat Commun* **2021**, *12* (1), 6063. DOI: 10.1038/s41467-021-26262-3.

(9) Luo, Y.; Shepard, G. D.; Ardelean, J. V.; Rhodes, D. A.; Kim, B.; Barmak, K.; Hone, J. C.; Strauf, S. Deterministic coupling of site-controlled quantum emitters in monolayer WSe_2 to plasmonic nanocavities. *Nat Nanotechnol* **2018**, *13* (12), 1137-1142. DOI: 10.1038/s41565-018-0275-z.

(10) Gao, T.; von Helversen, M.; Antón-Solanas, C.; Schneider, C.; Heindel, T. Atomically-thin single-photon sources for quantum communication. *npj 2D Materials and Applications* **2023**, *7* (1). DOI: 10.1038/s41699-023-00366-4.

(11) Tonndorf, P.; Schmidt, R.; Schneider, R.; Kern, J.; Buscema, M.; Steele, G. A.; Castellanos-Gomez, A.; van der Zant, H. S. J.; Michaelis de Vasconcellos, S.; Bratschitsch, R. Single-photon emission from localized excitons in an atomically thin semiconductor. *Optica* **2015**, *2* (4). DOI: 10.1364/optica.2.000347.

(12) Srivastava, A.; Sidler, M.; Allain, A. V.; Lembke, D. S.; Kis, A.; Imamoglu, A. Optically active quantum dots in monolayer WSe_2. *Nat Nanotechnol* **2015**, *10* (6), 491-496. DOI: 10.1038/nnano.2015.60.

(13) Li, H.; Contryman, A. W.; Qian, X.; Ardakani, S. M.; Gong, Y.; Wang, X.; Weisse, J. M.; Lee, C. H.; Zhao, J.; Ajayan, P. M.; et al. Optoelectronic crystal of artificial atoms in strain-textured molybdenum disulphide. *Nat Commun* **2015**, *6*, 7381. DOI: 10.1038/ncomms8381.

(14) Koperski, M.; Nogajewski, K.; Arora, A.; Cherkez, V.; Mallet, P.; Veuillen, J. Y.; Marcus, J.; Kossacki, P.; Potemski, M. Single photon emitters in exfoliated WSe_2 structures. *Nat Nanotechnol* **2015**, *10* (6), 503-506. DOI: 10.1038/nnano.2015.67.

(15) Kumar, S.; Kaczmarczyk, A.; Gerardot, B. D. Strain-Induced Spatial and Spectral Isolation of Quantum Emitters in Mono- and Bilayer WSe_2. *Nano Lett* **2015**, *15* (11), 7567-7573. DOI: 10.1021/acs.nanolett.5b03312.

(16) Moody, G.; Kavir Dass, C.; Hao, K.; Chen, C. H.; Li, L. J.; Singh, A.; Tran, K.; Clark, G.; Xu, X.; Berghauser, G.; et al. Intrinsic homogeneous linewidth and broadening mechanisms of excitons in monolayer transition metal dichalcogenides. *Nat Commun* **2015**, *6*, 8315. DOI: 10.1038/ncomms9315.

(17) He, Y. M.; Clark, G.; Schaibley, J. R.; He, Y.; Chen, M. C.; Wei, Y. J.; Ding, X.; Zhang, Q.; Yao, W.; Xu, X.; et al. Single quantum emitters in monolayer semiconductors. *Nat Nanotechnol* **2015**, *10* (6), 497-502. DOI: 10.1038/nnano.2015.75.

(18) Chakraborty, C.; Kinnischtzke, L.; Goodfellow, K. M.; Beams, R.; Vamivakas, A. N. Voltage-controlled quantum light from an atomically thin semiconductor. *Nat Nanotechnol* **2015**, *10* (6), 507-511. DOI: 10.1038/nnano.2015.79.

(19) Palacios-Berraquero, C.; Barbone, M.; Kara, D. M.; Chen, X.; Goykhman, I.; Yoon, D.; Ott, A. K.; Beitner, J.; Watanabe, K.; Taniguchi, T.; et al. Atomically thin quantum light-emitting diodes. *Nat Commun* **2016**, *7*, 12978. DOI: 10.1038/ncomms12978.

(20) Schwarz, S.; Kozikov, A.; Withers, F.; Maguire, J. K.; Foster, A. P.; Dufferwiel, S.; Hague, L.; Makhonin, M. N.; Wilson, L. R.; Geim, A. K.; et al. Electrically pumped single-defect light emitters in WSe_2. *2D Materials* **2016**, *3* (2). DOI: 10.1088/2053-1583/3/2/025038.

(21) Guo, S.; Germanis, S.; Taniguchi, T.; Watanabe, K.; Withers, F.; Luxmoore, I. J. Electrically Driven Site-Controlled Single Photon Source. *ACS Photonics* **2023**, *10* (8), 2549-2555. DOI: 10.1021/acsphotonics.3c00097.

(22) Branny, A.; Kumar, S.; Proux, R.; Gerardot, B. D. Deterministic strain-induced arrays of quantum emitters in a two-dimensional semiconductor. *Nat Commun* **2017**, *8*, 15053. DOI: 10.1038/ncomms15053.

(23) Azzam, S. I.; Parto, K.; Moody, G. Purcell enhancement and polarization control of single-photon emitters in monolayer WSe_2 using dielectric nanoantennas. *Nanophotonics* **2023**, *12* (3), 477-484. DOI: 10.1515/nanoph-2022-0628.

(24) Kim, H.; Moon, J. S.; Noh, G.; Lee, J.; Kim, J. H. Position and Frequency Control of Strain-Induced Quantum Emitters in WSe_2 Monolayers. *Nano Lett* **2019**, *19* (10), 7534-7539. DOI: 10.1021/acs.nanolett.9b03421.

(25) Parto, K.; Azzam, S. I.; Banerjee, K.; Moody, G. Defect and strain engineering of monolayer WSe_2 enables site-controlled single-photon emission up to 150 K. *Nat Commun* **2021**, *12* (1), 3585. DOI: 10.1038/s41467-021-23709-5.

(26) Luo, Y.; Liu, N.; Li, X.; Hone, J. C.; Strauf, S. Single photon emission in WSe_2 up 160 K by quantum yield control. *2D Materials* **2019**, *6* (3). DOI: 10.1088/2053-1583/ab15fe.

(27) Shepard, G. D.; Ajayi, O. A.; Li, X.; Zhu, X. Y.; Hone, J.; Strauf, S. Nanobubble induced formation of quantum emitters in monolayer semiconductors. *2D Materials* **2017**, *4* (2). DOI: 10.1088/2053-1583/aa629d.

(28) Darlington, T. P.; Carmesin, C.; Florian, M.; Yanev, E.; Ajayi, O.; Ardelean, J.; Rhodes, D. A.; Ghiotto, A.; Krayev, A.; Watanabe, K.; et al. Imaging Strain-Localized Excitons in Nanoscale Bubbles of Monolayer WSe_2 at Room Temperature. *Nat Nanotechnol* **2020**, *15* (10), 854-860. DOI: 10.1038/s41565-020-0730-5.

(29) Abramov, A. N.; Chestnov, I. Y.; Alimova, E. S.; Ivanova, T.; Mukhin, I. S.; Krizhanovskii, D. N.; Shelykh, I. A.; Iorsh, I. V.; Kravtsov, V. Photoluminescence imaging of single photon emitters within nanoscale strain profiles in monolayer WSe_2. *Nat Commun* **2023**, *14* (1), 5737. DOI: 10.1038/s41467-023-41292-9.

(30) Chang, S.; Yan, Y.; Geng, Y. Local Nanostrain Engineering of Monolayer MoS_2 Using Atomic Force Microscopy-Based Thermomechanical Nanoindentation. *Nano Lett* **2023**, *23* (20), 9219-9226. DOI: 10.1021/acs.nanolett.3c01809.

(31) Chuang, H. J.; Stevens, C. E.; Rosenberger, M. R.; Lee, S. J.; McCreary, K. M.; Hendrickson, J. R.; Jonker, B. T. Enhancing Single Photon Emission Purity via Design of van der Waals Heterostructures. *Nano Lett* **2024**, *24* (18), 5529-5535. DOI: 10.1021/acs.nanolett.4c00683.

(32) Cunningham, P. D.; Proscia, N. V.; LaGasse, S. W.; O'Hara, D. J.; McCreary, K. M.; Chuang, H.-J.; Povolotskyi, M.; Vurgaftman, I.; Jonker, B. T.; Simpkins, B. S. Site-Specific Exciton–Plasmon Coupling in Nanoindented WSe_2. *ACS Photonics* **2024**, *11* (8), 3250-3258. DOI: 10.1021/acsphotonics.4c00644.

(33) Lee, S.-J.; Chuang, H.-J.; Yeats, A. L.; McCreary, K. M.; O'Hara, D. J.; Jonker, B. T. Ferroelectric Modulation of Quantum Emitters in Monolayer WS_2. *ACS Nano* **2024**, *18* (36), 25349-25358. DOI: 10.1021/acsnano.4c10528.

(34) Li, X.; Jones, A. C.; Choi, J.; Zhao, H.; Chandrasekaran, V.; Pettes, M. T.; Piryatinski, A.; Tschudin, M. A.; Reiser, P.; Broadway, D. A.; et al. Proximity-induced chiral quantum light generation in strain-engineered WSe_2/$NiPS_3$ heterostructures. *Nat Mater* **2023**, *22* (11), 1311-1316. DOI: 10.1038/s41563-023-01645-7.

(35) Stevens, C. E.; Chuang, H. J.; Rosenberger, M. R.; McCreary, K. M.; Dass, C. K.; Jonker, B. T.; Hendrickson, J. R. Enhancing the Purity of Deterministically Placed Quantum Emitters in Monolayer WSe_2. *ACS Nano* **2022**, *16* (12), 20956-20963. DOI: 10.1021/acsnano.2c08553.

(36) Yücel, O.; Yagodkin, D.; Kirchhof, J. N.; Yu, Y.; Kumar, A. M.; Dewambrechies, A.; Kovalchuk, S.; Bolotin, K. I. Strain activation of localized states in WSe_2. *2D Materials* **2025**, *12* (3). DOI: 10.1088/2053-1583/add414.

(37) Peng, L.; Chan, H.; Choo, P.; Odom, T. W.; Sankaranarayanan, S.; Ma, X. Creation of Single-Photon Emitters in WSe_2 Monolayers Using Nanometer-Sized Gold Tips. *Nano Lett* **2020**, *20* (8), 5866-5872. DOI: 10.1021/acs.nanolett.0c01789.

(38) Lee, S. J.; Chuang, H. J.; McCreary, K. M.; Noyan, M. A.; Jonker, B. T. Voltage-Induced Degradation for Enhanced Purity and Reproducibility of Quantum Emission in Monolayer 2D Materials. *ACS Nano* **2025**, *19* (38), 33981-33990. DOI: 10.1021/acsnano.5c09799.

(39) Aslan, B.; Deng, M.; Heinz, T. F. Strain tuning of excitons in monolayer WSe_2. *Physical Review B* **2018**, *98* (11). DOI: 10.1103/PhysRevB.98.115308.

(40) Conley, H. J.; Wang, B.; Ziegler, J. I.; Haglund, R. F., Jr.; Pantelides, S. T.; Bolotin, K. I. Bandgap engineering of strained monolayer and bilayer MoS_2. *Nano Lett* **2013**, *13* (8), 3626-3630. DOI: 10.1021/nl4014748.

(41) Desai, S. B.; Seol, G.; Kang, J. S.; Fang, H.; Battaglia, C.; Kapadia, R.; Ager, J. W.; Guo, J.; Javey, A. Strain-induced indirect to direct bandgap transition in multilayer WSe_2. *Nano Lett* **2014**, *14* (8), 4592-4597. DOI: 10.1021/nl501638a.

(42) Hsu, W. T.; Lu, L. S.; Wang, D.; Huang, J. K.; Li, M. Y.; Chang, T. R.; Chou, Y. C.; Juang, Z. Y.; Jeng, H. T.; Li, L. J.; et al. Evidence of indirect gap in monolayer WSe_2. *Nat Commun* **2017**, *8* (1), 929. DOI: 10.1038/s41467-017-01012-6.

(43) Taghinejad, H.; Eftekhar, A. A.; Campbell, P. M.; Beatty, B.; Taghinejad, M.; Zhou, Y.; Perini, C. J.; Moradinejad, H.; Henderson, W. E.; Woods, E. V.; et al. Strain relaxation via formation of cracks in compositionally modulated two-dimensional semiconductor alloys. *npj 2D Materials and Applications* **2018**, *2* (1). DOI: 10.1038/s41699-018-0056-4.

(44) Panasci, S. E.; Schiliro, E.; Greco, G.; Cannas, M.; Gelardi, F. M.; Agnello, S.; Roccaforte, F.; Giannazzo, F. Strain, Doping, and Electronic Transport of Large Area Monolayer MoS_2 Exfoliated on Gold and Transferred to an Insulating Substrate. *ACS Appl Mater Interfaces* **2021**, *13* (26), 31248-31259. DOI: 10.1021/acsami.1c05185.

(45) Chen, S.; Li, B.; Dai, C.; Zhu, L.; Shen, Y.; Liu, F.; Deng, S.; Ming, F. Controlling Gold-Assisted Exfoliation of Large-Area MoS_2 Monolayers with External Pressure. *Nanomaterials (Basel)* **2024**, *14* (17). DOI: 10.3390/nano14171418.

(46) Smith, T. The hydrophilic nature of a clean gold surface. *Journal of Colloid and Interface Science* **1980**, *75* (1), 51-55. DOI: 10.1016/0021-9797(80)90348-3.

(47) Velicky, M.; Donnelly, G. E.; Hendren, W. R.; McFarland, S.; Scullion, D.; DeBenedetti, W. J. I.; Correa, G. C.; Han, Y.; Wain, A. J.; Hines, M. A.; et al. Mechanism of Gold-Assisted Exfoliation of Centimeter-Sized Transition-Metal Dichalcogenide Monolayers. *ACS Nano* **2018**, *12* (10), 10463-10472. DOI: 10.1021/acsnano.8b06101.

(48) Dang, J.; Sun, S.; Xie, X.; Yu, Y.; Peng, K.; Qian, C.; Wu, S.; Song, F.; Yang, J.; Xiao, S.; et al. Identifying defect-related quantum emitters in monolayer WSe_2. *npj 2D Materials and Applications* **2020**, *4* (1). DOI: 10.1038/s41699-020-0136-0.

(49) Schneider, L. M.; Lippert, S.; Kuhnert, J.; Ajayi, O.; Renaud, D.; Firoozabadi, S.; Ngo, Q.; Guo, R.; Kim, Y. D.; Heimbrodt, W.; et al. The influence of the environment on monolayer tungsten diselenide photoluminescence. *Nano-Structures & Nano-Objects* **2018**, *15*, 84-97. DOI: 10.1016/j.nanoso.2017.08.009.

(50) Daveau, R. S.; Vandekerckhove, T.; Mukherjee, A.; Wang, Z.; Shan, J.; Mak, K. F.; Vamivakas, A. N.; Fuchs, G. D. Spectral and spatial isolation of single tungsten diselenide quantum emitters using hexagonal boron nitride wrinkles. *APL Photonics* **2020**, *5* (9). DOI: 10.1063/5.0013825.

(51) Strasbourg, M. C.; Yanev, E. S.; Darlington, T. P.; Faagau, K.; Holtzman, L. N.; Barmak, K.; Hone, J. C.; Schuck, P. J.; Borys, N. J. Characterization of quantum dot-like emitters in programmable arrays of nanowrinkles of 1L-WSe_2. *Journal of Applied Physics* **2024**, *136* (4). DOI: 10.1063/5.0214410.

(52) Yao, K.; Zhang, S.; Yanev, E.; McCreary, K.; Chuang, H. J.; Rosenberger, M. R.; Darlington, T.; Krayev, A.; Jonker, B. T.; Hone, J. C.; et al. Nanoscale Optical Imaging of 2D Semiconductor Stacking Orders by Exciton-Enhanced Second Harmonic Generation. *Advanced Optical Materials* **2022**, *10* (12). DOI: 10.1002/adom.202200085.

(53) Shabani, S.; Darlington, T. P.; Gordon, C.; Wu, W.; Yanev, E.; Hone, J.; Zhu, X.; Dreyer, C. E.; Schuck, P. J.; Pasupathy, A. N. Ultralocalized Optoelectronic Properties of Nanobubbles

in 2D Semiconductors. *Nano Lett* **2022**, *22* (18), 7401-7407. DOI: 10.1021/acs.nanolett.2c02265.

(54) Jo, K.; Marino, E.; Lynch, J.; Jiang, Z.; Gogotsi, N.; Darlington, T. P.; Soroush, M.; Schuck, P. J.; Borys, N. J.; Murray, C. B.; et al. Direct nano-imaging of light-matter interactions in nanoscale excitonic emitters. *Nat Commun* **2023**, *14* (1), 2649. DOI: 10.1038/s41467-023-38189-y.

(55) Novoselov, K. S.; Geim, A. K.; Morozov, S. V.; Jiang, D.; Zhang, Y.; Dubonos, S. V.; Grigorieva, I. V.; Firsov, A. A. Electric field effect in atomically thin carbon films. *Science* **2004**, *306* (5696), 666-669. DOI: 10.1126/science.1102896.

(56) Sun, B.; Grap, T.; Frahm, T.; Scholz, S.; Knoch, J. Role of electron and ion irradiation in a reliable lift-off process with electron beam evaporation and a bilayer PMMA resist system. *Journal of Vacuum Science & Technology B, Nanotechnology and Microelectronics: Materials, Processing, Measurement, and Phenomena* **2021**, *39* (5). DOI: 10.1116/6.0001161.

(57) Reina, A.; Jia, X.; Ho, J.; Nezich, D.; Son, H.; Bulovic, V.; Dresselhaus, M. S.; Kong, J. Large area, few-layer graphene films on arbitrary substrates by chemical vapor deposition. *Nano Lett* **2009**, *9* (1), 30-35. DOI: 10.1021/nl801827v.

(58) Lee, Y.; Bae, S.; Jang, H.; Jang, S.; Zhu, S. E.; Sim, S. H.; Song, Y. I.; Hong, B. H.; Ahn, J. H. Wafer-scale synthesis and transfer of graphene films. *Nano Lett* **2010**, *10* (2), 490-493. DOI: 10.1021/nl903272n.

(59) Castellanos-Gomez, A.; Buscema, M.; Molenaar, R.; Singh, V.; Janssen, L.; van der Zant, H. S. J.; Steele, G. A. Deterministic transfer of two-dimensional materials by all-dry viscoelastic stamping. *2D Materials* **2014**, *1* (1). DOI: 10.1088/2053-1583/1/1/011002.

(60) Son, S.; Shin, Y. J.; Zhang, K.; Shin, J.; Lee, S.; Idzuchi, H.; Coak, M. J.; Kim, H.; Kim, J.; Kim, J. H.; et al. Strongly adhesive dry transfer technique for van der Waals heterostructure. *2D Materials* **2020**, *7* (4). DOI: 10.1088/2053-1583/abad0b.

(61) Stevens, C. E.; Chuang, H. J.; Rosenberger, M. R.; McCreary, K. M.; Dass, C. K.; Jonker, B. T.; Hendrickson, J. R. Enhancing the Purity of Deterministically Placed Quantum Emitters in Monolayer WSe(2). *ACS Nano* **2022**, *16* (12), 20956-20963. DOI: 10.1021/acsnano.2c08553.

CHAPTER 5

URANIUM DOPED GALLIUM NITRIDE EPITAXIAL THIN FILMS

Contribution of authors and co-authors

Manuscript in Chapter 5

Author: J. Pierce Fix

Contributions: conceived this work, grew the samples, and conducted optical and atomic force microscope characterization of the samples. Wrote the manuscript.

Author: Volvodymyr B. Buturlim

Contributions: transport measurements, analysis, and text revision for the first draft of the manuscript.

Co-Author: Aaron G. Penders

Contributions: TEM and EDS measurements and analysis, text preparation for the first draft of the manuscript.

Co-Author: Sohail Shah

Contributions: APT measurements and analysis, text preparation for the first draft of the manuscript.

Co-Author: Kevin D. Vallejo

Contributions: revision of the original manuscript.

Co-Author: Krzysztof Gofryk

Contributions: transport analysis, text revision for the first draft of the manuscript, project management (transport side).

Co-Author: Mukesh Bachhav

Contributions: analysis of TEM and APT, text revisions for the first draft of the manuscript, funding acquisition, project management (microscopy side).

Co-Author: Nicholas J. Borys

Contributions: conceived this work, wrote the manuscript.

Co-Author: Brelon J. May

Contributions: conceived this work, wrote the manuscript.

Summary of major contributions made to this work

In this work, I was responsible for growing the samples using MBE under the supervision of Dr. Brelon May and Dr. Kevin Vallejo at Idaho National Laboratory (INL). These samples were the first ever U-doped GaN samples grown by MBE. Our interest in this project is to ultimately investigate QEs from the uranium atoms at dilute doping concentrations. Evidence of narrow emission lines from the uranium atoms is presented in Section 6.2.3.

I was included in the project to not only grow the samples but also to measure topography and the optical properties of U-doped GaN at room temperature and cryogenic temperatures (4 K). At room temperature, I measured Raman scattering, UV-Vis scattering spectra, and the topography using AFM of the samples. For both room temperature and 4K, I carried out two-photon PL spectroscopy. The scanning transmission electron microscopy (STEM), transmission electron microscope – energy-dispersive X-ray spectroscopy (TEM-EDS), atom probe tomography (APT), and X-ray diffraction (XRD) measurements were all conducted by the INL team.

Manuscript information

J. Pierce Fix, Volodymyr B. Buturlim, Aaron G. Penders, Sohail Shah, Kevin D. Vallejo, Krzysztof Gofryk, Mukesh Bachhav, Nicholas J. Borys, Brelon J. May*

Submitted to Advanced Electronic Materials

Status of Manuscript:

☐Prepared for submission to a peer-reviewed journal

☒Officially submitted to a peer-reviewed journal

☐Accepted by a peer-reviewed journal

☐ Published in a peer-reviewed journal

Abstract

Gallium nitride (GaN) is near ubiquitous in modern day technologies forming the backbone of solid-state lighting and high-power electronics. Engineering the physical properties of GaN has been investigated to some degree by the incorporation or doping of most of the elements of the periodic table, but the actinides remain unexplored. Molecular beam epitaxy is used to demonstrate uranium doping of GaN single crystals. High structural quality of the host matrix is maintained despite partial elemental segregation of the uranium dopant into 1D structures at the levels presented here. Electronic transport measurements reveal relatively high conductivity, which persists down to cryogenic temperature and characterized by the formation of narrow gaps in the electronic band structures very close to the Fermi level. Photoluminescence measurements reveal the U-doped GaN exhibits optical behavior similar to that of the GaN substrate. The addition of actinide materials to a non-centrosymmetric, optically active, radiation hard, and electronically tunable host matrix opens a world of possibilities for investigating and leveraging elements with high electron correlations in the pursuit of novel devices.

Introduction

Hexagonal gallium nitride (GaN) is a wide-band gap semiconductor that has been leveraged for a wide variety of technological applications. It is well-known for use in high-power and high-frequency electronics as well as the active media for blue light emitting diodes.[1-3] GaN is also a robust semiconductor that is resilient in extreme environments, including those with significant radiation exposure.[4-6] In addition, with an intrinsic bandgap of 3.4 eV, the physical properties of GaN can be heavily modified by doping and crystalline defects. Doping GaN has been used extensively to modulate electrical conductivity,[7-9] as well as induce magnetism for potential spintronic applications.[10-17] Further, many dopants and defects in GaN form optically active states with strong transitions in the ultraviolet, visible, and near infrared portions of the electromagnetic spectrum.[18] At the single-defect or single-dopant level, many of these mid-gap states have appealing properties as either quantum light sources (i.e., single-photon emitters) and solid-state qubits.[19-30]

A large portion of elements from the periodic table have been incorporated into GaN as dopants or alloys using a wide-range of growth techniques.[9, 19, 20, 31-35] However, the actinide elements, which host of a range of physical phenomena associated with f-shell electrons, have remained largely unexplored. Such dopants and potential dopant-defect complexes have the potential to imbue GaN with electrical and magnetic properties which could be leveraged for solid-state qubits or memories for quantum technologies, all in a platform that is chemically inert and radiation resilient. Here, we report the initial exploration of uranium doped GaN (U:GaN). Molecular beam epitaxy (MBE) was used to synthesize thin films of U:GaN, spanning a range of U concentrations. The physical structure and stoichiometry of these films are fully characterized.

In addition, we report the temperature-dependent magneto-electrical and optical properties of several large-area single phase U:GaN films down to 4 K. A unique quasi-1D structures of the U dopants are observed, and in all cases the U dopants strongly modify the electrical and optical properties of the GaN. Our study here provides an initial foundation on which to explore more exotic properties of U:GaN, especially in the limits of lower concentrations of U that are relevant for solid-state qubit investigations.

Results and discussion

The results presented here are split into two primary parts. First, we explore the physical and stoichiometric properties of the U:GaN films using a calibration structure that is composed of alternating layers of unintentionally doped (uid)-GaN and U:GaN films with increasing concentrations of U. From these layers, we assess how the U atoms are incorporated into the GaN lattice and identify concentrations and limits of U before the crystalline structure of the GaN deteriorates. We also use atom probe tomography (APT) to characterize the spatial dispersion of the U atoms in the U:GaN films. In the second part, we study the crystalline structure, electrical, and optical properties of two single dopant concentration U:GaN systems.

Structural properties

Calibration sample: A calibration sample was deposited to rapidly assess the presumed limitations of U incorporation into the GaN lattice. Changes in the RHEED pattern, namely a transition from streaks to a ring-like pattern would signal a breakdown in the crystallinity of the host matrix. The calibration sample consisted of alternating layers of uid-GaN and U:GaN. The concentration of U was increased in subsequent layers by increasing the output power (OP) increased in 1% intervals starting at an OP of 26%. The deposition of each layer was 198 s, allowing for enough time for the electron-beam source to ramp to and stabilize at the next set point. The entire stack was deposited at a substrate temperature of 700°C and a nominal thickness of 35 nm was targeted for each layer. Figure 5.1a shows a TEM image of the multilayer calibration stack with a schematic overlay. Reflection high-energy electron diffraction (RHEED) images were acquired for each layer and shown on each side of the TEM micrograph. Starting from the bottom, the RHEED pattern of the uid-GaN buffer layer shows a streaky pattern with dim reconstructions signifying a smooth well-ordered surface. The reconstruction disappears during the deposition of the U:GaN layer at OP=26%, but the pattern remains streaky signifying the maintenance of a smooth growth. The 2✕ reconstruction reappears during the overgrowth of subsequent uid-GaN, signifying that high crystalline quality material can be retained after doping with U. At the start of the deposition of the OP=27% layer, arcing of the e-beam resulted in a mandatory pause of the growth process. Further details are provided in the supporting information. Following the pause and deposition of another uid-GaN layer, a RHEED pattern similar to the original uid-GaN layer is observed, indicating that the surface remained of sufficient quality to continue growth of additional U:GaN layers at increasingly greater OP values. These subsequent U:GaN layers showed a slight dimming in the intensity of the RHEED pattern, but very little changes overall even at the highest OP tested (30%).

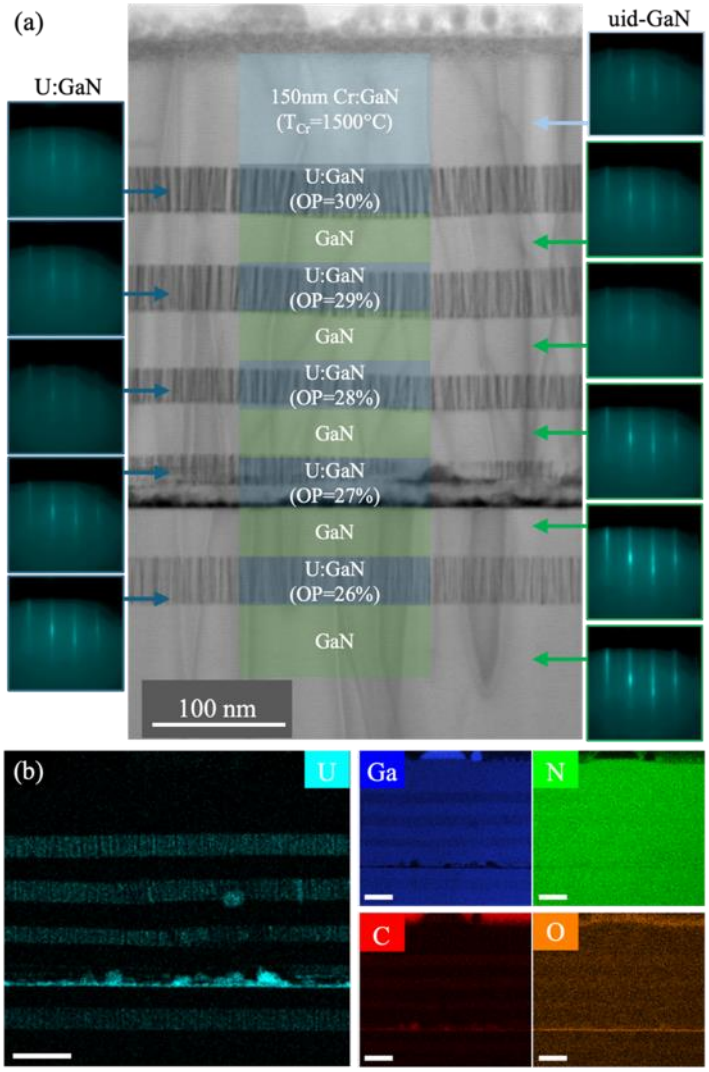

Figure 5.1– (a) Schematic of calibration sample overlaid on STEM image with RHEED patterns for each layer marked by arrows. (b) TEM-EDS maps showing elemental concentrations of species of interest. Scale bars are all 100 nm.

The average thickness of each layer is measured from the half-maximum of contrast variation of the TEM image. The average thicknesses of the uid-GaN and U:GaN layers in the calibration sample are 33.5±1.0 nm and 39.4±3.8 nm, respectively. Excluding the outlier thickness for the layer after the error the standard deviation of the U:GaN layers drops to 1.5 nm. Figure 5.1b shows the concentration of dopant and impurity elements in this stack measured by TEM-EDS. As expected, the concentration of U increases in each successive layer, from 1% to 2%. These measured values match the estimated concentrations based on relative growth rates of oxidized U films and GaN. Additional discussion and analysis of other elements observed in TEM-EDS are contained in the supporting information.

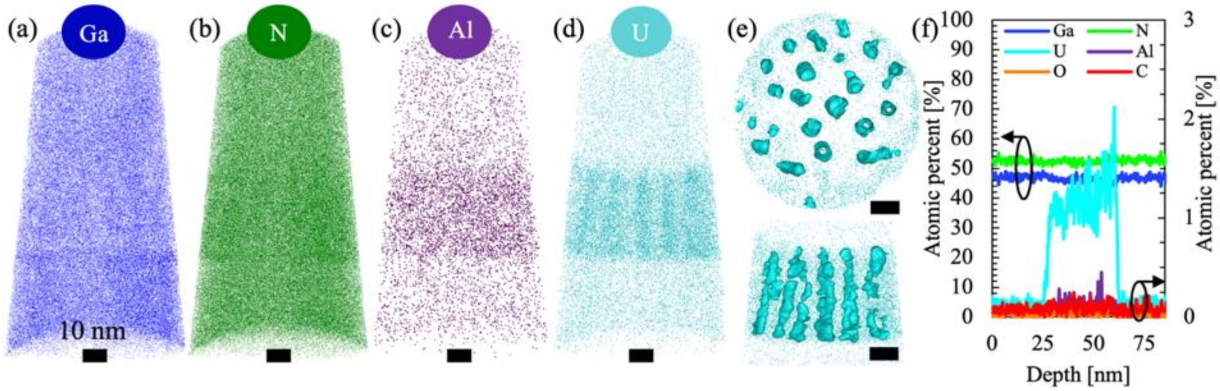

Figure 5.2 – 3D-APT reconstructions of the distribution of different elements (a) Ga, (b) N, (c) Al, and (d) U in the X-Z plane. (e) Volume rendering along with iso-concentration surfaces of U to visualize piping structure in the U-rich region. (f) Atomic fractions of different elemental species.

For APT measurements, stoichiometry analysis depends on carefully ranging all measured peaks within the mass spectrum (supporting information). Several datasets were acquired using laser energies ranging from 0.005 pJ to 0.01 pJ which yielded the expected stoichiometry of GaN and data was collected for several of the layers with varying OP%. However, the yield of measurements was quite low due to fractures at GaN/U interfaces. As can be seen from the atomic distribution maps in Figure 5.2a-d**,** which shows the OP=28% layer, Ga and N are uniformly distributed above, below (Figures 5.2a and 5.2b), and throughout the ~38 nm thick layer doped with U. Iso-concentration surfaces can be used to show regions in 3D that enclose elemental concentrations or densities above a threshold value.[36-38] APT offers 3D reconstruction of this segregation which can be more clearly seen in the iso-concentration (3%) reconstructions in Figure 5.2e viewed from the top (upper) and from the side (lower). The ratio of the atomic percentages for Ga and N is near unity throughout the system as seen in the 1-D concentration profile in Figure 5.2f. Slight enrichment of Al, just above background levels, is observed within the U-rich layer. The spatial segregation of the U overlaps with the higher signal of aluminum which is just above background, but the Al does not show the same degree of segregation, there is a slight increase (up to 0.25%) of Al inside the U-rich regions, but the uncertainty is high. While the average concentration of U relative to all surrounding species in the layer is measured at ~1.2% in the line scan, the local concentration is above 3%. The dopants segregate into U-rich columns parallel to the growth direction. The diameter and spacing of these highly doped columns is relatively uniform. The measured U concentration in the regions between the nanocolumns is the same as the uid-GaN spacer layers above, presenting an extremely asymmetric distribution of dopant species. While APT can only examine an extremely small volume of material, the similarities with contrast variation in lower magnification TEM images suggest phenomena persists at larger length scales.

Single phase samples: The information gathered from the calibration sample informed subsequent depositions of single layers of U:GaN with homogenously supplied U throughout the growth. Samples were fabricated with OP= 28% and 30%, which according to the calibration sample would correspond to average U concentrations in the layers of 1.8% and 2%, respectively. RHEED was monitored throughout the deposition of these samples (supporting information). As expected, very little change was observed throughout the deposition aside from a slight reduction in overall intensity.

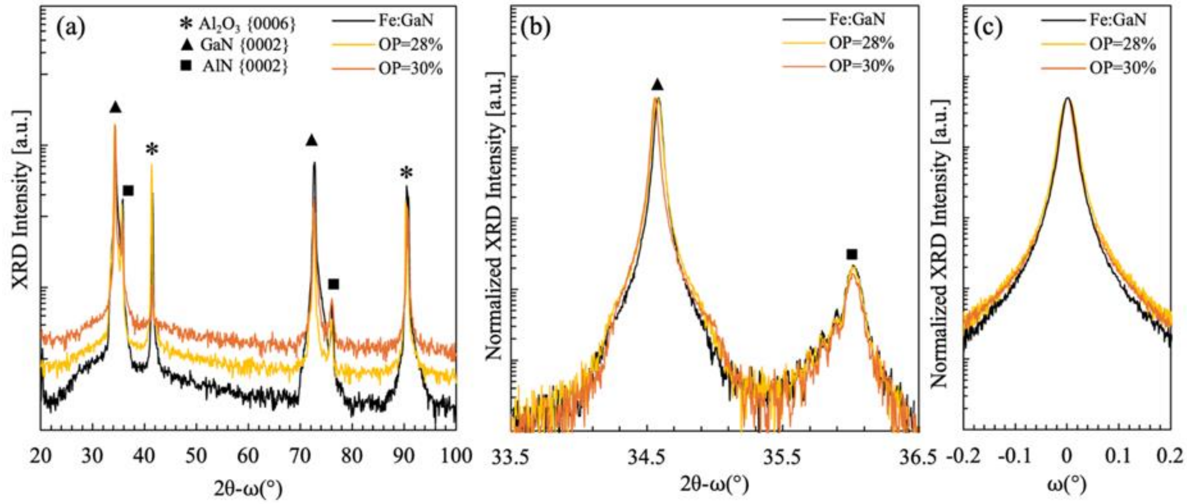

Figure 5.3 – (a) Wide angle XRD scan of starting substrate and U:GaN with different OP%; symbols mark the different groups of diffraction peaks, offset for clarity. (b) Higher resolution XRD scans of the GaN and AlN (0002) peaks with inset showing rocking curves of the GaN (0002) peak. 5×5µm AFM images of (c1) the starting template, (c2) OP=28%, and (c3) OP=30%

High resolution XRD was used to compare the long-range crystalline structure of the single-phase U:GaN samples to the commercial Fe:GaN template on which they were deposited. Small differences in the XRD patterns are identifiable in the wide angle scans (Figure 5.3a) between the Fe:GaN template (black), and the single-phase U:GaN layers. Higher angular resolution 2θ-ω scans around the first order GaN(0002) peak (Figure 5.3b) reveal a subtle shift in the GaN (0002) peak to lower angles. This shift signifies a stretching of the c-axis lattice parameter, which is expected when adding large U atoms. The single-phase U:GaN samples exhibit rocking curves that retain narrow full-width-at-half-maximum (FWHMs) of 0.025 and 0.019°, respectively (Figure 5.3c). The FWHM of the rocking curve of the GaN(0002) peak of the starting template is 0.023°. The similarities between the expected peak positions, absence of any additional peaks, and the narrow rocking curve FWHM remaining similar to that of the starting template are evidence that the structural quality of the U-doped crystal remains high, at least on par with that of the substrate.

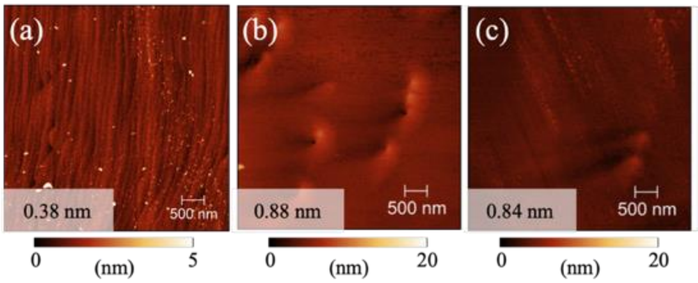

Figure 5.4 – 5×5µm AFM images of (a) the starting template, and U:GaN with (b) OP=28%, and (c) OP=30%.

To further characterize the quality of the single-phase U:GaN films, we analyzed their surface topographies using atomic force microscopy (AFM) as shown in Figure 5.4. The surface of the Fe:GaN template has a root mean squared (RMS) roughness of 0.38 nm. Similar to what was observed in the XRD, minimal differences are observed between samples and the starting template, indicating high-quality growth of continuous thin films of U:GaN for both OP values despite the disappearance of the atomic terraces that were present in the original substrate. The single-phase sample grown at OP=30% exhibits a slightly lower surface roughness than that of the OP=28% sample, which coincides with the sharper rocking curve. Neither significant islands nor hillock spiral structures are observed in either of the two single-phase U:GaN films. Sparse distributions of pits and hole-like defects are observed in both films which could be associated with dislocations.

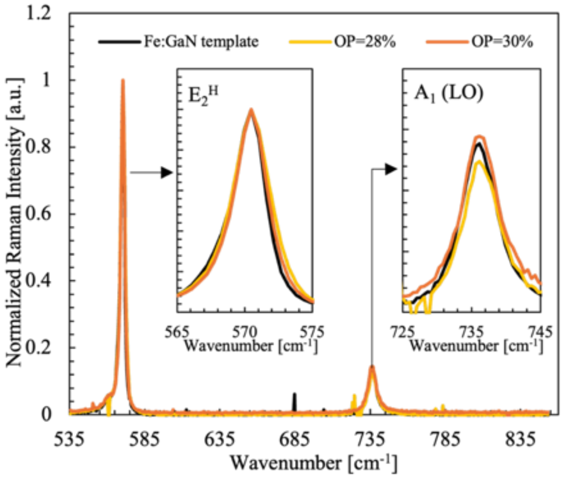

Figure 5.5 – Raman spectra of the Fe:GaN template and U:GaN samples

Raman (Figure 5.5) shows two clear modes with very little difference from the starting substrate. The E_2^H and A_1 (LO) modes are observable in all three films. As shown schematically, the E_2^H mode is an in-plane vibration of the nitrogen atoms that occurs at 568 cm^{-1} and the A_1 (LO) mode is an out-of-plane vibration of the nitrogen and gallium atoms along the c-axis that occurs at 734 cm^{-1}.[39] The energies of the E_2^H and A_1 modes of the U:GaN are only slightly larger (by less than 0.25 cm^{-1}) that those of the Fe:GaN growth substrate. These minute relative shifts could be indicative of a small amount of tensile strain in the U:GaN samples due to the incorporation of the U atoms, in agreement with the small shifts observed in via XRD (Figure 5.3).[40-42]

Transport properties

The temperature dependence of the electrical resistivity (ρ) of U:GaN samples is presented in Figure 5.6a. Overall, the resistivity exhibits negative dρ/dT in the entire temperature range studied, characteristic behavior of narrow gap or/and disordered semiconductors. The measured resistivity values of ~10-15 mΩ·cm at 300K, comparable with Si-doped GaN. The values of the ρ(T) in the high temperature range matches that of MBE-grown uid-GaN under similar conditions (Supporting information), but the U:GaN samples are significantly more conductive, especially at low temperature. A simple conduction model involves two parallel conduction channels: one corresponding to thermal activation of the carriers over a small energy gap and the second one related to the Mott variable range hopping processes.[43] The later describes low-temperature conduction in disordered or doped systems with localized charge-carrier states and has a characteristic temperature dependence of:

$$\sigma(T) = \sigma_h \exp\left[-\left(\frac{T_{Mott}}{T}\right)^{1/(d+1)}\right] \qquad \text{Eq 5.1}$$

where, σ_h is the pre-exponential factor for hopping conductivity, T_{Mott} is the Mott characteristic temperature, which related to the localization length for the charge carriers and the localized density of the states at the Fermi level, and $d$stands for a system dimensionality.[44] Within this approach (d=2) the resistivity is given by the formula:

$$\frac{1}{\rho(T)} = \sigma_a\, exp\left[\frac{-E_g}{2k_BT}\right] + \sigma_h\, exp\left[-\left(\frac{T_{Mott}}{T}\right)^{1/3}\right] \qquad \text{Eq 5.2}$$

where, σ_a is the pre-exponential factor for thermally activated conductivity, E_g is the activation energy gap, and k_B is the Boltzmann constant. Fitting the resistivity with Equation 5.2 (lines in Figure 5.6(a)) yields parameters: σ_a = 0.071 and 0.082 $(\Omega\cdot\text{cm})^{-1}$, E_g = 59.86 and 47.26 meV, σ_h = 0.046 and 0.072 $(\Omega\cdot\text{cm})^{-1}$, T_{Mott} = 0.104 and 0.003 K for OP = 30 % and 28 % samples, respectively. The low value of the T_{Mott} means larger localized length, or less confined wave function for the localized charge carriers, and a finite weak density of localized states at the Fermi level, which lies below a mobility edge (E_C), meaning the electrons must gain hopping energy

$(E_C - E_F)$ to conduct. From the fitted data, OP = 28 % sample has lower Mott temperature than the OP = 30 % sample.

Hall effect measurements (see Supporting information) of U:GaN samples reveal that Hall coefficient is negative in the whole temperature range measured, pointing to electrons being primary carriers for the doped samples. At 300 K the Hall coefficient (R_H) of U:GaN samples, Figure 5.6b, amounts to about -1 and -1.2 cm^3C^{-1} for OP=28% and 30%, respectively. These values are 10^2–10^4 times larger than those typical for simple metals but lower than what has been reported for doped GaN.[45] With decreasing temperature, the R_H stays relatively constant down to ~ 50 K at which $R_H(T)$ starts to increase. Considering a single-band model we derive the Hall carrier concentration (n), Figure 5.6c, which remains fairly constant at ~6×10^{18} and ~5×10^{18} electrons·cm^{-3} for OP=28% and 30%, respectively. The values change very little over most of the temperature range suggesting that the carriers are in a saturated regime and freeze out might occur < 50K, where variable-range hopping starts to dominate. Within this simplified single band approximation the temperature dependence of the Hall mobility (μ) can also be obtained (Figure 5.6d). The mobilities are measured to be 117 and 80 $cm^2V^{-1}s^{-1}$ at 300 K for the OP=28% and 30% samples, respectively. The mobility decreases with decreasing temperature, suggesting that ionized impurity scattering is dominant in these systems.[46] It is worth noting that the higher doping in the OP=30% sample actually resulted in a higher overall resistivity, with a lower carrier concentration and mobility. This could be due to increased segregation of the U dopants into nanostructures as opposed to doping the GaN but is still under investigation.

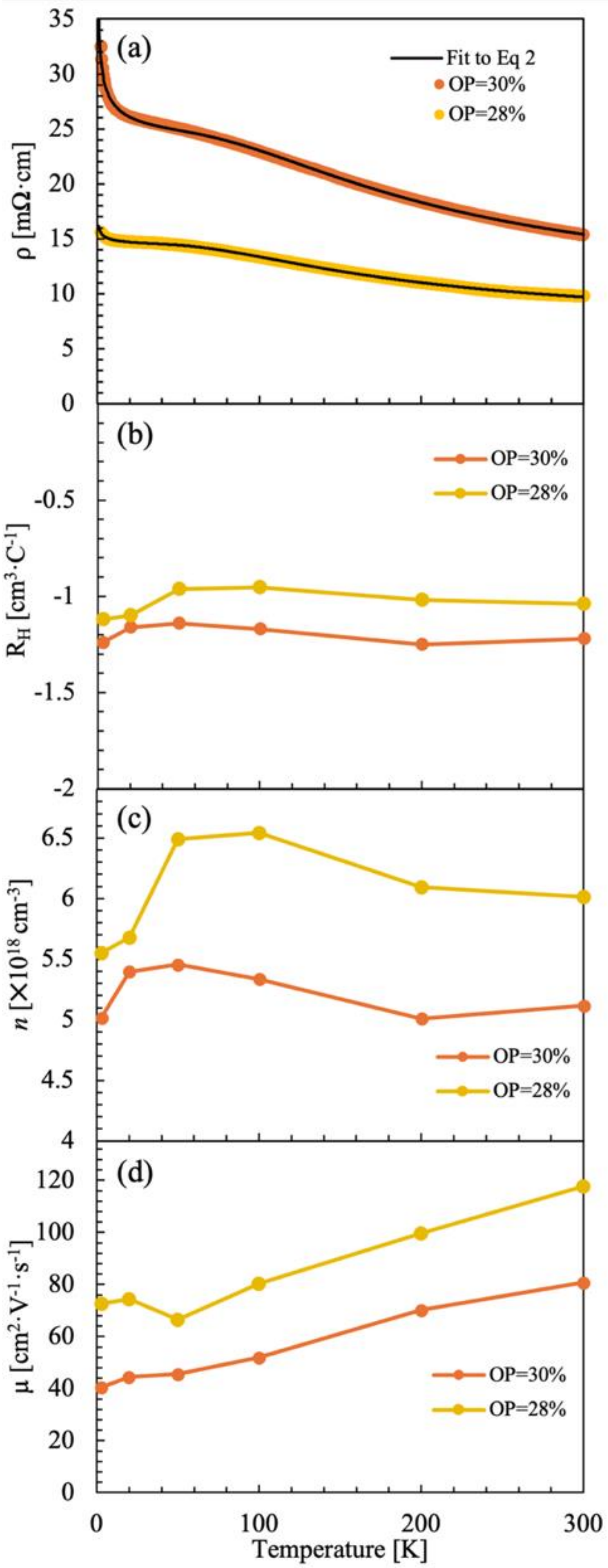

Figure 5.6 – (a) Electrical resistivity, (b) Hall coefficient, (c) carrier concentration, and (d) mobility as function of temperature for U:GaN films with different OP.

Negative magnetoresistance is observed at low temperature (Supporting information) in both U:GaN samples. This is in agreement with the presence of Mott variable hoping that govern conductivity at this temperature range.[47, 48] Above 25 K, magnetoresitivity is evolving to become small and positive, with a maximum measured effect at 8 T and 2 K of 4% and 10% for the OP 28% and 30% samples, respectively.

Optical properties

Band-edge absorption at 300 K of the samples are compared to the template in Figure 5.7a. From extrapolation, we estimate that the band edges for the Fe:GaN, U:GaN grown at OP=28%, and the U:GaN grown at OP=30%, are 3.35 eV, 3.34 eV, and 3.33 eV, respectively. All of the samples have a Stokes shift between the PL band and the absorption edge of ~ 30 meV, which is likely due to trapping/localization of excitons to impurities and defect states. Figure 5.7b reports the band-edge photoluminescence (PL) of the U:GaN layers and Fe:GaN growth template under two-photon excitation at room temperature. Band edge emission is observed for all samples and the intensity decreases as the amount of U is increased. Even at these relatively high doping concentrations, the direct bandgap PL from the U:GaN is not fully suppressed by non-radiative recombination centers (dislocations, impurities, etc.). Future time-resolved spectroscopy measurements could be used to quantify the amount of non-radiative losses due to the U doping. The highest-energy emission band occurs at 3.38 eV for the Fe:GaN growth template and then at 3.38 eV and 3.37 eV for the single-phase U:GaN layers grown at OP=28% and OP=30%, respectively. All of these emission bands lie in close proximity to band-edge emission of bulk GaN (~3.40 eV).[18, 49, 50] All three samples also exhibit a lower-energy peak around 3.27-3.29 eV. This emission peak is ~90 meV lower in energy which is commensurate with it being an LO-phonon replica of the higher-energy peak. We note that as the amount of U in the system is increased, the relative intensity of this peak increases.

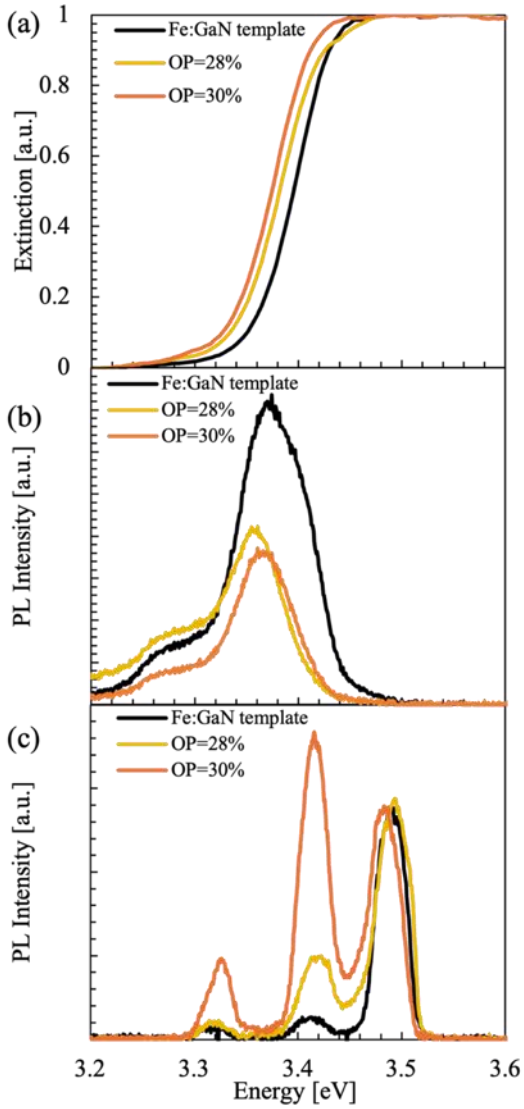

Figure 5.7 – (a) Room temperature UV-vis spectroscopy and (b) PL. (c) Low temperature (4 K) PL of U:GaN compared to the Fe-doped template.

Based on the XRD and Raman characterization, the slight redshift in the room temperature PL for the U:GaN samples is unlikely due to strain. Rather, considering that both the absorption edge extends to increasingly lower energies and the relative intensity of the phonon replica increases with higher U content, the PL measurements indicate that the U dopants create an impurity band (or high-concentration of dopant/defect states) near the band-edge of the GaN. These states increase the strength of the low-energy absorption at the band-edge leading to stronger reabsorption of the high-energy PL at the band-edge. Such state could also lead to trapping of excitons to lower-energy states, but such a systematic shift is not prevalent in the phonon-replica peaks.

The band-edge PL at 4 K (under two-photon excitation) is shown in Figure 5.7c and better resolves the trends observed at room temperature. For all three systems, three primary emission bands are observed between 3.25 and 3.50 eV. The highest energy emission peak is likely dominated by defect-bound free excitons.[49] The two lower-energy peaks which are 90 and 180 meV lower than this highest-energy peak are most likely phonon replicas. Again, only small shifts are seen in the phonon replica peaks, and their relative intensities increase with increasing concentration of U dopants, supporting our hypothesis of enhanced defect-band absorption just below the GaN band-edge.

Conclusion

Gallium nitride was effectively doped with uranium using molecular beam epitaxy. When doped with concentrations in the range of a few percent, the U atoms segregate into vertically oriented structures withing a lesser-doped GaN matrix. Uranium doping at these levels yields GaN with electrical conductivity and modest mobility that is retained down to cryogenic temperatures. Over the electrical transport is driven by the formation of narrow gaps in the electronic band structure near the Fermi energy. Diffraction and Raman spectroscopy measurements showed that the structural quality remained nearly identical to the underlying substrate, and optical measurements reveal a slightly altered, but persistent emission from the near the GaN band edge. The synthesis of these non-uniform doping profiles, which have interesting low temperature properties, without sacrificing the structural or optical properties of a well-studied host matrix could open up pathways investigating the physics of heavy elements or integrating them into novel device schemes.

Experimental methods

Sample fabrication

Monocrystalline GaN thin films were fabricated using a Veeco GenXplor plasma-assisted molecular beam epitaxy system, with a base pressure of $<2\times10^{-10}$ Torr. Unintentionally doped and Fe-doped insulating GaN(0001) templates were mounted onto sample holders using a 10 x 10 mm faceplate with a Si backing wafer. No external surface preparation was performed. The substrates are heated to 200°C under a vacuum of $<1\times10^{-7}$ Torr for two hours prior to introduction to the growth chamber. Upon transfer to the growth chamber the substrates are heated to 700°C as measured with an emissivity correct pyrometer and kSA BandiT system operating in black body mode, both calibrated to the Si 7×7 reconstruction. The GaN templates were exposed to several flashes of Ga to remove any native oxide prior to beginning the deposition.

The Ga was supplied using a standard Knudsen cell with a flux of 10 atoms $\mathrm{nm^{-2}\cdot s^{-1}}$, and nitrogen was supplied using a Veeco radio frequency plasma source operating at 300 W and a nitrogen flow rate of 2.0 sccm, which yielded a chamber pressure of ~1.81e-5 torr just prior to growth. This resulted in a nitrogen limited growth rate of ~16 nm/min estimated from reflection high energy electron diffraction (RHEED) transients measured on a separate GaN substrate prior to growth. To avoid excess Ga accumulation during the growth, the time taken to desorb surplus Ga was also recorded during these transients. This resulted in a typical cycle of 60s Ga+N followed by ~6s of only N which was repeated continuously until the desired thicknesses was reached. RHEED intensity was monitored continuously throughout the growth to ensure a bright pattern returned, sometimes requiring manual intervention to extend the time which the substrate was exposed to N. Uranium source material with a purity of 99.99% was placed in an graphite liner and evaporated using a Telemark 575 electron beam evaporator with a 10 kW power source. The charge is initially melted using a collapsing circular sweep pattern; once melted the pattern is transitioned to focus at a single point in the center to provide a more temporally stable flux. Upon termination of the growth the source is cooled under the larger sweep pattern. Deposition of U on alternative substrates at a similar using an output power (OP) of 30% (~3 kW) revealed a growth rate of about 0.4 $nm \cdot min^{-1}$. Assuming fully dense film of U which oxidized into the crystalline form of UO_2, and an original U sticking coefficient of 1, this gives an estimated flux of 0.16 atoms $nm^{-2} \cdot s^{-1}$. This study focuses on the growth and analysis of a calibration sample where U:GaN layers with increasing U amounts are interspaced by uid-GaN layers on uid-GaN templates. This sample is capped with a Cr-doped GaN layer to serve as a marker for the top of the sample for fabrication of lift outs for microscopy. Subsequently, single concentration samples were deposited on insulating Fe:GaN templates to allow for detailed characterization of dopant dependent physical properties.

Structural properties

Were analyzed in-situ using RHEED and ex-situ using various other techniques. The atom probe tomography (APT) tips were prepared using the conventional focused ion beam

(FIB) lift out process using the Quanta 3D FEG [1] . The final tip diameter for all samples was in the range of 50-80 nm while a 5 kV cleaning process was carried out prior to loading them into the APT. Measurements were carried out using the local electrode atom probe (LEAP) 5000 XR in the Irradiated Materials Characterization Laboratory (IMCL) at Idaho National Laboratory. A pulsed UV laser (λ= 355 nm) was utilized with a pulse energy of 6 fJ (0.006 pJ), a pulse repetition rate of 125 kHz and a detection rate of 0.5%. The chamber pressure was maintained at ~10^{-11} mbar and the temperature of the specimen at 50 K. The data reconstruction was carried out in APSuite 6.3 using the time of flight and ion position on detector data. A constant shank angle was used to reconstruct the datasets, assuming a hemispherical end shape.

Ex-situ X-ray diffraction using a Bruker D8 Advanced X-ray diffractometer with a Ge double-bounce monochromator.

The Raman measurements were performed using a TRIOS AFM-Raman platform (HORIBA Scientific). Our incident laser was focused, and the signal was collected with a Nikon LU Plan Fluor 100x 0.90 A objective. An Andor Kymera 328I spectrograph and an Andor iXon Ultra 888 EMCCD camera were used to detect the signal. The incident laser was a Cobolt Samba 100 532 nm CW laser. Each Raman spectra is averaged over 16 pixels from an area of 15 x 15 um^2. Each pixel was integrated for the following times: 4 seconds for the Fe:GaN substrate and uid-GaN. 10 seconds for the U:GaN samples. The incident laser powers used for each measurement: 266 uW for the Fe:GaN substrate and uid-GaN. And 570 uW for the U:GaN samples. Each pixel was background subtracted before averaging and each average spectra was calibrated to the Si Raman mode at 520 cm^{-1}.

Transport properties

The temperature dependances of the electrical resistivity and Hall coefficient were measured using a Quantum Design DynaCool-9 physical property measurement System (PPMS-9). The aluminum wires were attached to the surface of the films using 7KF Convertible Manual Wire Bonder (West-Bond). The resistivity, Hall resistivity, and magnetoresistance were measured in the temperature range of 300 – 3 K and maximum magnetic field of up to 8 T.

Optical properties

The two-photon PL was taken with a Laser source Chameleon Discovery NX VUE Coherent pulsed tunable laser. The laser was focused and the signal was collected by a Nikon Plan Fluor ELWD 40x/0.60 objective. The signal was coupled into a QP200-2-UV-VIS optical fiber which was coupled to a USB4000 OceanOptics spectrometer with a detection range of 200-530 nm with no entrance slit. The spectrometer was calibrated by fitting a polynomial to the pixel position of known emission wavelengths of a Ocean Insight HG-2 Mercury Calibration Source. Point spectra were taken from each sample at room temperature and 4K. Each spectra was taken with 2 second integration and background subtracted.

UV-VIS was collected from the samples using a Shimadzu UV-2101PC UV-VIS Spectrophotometer. The system has a detection range of 200-900 nm. The samples were placed in a cuvette, and the position of the cuvette in the holder was adjusted to ensure the sample was interacting with the lamp light by tuning the lamp to green light and using an index card to see when the light on the card was blocked by the sample.

Acknowledgements

Funding: BM, SS, AP and MB acknowledge the support from Idaho National Laboratory's Laboratory Directed Research and Development program under DOE Idaho Operations Office Contract DE-AC07-05ID14517. MB also acknowledges the support of Nuclear Science User Facilities scientific technique and expertise development activities. KG, VB, and SR acknowledge the support from the US Department of Energy, Basic Energy Sciences, Materials Sciences, and Engineering Division. KV acknowledges the Center for Thermal Energy Transport under Irradiation (TETI), an Energy Frontier Research Center funded by the U.S. Department of Energy, Office of Science, Office of Basic Energy Sciences at Idaho National Laboratory (INL). JF and NB acknowledge the characterization facilities and support of the MonArk NSF Quantum Foundry, supported by the National Science Foundation Q-AMASE-i program under NSF award No. DMR-1906383.

Data availability statement

The data that support the findings of this study are available from the corresponding author upon reasonable request.

Supporting information: Uranium doped gallium nitride epitaxial thin films

Additional atom probe tomography (APT) and transmission electron microscopy (TEM)

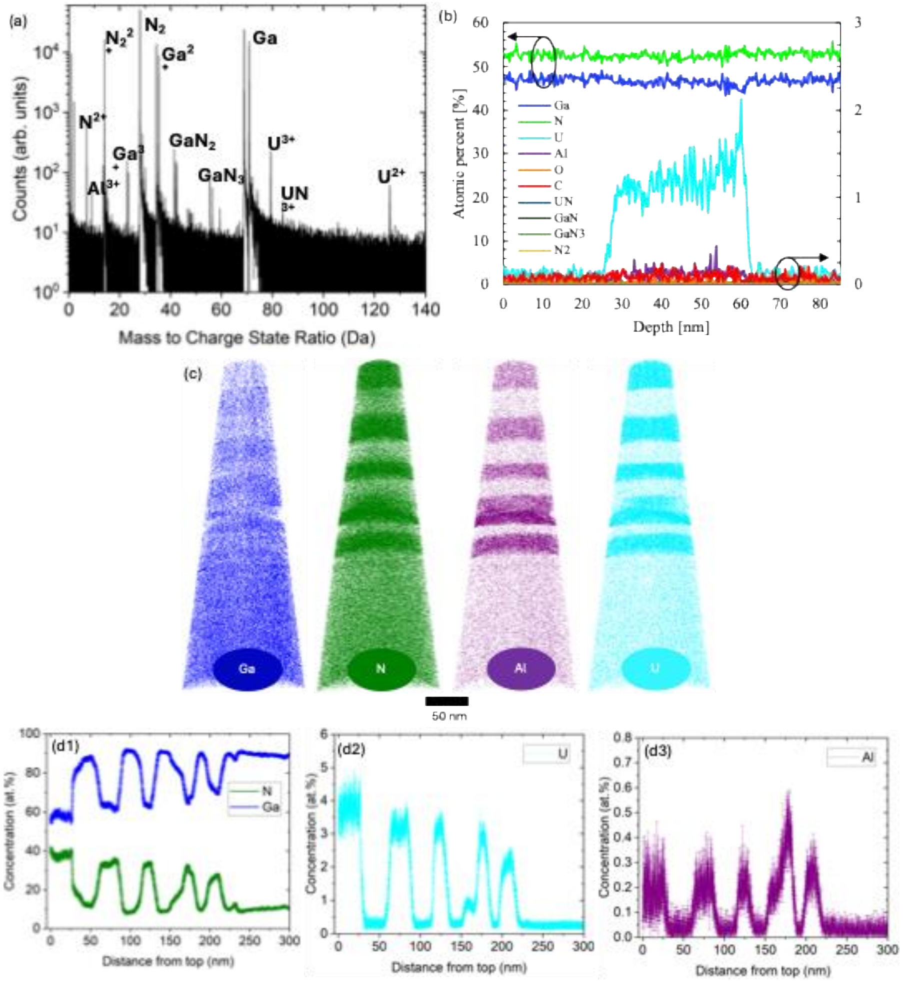

Figure S5.1 – (a) Mass spectrum of APT superlattice region (b) extracted atomic% of different elements from the mass spectrum collected from APT. (c) APT images taken of the entire stack at higher energies, and the resulting (d) elemental concentrations observed for (1) N and Ga, (2) U, and (3) Al.

No peaks are observed in the APT mass spectra shown in Figure S5.1(a), which demonstrates that the presence of compounds other than Ga, N, U, and Al are at least below the noise floor of detection using this technique. In particular the absence of C/O peaks in the APT are notable, as APT involves ablation of the surface contaminants as part of the measurement. This carries across the full depth of the same region of the sample shown in the main manuscript (Figure S5.1(b)). Previous studies have shown parameters used to acquire APT measurements, like the laser energy, strongly affect the overall stoichiometry of Ga:N due to preferential evaporation and multiple evaporation events.[51, 52] However, low laser energy also limits the volume of material that can be investigated in reasonable amounts of time. Therefore, additional datasets were acquired at higher laser energies (10 pJ) to capture multiple layers of U shown in Figure S5.1(c,d). While the microstructure, and clear differences between doped and undoped regions can be seen, the actual values of the relative stoichiometries are very off.

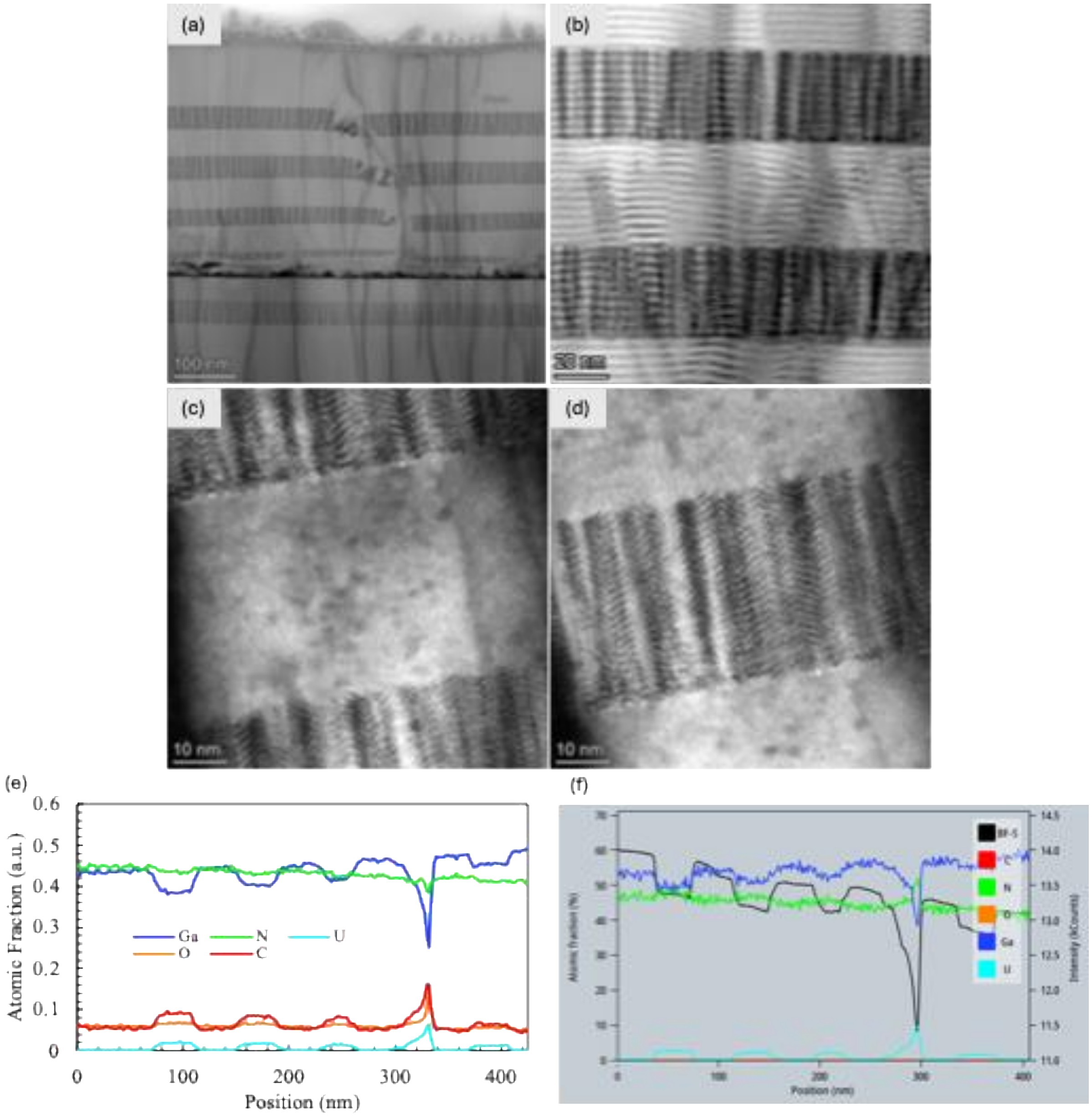

Figure S5.2 – STEM images of a separate area of the calibration sample in the main manuscript. (a) showing large scale defect as a result of the growth interruption. (b) different multilayers at higher magnification, and (c,d) focusing on the interface between layers.

Additional STEM images show distinct contrast variations in the U:GaN layers, which according the EDS measurements shown in the main manuscript are due to U segregation. Defects that arise at the growth interruption are also seen to propagate through all subsequent layers.

Curiously, defects originating below this layer also appear to terminate at this same region. The interface between the U:GaN and uid-GaN layers is also seen to be quite sharp.

Contrary to the APT measurements, TEM-EDS reveals elements beyond Ga, N, and U (Figure S5.2(e)). There is a high concentration of oxygen hovering around 6% in the uid-GaN sections and increasing slightly in the presence of uranium. The higher O% in these regions is not surprising as U getters oxygen, and the sample is exposed to air during preparation of the TEM. In addition, the presence of carbon (C) mirrors that of O but increases to ~10% in the U:GaN layers. However, these background concentrations of O and C are significantly higher than anticipated for growth of GaN via MBE. And the residual gas analyzer does not observe a peak for O or CO during deposition. The TEM-EDS line scans (Figure S5.2(e)) show a relative homogeneity of N across the stack, and in the U:GaN sections lower Ga%, and higher O% and C%. When looking at the U distribution in conjunction with the HAADF image in the main text (Figure 5.1) additional information is revealed. The dark contrast in the region where the growth was paused is due primarily to the formation of U+N material; there is also an increase in oxygen and carbon. However, these species, especially O, are primarily at the interface and not directly tied to the regions with high U. Conversely, the regions with high U show markedly lower Ga and slightly lower N. However, as APT showed no O/C in the films, the TEM-EDS concentrations can be adjusted to match (Figure S5.2(f)), and the values then match the values acquired using low energy APT quite well. Together this illustrates and interesting effect of increased adhesion of both O and C molecules on U:GaN region compared to uid-GaN.

Additional RHEED images of single-phase samples

Figure S5.3 – Schematics and RHEED images for (a) uid-GaN, (b) OP%=28, and (c) OP%=30. The yellow number in the top corner of each image denotes the time elapsed throughout the growth for each image. The rightmost images show RHEED patterns taken at the end of growth, labeled with optional rotations relative to the starting image shown.

Figure S5.3 shows schematics and RHEED images of uid-GaN and U:GaN samples at OP=28% and 30%. Unfortunately, RHEED patterns at multiple rotations were not able to be obtained for all samples due to shadowing of the sample holder, and some patterns are quite limited even in the position they were taken. However, little change is observed throughout the growth of any of the patterns, signifying little change in structural parameters throughout the growth, similar to what is discussed in the main text.

Additional electrical transport

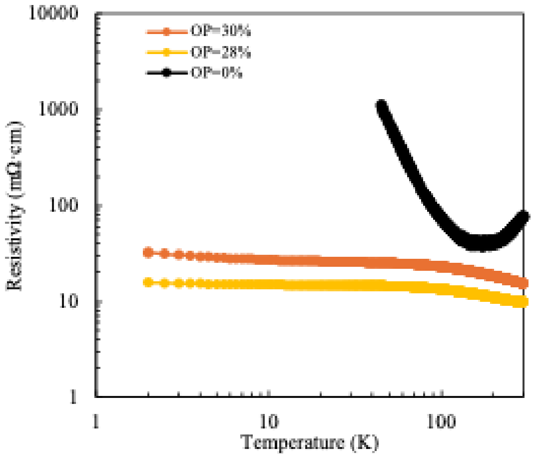

Figure S5.4 – Resistivity as a function of temperature for the samples discussed in the manuscript alongside MBE-grown uid-GaN sample.

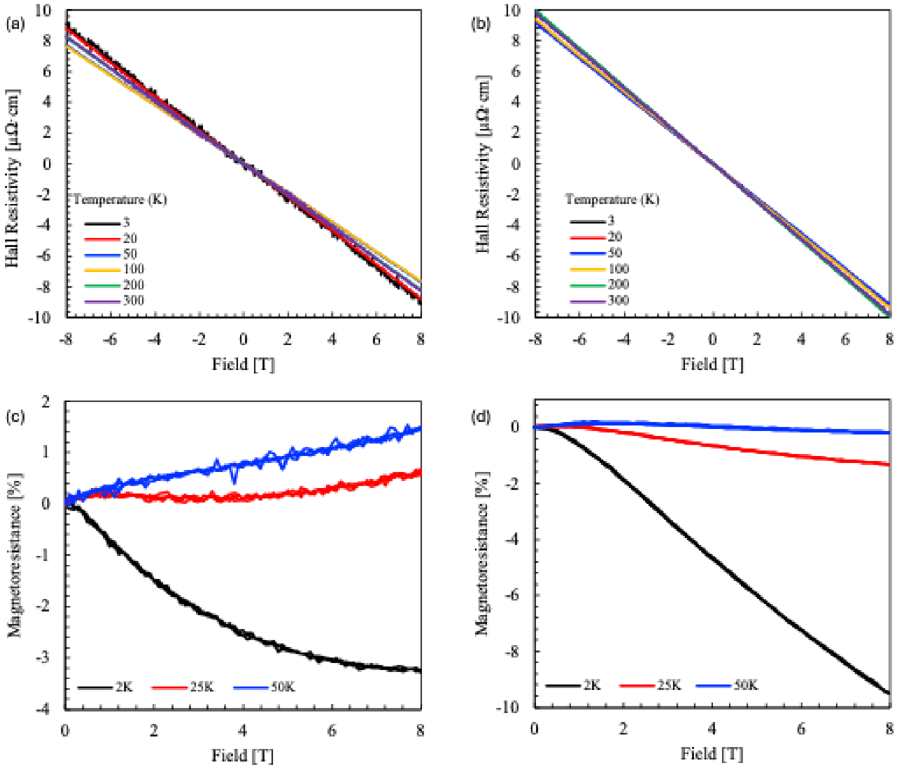

Figure S5.5 – Hall measurements of (a) the OP=28% and (b) the OP=30% samples at different temperatures. Magnetoresistance of the (c) the OP=28% and (d) the OP=30% samples.

References

(1) Udabe, A.; Baraia-Etxaburu, I.; Diez, D. G. Gallium Nitride Power Devices: A State of the Art Review. *IEEE Access* **2023**, *11*, 48628-48650. DOI: 10.1109/ACCESS.2023.3277200.

(2) Akasaki, I. Fascinating journeys into blue light (Nobel Lecture). *Annalen der Physik* **2015**, *527* (5-6), 311-326.

(3) Buffolo, M.; Caria, A.; Piva, F.; Roccato, N.; Casu, C.; De Santi, C.; Trivellin, N.; Meneghesso, G.; Zanoni, E.; Meneghini, M. Defects and reliability of GaN-based LEDs: review and perspectives. *physica status solidi (a)* **2022**, *219* (8), 2100727.

(4) Kozak, J. P.; Zhang, R.; Porter, M.; Song, Q.; Liu, J.; Wang, B.; Wang, R.; Saito, W.; Zhang, Y. Stability, reliability, and robustness of GaN power devices: A review. *IEEE Transactions on Power Electronics* **2023**, *38* (7), 8442-8471.

(5) Pearton, S. J.; Deist, R.; Ren, F.; Liu, L.; Polyakov, A. Y.; Kim, J. Review of radiation damage in GaN-based materials and devices. *Journal of Vacuum Science & Technology A* **2013**, *31* (5), 050801. DOI: 10.1116/1.4799504.

(6) Polyakov, A. Y.; Pearton, S. J.; Frenzer, P.; Ren, F.; Liu, L.; Kim, J. Radiation effects in GaN materials and devices. *Journal of Materials Chemistry C* **2013**, *1* (5), 877-887, 10.1039/C2TC00039C. DOI: 10.1039/C2TC00039C.

(7) Ueno, K.; Taiga, F.; Kobayashi, A.; Fujioka, H. Optical characteristics of highly conductive n-type GaN prepared by pulsed sputtering deposition. *Scientific Reports* **2019**, *9* (1), 20242. DOI: 10.1038/s41598-019-56306-0.

(8) Sheu, J.-K.; Chi, G. Thedoping process and dopant characteristics of GaN. *Journal of Physics: Condensed Matter* **2002**, *14* (22), R657.

(9) Tahan, M.; Nayan, N.; Sahdan, M. Z.; Suhaili, A.; Bakri, E. R. R.; Abdullah, S. A.; Sari, Y.; Shuhaimi, A.; Bakar, A.; Aldalbahi, A. Mini review of n-type and p-type doped GaN thin films. *PROCEEDING OF SCIENCE, ENGINEERING & NANOTECHNOLOGY* **2017**, *7* (8), 6.

(10) Nishizawa, N.; Munekata, H. Lateral-Type Spin-Photonics Devices: Development and Applications. *Micromachines (Basel)* **2021**, *12* (6). DOI: 10.3390/mi12060644.

(11) Wolos, A.; Palczewska, M.; Zajac, M.; Gosk, J.; Kaminska, M.; Twardowski, A.; Bockowski, M.; Grzegory, I.; Porowski, S. Optical and magnetic properties of Mn in bulk GaN. *Physical Review B* **2004**, *69* (11), 115210.

(12) El-Masry, N. A.; Zavada, J. M.; Nepal, N.; Bedair, S. M. 12 - Ferromagnetic behavior in transition metal-doped III-N semiconductors. In *Rare Earth and Transition Metal Doping of Semiconductor Materials*, Dierolf, V., Ferguson, I. T., Zavada, J. M. Eds.; Woodhead Publishing, 2016; pp 395-433, DOI: https://doi.org/10.1016/B978-0-08-100041-0.00012-3.

(13) Hashimoto, M.; Zhou, Y.-K.; Kanamura, M.; Asahi, H. High temperature (>400 K) ferromagnetism in III-V-based diluted magnetic semiconductor GaCrN grown by ECR molecular-beam epitaxy. *Solid State Communications* **2002**, *122*, 37-39.

(14) Park, S. E.; Lee, H.-J.; Cho, Y. C.; Jeong, S.-Y.; Cho, C. R.; Cho, S. Room-temperature ferromagnetism in Cr-doped GaN single crystals. *Applied Physics Letters* **2002**, *80* (22), 4187-4189. DOI: 10.1063/1.1483115.

(15) Sasaki, T.; Sonoda, S.; Yamamoto, Y.; Suga, K.-i.; Shimizu, S.; Kindo, K.; Hori, H. Magnetic and transport characteristics on high Curie temperature ferromagnet of Mn-doped GaN. *Journal of Applied Physics* **2002**, *91* (10), 7911-7913. DOI: 10.1063/1.1451879.

(16) Tandon, N.; Das, G. P.; Kshirsagar, A. Electronic structure of GaN codoped with Mn and Cr. *Physical Review B* **2008**, *77* (20). DOI: 10.1103/PhysRevB.77.205206.

(17) Korotkov, R.; Gregie, J.; Wessels, B. W. Optical properties of the deep Mn acceptor in GaN: Mn. *Applied Physics Letters* **2002**, *80* (10), 1731-1733.

(18) Reshchikov, M. A.; Morkoç, H. Luminescence properties of defects in GaN. *Journal of Applied Physics* **2005**, *97* (6). DOI: 10.1063/1.1868059.

(19) Steckl, A. J.; Zavada, J. M. Optoelectronic Properties and Applications of Rare-Earth-Doped GaN. *MRS Bulletin* **1999**, *24* (9), 33-38. DOI: 10.1557/S0883769400053045.

(20) Zavada, J. M. Revisiting Impurity Doping of III-Nitride Materials for Photonic Device Applications. *ECS Transactions* **2013**, *50* (6), 253.

(21) Hong, K. S.; Lim, H. J.; Ko, Y. H.; Kim, K. J.; Lee, J.; Song, J. H.; Kim, S. H.; Choi, J.; Lee, S. G.; Lee, W. J. Boosting Single-Photon Extraction Efficiency in GaN Through Radiative Mode Conversion. *Laser & Photonics Reviews* **2025**, *19* (10), 2401966.

(22) Nguyen, M.; Zhu, T.; Kianinia, M.; Massabuau, F.; Aharonovich, I.; Toth, M.; Oliver, R.; Bradac, C. Effects of microstructure and growth conditions on quantum emitters in gallium nitride. *APL Materials* **2019**, *7* (8). DOI: 10.1063/1.5098794.

(23) Jun, S.; Choi, M.; Kim, B.; Morassi, M.; Tchernycheva, M.; Song, H. G.; Yeo, H. S.; Gogneau, N.; Cho, Y. H. Enhancement of Single-Photon Purity and Coherence of III-Nitride Quantum Dot with Polarization-Controlled Quasi-Resonant Excitation. *Small* **2023**, *19* (5), 2205229.

(24) Dalla, N.; Kulboka, P.; Kobecki, M.; Misiak, J.; Prystawko, P.; Turski, H.; Kossacki, P.; Jakubczyk, T. Off-resonant photoluminescence spectroscopy of high-optical quality single photon emitters in GaN. *Solid State Communications* **2025**, *397*, 115845.

(25) Geng, Y.; Jena, D.; Fuchs, G. D.; Zipfel, W. R.; Rana, F. Optical dipole structure and orientation of GaN defect single-photon emitters. *ACS Photonics* **2023**, *10* (10), 3723-3729.

(26) Geng, Y.; Nomoto, K. Ultrafast spectral diffusion of GaN defect single photon emitters. *Applied Physics Letters* **2023**, *123* (17). DOI: 10.1063/5.0171855.

(27) Berhane, A. M.; Jeong, K.-Y.; Bradac, C.; Walsh, M.; Englund, D.; Toth, M.; Aharonovich, I. Photophysics of GaN single-photon emitters in the visible spectral range. *Physical Review B* **2018**, *97* (16), 165202.

(28) Holmes, M. J.; Kako, S.; Choi, K.; Arita, M.; Arakawa, Y. Single photons from a hot solid-state emitter at 350 K. *ACS photonics* **2016**, *3* (4), 543-546.

(29) Kim, H.; Song, Y. H.; Ko, Y. H.; Cho, Y. H. Spatial Distribution Control of Room-Temperature Single Photon Emitters in the Telecom Range from GaN Thin Films Grown on Patterned Sapphire Substrates. *Advanced Quantum Technologies* **2025**, *8* (2), 2400177.

(30) Sato, S.-i.; Deki, M.; Nakamura, T.; Nishimura, T.; Stavrevski, D.; Greentree, A. D.; Gibson, B. C.; Ohshima, T. Photoluminescence properties of praseodymium ions implanted into submicron regions in gallium nitride. *Japanese Journal of Applied Physics* **2019**, *58* (5), 051011.

(31) Kucheyev, S. O.; Williams, J. S.; Pearton, S. J. Ion implantation into GaN. *Materials Science and Engineering: R: Reports* **2001**, *33* (2-3), 51-108.

(32) Hite, J. K.; Zavada, J. M. Dilute magnetic III-N semiconductors based on rare earth doping. *ECS Journal of Solid State Science and Technology* **2019**, *8* (9), P527.

(33) Pampili, P.; Parbrook, P. J. Doping of III-nitride materials. *Materials Science in Semiconductor Processing* **2016**, (August), 0-1. DOI: 10.1016/j.mssp.2016.11.006.

(34) Shakil, M.; Hussain, A.; Zafar, M.; Ahmad, S.; Khan, M. I.; Masood, M. K.; Majid, A. Ferromagnetism in GaN doped with transition metals and rare-earth elements: A review. *Chinese Journal of Physics* **2018**, *56* (4), 1570-1577. DOI: 10.1016/j.cjph.2018.05.018.

(35) Zavada, J. M. 8 - Rare Earth Impurities in Wide Gap Semiconductors. In *Processing of Wide Band Gap Semiconductors*, Pearton, S. J. Ed.; William Andrew Publishing, 2000; pp 354-392, DOI: https://doi.org/10.1016/B978-081551439-8.50010-9.

(36) Gnaser, H. Atom probe tomography of nanostructures. *Surface and Interface Analysis* **2014**, *46* (S1), 383-388.

(37) Shah, S.; Howard, C.; Kombaiah, B.; Dasari, S.; Teng, F.; Wang, Y.; Daniel, J.; Bachhav, M. Correlating microstructure and mechanical properties of harvested high dose Zorita light water reactor internals. *Journal of Nuclear Materials* **2024**, *599*, 155241.

(38) Shah, S.; Thronsen, E.; De Geuser, F.; Hatzoglou, C.; Marioara, C. D.; Holmestad, R.; Holmedal, B. On the use of a cluster identification method and a statistical approach for analyzing atom probe tomography data for GP zones in Al–Zn–Mg (–Cu) alloys. *Microscopy and Microanalysis* **2024**, *30* (1), 1-13.

(39) Harima, H. Properties of GaN and related compounds studied by means of Ramanscattering. *Journal of Physics: Condensed Matter* **2002**, *14* (38), R967.

(40) Davydov, V. Y.; Averkiev, N.; Goncharuk, I.; Nelson, D.; Nikitina, I.; Polkovnikov, A.; Smirnov, A.; Jacobson, M.; Semchinova, O. Raman and photoluminescence studies of biaxial strain in GaN epitaxial layers grown on 6H–SiC. *Journal of applied physics* **1997**, *82* (10), 5097-5102.

(41) Atheek, P.; Puviarasu, P.; Basha, S. M.; Balaji, G. Role of micro-Raman technique in material characterization of GaN wide bandgap semiconductor. *Progress in Crystal Growth and Characterization of Materials* **2025**, *71* (2), 100665.

(42) Kuchuk, A. V.; de Oliveira, F. M.; Ghosh, P. K.; Mazur, Y. I.; Stanchu, H. V.; Teodoro, M. D.; Ware, M. E.; Salamo, G. J. Coherent-interface-induced strain in large lattice-mismatched materials: A new approach for modeling Raman shift. *Nano Research* **2022**, *15* (3), 2405-2412.

(43) Mott, N. F. Conduction in non-crystalline materials: III. Localized states in a pseudogap and near extremities of conduction and valence bands. *Philosophical Magazine* **1969**, *19* (160), 835-852.

(44) Gofryk, K.; Kaczorowski, D.; Plackowski, T.; Mucha, J.; Leithe-Jasper, A.; Schnelle, W.; Grin, Y. Magnetic, transport, and thermal properties of the half-Heusler compounds ErPdSb and YPdSb. *Physical Review B—Condensed Matter and Materials Physics* **2007**, *75* (22), 224426.

(45) Kajikawa, Y. Hall factor for hopping conduction in n-and p-type GaN. *physica status solidi c* **2017**, *14* (1-2), 1600129.

(46) Rode, D. L. *Semiconductors and Semimetals*; Academic Press, 1975.

(47) Tremblay, F.; Pepper, M.; Ritchie, D.; Peacock, D.; Frost, J.; Jones, G. Negative magnetoresistance in the variable-range-hopping regime in n-type GaAs. *Physical Review B* **1989**, *39* (11), 8059.

(48) Zhao, H. L.; Spivak, B. Z.; Gelfand, M. P.; Feng, S. Negative magnetoresistance in variable-range-hopping conduction. *Physical Review B* **1991**, *44* (19), 10760.

(49) Reshchikov, M. A. Measurement and analysis of photoluminescence in GaN. *Journal of applied physics* **2021**, *129* (12).

(50) Monemar, B.; Paskov, P.; Bergman, J.; Toropov, A.; Shubina, T.; Malinauskas, T.; Usui, A. Recombination of free and bound excitons in GaN. *physica status solidi (b)* **2008**, *245* (9), 1723-1740.

(51) Di Russo, E.; Blum, I.; Houard, J.; Gilbert, M.; Da Costa, G.; Blavette, D.; Rigutti, L. Compositional accuracy of atom probe tomography measurements in GaN: Impact of experimental parameters and multiple evaporation events. *Ultramicroscopy* **2018**, *187*, 126-134.

(52) Morris, R.; Cuduvally, R.; Melkonyan, D.; Fleischmann, C.; Zhao, M.; Arnoldi, L.; van der Heide, P.; Vandervorst, W. Toward accurate composition analysis of GaN and AlGaN using atom probe tomography. *Journal of Vacuum Science & Technology B* **2018**, *36* (3).

CHAPTER 6

CONCLUDING REMARKS

6.1 Summary

The work conducted in this thesis accomplished many of the proposed objectives. As is common in scientific research, the initial goals evolved in response to the results, leading to more compelling, deeper questions. The study in Chapter 3 began as an investigation of QEs at the interface but developed into a study of the nanoscale properties of the lateral heterostructure $MoS_2/Mo_{(x)}W_{(1-x)}S_2/WS_2$. The non-uniform alloy concentration at the interface inspired the initial objectives of Chapter 4.

The initial goal of Chapter 4 was to investigate the role of dark excitons in the formation mechanism of QEs, as proposed by Linhart *et al.*[1], by nanoindenting 1L-TMD alloys using an AFM probe. This objective led to additional questions about the indentation process itself. The work in Chapter 4 addressed several of these questions, such as how to determine when the indented material has torn.

In Chapter 5, U-doped GaN was grown and optically characterized for the first time to the best of our knowledge. Although this study did not focus on investigating QEs, which remains our primary interest, it establishes a foundation for future work targeting QEs in these samples.

In summary, this thesis demonstrates optical band gap modulation through stoichiometric tuning of a TMD lateral heterostructure interface, the application of localized tensile strain in TMDs, and doping of a wide-bandgap semiconductor. Collectively, this work lays the groundwork for future studies aimed at using these band gap modulation techniques to control QEs.

6.2 Future research outlook

6.2.1 Investigating quantum emitters in single-layer transition metal dichalcogenide alloys using nanoindentation

Because of the work done to optimize nanoindentation using an AFM probe in Chapter 4, the initial goal of investigating the role of dark excitons in the proposed formation mechanism of QEs, discussed in Chapter 1, can be continued. By optimizing the nanoindentation process, we can induce a consistent amount of strain in each alloy, enabling a systematic study of the effect of dark excitons on the QE formation mechanism. Before indenting the alloys again, we decided to first attempt to produce localized strain and induce narrow emitters in an uncontrolled manner as a proof of concept.

To demonstrate that strain and narrow emitters can be induced in the $MoWS_2$ and $MoWSe_2$ alloys, a heterostructure consisting of monolayer W-rich $Mo_{0.02}W_{0.98}S_2$ on multilayer hBN was fabricated. As a result of transferring the 1L alloy onto the hBN, the monolayer is not perfectly flat but instead forms nanobubbles. The room-temperature PL characterization of the sample is shown in Figure 6.1.

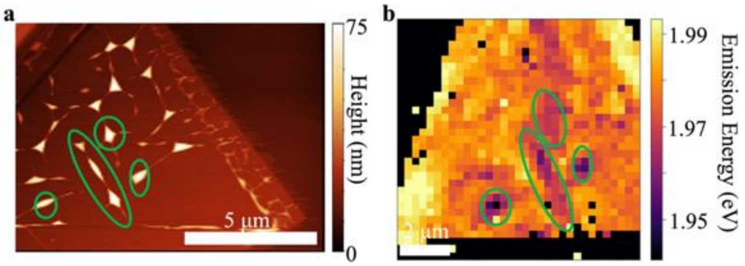

Figure 6.1– Room-temperature PL evidence of strain in W-rich $Mo_{0.02}W_{0.98}S_2$. (a) Topography map of a 1L-W-rich $Mo_{0.02}W_{0.98}S_2$/hbN heterostructure. (b) Is the room-temperature PL emission energy map of the heterostructure. The lower energy regions circled in green correspond to the nanobubbles circled in panel (a).

1L-$Mo_{0.02}W_{0.98}S_2$ nanobubbles, as seen in the topography scan in Figure 6.1a, appear as dark regions in the emission energy map in Figure 6.1b. These dark regions correspond to a shift to lower energies (redshift) in the room temperature PL emission energy, indicating the presence of tensile strain. Figure 6.1b demonstrates that strain can be observed in the alloys. When the sample was cooled to 4 K, signs of a narrowband emission were observed, as shown in Figure 6.2a. The emitter can be localized to a nanobubble by cross-correlating the integrated intensity map and the height map, as shown in the Figures. 6.2b and 6.2c, respectively.

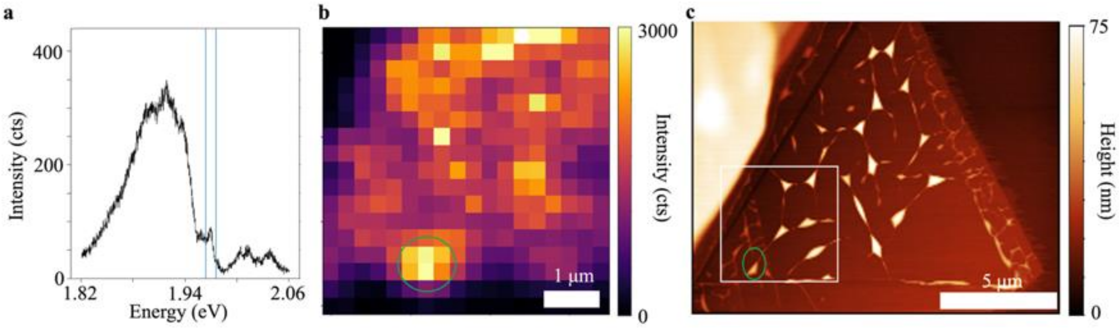

Figure 6.2 – 4 K PL evidence of localized emission from nanobubbles in $Mo_{0.02}W_{0.98}S_2$/hBN. (a) Integrated intensity map, integrated from 1.96 to 1.97 eV, of the region of interest. (b) Point spectra from the region circled in green in the intensity map. (c) Topography map of the sample, showing the location of the intensity map, marked by the white square. The nanobubble of interest in panel (a) is circled in green.

The evidence of strain and narrow emitters in a W-rich TMD alloy lays the foundation for controllably inducing strain in these alloys using the nanoindentation techniques described in Chapter 4 and for studying how the formation of QEs varies as a function of molybdenum and tungsten concentration.

6.2.2 Addressing the scalability issues of single-layer transition metal dichalcogenide

In Chapter 4, a heterostructure consisting of ~8 nm thick graphite on top of indented 1L-WSe_2 was fabricated. The exfoliation and identification of both the 1L-WSe_2 and graphite, as well as the stacking of the graphite onto the 1L-TMD, required two to three days. Sample fabrication time remains a major limitation for scaling 1L-TMDs to industrial applications. To accelerate this process, researchers have begun employing artificial intelligence (AI) software and robotics. For instance, recent studies have demonstrated that AI can analyze microscope images of exfoliated material flakes and identify which ones are monolayers[2]. Additionally, robotic systems have been programmed to stack these materials and assemble heterostructures[3]. The integration of AI and robotics offers a promising path toward scalable production of heterostructures for device applications.

6.2.3 Observing narrow emitters in uranium-doped gallium nitride

Based on the initial room temperature optical characterization of the U-doped GaN samples presented in Chapter 5, the next steps are to perform more in-depth characterization at cryogenic temperatures (4 K) to investigate narrow emitters in these samples and to correlate them with the uranium dopants. We will also need to grow additional samples with lower uranium concentrations.

Preliminary 4 K spectra show emission lines that may be associated with the uranium dopants. As shown in Figure 6.3, these emission lines appear in the IR region and are present only in the two samples with the lowest dopant concentrations. The sample with the highest dopant concentration did not exhibit these emission lines and was therefore excluded from the manuscript.

The highest dopant concentration sample was not U-doped GaN but a UN_x layer sandwiched between pure GaN. As a result, we can conclude that the IR emission is unique to the U-doped GaN samples. Since only two U-doped GaN samples are currently available, the need for additional samples is evident. Growing more U-doped GaN samples with varying uranium concentrations would enable a more comprehensive study of the concentration dependence of the emitters measured at 4 K.

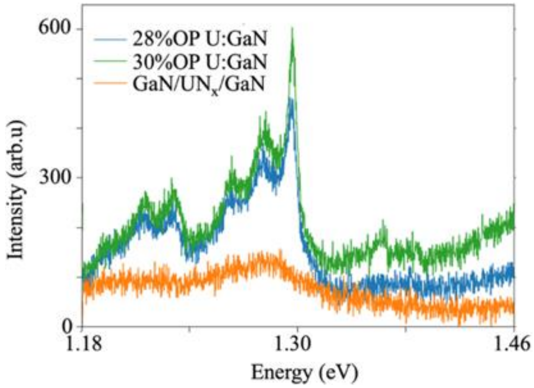

Figure 6.3 – 4K PL evidence of localized emission from the U-doped GaN samples. The emitters are observed in the lower uranium concentration samples.

6.3 Final remarks

Low-dimensional semiconductors and doped thin films represent an exciting avenue for QE research. The many ways to tune the optical properties of these materials, as discussed in this thesis, offer promising opportunities for continued exploration. In particular, unraveling the role of dark excitons in the formation mechanism of QEs in W-rich TMDs will help researchers better engineer QEs in these materials for a variety of applications.

Over the past 5.5 years in the Borys Lab, I have worked on each of the projects discussed in this thesis and participated in many lively discussions with my colleagues. I have learned to appreciate the value of careful, well-designed scientific experiments. I have found great satisfaction and pride in conducting thorough experiments—work that often led to more questions than answers. I feel very fortunate to have worked in such a supportive scientific environment, surrounded by colleagues who have both challenged and encouraged me through the inevitable ups and downs of research.

References

(1) Linhart, L.; Paur, M.; Smejkal, V.; Burgdorfer, J.; Mueller, T.; Libisch, F. Localized Intervalley Defect Excitons as Single-Photon Emitters in WSe_2. *Phys Rev Lett* **2019**, *123* (14), 146401. DOI: 10.1103/PhysRevLett.123.146401.

(2) Yang, J.; Yin, R. A.; Jiang, C.; Hu, Y.; Zhu, X.; Hu, X.; Kumar, S.; Holmes, S. K.; Wang, X.; Zhai, X.; et al. Zero-Shot Autonomous Microscopy for Scalable and Intelligent Characterization of 2D Materials. *ACS Nano* **2025**, *19* (40), 35493-35502. DOI: 10.1021/acsnano.5c09057.

(3) Mannix, A. J.; Ye, A.; Sung, S. H.; Ray, A.; Mujid, F.; Park, C.; Lee, M.; Kang, J. H.; Shreiner, R.; High, A. A.; et al. Robotic four-dimensional pixel assembly of van der Waals solids. *Nat Nanotechnol* **2022**, *17* (4), 361-366. DOI: 10.1038/s41565-021-01061-5.

CUMULATIVE REFERENCES CITED

(1) Abramov, A. N.; Chestnov, I. Y.; Alimova, E. S.; Ivanova, T.; Mukhin, I. S.; Krizhanovskii, D. N.; Shelykh, I. A.; Iorsh, I. V.; Kravtsov, V. Photoluminescence imaging of single photon emitters within nanoscale strain profiles in monolayer WSe_2. *Nat Commun* **2023**, *14* (1), 5737. DOI: 10.1038/s41467-023-41292-9.

(2) Aharonovich, I.; Englund, D.; Toth, M. Solid-state single-photon emitters. *Nature Photonics* **2016**, *10* (10), 631-641. DOI: 10.1038/nphoton.2016.186.

(3) Akasaki, I. Fascinating journeys into blue light (Nobel Lecture). *Annalen der Physik* **2015**, *527* (5-6), 311-326. DOI: 10.1002/andp.201500803.

(4) Ang, Y. S.; Yang, H. Y.; Ang, L. K. Universal Scaling Laws in Schottky Heterostructures Based on Two-Dimensional Materials. *Phys Rev Lett* **2018**, *121* (5), 056802. DOI: 10.1103/PhysRevLett.121.056802.

(5) Aslan, B.; Deng, M.; Heinz, T. F. Strain tuning of excitons in monolayer WSe_2. *Physical Review B* **2018**, *98* (11). DOI: 10.1103/PhysRevB.98.115308.

(6) Atheek, P.; Puviarasu, P.; Basha, S. M.; Balaji, G. Role of micro-Raman technique in material characterization of GaN wide bandgap semiconductor. *Progress in Crystal Growth and Characterization of Materials* **2025**, *71* (2), 100665. DOI: 10.1016/j.pcrysgrow.2025.100665.

(7) Atkin, J. M.; Berweger, S.; Jones, A. C.; Raschke, M. B. Nano-Optical Imaging and Spectroscopy of Order, Phases, and Domains in Complex Solids. *Advances in Physics* **2012**, *61* (6), 745-842. DOI: 10.1080/00018732.2012.737982.

(8) Azzam, S. I.; Parto, K.; Moody, G. Purcell enhancement and polarization control of single-photon emitters in monolayer WSe_2 using dielectric nanoantennas. *Nanophotonics* **2023**, *12* (3), 477-484. DOI: 10.1515/nanoph-2022-0628.

(9) Bao, W.; Borys, N. J.; Ko, C.; Suh, J.; Fan, W.; Thron, A.; Zhang, Y.; Buyanin, A.; Zhang, J.; Cabrini, S.; et al. Visualizing nanoscale excitonic relaxation properties of disordered edges and grain boundaries in monolayer molybdenum disulfide. *Nat Commun* **2015**, *6*, 7993. DOI: 10.1038/ncomms8993.

(10) Basnet, R.; Doha, M.; Hironaka, T.; Pandey, K.; Davari, S.; Welch, K.; Churchill, H.; Hu, J. Growth and Strain Engineering of Trigonal Te for Topological Quantum Phases in Non-Symmorphic Chiral Crystals. *Crystals* **2019**, *9* (10). DOI: 10.3390/cryst9100486.

(11) Berhane, A. M.; Jeong, K.-Y.; Bradac, C.; Walsh, M.; Englund, D.; Toth, M.; Aharonovich, I. Photophysics of GaN single-photon emitters in the visible spectral range. *Physical Review B* **2018**, *97* (16). DOI: 10.1103/PhysRevB.97.165202.

(12) Berhane, A. M.; Jeong, K. Y.; Bodrog, Z.; Fiedler, S.; Schroder, T.; Trivino, N. V.; Palacios, T.; Gali, A.; Toth, M.; Englund, D.; et al. Bright Room-Temperature Single-Photon Emission from Defects in Gallium Nitride. *Adv Mater* **2017**, *29* (12). DOI: 10.1002/adma.201605092.

(13) Berkdemir, A.; Gutierrez, H. R.; Botello-Mendez, A. R.; Perea-Lopez, N.; Elias, A. L.; Chia, C. I.; Wang, B.; Crespi, V. H.; Lopez-Urias, F.; Charlier, J. C.; et al. Identification of Individual and Few Layers of WS_2 Using Raman Spectroscopy. *Scientific Reports* **2013**, *3*, 1755. DOI: 10.1038/srep01755.

(14) Berweger, S.; Zhang, H.; Sahoo, P. K.; Kupp, B. M.; Blackburn, J. L.; Miller, E. M.; Wallis, T. M.; Voronine, D. V.; Kabos, P.; Nanayakkara, S. U. Spatially Resolved Persistent Photoconductivity in MoS_2-WS_2 Lateral Heterostructures. *ACS Nano* **2020**, *14* (10), 14080-14090. DOI: 10.1021/acsnano.0c06745.

(15) Binnewies, M.; Glaum, R.; Schmidt, M.; Schmidt, P. Chemical Vapor Transport Reactions – A Historical Review. *Zeitschrift für anorganische und allgemeine Chemie* **2013**, *639* (2), 219-229. DOI: 10.1002/zaac.201300048.

(16) Binnewies, M.; Schmidt, M.; Schmidt, P. Chemical Vapor Transport Reactions – Arguments for Choosing a Suitable Transport Agent. *Zeitschrift für anorganische und allgemeine Chemie* **2017**, *643* (21), 1295-1311. DOI: 10.1002/zaac.201700055.

(17) Branny, A.; Kumar, S.; Proux, R.; Gerardot, B. D. Deterministic strain-induced arrays of quantum emitters in a two-dimensional semiconductor. *Nat Commun* **2017**, *8*, 15053. DOI: 10.1038/ncomms15053.

(18) Buffolo, M.; Caria, A.; Piva, F.; Roccato, N.; Casu, C.; De Santi, C.; Trivellin, N.; Meneghesso, G.; Zanoni, E.; Meneghini, M. Defects and reliability of GaN-based LEDs: review and perspectives. *physica status solidi (a)* **2022**, *219* (8), 2100727. DOI: 10.1002/pssa.202100727.

(19) Butler, S. Z.; Hollen, S. M.; Cao, L.; Cui, Y.; Gupta, J. A.; Gutierrez, H. R.; Heinz, T. F.; Hong, S. S.; Huang, J.; Ismach, A. F.; et al. Progress, challenges, and opportunities in two-dimensional materials beyond graphene. *ACS Nano* **2013**, *7* (4), 2898-2926. DOI: 10.1021/nn400280c.

(20) Cao, Y.; Luo, X.; Han, S.; Yuan, C.; Yang, Y.; Li, Q.; Yu, T.; Ye, S. Influences of Carrier Gas Flow Rate on the Morphologies of MoS_2 Flakes. *Chemical Physics Letters* **2015**, *631-632*, 30-33. DOI: 10.1016/j.cplett.2015.05.001.

(21) Castellanos-Gomez, A.; Buscema, M.; Molenaar, R.; Singh, V.; Janssen, L.; van der Zant, H. S. J.; Steele, G. A. Deterministic transfer of two-dimensional materials by all-dry viscoelastic stamping. *2D Materials* **2014**, *1* (1). DOI: 10.1088/2053-1583/1/1/011002.

(22) Castellanos-Gomez, A.; Roldan, R.; Cappelluti, E.; Buscema, M.; Guinea, F.; van der Zant, H. S.; Steele, G. A. Local strain engineering in atomically thin MoS_2. *Nano Lett* **2013**, *13* (11), 5361-5366. DOI: 10.1021/nl402875m.

(23) Chakraborty, C.; Kinnischtzke, L.; Goodfellow, K. M.; Beams, R.; Vamivakas, A. N. Voltage-controlled quantum light from an atomically thin semiconductor. *Nat Nanotechnol* **2015**, *10* (6), 507-511. DOI: 10.1038/nnano.2015.79.

(24) Chang, S.; Yan, Y.; Geng, Y. Local Nanostrain Engineering of Monolayer MoS_2 Using Atomic Force Microscopy-Based Thermomechanical Nanoindentation. *Nano Lett* **2023**, *23* (20), 9219-9226. DOI: 10.1021/acs.nanolett.3c01809.

(25) Chen, D. R.; Hofmann, M.; Yao, H. M.; Chiu, S. K.; Chen, S. H.; Luo, Y. R.; Hsu, C. C.; Hsieh, Y. P. Lateral Two-Dimensional Material Heterojunction Photodetectors with Ultrahigh Speed and Detectivity. *ACS Appl Mater Interfaces* **2019**, *11* (6), 6384-6388. DOI: 10.1021/acsami.8b19093.

(26) Chen, K.; Wan, X.; Wen, J. X.; Xie, W. G.; Kang, Z. W.; Zeng, X. L.; Chen, H. J.; Xu, J. B. Electronic Properties of MoS_2-WS_2 Heterostructures Synthesized with Two-Step Lateral Epitaxial Strategy. *Acs Nano* **2015**, *9* (10), 9868-9876. DOI: 10.1021/acsnano.5b03188.

(27) Chen, K.; Wan, X.; Xie, W.; Wen, J.; Kang, Z.; Zeng, X.; Chen, H.; Xu, J. Lateral Built-In Potential of Monolayer MoS_2-WS_2 In-Plane Heterostructures by a Shortcut Growth Strategy. *Adv Mater* **2015**, *27* (41), 6431-6437. DOI: 10.1002/adma.201502375.

(28) Chen, S.; Li, B.; Dai, C.; Zhu, L.; Shen, Y.; Liu, F.; Deng, S.; Ming, F. Controlling Gold-Assisted Exfoliation of Large-Area MoS_2 Monolayers with External Pressure. *Nanomaterials (Basel)* **2024**, *14* (17). DOI: 10.3390/nano14171418.

(29) Chen, Y.; Dumcenco, D. O.; Zhu, Y.; Zhang, X.; Mao, N.; Feng, Q.; Zhang, M.; Zhang, J.; Tan, P. H.; Huang, Y. S.; et al. Composition-Dependent Raman Modes of $Mo_{(1-x)}W_{(x)}S_2$ Monolayer Alloys. *Nanoscale* **2014**, *6* (5), 2833-2839. DOI: 10.1039/c3nr05630a.

(30) Chen, Y.; Xi, J.; Dumcenco, D. O.; Liu, Z.; Suenaga, K.; Wang, D.; Shuai, Z.; Huang, Y. S.; Xie, L. Tunable Band Gap Photoluminescence from Atomically Thin Transition-Metal Dichalcogenide Alloys. *ACS Nano* **2013**, *7* (5), 4610-4616. DOI: 10.1021/nn401420h.

(31) Chen, Y.-C.; Lin, S.-C.; Chou, J.-P.; Tsai, Y.-C.; Huang, C.-T.; Lee, C.-J.; Chang, W.-H. Stable Single Photon Emitters with Large Debye–Waller Factor in Silica. *ACS Photonics* **2025**, *12* (3), 1461-1469. DOI: 10.1021/acsphotonics.4c02001.

(32) Cheng, J.; Wang, C.; Zou, X.; Liao, L. Recent Advances in Optoelectronic Devices Based on 2D Materials and Their Heterostructures. *Advanced Optical Materials* **2019**, *7* (1). DOI: 10.1002/adom.201800441.

(33) Chu, Z.; Han, A.; Lei, C.; Lopatin, S.; Li, P.; Wannlund, D.; Wu, D.; Herrera, K.; Zhang, X.; MacDonald, A. H.; et al. Energy-Resolved Photoconductivity Mapping in a Monolayer-Bilayer WSe_2 Lateral Heterostructure. *Nano Lett* **2018**, *18* (11), 7200-7206. DOI: 10.1021/acs.nanolett.8b03318.

(34) Chuang, H. J.; Stevens, C. E.; Rosenberger, M. R.; Lee, S. J.; McCreary, K. M.; Hendrickson, J. R.; Jonker, B. T. Enhancing Single Photon Emission Purity via Design of van der Waals Heterostructures. *Nano Lett* **2024**, *24* (18), 5529-5535. DOI: 10.1021/acs.nanolett.4c00683.

(35) Conley, H. J.; Wang, B.; Ziegler, J. I.; Haglund, R. F., Jr.; Pantelides, S. T.; Bolotin, K. I. Bandgap engineering of strained monolayer and bilayer MoS_2. *Nano Lett* **2013**, *13* (8), 3626-3630. DOI: 10.1021/nl4014748.

(36) Crampton, K. T.; Lee, J.; Apkarian, V. A. Ion-Selective, Atom-Resolved Imaging of a 2D Cu_2N Insulator: Field and Current Driven Tip-Enhanced Raman Spectromicroscopy Using a Molecule-Terminated Tip. *Acs Nano* **2019**, *13* (6), 6363-6371. DOI: 10.1021/acsnano.9b02744.

(37) Cui, Q.; Ceballos, F.; Kumar, N.; Zhao, H. Transient Absorption Microscopy of Monolayer and Bulk WSe_2. *ACS Nano* **2014**, *8* (3), 2970-2976. DOI: 10.1021/nn500277y.

(38) Cunningham, P. D.; Proscia, N. V.; LaGasse, S. W.; O'Hara, D. J.; McCreary, K. M.; Chuang, H.-J.; Povolotskyi, M.; Vurgaftman, I.; Jonker, B. T.; Simpkins, B. S. Site-Specific Exciton–Plasmon Coupling in Nanoindented WSe_2. *ACS Photonics* **2024**, *11* (8), 3250-3258. DOI: 10.1021/acsphotonics.4c00644.

(39) Dalla, N.; Kulboka, P.; Kobecki, M.; Misiak, J.; Prystawko, P.; Turski, H.; Kossacki, P.; Jakubczyk, T. Off-resonant photoluminescence spectroscopy of high-optical quality single photon emitters in GaN. *Solid State Communications* **2025**, *397*. DOI: 10.1016/j.ssc.2025.115845.

(40) Dang, J.; Sun, S.; Xie, X.; Yu, Y.; Peng, K.; Qian, C.; Wu, S.; Song, F.; Yang, J.; Xiao, S.; et al. Identifying defect-related quantum emitters in monolayer WSe_2. *npj 2D Materials and Applications* **2020**, *4* (1). DOI: 10.1038/s41699-020-0136-0.

(41) Darlington, T. P.; Carmesin, C.; Florian, M.; Yanev, E.; Ajayi, O.; Ardelean, J.; Rhodes, D. A.; Ghiotto, A.; Krayev, A.; Watanabe, K.; et al. Imaging Strain-Localized Excitons in Nanoscale Bubbles of Monolayer WSe_2 at Room Temperature. *Nat Nanotechnol* **2020**, *15* (10), 854-860. DOI: 10.1038/s41565-020-0730-5.

(42) Daveau, R. S.; Vandekerckhove, T.; Mukherjee, A.; Wang, Z.; Shan, J.; Mak, K. F.; Vamivakas, A. N.; Fuchs, G. D. Spectral and spatial isolation of single tungsten diselenide quantum emitters using hexagonal boron nitride wrinkles. *APL Photonics* **2020**, *5* (9). DOI: 10.1063/5.0013825.

(43) Davydov, V. Y.; Averkiev, N.; Goncharuk, I.; Nelson, D.; Nikitina, I.; Polkovnikov, A.; Smirnov, A.; Jacobson, M.; Semchinova, O. Raman and photoluminescence studies of biaxial strain in GaN epitaxial layers grown on 6H–SiC. *Journal of applied physics* **1997**, *82* (10), 5097-5102. DOI: https://doi.org/10.1063/1.366310.

(44) Desai, S. B.; Seol, G.; Kang, J. S.; Fang, H.; Battaglia, C.; Kapadia, R.; Ager, J. W.; Guo, J.; Javey, A. Strain-induced indirect to direct bandgap transition in multilayer WSe_2. *Nano Lett* **2014**, *14* (8), 4592-4597. DOI: 10.1021/nl501638a.

(45) Dhara, S.; Jariwala, D.; Das, S. *Nanoscopy and Nanospectroscopy*; 2023. DOI: 10.1201/9781003248323.

(46) Di Russo, E.; Blum, I.; Houard, J.; Gilbert, M.; Da Costa, G.; Blavette, D.; Rigutti, L. Compositional accuracy of atom probe tomography measurements in GaN: Impact of experimental parameters and multiple evaporation events. *Ultramicroscopy* **2018**, *187*, 126-134. DOI: https://doi.org/10.1016/j.ultramic.2018.02.001.

(47) Eaton, P.; West, P. *Atomic Force Microscopy*; 2010. DOI: 10.1093/acprof:oso/9780199570454.001.0001.

(48) Echeverry, J. P.; Urbaszek, B.; Amand, T.; Marie, X.; Gerber, I. C. Splitting between bright and dark excitons in transition metal dichalcogenide monolayers. *Physical Review B* **2016**, *93* (12). DOI: 10.1103/PhysRevB.93.121107.

(49) El-Masry, N. A.; Zavada, J. M.; Nepal, N.; Bedair, S. M. 12 - Ferromagnetic behavior in transition metal-doped III-N semiconductors. In *Rare Earth and Transition Metal Doping of Semiconductor Materials*, Dierolf, V., Ferguson, I. T., Zavada, J. M. Eds.; Woodhead Publishing, 2016; pp 395-433, DOI: https://doi.org/10.1016/B978-0-08-100041-0.00012-3.

(50) Gadelha, A. C.; Ohlberg, D. A. A.; Rabelo, C.; Neto, E. G. S.; Vasconcelos, T. L.; Campos, J. L.; Lemos, J. S.; Ornelas, V.; Miranda, D.; Nadas, R.; et al. Localization of Lattice Dynamics in Low-Angle Twisted Bilayer Graphene. *Nature* **2021**, *590* (7846), 405-409. DOI: 10.1038/s41586-021-03252-5.

(51) Gao, T.; von Helversen, M.; Antón-Solanas, C.; Schneider, C.; Heindel, T. Atomically-thin single-photon sources for quantum communication. *npj 2D Materials and Applications* **2023**, *7* (1). DOI: 10.1038/s41699-023-00366-4.

(52) Gardiner, D. J. Introduction to Raman Scattering. Springer Berlin Heidelberg, 1989; pp 1-12, DOI: 10.1007/978-3-642-74040-4_1.

(53) Geng, Y.; Jena, D.; Fuchs, G. D.; Zipfel, W. R.; Rana, F. Optical Dipole Structure and Orientation of GaN Defect Single-Photon Emitters. *ACS Photonics* **2023**, *10* (10), 3723-3729. DOI: 10.1021/acsphotonics.3c00917.

(54) Geng, Y.; Nomoto, K. Ultrafast spectral diffusion of GaN defect single photon emitters. *Applied Physics Letters* **2023**, *123* (17). DOI: 10.1063/5.0171855.

(55) Gnaser, H. Atom probe tomography of nanostructures. *Surface and Interface Analysis* **2014**, *46* (S1), 383-388. DOI: https://doi.org/10.1002/sia.5507.

(56) Gofryk, K.; Kaczorowski, D.; Plackowski, T.; Mucha, J.; Leithe-Jasper, A.; Schnelle, W.; Grin, Y. Magnetic, transport, and thermal properties of the half-Heusler compounds ErPdSb and YPdSb. *Physical Review B—Condensed Matter and Materials Physics* **2007**, *75* (22), 224426. DOI: http://dx.doi.org/10.1103/PhysRevB.75.224426.

(57) Gołasa, K.; Grzeszczyk, M.; Bożek, R.; Leszczyński, P.; Wysmołek, A.; Potemski, M.; Babiński, A. Resonant Raman Scattering in MoS_2—From Bulk to Monolayer. *Solid State Communications* **2014**, *197*, 53-56. DOI: 10.1016/j.ssc.2014.08.009.

(58) Grußmayer, K. S.; Herten, D.-P. Photon Antibunching in Single Molecule Fluorescence Spectroscopy. Springer International Publishing, 2014; pp 159-190, DOI: 10.1007/4243_2014_71.

(59) Guo, S.; Germanis, S.; Taniguchi, T.; Watanabe, K.; Withers, F.; Luxmoore, I. J. Electrically Driven Site-Controlled Single Photon Source. *ACS Photonics* **2023**, *10* (8), 2549-2555. DOI: 10.1021/acsphotonics.3c00097.

(60) Gupta, S.; Yang, J. H.; Yakobson, B. I. Two-Level Quantum Systems in Two-Dimensional Materials for Single Photon Emission. *Nano Lett* **2019**, *19* (1), 408-414. DOI: 10.1021/acs.nanolett.8b04159.

(61) Gurugubelli, V. K.; Karmalkar, S. Analytical Theory of the Space-Charge Region of Lateral *p-n* Junctions in Nanofilms. *Journal of Applied Physics* **2015**, *118* (3). DOI: 10.1063/1.4926478.

(62) Han, Y.; Li, M. Y.; Jung, G. S.; Marsalis, M. A.; Qin, Z.; Buehler, M. J.; Li, L. J.; Muller, D. A. Sub-Nanometre Channels Embedded in Two-Dimensional Materials. *Nat Mater* **2018**, *17* (2), 129-133. DOI: 10.1038/nmat5038.

(63) Harima, H. Properties of GaN and related compounds studied by means of Ramanscattering. *Journal of Physics: Condensed Matter* **2002**, *14* (38), R967. DOI: 10.1088/0953-8984/14/38/201.

(64) Hashimoto, M.; Zhou, Y.-K.; Kanamura, M.; Asahi, H. High temperature (>400 K) ferromagnetism in III-V-based diluted magnetic semiconductor GaCrN grown by ECR

molecular-beam epitaxy. *Solid State Communications* **2002**, *122*, 37-39. DOI: 10.1016/S0038-1098(02)00073-X.

(65) He, Y. M.; Clark, G.; Schaibley, J. R.; He, Y.; Chen, M. C.; Wei, Y. J.; Ding, X.; Zhang, Q.; Yao, W.; Xu, X.; et al. Single quantum emitters in monolayer semiconductors. *Nat Nanotechnol* **2015**, *10* (6), 497-502. DOI: 10.1038/nnano.2015.75.

(66) Hite, J. K.; Zavada, J. M. Dilute magnetic III-N semiconductors based on rare earth doping. *ECS Journal of Solid State Science and Technology* **2019**, *8* (9), P527. DOI: http://dx.doi.org/10.1149/2.0261909jss.

(67) Holmes, M. J.; Kako, S.; Choi, K.; Arita, M.; Arakawa, Y. Single Photons from a Hot Solid-State Emitter at 350 K. *ACS Photonics* **2016**, *3* (4), 543-546. DOI: 10.1021/acsphotonics.6b00112.

(68) Hong, K. S.; Lim, H. J.; Ko, Y. H.; Kim, K. J.; Lee, J.; Song, J. H.; Kim, S. H.; Choi, J.; Lee, S. G.; Lee, W. J. Boosting Single-Photon Extraction Efficiency in GaN Through Radiative Mode Conversion. *Laser & Photonics Reviews* **2025**, *19* (10). DOI: 10.1002/lpor.202401966.

(69) Hong, M.; Miller, A.; León-Montiel, R. d. J.; You, C.; Magaña-Loaiza, O. S. Engineering Super-Poissonian Photon Statistics of Spatial Light Modes. *Laser & Photonics Reviews* **2023**, *17* (10). DOI: 10.1002/lpor.202300117.

(70) Hsu, W. T.; Lu, L. S.; Wang, D.; Huang, J. K.; Li, M. Y.; Chang, T. R.; Chou, Y. C.; Juang, Z. Y.; Jeng, H. T.; Li, L. J.; et al. Evidence of indirect gap in monolayer WSe_2. *Nat Commun* **2017**, *8* (1), 929. DOI: 10.1038/s41467-017-01012-6.

(71) Huang, C.; Wu, S.; Sanchez, A. M.; Peters, J. J.; Beanland, R.; Ross, J. S.; Rivera, P.; Yao, W.; Cobden, D. H.; Xu, X. Lateral Heterojunctions within Monolayer $MoSe_2$-WSe_2 Semiconductors. *Nat Mater* **2014**, *13* (12), 1096-1101. DOI: 10.1038/nmat4064.

(72) Huang, T.-X.; Cong, X.; Wu, S.-S.; Lin, K.-Q.; Yao, X.; He, Y.-H.; Wu, J.-B.; Bao, Y.-F.; Huang, S.-C.; Wang, X.; et al. Probing the Edge-Related Properties of Atomically Thin MoS_2 at Nanoscale. *Nature Communications* **2019**, *10* (1). DOI: 10.1038/s41467-019-13486-7.

(73) Huang, Y.; Sutter, E.; Shi, N. N.; Zheng, J.; Yang, T.; Englund, D.; Gao, H. J.; Sutter, P. Reliable Exfoliation of Large-Area High-Quality Flakes of Graphene and Other Two-Dimensional Materials. *ACS Nano* **2015**, *9* (11), 10612-10620. DOI: 10.1021/acsnano.5b04258.

(74) Ilatikhameneh, H.; Ameen, T.; Chen, F.; Sahasrabudhe, H.; Klimeck, G.; Rahman, R. Dramatic Impact of Dimensionality on the Electrostatics of *P-N* Junctions and Its Sensing and Switching Applications. *IEEE Transactions on Nanotechnology* **2018**, *17* (2), 293-298. DOI: 10.1109/tnano.2018.2799960.

(75) Jaculbia, R. B.; Imada, H.; Miwa, K.; Iwasa, T.; Takenaka, M.; Yang, B.; Kazuma, E.; Hayazawa, N.; Taketsugu, T.; Kim, Y. Single-molecule resonance Raman effect in a plasmonic nanocavity. *Nat Nanotechnol* **2020**, *15* (2), 105-110. DOI: 10.1038/s41565-019-0614-8.

(76) Jiang, S.; Zhang, Y.; Zhang, R.; Hu, C. R.; Liao, M. H.; Luo, Y.; Yang, J. L.; Dong, Z. C.; Hou, J. G. Distinguishing Adjacent Molecules on a Surface using Plasmon-Enhanced Raman Scattering. *Nature Nanotechnology* **2015**, *10* (10), 865-869. DOI: 10.1038/nnano.2015.170.

(77) Jo, K.; Kumar, P.; Orr, J.; Anantharaman, S. B.; Miao, J.; Motala, M. J.; Bandyopadhyay, A.; Kisslinger, K.; Muratore, C.; Shenoy, V. B.; et al. Direct Optoelectronic Imaging of 2D Semiconductor-3D Metal Buried Interfaces. *ACS Nano* **2021**, *15* (3), 5618-5630. DOI: 10.1021/acsnano.1c00708.

(78) Jo, K.; Marino, E.; Lynch, J.; Jiang, Z.; Gogotsi, N.; Darlington, T. P.; Soroush, M.; Schuck, P. J.; Borys, N. J.; Murray, C. B.; et al. Direct nano-imaging of light-matter interactions in nanoscale excitonic emitters. *Nat Commun* **2023**, *14* (1), 2649. DOI: 10.1038/s41467-023-38189-y.

(79) Jorio, A.; Saito, R.; Dresselhaus, G.; Dresselhaus, M. S. Quantum Description of Raman Scattering. In *Raman Spectroscopy in Graphene Related Systems*, 2011; pp 103-119, DOI: 10.1002/9783527632695.ch5.

(80) Jun, S.; Choi, M.; Kim, B.; Morassi, M.; Tchernycheva, M.; Song, H. G.; Yeo, H. S.; Gogneau, N.; Cho, Y. H. Enhancement of Single-Photon Purity and Coherence of III-Nitride Quantum Dot with Polarization-Controlled Quasi-Resonant Excitation. *Small* **2023**, *19* (5), e2205229. DOI: 10.1002/smll.202205229.

(81) Jun, S.; Choi, M.; Kim, B.; Morassi, M.; Tchernycheva, M.; Song, H. G.; Yeo, H. S.; Gogneau, N.; Cho, Y. H. Enhancement of Single-Photon Purity and Coherence of III-Nitride Quantum Dot with Polarization-Controlled Quasi-Resonant Excitation. *Small* **2023**, *19* (5), 2205229. DOI: 10.1002/smll.202205229.

(82) Kajikawa, Y. Hall factor for hopping conduction in n-and p-type GaN. *physica status solidi c* **2017**, *14* (1-2), 1600129. DOI: 10.1002/pssc.201600129.

(83) Kalt, H.; Klingshirn, C.; Kalt, H. *Linear optical properties of semiconductors*; Springer, 2019. DOI: https://doi.org/10.1007/978-3-030-24152-0.

(84) Kastl, C.; Chen, C. T.; Kuykendall, T.; Shevitski, B.; Darlington, T. P.; Borys, N. J.; Krayev, A.; Schuck, P. J.; Aloni, S.; Schwartzberg, A. M. The Important Role of Water in Growth of Monolayer Transition Metal Dichalcogenides. *2D Materials* **2017**, *4* (2), 021024. DOI: 10.1088/2053-1583/aa5f4d.

(85) Kern, J.; Niehues, I.; Tonndorf, P.; Schmidt, R.; Wigger, D.; Schneider, R.; Stiehm, T.; Michaelis de Vasconcellos, S.; Reiter, D. E.; Kuhn, T.; et al. Nanoscale Positioning of Single-Photon Emitters in Atomically Thin WSe_2. *Adv Mater* **2016**, *28* (33), 7101-7105. DOI: 10.1002/adma.201600560.

(86) Kim, H.; Moon, J. S.; Noh, G.; Lee, J.; Kim, J. H. Position and Frequency Control of Strain-Induced Quantum Emitters in WSe_2 Monolayers. *Nano Lett* **2019**, *19* (10), 7534-7539. DOI: 10.1021/acs.nanolett.9b03421.

(87) Kim, H.; Song, Y. H.; Ko, Y. H.; Cho, Y. H. Spatial Distribution Control of Room-Temperature Single Photon Emitters in the Telecom Range from GaN Thin Films Grown on Patterned Sapphire Substrates. *Advanced Quantum Technologies* **2024**, *8* (2). DOI: 10.1002/qute.202400177.

(88) Kim, Y.; Yun, S. J.; Lee, E.; Kim, J. Near-Field Visualization of Charge Transfer at $MoSe_2/WSe_2$ Lateral Heterojunction. *Optical Materials Express* **2019**, *9* (4). DOI: 10.1364/ome.9.001864.

(89) Klein, J.; Sigl, L.; Gyger, S.; Barthelmi, K.; Florian, M.; Rey, S.; Taniguchi, T.; Watanabe, K.; Jahnke, F.; Kastl, C.; et al. Engineering the Luminescence and Generation of Individual Defect Emitters in Atomically Thin MoS_2. *ACS Photonics* **2021**, *8* (2), 669-677. DOI: 10.1021/acsphotonics.0c01907.

(90) Klingshirn, C. F. *Semiconductor Optics*; Springer, 2012. DOI: https://doi.org/10.1007/978-3-642-28362-8.

(91) Koperski, M.; Nogajewski, K.; Arora, A.; Cherkez, V.; Mallet, P.; Veuillen, J. Y.; Marcus, J.; Kossacki, P.; Potemski, M. Single photon emitters in exfoliated WSe_2 structures. *Nat Nanotechnol* **2015**, *10* (6), 503-506. DOI: 10.1038/nnano.2015.67.

(92) Korotkov, R.; Gregie, J.; Wessels, B. W. Optical properties of the deep Mn acceptor in GaN: Mn. *Applied Physics Letters* **2002**, *80* (10), 1731-1733. DOI: https://doi.org/10.1063/1.1456544.

(93) Kośmider, K.; González, J. W.; Fernández-Rossier, J. Large spin splitting in the conduction band of transition metal dichalcogenide monolayers. *Physical Review B* **2013**, *88* (24). DOI: 10.1103/PhysRevB.88.245436.

(94) Kozak, J. P.; Zhang, R.; Porter, M.; Song, Q.; Liu, J.; Wang, B.; Wang, R.; Saito, W.; Zhang, Y. Stability, reliability, and robustness of GaN power devices: A review. *IEEE Transactions on Power Electronics* **2023**, *38* (7), 8442-8471. DOI: 10.1109/TPEL.2023.3266365.

(95) Krayev, A.; Bailey, C. S.; Jo, K.; Wang, S.; Singh, A.; Darlington, T.; Liu, G. Y.; Gradecak, S.; Schuck, P. J.; Pop, E.; et al. Dry Transfer of Van Der Waals Crystals to Noble Metal Surfaces To Enable Characterization of Buried Interfaces. *Acs Applied Materials & Interfaces* **2019**, *11* (41), 38218-38225. DOI: 10.1021/acsami.9b09798.

(96) Kucheyev, S. O.; Williams, J. S.; Pearton, S. J. Ion implantation into GaN. *Materials Science and Engineering: R: Reports* **2001**, *33* (2-3), 51-108. DOI: 10.1016/S0927-796X(01)00028-6.

(97) Kuchuk, A. V.; de Oliveira, F. M.; Ghosh, P. K.; Mazur, Y. I.; Stanchu, H. V.; Teodoro, M. D.; Ware, M. E.; Salamo, G. J. Coherent-interface-induced strain in large lattice-mismatched materials: A new approach for modeling Raman shift. *Nano Research* **2022**, *15* (3), 2405-2412. DOI: 10.1007/s12274-021-3855-4.

(98) Kumar, S.; Kaczmarczyk, A.; Gerardot, B. D. Strain-Induced Spatial and Spectral Isolation of Quantum Emitters in Mono- and Bilayer WSe_2. *Nano Lett* **2015**, *15* (11), 7567-7573. DOI: 10.1021/acs.nanolett.5b03312.

(99) Lai, Y.-Y.; Chen, P.-H.; Chen, C.-A.; Lee, Y.-H.; Deng, H. Single-Photon Emission from Rewritable Nanoimprinted Localized Emitter Arrays in Atomically Thin Crystals. *ACS Photonics* **2022**, *9* (3), 752-757. DOI: 10.1021/acsphotonics.1c01543.

(100) Lau, K. W.; Calvin; Gong, Z. R.; Yu, H. Y.; Yao, W. Interface Excitons at Lateral Heterojunctions in Monolayer Semiconductors. *Physical Review B* **2018**, *98* (11), 115427. DOI: 10.1103/PhysRevB.98.115427.

(101) Lee, C.; Jeong, B. G.; Yun, S. J.; Lee, Y. H.; Lee, S. M.; Jeong, M. S. Unveiling Defect-Related Raman Mode of Monolayer WS_2 *Via* Tip-Enhanced Resonance Raman Scattering. *ACS Nano* **2018**, *12* (10), 9982-9990. DOI: 10.1021/acsnano.8b04265.

(102) Lee, S.-J.; Chuang, H.-J.; Yeats, A. L.; McCreary, K. M.; O'Hara, D. J.; Jonker, B. T. Ferroelectric Modulation of Quantum Emitters in Monolayer WS_2. *ACS Nano* **2024**, *18* (36), 25349-25358. DOI: 10.1021/acsnano.4c10528.

(103) Lee, S. J.; Chuang, H. J.; McCreary, K. M.; Noyan, M. A.; Jonker, B. T. Voltage-Induced Degradation for Enhanced Purity and Reproducibility of Quantum Emission in Monolayer 2D Materials. *ACS Nano* **2025**, *19* (38), 33981-33990. DOI: 10.1021/acsnano.5c09799.

(104) Lee, S. J.; Chuang, H. J.; Yeats, A. L.; McCreary, K. M.; O'Hara, D. J.; Jonker, B. T. Ferroelectric Modulation of Quantum Emitters in Monolayer WS_2. *ACS Nano* **2024**, *18* (36), 25349-25358. DOI: 10.1021/acsnano.4c10528.

(105) Lee, Y.; Bae, S.; Jang, H.; Jang, S.; Zhu, S. E.; Sim, S. H.; Song, Y. I.; Hong, B. H.; Ahn, J. H. Wafer-scale synthesis and transfer of graphene films. *Nano Lett* **2010**, *10* (2), 490-493. DOI: 10.1021/nl903272n.

(106) Li, H.; Contryman, A. W.; Qian, X.; Ardakani, S. M.; Gong, Y.; Wang, X.; Weisse, J. M.; Lee, C. H.; Zhao, J.; Ajayan, P. M.; et al. Optoelectronic crystal of artificial atoms in strain-textured molybdenum disulphide. *Nat Commun* **2015**, *6*, 7381. DOI: 10.1038/ncomms8381.

(107) Li, M. Y.; Pu, J.; Huang, J. K.; Miyauchi, Y.; Matsuda, K.; Takenobu, T.; Li, L. J. Self-Aligned and Scalable Growth of Monolayer WSe_2-MoS_2 Lateral Heterojunctions. *Adv Funct Mater* **2018**, *28* (17), 1706860. DOI: 10.1002/adfm.201706860.

(108) Li, M. Y.; Shi, Y.; Cheng, C. C.; Lu, L. S.; Lin, Y. C.; Tang, H. L.; Tsai, M. L.; Chu, C. W.; Wei, K. H.; He, J. H.; et al. Epitaxial Growth of a Monolayer WSe_2-MoS_2 Lateral *P-N* Junction with an Atomically Sharp Interface. *Science* **2015**, *349* (6247), 524-528. DOI: 10.1126/science.aab4097.

(109) Li, X.; Jones, A. C.; Choi, J.; Zhao, H.; Chandrasekaran, V.; Pettes, M. T.; Piryatinski, A.; Tschudin, M. A.; Reiser, P.; Broadway, D. A.; et al. Proximity-induced chiral quantum light generation in strain-engineered WSe_2/$NiPS_3$ heterostructures. *Nat Mater* **2023**, *22* (11), 1311-1316. DOI: 10.1038/s41563-023-01645-7.

(110) Linhart, L.; Paur, M.; Smejkal, V.; Burgdorfer, J.; Mueller, T.; Libisch, F. Localized Intervalley Defect Excitons as Single-Photon Emitters in WSe_2. *Phys Rev Lett* **2019**, *123* (14), 146401. DOI: 10.1103/PhysRevLett.123.146401.

(111) Liu, Y.; Weiss, N. O.; Duan, X.; Cheng, H.-C.; Huang, Y.; Duan, X. Van der Waals heterostructures and devices. *Nature Reviews Materials* **2016**, *1* (9). DOI: 10.1038/natrevmats.2016.42.

(112) Luo, Y.; Liu, N.; Li, X.; Hone, J. C.; Strauf, S. Single photon emission in WSe_2 up 160 K by quantum yield control. *2D Materials* **2019**, *6* (3). DOI: 10.1088/2053-1583/ab15fe.

(113) Luo, Y.; Shepard, G. D.; Ardelean, J. V.; Rhodes, D. A.; Kim, B.; Barmak, K.; Hone, J. C.; Strauf, S. Deterministic coupling of site-controlled quantum emitters in monolayer WSe_2 to plasmonic nanocavities. *Nat Nanotechnol* **2018**, *13* (12), 1137-1142. DOI: 10.1038/s41565-018-0275-z.

(114) Mak, K. F.; Lee, C.; Hone, J.; Shan, J.; Heinz, T. F. Atomically thin MoS_2: a new direct-gap semiconductor. *Phys Rev Lett* **2010**, *105* (13), 136805. DOI: 10.1103/PhysRevLett.105.136805.

(115) Mak, K. F.; Shan, J. Photonics and Optoelectronics of 2D Semiconductor Transition Metal Dichalcogenides. *Nature Photonics* **2016**, *10* (4), 216-226. DOI: 10.1038/nphoton.2015.282.

(116) Mannix, A. J.; Ye, A.; Sung, S. H.; Ray, A.; Mujid, F.; Park, C.; Lee, M.; Kang, J. H.; Shreiner, R.; High, A. A.; et al. Robotic four-dimensional pixel assembly of van der Waals solids. *Nat Nanotechnol* **2022**, *17* (4), 361-366. DOI: 10.1038/s41565-021-01061-5.

(117) Meng, L.; Zhang, Y.; Hu, S.; Wang, X.; Liu, C.; Guo, Y.; Wang, X.; Yan, X. Two Dimensional WS_2 Lateral Heterojunctions by Strain Modulation. *Applied Physics Letters* **2016**, *108* (26). DOI: 10.1063/1.4954991.

(118) Molas, M. R.; Nogajewski, K.; Potemski, M.; Babinski, A. Raman Scattering Excitation Spectroscopy of Monolayer WS_2. *Sci Rep* **2017**, *7* (1), 5036. DOI: 10.1038/s41598-017-05367-0.

(119) Molina-Sanchez, A.; Wirtz, L. Phonons in Single-Layer and Few-Layer MoS_2 and WS_2. *Physical Review B* **2011**, *84* (15), 155413. DOI: 10.1103/PhysRevB.84.155413.

(120) Monemar, B.; Paskov, P.; Bergman, J.; Toropov, A.; Shubina, T.; Malinauskas, T.; Usui, A. Recombination of free and bound excitons in GaN. *physica status solidi (b)* **2008**, *245* (9), 1723-1740. DOI: 10.1002/pssb.200844059.

(121) Montblanch, A. R.; Barbone, M.; Aharonovich, I.; Atature, M.; Ferrari, A. C. Layered materials as a platform for quantum technologies. *Nat Nanotechnol* **2023**, *18* (6), 555-571. DOI: 10.1038/s41565-023-01354-x.

(122) Moody, G.; Kavir Dass, C.; Hao, K.; Chen, C. H.; Li, L. J.; Singh, A.; Tran, K.; Clark, G.; Xu, X.; Berghauser, G.; et al. Intrinsic homogeneous linewidth and broadening mechanisms of excitons in monolayer transition metal dichalcogenides. *Nat Commun* **2015**, *6*, 8315. DOI: 10.1038/ncomms9315.

(123) Moody, G.; Sorger, V. J.; Blumenthal, D. J.; Juodawlkis, P. W.; Loh, W.; Sorace-Agaskar, C.; Jones, A. E.; Balram, K. C.; Matthews, J. C. F.; Laing, A.; et al. 2022 Roadmap on integrated quantum photonics. *Journal of Physics: Photonics* **2022**, *4* (1). DOI: 10.1088/2515-7647/ac1ef4.

(124) Moon, H.; Grosso, G.; Chakraborty, C.; Peng, C.; Taniguchi, T.; Watanabe, K.; Englund, D. Dynamic Exciton Funneling by Local Strain Control in a Monolayer Semiconductor. *Nano Lett* **2020**, *20* (9), 6791-6797. DOI: 10.1021/acs.nanolett.0c02757.

(125) Morris, R.; Cuduvally, R.; Melkonyan, D.; Fleischmann, C.; Zhao, M.; Arnoldi, L.; van der Heide, P.; Vandervorst, W. Toward accurate composition analysis of GaN and AlGaN using atom probe tomography. *Journal of Vacuum Science & Technology B* **2018**, *36* (3). DOI: 10.1116/1.5019693.

(126) Mott, N. F. Conduction in non-crystalline materials: III. Localized states in a pseudogap and near extremities of conduction and valence bands. *Philosophical Magazine* **1969**, *19* (160), 835-852. DOI: 10.1080/14786436908216338.

(127) Mueller, T.; Malic, E. Exciton physics and device application of two-dimensional transition metal dichalcogenide semiconductors. *npj 2D Materials and Applications* **2018**, *2* (1). DOI: 10.1038/s41699-018-0074-2.

(128) Nguyen, M.; Zhu, T.; Kianinia, M.; Massabuau, F.; Aharonovich, I.; Toth, M.; Oliver, R.; Bradac, C. Effects of microstructure and growth conditions on quantum emitters in gallium nitride. *APL Materials* **2019**, *7* (8). DOI: 10.1063/1.5098794.

(129) Nishizawa, N.; Munekata, H. Lateral-Type Spin-Photonics Devices: Development and Applications. *Micromachines (Basel)* **2021**, *12* (6). DOI: 10.3390/mi12060644.

(130) Novoselov, K. S.; Geim, A. K.; Morozov, S. V.; Jiang, D.; Zhang, Y.; Dubonos, S. V.; Grigorieva, I. V.; Firsov, A. A. Electric field effect in atomically thin carbon films. *Science* **2004**, *306* (5696), 666-669. DOI: 10.1126/science.1102896.

(131) Novotny, L.; Hecht, B. *Principles of Nano-Optics*; 2012. DOI: 10.1017/cbo9780511794193.

(132) Palacios-Berraquero, C.; Barbone, M.; Kara, D. M.; Chen, X.; Goykhman, I.; Yoon, D.; Ott, A. K.; Beitner, J.; Watanabe, K.; Taniguchi, T.; et al. Atomically thin quantum light-emitting diodes. *Nat Commun* **2016**, *7*, 12978. DOI: 10.1038/ncomms12978.

(133) Pampili, P.; Parbrook, P. J. Doping of III-nitride materials. *Materials Science in Semiconductor Processing* **2016**, (August), 0-1. DOI: 10.1016/j.mssp.2016.11.006.

(134) Panasci, S. E.; Schiliro, E.; Greco, G.; Cannas, M.; Gelardi, F. M.; Agnello, S.; Roccaforte, F.; Giannazzo, F. Strain, Doping, and Electronic Transport of Large Area Monolayer MoS_2 Exfoliated on Gold and Transferred to an Insulating Substrate. *ACS Appl Mater Interfaces* **2021**, *13* (26), 31248-31259. DOI: 10.1021/acsami.1c05185.

(135) Pant, A.; Mutlu, Z.; Wickramaratne, D.; Cai, H.; Lake, R. K.; Ozkan, C.; Tongay, S. Fundamentals of Lateral and Vertical Heterojunctions of Atomically Thin Materials. *Nanoscale* **2016**, *8* (7), 3870-3887. DOI: 10.1039/c5nr08982d.

(136) Paralikis, A.; Piccinini, C.; Madigawa, A. A.; Metuh, P.; Vannucci, L.; Gregersen, N.; Munkhbat, B. Tailoring polarization in WSe_2 quantum emitters through deterministic strain engineering. *NPJ 2D Mater Appl* **2024**, *8* (1), 59. DOI: 10.1038/s41699-024-00497-2.

(137) Park, J.; Kim, M. S.; Park, B.; Oh, S. H.; Roy, S.; Kim, J.; Choi, W. Composition-Tunable Synthesis of Large-Scale $Mo_{1-x}W_xS_2$ Alloys with Enhanced Photoluminescence. *ACS Nano* **2018**, *12* (6), 6301-6309. DOI: 10.1021/acsnano.8b03408.

(138) Park, K.-d.; Jiang, T.; Clark, G.; Xu, X.; Raschke, M. B. Radiative Control of Dark Excitons at Room Temperature by Nano-Optical Antenna-Tip Purcell Effect. *Nature Nanotechnology* **2018**, *13* (1), 59-64. DOI: 10.1038/s41565-017-0003-0.

(139) Park, K. D.; Khatib, O.; Kravtsov, V.; Clark, G.; Xu, X.; Raschke, M. B. Hybrid Tip-Enhanced Nanospectroscopy and Nanoimaging of Monolayer WSe_2 with Local Strain Control. *Nano Lett* **2016**, *16* (4), 2621-2627. DOI: 10.1021/acs.nanolett.6b00238.

(140) Park, S. E.; Lee, H.-J.; Cho, Y. C.; Jeong, S.-Y.; Cho, C. R.; Cho, S. Room-temperature ferromagnetism in Cr-doped GaN single crystals. *Applied Physics Letters* **2002**, *80* (22), 4187-4189. DOI: 10.1063/1.1483115.

(141) Parto, K.; Azzam, S. I.; Banerjee, K.; Moody, G. Defect and strain engineering of monolayer WSe_2 enables site-controlled single-photon emission up to 150 K. *Nat Commun* **2021**, *12* (1), 3585. DOI: 10.1038/s41467-021-23709-5.

(142) Pearton, S. J.; Deist, R.; Ren, F.; Liu, L.; Polyakov, A. Y.; Kim, J. Review of radiation damage in GaN-based materials and devices. *Journal of Vacuum Science & Technology A* **2013**, *31* (5), 050801. DOI: 10.1116/1.4799504.

(143) Peng, L.; Chan, H.; Choo, P.; Odom, T. W.; Sankaranarayanan, S.; Ma, X. Creation of Single-Photon Emitters in WSe_2 Monolayers Using Nanometer-Sized Gold Tips. *Nano Lett* **2020**, *20* (8), 5866-5872. DOI: 10.1021/acs.nanolett.0c01789.

(144) Pimenta, M. A.; Del Corro, E.; Carvalho, B. R.; Fantini, C.; Malard, L. M. Comparative Study of Raman Spectroscopy in Graphene and MoS_2-Type Transition Metal Dichalcogenides. *Acc Chem Res* **2015**, *48* (1), 41-47. DOI: 10.1021/ar500280m.

(145) Polyakov, A. Y.; Pearton, S. J.; Frenzer, P.; Ren, F.; Liu, L.; Kim, J. Radiation effects in GaN materials and devices. *Journal of Materials Chemistry C* **2013**, *1* (5), 877-887, 10.1039/C2TC00039C. DOI: 10.1039/C2TC00039C.

(146) Ramezani, F.; Strasbourg, M.; Parvez, S.; Saxena, R.; Jariwala, D.; Borys, N. J.; Whitaker, B. M. Predicting quantum emitter fluctuations with time-series forecasting models. *Sci Rep* **2024**, *14* (1), 6920. DOI: 10.1038/s41598-024-56517-0.

(147) Ramirez-Aguilar, K. A.; Rowlen, K. L. Tip Characterization from AFM Images of Nanometric Spherical Particles. *Langmuir* **1998**, *14* (9), 2562-2566. DOI: 10.1021/la971277o.

(148) Reina, A.; Jia, X.; Ho, J.; Nezich, D.; Son, H.; Bulovic, V.; Dresselhaus, M. S.; Kong, J. Large area, few-layer graphene films on arbitrary substrates by chemical vapor deposition. *Nano Lett* **2009**, *9* (1), 30-35. DOI: 10.1021/nl801827v.

(149) Reshchikov, M. A. Measurement and analysis of photoluminescence in GaN. *Journal of applied physics* **2021**, *129* (12). DOI: 10.1063/5.0041608.

(150) Reshchikov, M. A.; Morkoç, H. Luminescence properties of defects in GaN. *Journal of Applied Physics* **2005**, *97* (6). DOI: 10.1063/1.1868059.

(151) Reuter, D.; Werner, C.; Wieck, A. D.; Petrosyan, S. Depletion Characteristics of Two-Dimensional Lateral *P-N*-Junctions. *Applied Physics Letters* **2005**, *86* (16). DOI: 10.1063/1.1897829.

(152) Rode, D. L. *Semiconductors and Semimetals*; Academic Press, 1975. DOI: 10.1016/S0080-8784(08)60331-2.

(153) Rosenberger, M. R.; Dass, C. K.; Chuang, H. J.; Sivaram, S. V.; McCreary, K. M.; Hendrickson, J. R.; Jonker, B. T. Quantum Calligraphy: Writing Single-Photon Emitters in a Two-Dimensional Materials Platform. *ACS Nano* **2019**, *13* (1), 904-912. DOI: 10.1021/acsnano.8b08730.

(154) Sahoo, P. K.; Zong, H.; Liu, J.; Xue, W.; Lai, X.; Gutiérrez, H. R.; Voronine, D. V. Probing Nano-Heterogeneity and Aging Effects in Lateral 2D Heterostructures using Tip-Enhanced Photoluminescence. *Optical Materials Express* **2019**, *9* (4). DOI: 10.1364/ome.9.001620.

(155) Sasaki, T.; Sonoda, S.; Yamamoto, Y.; Suga, K.-i.; Shimizu, S.; Kindo, K.; Hori, H. Magnetic and transport characteristics on high Curie temperature ferromagnet of Mn-doped GaN. *Journal of Applied Physics* **2002**, *91* (10), 7911-7913. DOI: 10.1063/1.1451879.

(156) Sato, S.-i.; Deki, M.; Nakamura, T.; Nishimura, T.; Stavrevski, D.; Greentree, A. D.; Gibson, B. C.; Ohshima, T. Photoluminescence properties of praseodymium ions implanted into submicron regions in gallium nitride. *Japanese Journal of Applied Physics* **2019**, *58* (5). DOI: 10.7567/1347-4065/ab142b.

(157) Schmidt, P.; Binnewies, M.; Glaum, R.; Schmidt, M. Chemical Vapor Transport Reactions–Methods, Materials, Modeling. In *Advanced Topics on Crystal Growth*, 2013; DOI: 10.5772/55547.

(158) Schneider, C.; Glazov, M. M.; Korn, T.; Hofling, S.; Urbaszek, B. Two-dimensional semiconductors in the regime of strong light-matter coupling. *Nat Commun* **2018**, *9* (1), 2695. DOI: 10.1038/s41467-018-04866-6.

(159) Schneider, L. M.; Lippert, S.; Kuhnert, J.; Ajayi, O.; Renaud, D.; Firoozabadi, S.; Ngo, Q.; Guo, R.; Kim, Y. D.; Heimbrodt, W.; et al. The influence of the environment on monolayer tungsten diselenide photoluminescence. *Nano-Structures & Nano-Objects* **2018**, *15*, 84-97. DOI: 10.1016/j.nanoso.2017.08.009.

(160) Schwarz, S.; Kozikov, A.; Withers, F.; Maguire, J. K.; Foster, A. P.; Dufferwiel, S.; Hague, L.; Makhonin, M. N.; Wilson, L. R.; Geim, A. K.; et al. Electrically pumped single-defect light emitters in WSe_2. *2D Materials* **2016**, *3* (2). DOI: 10.1088/2053-1583/3/2/025038.

(161) Shabani, S.; Darlington, T. P.; Gordon, C.; Wu, W.; Yanev, E.; Hone, J.; Zhu, X.; Dreyer, C. E.; Schuck, P. J.; Pasupathy, A. N. Ultralocalized Optoelectronic Properties of Nanobubbles in 2D Semiconductors. *Nano Lett* **2022**, *22* (18), 7401-7407. DOI: 10.1021/acs.nanolett.2c02265.

(162) Shah, S.; Howard, C.; Kombaiah, B.; Dasari, S.; Teng, F.; Wang, Y.; Daniel, J.; Bachhav, M. Correlating microstructure and mechanical properties of harvested high dose Zorita light water reactor internals. *Journal of Nuclear Materials* **2024**, *599*, 155241. DOI: 10.1016/j.jnucmat.2024.155241.

(163) Shah, S.; Thronsen, E.; De Geuser, F.; Hatzoglou, C.; Marioara, C. D.; Holmestad, R.; Holmedal, B. On the use of a cluster identification method and a statistical approach for

analyzing atom probe tomography data for GP zones in Al–Zn–Mg (–Cu) alloys. *Microscopy and Microanalysis* **2024**, *30* (1), 1-13. DOI: 10.1093/micmic/ozad133.

(164) Shakil, M.; Hussain, A.; Zafar, M.; Ahmad, S.; Khan, M. I.; Masood, M. K.; Majid, A. Ferromagnetism in GaN doped with transition metals and rare-earth elements: A review. *Chinese Journal of Physics* **2018**, *56* (4), 1570-1577. DOI: 10.1016/j.cjph.2018.05.018.

(165) Shearer, M. J.; Li, M.-Y.; Li, L.-J.; Jin, S.; Hamers, R. J. Nanoscale Surface Photovoltage Mapping of 2D Materials and Heterostructures by Illuminated Kelvin Probe Force Microscopy. *The Journal of Physical Chemistry C* **2018**, *122* (25), 13564-13571. DOI: 10.1021/acs.jpcc.7b12579.

(166) Shepard, G. D.; Ajayi, O. A.; Li, X.; Zhu, X. Y.; Hone, J.; Strauf, S. Nanobubble induced formation of quantum emitters in monolayer semiconductors. *2D Materials* **2017**, *4* (2). DOI: 10.1088/2053-1583/aa629d.

(167) Sheu, J.-K.; Chi, G. Thedoping process and dopant characteristics of GaN. *Journal of Physics: Condensed Matter* **2002**, *14* (22), R657. DOI: 10.1088/0953-8984/14/22/201.

(168) Smith, T. The hydrophilic nature of a clean gold surface. *Journal of Colloid and Interface Science* **1980**, *75* (1), 51-55. DOI: 10.1016/0021-9797(80)90348-3.

(169) So, J. P.; Kim, H. R.; Baek, H.; Jeong, K. Y.; Lee, H. C.; Huh, W.; Kim, Y. S.; Watanabe, K.; Taniguchi, T.; Kim, J.; et al. Electrically driven strain-induced deterministic single-photon emitters in a van der Waals heterostructure. *Sci Adv* **2021**, *7* (43), eabj3176. DOI: 10.1126/sciadv.abj3176.

(170) Son, S.; Shin, Y. J.; Zhang, K.; Shin, J.; Lee, S.; Idzuchi, H.; Coak, M. J.; Kim, H.; Kim, J.; Kim, J. H.; et al. Strongly adhesive dry transfer technique for van der Waals heterostructure. *2D Materials* **2020**, *7* (4). DOI: 10.1088/2053-1583/abad0b.

(171) Sortino, L.; Zotev, P. G.; Phillips, C. L.; Brash, A. J.; Cambiasso, J.; Marensi, E.; Fox, A. M.; Maier, S. A.; Sapienza, R.; Tartakovskii, A. I. Bright single photon emitters with enhanced quantum efficiency in a two-dimensional semiconductor coupled with dielectric nano-antennas. *Nat Commun* **2021**, *12* (1), 6063. DOI: 10.1038/s41467-021-26262-3.

(172) Splendiani, A.; Sun, L.; Zhang, Y.; Li, T.; Kim, J.; Chim, C. Y.; Galli, G.; Wang, F. Emerging photoluminescence in monolayer MoS_2. *Nano Lett* **2010**, *10* (4), 1271-1275. DOI: 10.1021/nl903868w.

(173) Srivastava, A.; Sidler, M.; Allain, A. V.; Lembke, D. S.; Kis, A.; Imamoglu, A. Optically active quantum dots in monolayer WSe_2. *Nat Nanotechnol* **2015**, *10* (6), 491-496. DOI: 10.1038/nnano.2015.60.

(174) Steckl, A. J.; Zavada, J. M. Optoelectronic Properties and Applications of Rare-Earth-Doped GaN. *MRS Bulletin* **1999**, *24* (9), 33-38. DOI: 10.1557/S0883769400053045.

(175) Stevens, C. E.; Chuang, H. J.; Rosenberger, M. R.; McCreary, K. M.; Dass, C. K.; Jonker, B. T.; Hendrickson, J. R. Enhancing the Purity of Deterministically Placed Quantum Emitters in Monolayer WSe_2. *ACS Nano* **2022**, *16* (12), 20956-20963. DOI: 10.1021/acsnano.2c08553.

(176) Strasbourg, M. C.; Yanev, E. S.; Darlington, T. P.; Faagau, K.; Holtzman, L. N.; Barmak, K.; Hone, J. C.; Schuck, P. J.; Borys, N. J. Characterization of quantum dot-like emitters in programmable arrays of nanowrinkles of 1L-WSe_2. *Journal of Applied Physics* **2024**, *136* (4). DOI: 10.1063/5.0214410.

(177) Su, W.; Kumar, N.; Krayev, A.; Chaigneau, M. *In Situ* Topographical Chemical and Electrical Imaging of Carboxyl Graphene Oxide at the Nanoscale. *Nat Commun* **2018**, *9* (1), 2891. DOI: 10.1038/s41467-018-05307-0.

(178) Su, W.; Kumar, N.; Mignuzzi, S.; Crain, J.; Roy, D. Nanoscale Mapping of Excitonic Processes in Single-Layer MoS_2 Using Tip-Enhanced Photoluminescence Microscopy. *Nanoscale* **2016**, *8* (20), 10564-10569. DOI: 10.1039/c5nr07378b.

(179) Sun, B.; Grap, T.; Frahm, T.; Scholz, S.; Knoch, J. Role of electron and ion irradiation in a reliable lift-off process with electron beam evaporation and a bilayer PMMA resist system. *Journal of Vacuum Science & Technology B, Nanotechnology and Microelectronics: Materials, Processing, Measurement, and Phenomena* **2021**, *39* (5). DOI: 10.1116/6.0001161.

(180) Taghinejad, H.; Eftekhar, A. A.; Campbell, P. M.; Beatty, B.; Taghinejad, M.; Zhou, Y.; Perini, C. J.; Moradinejad, H.; Henderson, W. E.; Woods, E. V.; et al. Strain relaxation via formation of cracks in compositionally modulated two-dimensional semiconductor alloys. *npj 2D Materials and Applications* **2018**, *2* (1). DOI: 10.1038/s41699-018-0056-4.

(181) Tahan, M.; Nayan, N.; Sahdan, M. Z.; Suhaili, A.; Bakri, E. R. R.; Abdullah, S. A.; Sari, Y.; Shuhaimi, A.; Bakar, A.; Aldalbahi, A. Mini review of n-type and p-type doped GaN thin films. *PROCEEDING OF SCIENCE, ENGINEERING & NANOTECHNOLOGY* **2017**, *7* (8), 6.

(182) Tandon, N.; Das, G. P.; Kshirsagar, A. Electronic structure of GaN codoped with Mn and Cr. *Physical Review B* **2008**, *77* (20). DOI: 10.1103/PhysRevB.77.205206.

(183) Tang, C. W.; He, Z.; Chen, W. B.; Jia, S.; Lou, J.; Voronine, D. V. Quantum Plasmonic Hot-Electron Injection in Lateral $WSe_2/MoSe_2$ Heterostructures. *Physical Review B* **2018**, *98* (4), 041402. DOI: 10.1103/PhysRevB.98.041402.

(184) Tonndorf, P.; Schmidt, R.; Schneider, R.; Kern, J.; Buscema, M.; Steele, G. A.; Castellanos-Gomez, A.; van der Zant, H. S. J.; Michaelis de Vasconcellos, S.; Bratschitsch, R. Single-photon emission from localized excitons in an atomically thin semiconductor. *Optica* **2015**, *2* (4). DOI: 10.1364/optica.2.000347.

(185) Tremblay, F.; Pepper, M.; Ritchie, D.; Peacock, D.; Frost, J.; Jones, G. Negative magnetoresistance in the variable-range-hopping regime in n-type GaAs. *Physical Review B* **1989**, *39* (11), 8059. DOI: 10.1103/PhysRevB.39.8059.

(186) Tyurnina, A. V.; Bandurin, D. A.; Khestanova, E.; Kravets, V. G.; Koperski, M.; Guinea, F.; Grigorenko, A. N.; Geim, A. K.; Grigorieva, I. V. Strained Bubbles in van der Waals Heterostructures as Local Emitters of Photoluminescence with Adjustable Wavelength. *ACS Photonics* **2019**, *6* (2), 516-524. DOI: 10.1021/acsphotonics.8b01497.

(187) Udabe, A.; Baraia-Etxaburu, I.; Diez, D. G. Gallium Nitride Power Devices: A State of the Art Review. *IEEE Access* **2023**, *11*, 48628-48650. DOI: 10.1109/ACCESS.2023.3277200.

(188) Ueno, K.; Taiga, F.; Kobayashi, A.; Fujioka, H. Optical characteristics of highly conductive n-type GaN prepared by pulsed sputtering deposition. *Scientific Reports* **2019**, *9* (1), 20242. DOI: 10.1038/s41598-019-56306-0.

(189) Umakoshi, T.; Tanaka, M.; Saito, Y.; Verma, P. White Nanolight Source for Optical Nanoimaging. *Sci Adv* **2020**, *6* (23), eaba4179. DOI: 10.1126/sciadv.aba4179.

(190) Velicky, M.; Donnelly, G. E.; Hendren, W. R.; McFarland, S.; Scullion, D.; DeBenedetti, W. J. I.; Correa, G. C.; Han, Y.; Wain, A. J.; Hines, M. A.; et al. Mechanism of Gold-Assisted

Exfoliation of Centimeter-Sized Transition-Metal Dichalcogenide Monolayers. *ACS Nano* **2018**, *12* (10), 10463-10472. DOI: 10.1021/acsnano.8b06101.

(191) Velicky, M.; Rodriguez, A.; Bousa, M.; Krayev, A. V.; Vondracek, M.; Honolka, J.; Ahmadi, M.; Donnelly, G. E.; Huang, F.; Abruna, H. D.; et al. Strain and Charge Doping Fingerprints of the Strong Interaction between Monolayer MoS_2 and Gold. *J Phys Chem Lett* **2020**, *11* (15), 6112-6118. DOI: 10.1021/acs.jpclett.0c01287.

(192) Verma, P. Tip-Enhanced Raman Spectroscopy: Technique and Recent Advances. *Chem Rev* **2017**, *117* (9), 6447-6466. DOI: 10.1021/acs.chemrev.6b00821.

(193) Walls, D. F. M., G,J. *Quantum Optics*, Second ed.; Springer Berlin Heidelberg, 2008. DOI: 10.1007/978-3-540-28574-8.

(194) Wang, G.; Robert, C.; Glazov, M. M.; Cadiz, F.; Courtade, E.; Amand, T.; Lagarde, D.; Taniguchi, T.; Watanabe, K.; Urbaszek, B.; et al. In-Plane Propagation of Light in Transition Metal Dichalcogenide Monolayers: Optical Selection Rules. *Phys Rev Lett* **2017**, *119* (4), 047401. DOI: 10.1103/PhysRevLett.119.047401.

(195) Wang, G.; Robert, C.; Suslu, A.; Chen, B.; Yang, S.; Alamdari, S.; Gerber, I. C.; Amand, T.; Marie, X.; Tongay, S.; et al. Spin-orbit engineering in transition metal dichalcogenide alloy monolayers. *Nat Commun* **2015**, *6*, 10110. DOI: 10.1038/ncomms10110.

(196) Wang, Q. H.; Kalantar-Zadeh, K.; Kis, A.; Coleman, J. N.; Strano, M. S. Electronics and optoelectronics of two-dimensional transition metal dichalcogenides. *Nat Nanotechnol* **2012**, *7* (11), 699-712. DOI: 10.1038/nnano.2012.193.

(197) Wang, Z.; Liu, P.; Ito, Y.; Ning, S.; Tan, Y.; Fujita, T.; Hirata, A.; Chen, M. Chemical Vapor Deposition of Monolayer $Mo_{(1-x)}W_{(x)}S_2$ Crystals with Tunable Band Gaps. *Sci Rep* **2016**, *6*, 21536. DOI: 10.1038/srep21536.

(198) Wittke, J. P.; Kiss, Z. J.; Duncan, R. C.; McCormick, J. J. Uranium-doped calcium fluoride as a laser material. *Proceedings of the IEEE* **1963**, *51* (1), 56-62. DOI: 10.1109/proc.1963.1659.

(199) Wolos, A.; Palczewska, M.; Zajac, M.; Gosk, J.; Kaminska, M.; Twardowski, A.; Bockowski, M.; Grzegory, I.; Porowski, S. Optical and magnetic properties of Mn in bulk GaN. *Physical Review B* **2004**, *69* (11), 115210. DOI: 10.1103/PhysRevB.69.115210.

(200) Wu, W.; Zhang, Q.; Zhou, X.; Li, L.; Su, J.; Wang, F.; Zhai, T. Self-Powered Photovoltaic Photodetector Established on Lateral Monolayer MoS_2-WS_2 Heterostructures. *Nano Energy* **2018**, *51*, 45-53. DOI: 10.1016/j.nanoen.2018.06.049.

(201) Xue, W.; Sahoo, P. K.; Liu, J.; Zong, H.; Lai, X.; Ambardar, S.; Voronine, D. V. Nano-Optical Imaging of Monolayer $MoSe_2$-WSe_2 Lateral Heterostructure with Subwavelength Domains. *Journal of Vacuum Science & Technology A* **2018**, *36* (5). DOI: 10.1116/1.5035437.

(202) Yanev, E. S.; Darlington, T. P.; Ladyzhets, S. A.; Strasbourg, M. C.; Trovatello, C.; Liu, S.; Rhodes, D. A.; Hall, K.; Sinha, A.; Borys, N. J.; et al. Programmable nanowrinkle-induced room-temperature exciton localization in monolayer WSe_2. *Nat Commun* **2024**, *15* (1), 1543. DOI: 10.1038/s41467-024-45936-2.

(203) Yang, J.; Yin, R. A.; Jiang, C.; Hu, Y.; Zhu, X.; Hu, X.; Kumar, S.; Holmes, S. K.; Wang, X.; Zhai, X.; et al. Zero-Shot Autonomous Microscopy for Scalable and Intelligent Characterization of 2D Materials. *ACS Nano* **2025**, *19* (40), 35493-35502. DOI: 10.1021/acsnano.5c09057.

(204) Yao, K.; Zhang, S.; Yanev, E.; McCreary, K.; Chuang, H. J.; Rosenberger, M. R.; Darlington, T.; Krayev, A.; Jonker, B. T.; Hone, J. C.; et al. Nanoscale Optical Imaging of 2D Semiconductor Stacking Orders by Exciton-Enhanced Second Harmonic Generation. *Advanced Optical Materials* **2022**, *10* (12). DOI: 10.1002/adom.202200085.

(205) Yasaei, P.; Murthy, A. A.; Xu, Y.; Dos Reis, R.; Shekhawat, G. S.; Dravid, V. P. Spatial Mapping of Hot-Spots at Lateral Heterogeneities in Monolayer Transition Metal Dichalcogenides. *Adv Mater* **2019**, *31* (24), e1808244. DOI: 10.1002/adma.201808244.

(206) Yu, C. H.; Yu, Y.; Adsit, L. M.; Chang, J. T.; Barchini, J.; Moberly, A. H.; Benisty, H.; Kim, J.; Young, B. K.; Heng, K.; et al. The Cousa objective: a long-working distance air objective for multiphoton imaging in vivo. *Nat Methods* **2024**, *21* (1), 132-141. DOI: 10.1038/s41592-023-02098-1.

(207) Yu, Y.; Seo, I. C.; Luo, M.; Lu, K.; Son, B.; Tan, J. K.; Nam, D. Tunable single-photon emitters in 2D materials. *Nanophotonics* **2024**, *13* (19), 3615-3629. DOI: 10.1515/nanoph-2024-0050.

(208) Yücel, O.; Yagodkin, D.; Kirchhof, J. N.; Yu, Y.; Kumar, A. M.; Dewambrechies, A.; Kovalchuk, S.; Bolotin, K. I. Strain activation of localized states in WSe_2. *2D Materials* **2025**, *12* (3). DOI: 10.1088/2053-1583/add414.

(209) Zavada, J. M. 8 - Rare Earth Impurities in Wide Gap Semiconductors. In *Processing of Wide Band Gap Semiconductors*, Pearton, S. J. Ed.; William Andrew Publishing, 2000; pp 354-392, DOI: https://doi.org/10.1016/B978-081551439-8.50010-9.

(210) Zavada, J. M. Revisiting Impurity Doping of III-Nitride Materials for Photonic Device Applications. *ECS Transactions* **2013**, *50* (6), 253-259. DOI: 10.1149/05006.0253ecst.

(211) Zhang, J.; Xie, W.; Zhao, J.; Zhang, S. Band Alignment of Two-Dimensional Lateral Heterostructures. *2D Materials* **2016**, *4* (1). DOI: 10.1088/2053-1583/aa50cc.

(212) Zhang, Q.; Zhen, Z.; Yang, Y.; Gan, G.; Jariwala, D.; Cui, X. Negative Refraction Inspired Polariton Lens in Van Der Waals Lateral Heterojunctions. *Applied Physics Letters* **2019**, *114* (22). DOI: 10.1063/1.5098346.

(213) Zhang, R.; Zhang, Y.; Dong, Z. C.; Jiang, S.; Zhang, C.; Chen, L. G.; Zhang, L.; Liao, Y.; Aizpurua, J.; Luo, Y.; et al. Chemical Mapping of a Single Molecule by Plasmon-Enhanced Raman Scattering. *Nature* **2013**, *498* (7452), 82-86. DOI: 10.1038/nature12151.

(214) Zhang, X.; Qiao, X. F.; Shi, W.; Wu, J. B.; Jiang, D. S.; Tan, P. H. Phonon and Raman Scattering of Two-Dimensional Transition Metal Dichalcogenides from Monolayer, Multilayer to Bulk Material. *Chemical Society Reviews* **2015**, *44* (9), 2757-2785. DOI: 10.1039/c4cs00282b.

(215) Zhang, X. Q.; Lin, C. H.; Tseng, Y. W.; Huang, K. H.; Lee, Y. H. Synthesis of Lateral Heterostructures of Semiconducting Atomic Layers. *Nano Lett* **2015**, *15* (1), 410-415. DOI: 10.1021/nl503744f.

(216) Zhang, X. X.; You, Y.; Zhao, S. Y.; Heinz, T. F. Experimental Evidence for Dark Excitons in Monolayer WSe_2. *Phys Rev Lett* **2015**, *115* (25), 257403. DOI: 10.1103/PhysRevLett.115.257403.

(217) Zhang, Z.; Chen, P.; Duan, X.; Zang, K.; Luo, J.; Duan, X. Robust Epitaxial Growth of Two-Dimensional Heterostructures, Multiheterostructures, and Superlattices. *Science* **2017**, *357* (6353), 788-792. DOI: 10.1126/science.aan6814.

(218) Zhao, H. L.; Spivak, B. Z.; Gelfand, M. P.; Feng, S. Negative magnetoresistance in variable-range-hopping conduction. *Physical Review B* **1991**, *44* (19), 10760. DOI: 10.1103/PhysRevB.44.10760.

(219) Zheng, B.; Ma, C.; Li, D.; Lan, J.; Zhang, Z.; Sun, X.; Zheng, W.; Yang, T.; Zhu, C.; Ouyang, G.; et al. Band Alignment Engineering in Two-Dimensional Lateral Heterostructures. *J Am Chem Soc* **2018**, *140* (36), 11193-11197. DOI: 10.1021/jacs.8b07401.